

Clickable surfaces for selective recognition of oligosaccharides

Joshua Ryan Norman

A thesis submitted to

The University of Birmingham

For the degree of DOCTOR OF PHILOSOPHY

School of Chemical Engineering, College of physical Sciences and Engineering, The University of Birmingham

January 2020

UNIVERSITY OF
BIRMINGHAM

University of Birmingham Research Archive

e-theses repository

This unpublished thesis/dissertation is copyright of the author and/or third parties. The intellectual property rights of the author or third parties in respect of this work are as defined by The Copyright Designs and Patents Act 1988 or as modified by any successor legislation.

Any use made of information contained in this thesis/dissertation must be in accordance with that legislation and must be properly acknowledged. Further distribution or reproduction in any format is prohibited without the permission of the copyright holder.

Abstract

With the emergent role of protein glycosylation as a potential biomarker of disease, new technologies are required to selectively recognise unique glycan structures symptomatically expressed in disease states. Currently, glycan recognition is achieved through methods lacking high affinity and selectivity or through complex analytical methods and are poorly suited to clinical laboratories.

In this thesis we propose an alternative glycan sensing strategy based on molecular self-assembly and imprinting of glycan ligands with phenyl boronic acid (PBA), imbuing selective oligosaccharide recognition to a surface. This strategy employs extensive use of the copper catalysed click reaction providing a simple highly biocompatible and adaptable self-assembled monolayer intended to form a foundation for future modifications.

The synthesis and characterisation of various SAM monomers has been described here alongside azide functionalised-PBA CuAAC ligands and PBA terminated SAM monomers. SAMs formed with these were characterised for surface organisation and the CuAAC reaction yield established thus confirming reaction utility in functionalisation of alkyne terminated SAMs. Saccharide binding of PBA functional SAMs was then examined accounting for surface organisation between SAM

monomer designs. Having determined a suitable SAM for functionalisation, we then produced a novel oligosaccharide-PBA imprinted surface demonstrating high selectivity between structurally different oligosaccharides. An overview of this thesis is provided below.

Chapter. 1: Here we provide background to the research in the field discussing the changes in glycan expression in disease, current detection methods and introduce boronic acid as a saccharide binding compound. This then proceeds to discuss the emergence of nanotechnology and molecular imprinting in biosensor design with examination of the limitations of the current research.

Chapter 2: A brief explanation of the employed surface characterisation methods is given providing clarity to the techniques used in this research.

Chapter 3: Describes the synthesis and characterisation of the alkyne and PBA terminated SAM monomers and azide functional CuAAC ligands.

Chapter 4: Examines the organisation and formation of the SAMs produced with synthesised compounds through various surface characterisation techniques.

Chapter 5: Saccharide binding to PBA terminated SAMs and surface functionalised SAMs was investigated using SPR analysis. Here we describe the synthesis of molecularly imprinted surfaces for the oligosaccharide stachyose.

Chapter 6: Conclusions and future work

Chapter 7: methods

Chapter 8: References

Acknowledgements

I would first like to begin by extending my warmest thanks and utmost appreciation to my academic supervisors Paula and Stefano. Your optimism, kind words and tremendous professionalism have kept me going these past years and without you, this thesis would not be here today.

Second but no less important, I give my thanks to Kamlesh, Fatima, Monika, Philipa, Barbara gomes, Eleonora, Guiseppe, Francia, Yazmin, Alice, Barbara Simoes, Dario, Laura brooks, Laura Buccoli, Nasim, Pushpa, Seyed and Setarah. Additionally I would like to thank our wonderful post-docs Lewis, Eduardo, Josh, Marcos and Craig. Your input has been invaluable throughout this research and I truly appreciate the time you have given me.

To the academic staff who I have had the pleasure of meeting and working with namely Lynn, Chris, Mala, Helen, Elaine, Ronnie and Angela and our friends over in chemistry, Cecile, Chi and Chris, your work in keeping everything running truly is appreciated.

Lastly, to my mum, dad, two brothers and my partner, Jen, I cannot express enough my appreciation for your patience and kindness that enabled me to get here, thank you.

Table of Contents

Abstract i
Acknowledgements iv
Abbreviations and definitions ix
Chapter 1 1
Introduction 1
1.1 Chapter outline 2
1.2 Introduction to carbohydrates and glycoproteins 4
1.2.1 Protein glycosylation 5
1.2.2 *N* and *O*-linked glycosylation. 8
1.2.3 Aberrant glycosylation in disease 10
1.2.4 Monosaccharides 16
1.2.5 Di, oligo & polysaccharides 21
1.3 Glycan & saccharide recognition methods 23
1.3.1 Anti-glycan antibodies 24
1.3.2 Lectins 28
1.3.3 Boronic acids 32
1.3.4 Boronic acids in carbohydrate sensing technology 36
1.4 Nanotechnology: self-assembled monolayers 41
1.4.1 Self-assembled monolayers 43
1.4.2 Alkanethiol SAMs on Au substrates 45
1.4.3 SAM surface defects 48
1.4.4 Multi-component SAMs 51
1.4.5 Monolayer functionalisation 53
1.4.6 Cu(I)-catalysed azide-alkyne cycloaddition 57
1.4.7 Molecular imprinting & artificial antibodies 62
1.5 Concluding remarks 77
1.6 Aims & objectives 79
Chapter 2 84
Surface characterisation techniques 84
2.1 Chapter introduction 85
2.2 Contact angle goniometry 86
2.3 Ellipsometry 91
2.4 X-ray photoelectron spectroscopy 100
2.5 Surface plasmon resonance 106

Chapter 3 112
SYNTHESIS OF SAM COMPONENTS 112
3.1 Introduction 113
3.1.1 Objectives 117
3.2 Synthesis of SAM monomers 119
3.2.1 Branched monomer: DFC 120
3.2.2 Short (C_2) monomer: DTPAlk 124
3.2.3 Long (C_{10}) monomer: MBDAlk 129
3.3 Synthesis of azide functionalised CuAAC ligands 133
3.3.1 Synthesis of benzyl azide and 3-(azidomethyl)phenyl boronic acid 134
3.3.2 Pinacol protection of AzBA 138
3.3 Synthesis of PBA terminated SAM monomers 140
3.3.1 Synthesis of PBA terminated C_2 SAM monomer from DTPAlk and AzBA 142
3.3.2 Synthesis of PBA terminated C_{10} SAM monomer from MBDAlk and AzBA 148
3.5 Conclusion 152
Chapter 4 153
Formation and characterisation of alkyne and PBA terminated SAMs 153
4.1 Chapter introduction 154
4.2 Objectives 156
4.2 Formation and characterisation of alkyne-terminated SAMs on gold surfaces 158
4.2.1 DTPAlk short chain SAM generation and characterisation . 159
4.2.2 MBDALk long chain SAM generation and characterisation .. 163
4.2.3 DFC branched SAM generation and characterisation 167
4.2.4 Comparison of DTPAlk, MBDALk and DFC SAMs and effect of backbone composition on SAM organisation 172
4.3 Formation and characterisation of PBA-terminated SAMs on gold surfaces 174
4.3.1 Characterisation of DcB and McB PBA-terminated monolayers by ellipsometry, contact angle and XPS 175
4.4 AzBA functionalisation of alkyne terminated SAMs via CuAAC reaction 184
4.4.1 Surface characterisation of AzBA functionalised DTPAlk, MBDAlk and DFC SAMs via surface CuAAC reaction 186
4.5 Conclusion 193

Chapter 5 196
Saccharide probing of PBA-terminated SAMs and molecular imprinting of stachyose 196
5.1 Introduction 197
5.1.1 Objectives 200
5.2 Saccharide binding of McB and DcB PBA terminated SAMs 202
5.2.1 Non-specific adsorption of monosaccharides to gold substrate or SAMs 203
5.2.2 pH optimisation of McB SAM for fructose binding 207
5.2.3 Comparison of DcB and McB SAMs for monosaccharide binding 213
5.3 AzBA surface functionalised DTPAlk and MBDAlk response to monosaccharide and oligosaccharide binding 218
5.4 Development of stachyose specific MIS 232
5.4.1 AzOEG functionalisation of MBDAlk SAM via CuAAC reaction 235
5.4.2 Proof of concept: Molecular imprinting of stachyose 238
5.5 Conclusions 253
Chapter 6 257
Conclusions and future work 257
6.1 Conclusions 257
6.2 Adaption of the current technique to glycoprotein detection 260
6.3 Proposed development towards clinical assay design 263
Chapter 7 266
Methods & settings 266
7.1.1 NMR spectroscopy 266
7.1.2 Mass spectroscopy 266
7.1.3 X-ray photoelectron spectroscopy (XPS) 267
7.1.4 Surface plasmon resonance (SPR) 268
7.1.5 Contact angle 269
7.1.6 Ellipsometry 269
7.2 Chemical synthesis 270
7.2.1 Di-functionalised cystine 270
7.2.2: 3-((azidomethyl)phenyl) boronic acid (AzBA) 274
7.2.3: 3-((azidomethyl)phenyl) boronic acid pinacol ester 275
7.2.4 Benzyl azide (AzBEN) 276
7.2.5: 3,3'disulfanediylbis(*N*-(prop-2-yn-1-yl)propenamide (DTPAlk) 276

7.2.6:_((((((3,3'disulfanediylbis(propanoyl))bis(azanediyl))bis(methylene))bis(4,5-dihydro-1H-1,2,3-triazole-4,1-diyl))bis(methylene))bis(3,1-phenylene))diboronic acid (DCB) . 278
7.2.7: 11-mercapto-N-(prop-2-yn-1-yl)undecanamide (MBDAlk) 279
7.2.8: S-(11-oxo-11-(prop-2-yn-1-ylamino)undecyl) ethanethioate (pMBDAlk) 280
7.2.9: (3-((4-((11-(acetylthio)undecanamido)methyl)-1H-1,2,3-triazol-1-yl)methyl)phenyl)boronic acid (pMcB) 281
7.3 Surface preparation & chemical modification..... 283
7.3.1 Chemical cleaning of Au substrates 283
7.3.2 Self-assembled monolayer formation of DFC, DTPAlk or MBDAlk on clean Au substrates 283
7.3.3 Terminal modification of SAMs by CuAAC reaction with AzOEG, AzBA or AzBEN 284
7.3.4 Preparation of DcB monolayer 285
7.3.5 *In situ* deprotection of pMcB and formation of McB monolayer 285
7.3.6 Stachyose-boronic acid surface template formation through CuAAC reaction 286
7.4 Appendix..... 288
7.4.1 DFC synthesis and characterisation 288
7.4.2 Characterisation of DTPAlk 295
7.4.3 Characterisation of MBDAlk 297
7.4.4 Characterisation of pMBDAlk 301
7.4.4 Characterisation of AzBEN 303
7.4.5 Characterisation of AzBA 304
7.4.6 Characterisation of pinAzBA 306
7.4.7 Characterisation of DcB 310
7.4.8 Characterisation of pMcB 313
References..... 316

Abbreviations and definitions

AzBA: 3-(Azidomethyl)phenyl boronic acid

AzBEN: Benzyl azide

BA: Boronic acid

DcB: PBA terminated short chain (C_2) dithiol

DFC: Alkyne – acryloyl functional cystine

DTPAlk: Short chain (C_2) linear SAM monomer

ELISA: Enzyme-linked immunosorbent assay

ESI-MS: Electrospray ionisation mass spectroscopy

MBDAlk: Long chain (C_{10}) linear SAM monomer

McB: PBA terminated long chain (C_{10}) thiol

MIP: Molecularly imprinted polymer

MIS: Molecularly imprinted surface

NMR: Nuclear magnetic resonance

NSA: Non-specific adsorption

OEG: Oligoethylene glycol

PBA: Phenyl boronic acid

Pca: Prostate cancer

PEG: Poly(ethylene) glycol

pinAzBA: Pinacol protected phenyl boronic acid

PSA: Prostate specific antigen

SAM: Self assembled monolayer

SPR: Surface plasmon resonance

XPS: X-ray photoelectron spectrscopy

UHP: Ultra high purity

Chapter 1.

Section 1.3.1 of this chapter is reproduced from the paper "The challenges of glycan recognition with natural and artificial receptors" Tomasonne, S; Allabush, F; Taggur, YK; Norman, J; Köpf, M; Tucker, JHR; Mendes, PM; Chem Soc Rev. 1-18, 2019

Introduction

Abstract: With the discovery of better and new biomarkers, naturally there is a commitment to develop diagnostic technology that can bring about their application to the clinical laboratory. In this chapter we will discuss the literature regarding the aberrant glycosylation of cancer biomarkers. This will develop into the potential application of molecular self-assembly as a potential diagnostic platform when coupled with glycan sensing moieties. Through summarising and discussion of major research themes in this area, pitfalls and problems in application of this will be presented providing clarity for the importance of this research.

1.1 Chapter outline

Despite our ever-increasing technological capacity in the clinical laboratory, the detection and differentiation of complex glycan structures remains problematic. The absolute heterogeneity brought about by subtle structural differences provides an outstandingly complicated biological system through which only sensitive and clinically impractical techniques can circumvent (*i.e.* mass spectroscopy). The focus of this research has been on the study and development of a new generation of diagnostic platforms: molecular self-assembly and the generation of artificial antibodies. The potential of these to differentiate complex glycoforms will be explored in this literature review allowing a transition to the research conducted providing clarity on the design, application and intention in writing this thesis.

This chapter will begin with a brief introduction to glycans expanding on *N*-linked and *O*-linked glycosylation. This will introduce biosynthesis of these glycans leading into the recognition of aberrant glycosylation in disease caused by disruption to these pathways. The complexity of glycan structures will then be expanded in examination of monosaccharides and their configurations. Once the complexity of carbohydrates is established, current detection techniques will be discussed.

Once the problems in detection are established, this chapter will move to review the current research in nanotechnology and the development/study of molecular self-assembly with emphasis on self-assembled monolayers (SAMs). These SAMs will then be examined for their application to biosensor design along with boronic acids as a potential addition for detection of glycans. Molecular imprinting and design of 'artificial antibodies' will then be discussed culminating in the current status of the field.

1.2 Introduction to carbohydrates and glycoproteins

Carbohydrates, proteins and nucleic acids form the three main subsets of biopolymers and of these, carbohydrates are the most diverse. Being originally thought of as only nutritional or structural material, advances in our understanding of biology has revealed a far more complex nature to carbohydrates being responsible for a myriad of regulatory activity (1,2).

Structurally, carbohydrates range from simple monosaccharide units composed of carbon, oxygen and hydrogen to complex biomolecules containing numerous monosaccharide units with varying degrees of branching or chemical moieties. Physiological function extends from essential cellular processes *i.e.* glucose metabolism in ATP production to extensive regulatory functions such as seen for the large sulphated saccharide family, the glycosaminoglycans (3–5).

Alongside isolated physiological function, carbohydrates are also essential components in DNA as deoxyribose and in posttranslational modification of proteins imparting essential functions. For instance, seen for sialyl Lewis X structures in lymphocyte signalling or in expression of blood group saccharides A, B and O (6,7). Owing to the diversity and essential function of these biomolecules, the study of the

glycome has revealed numerous aberrations that can occur from genetic defects to autoimmunity to implications in human ageing (8–10). Not surprisingly, malignant cell growth has also shown an altered glycosylation profile potentially providing a new class of biomarkers for disease such as cancer (11).

Unfortunately, the complexity of glycan structures and glycosylation pathways complicates detection and quantification of potential glycan biomarkers. Despite this issue, approaches at glycoprofiling have been successful in isolation (*i.e.* through electrophoresis or chromatography) and in analysis through mass spectroscopy and lectin arrays (12). Regardless of advances, the clinical utility of glycan biomarkers is still lacking due to clinical impracticality of current glycoprofiling techniques. As such, it is essential that new simple and reproducible glycan detecting technologies are developed to make use of this new wealth of information.

1.2.1 Protein glycosylation

The glycosylation of proteins is an essential post-translational modification and underpins a critical quality control step in protein synthesis. In the addition of saccharide units to a protein, the intrinsic physical properties are altered promoting folding and maturation whilst preventing aggregation through transformation of hydrophobic regions. These structures

additionally serve as regulatory elements for misfolding of proteins enabling saccharide recognition by glycosidases or lectins that may promote protein degradation (13–15).

While there exists five distinct forms of glycosylation namely: glypiation along with *N, O, P* and *C*–linked, we will only discuss *N*–linked and *O*–linked in this review due to the distribution and importance in disease. Graphical representation of glycans will use the symbol nomenclature for glycans (SNFG) system as per *Fig. 1* to display complex carbohydrate structures as simply as possible.

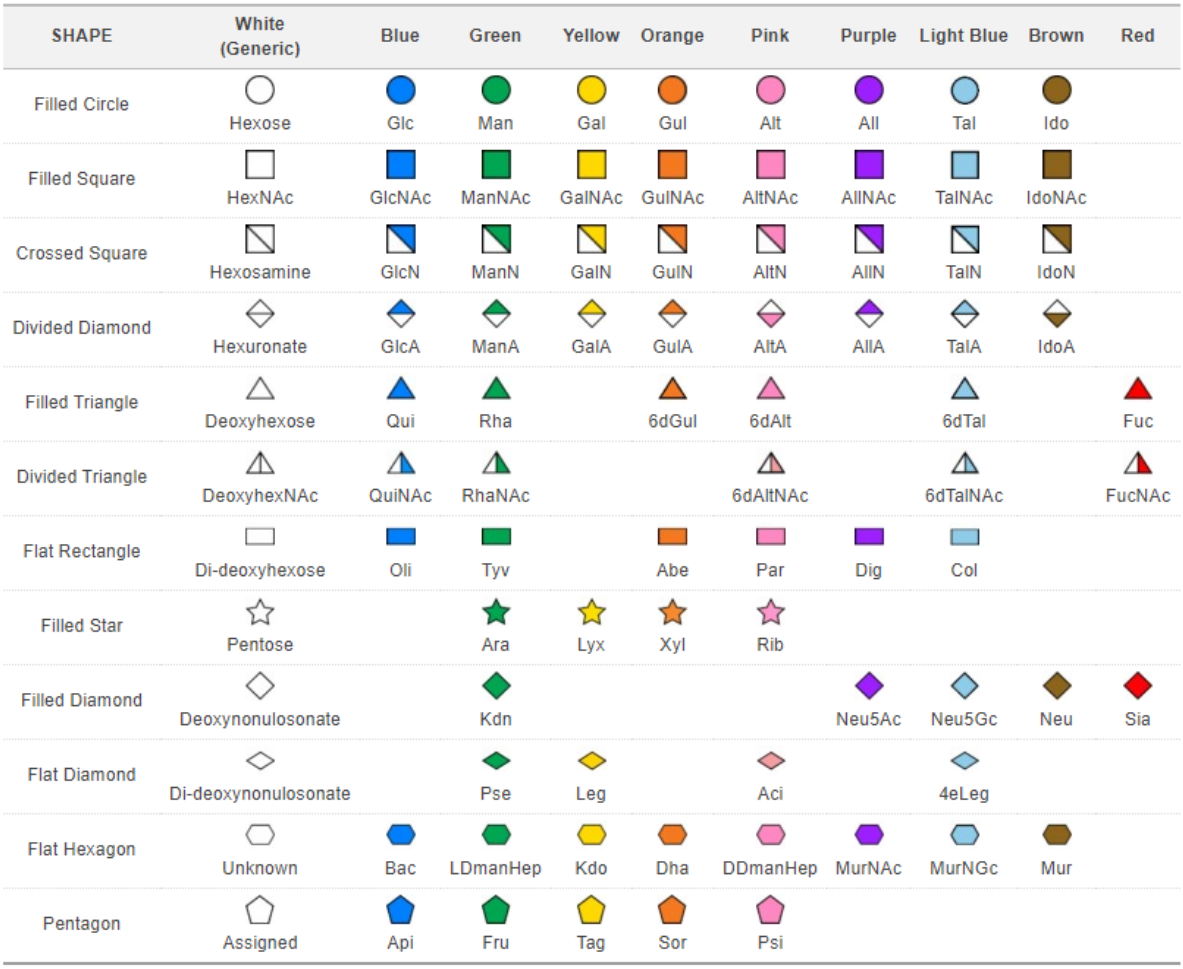


Fig. 1: SNFG glycan pictorial representation system using coloured shapes for specific saccharide units. Bonds labels between saccharides are included in diagrams [image taken from (16)].

1.2.2 *N* and *O*-linked glycosylation.

Forming the most widely distributed form of glycosylation with a quarter of all eukaryotic proteins displaying this carbohydrate-peptide linkage, *N*-linked glycosylation is highly conserved and essential post-translational modification (14,17). The process of glycopeptide linkage is observed to be homologous between the prokaryotic periplasmic membrane and endoplasmic reticulum (ER) membrane enabling comprehensive study of these mechanisms. Similarities are observed in the attachment of an oligosaccharide to an isoprenoid lipid (dolichol in eukaryotes) acting as a carrier to enable attachment to a protein (18).

Glycopeptide linkage for *N*-linked glycans occurs through an asparagine residue defined in a conserved amino acid sequence: Asn*x*Ser/Thr ('*x*' may be any amino acid except proline)(17,19). A relatively large glycan, $Glc_3Man_9GlcNAc_2$ is enzymatically transferred to this from a dolichol carrier through action of oligosaccharyltransferase in the ER. This glycan is sequentially recognised through various lectins: malectin, calnexin and calreticulin and ER chaperones and trimmed of glucose units through glucosidases. On removal of the third glucose, folding status is probed by glycoprotein glucosyltransferase (UGGT) that associates with $Man_3GlcNAc_2$. Unfolded protein provides a substrate for UGGT docking allowing reattachment of a glucose to the glycan chain and retaining it in the ER. Correctly folded

glycoproteins are unable to bind UGGT and undergo further glycan digestion or relocate to the golgi for chain elongation (*Fig. 2*) (17,20–23).

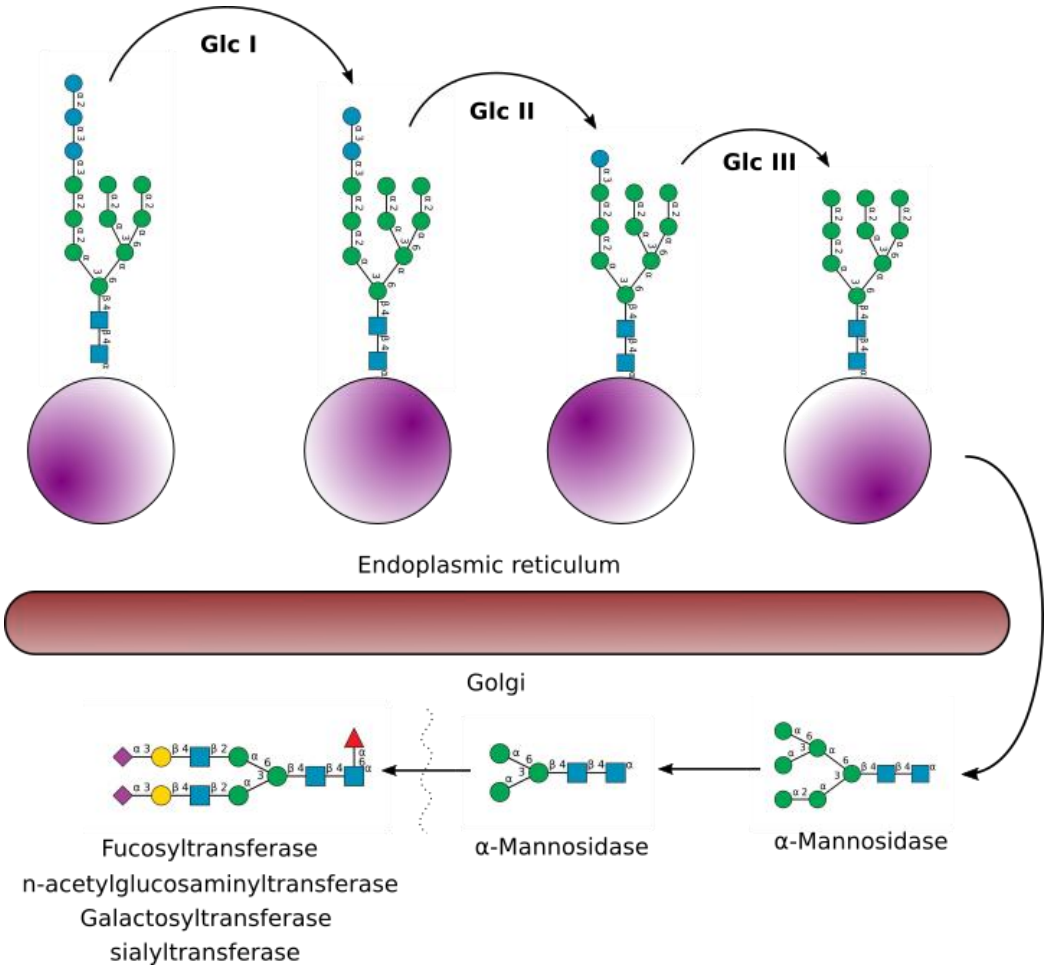


Fig. 2: Biosynthetic route for *N*-linked glycosylation in the ER starting with attachment of $Glc_3Man_9GlcNAc_2$ with sequential glucose removal before chain elongation or further saccharide removal in the golgi.

The *O*-linked glycans form through any amino acid expressing a free hydroxyl group hence, they can occur on Ser, Thr, Tyr and Hyp (hydroxyproline and hydrolysine) and occur in both α and β anomeric configurations. Conversely to *N*-linked glycan biosynthesis, *O*-linked glycans do not form from a common glycan, rather, they are added sequentially typically in the golgi and may be single saccharides or elongate from various monosaccharides including mannose, fucose and *N*-acetylgalactosamine (13,24–27). Whilst gene expression controls protein translation, glycosylation pathways have no written code hence, rely on a complex system of chaperones, translocation and expression of glycosyltransferases. Because of this, altered gene expression can provide drastic changes to the cellular glycoprofile. The co-appearance of *N* and *O*-linked glycans on numerous glycoproteins therefore provide an excellent marker of cellular malignancy where aberrations in structure mark disruption in these pathways (13).

1.2.3 Aberrant glycosylation in disease

Altered glycan expression clinically manifests in a variety of disease states being brought about by congenital disorder, infection, age and cancer (28). Physiological effects are typically severe being incompatible with life in some congenital disorders while also being recognised in Alzheimer’s, cardiac

conditions and autoimmune disease (29–33). In cancer however, these changes are acute, manifesting as a by-product of oncogene expression providing disturbed glycosyltransferase transcriptional signalling (34). For example, on producing tumours in mice through *polyomavirus* middle T antigen oncogene, Granovsky *et al* (2000) demonstrated that β1,6N-acetylglucosaminyltransferase V (MGAT5) deficient mice showed significantly less tumour growth than MGAT5 positive littermates. Interestingly, a positive feedback loop was observed between MGAT5 products and phosphatidylinositol 3kinase–protein kinase (PI3K) signalling thus supporting amplification of oncogene expression through glycosyltranferase expression (35).

It is recognised that in almost every cancer glycosyltransferases are upregulated producing several very common tumour antigens notably: sialyl-Lewis^{x} (sLe^{x}), sialyl-Lewis^{a} (sLe^{a}), sialyl-Tn (sTn) and Thomsen-Friedenreich (Tf) antigen (36–39) (*Fig. 3*). While present on both *N* and *O*-linked structures, these antigens are more commonly *O*-linked structures, brought about by increased expression of sialyltransferases and fucosyltransferases that catalyse transfer of sialic acid and fucose to the common *O*-linked structure GalNac (40–43). Typically, N-linked expression however shows increased branching and sialic acid and change in fucose

content originating from overexpression of β1-6-N-acetylglucosaminyl transferase-5 (GnT5), sialyltransferases and fucosyltransferases (36,44–46).

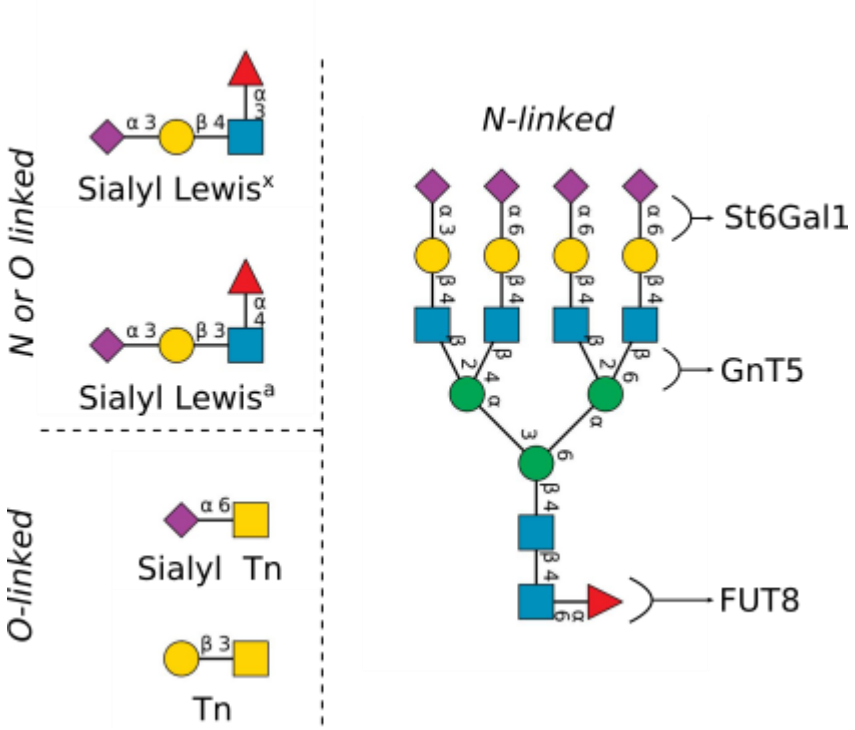


Fig. 3: Common carbohydrate antigens occurring as result of aberration to glycosynthetic pathways and expression of glycosyltransferase *i.e.* α-N-acetylgalactosaminide α-2,6-sialyltransferase-1 (St6GalNAc-1), β1,6-N-acetylglucosaminyl transferase-5 (GnT5) and fucosyltransferases 8 (FUT8) [Glycan structures produced with DrawGlycan-SNFG, version 1.0] (45,47–49).

Given the prevalent occurrence of changes to the expressed glycoproteome in cancer, naturally we can assume there is diagnostic and prognostic value in their detection. An interesting example of such inquiry is recognised in the altered glycan expression on the prostate cancer (PCa) tumour marker: prostate specific antigen (PSA).

PCa is the leading cause of male cancer incidence and contributes significantly to male mortality but despite this, current detection methods using a PSA cut off >4 ng/mL using highly sensitive enzyme linked immunosorbent assays (ELISA) have significant problems. Despite current clinical assays achieving significantly lower limits of detection than the PSA cut-off value such as the Roche Elecsys total PSA ELISA limit of detection 2 pg/mL, the clinical sensitivity and specificity is low causing significant false positive and negative results (50–52). This is due to PSA not being a true marker of PCa but rather, of destruction to prostate architecture allowing leakage of PSA from prostate to circulation (53).

Interestingly, PSA demonstrates significant changes in glycosylation patterns correlated with disease state *i.e.* benign from malignant disease. The glycan structures of PSA have been extensively studied over the past decade in attempts to elucidate new PCa biomarkers. This however has been complicated by differences in glycoprofiling techniques and PSA sources between

research generating conflicting results as shown in *Table. 1.* Application of mass spectroscopy in glycoprofiling of healthy PSA demonstrated significantly higher sensitivity than previously used lectin and HPLC methods and could provide valuable insight into the glycoproteome of PCa but is unfortunately impractical in the clinical laboratory (54). Despite conflicting views on PSA glycoprofile a general consensus shows a decrease in fucosylation, increased branching and increase in α2-3 sialic acid and *O*-linked glycosylation, consistent with altered expression of glycosyltransferases in PCa tissue (55–58).

Table. 1: Various methods used to profile glycan structures of PSA and results. Symbols: (+) increase, (-) decrease, (±) non-directional change. (* results compare serum from PCa patient to glycan profile of LNCaP cells), (**results compare serum from PCa patients to serum from benign prostate hyperplasia (BPH)).

Ref	Sample	Purification	Analysis	Glycoprofile changes
(59)	LNCaP	Immunoaffinity	Electrophoresis	(+) branching
(60)	LNCaP	Affinity chromatography	MALDI-TOF MS HPLC-ESI MS	(-) Neu5Ac (+) Fuc (+) GalNAc (+) α1,2Gal
(61)	LNCaP Human serum	Ion-exchange chromatography	MALDI-TOF MS Lectin affinity	(+) α2,3Neu5Ac
(62)	Human urine	Ion-exchange chromatography	Lectin affinity	(-) glycans (+) branching
(63)	Human serum: PCa(+)	Affinity chromatography	Lectin affinity Chemiluminescence Electrophoresis	(-) Fuc (-) α2,3Neu5Ac (+) sLe^{x}**
(64)	Human serum: PCa(+)	Immunoaffinity	MALDI-TOF MS MALDI-QIT MS	(+) α2,3Neu5Ac
(65)	Human serum: PCa(+) Human serum: BPH(+)	Affinity chromatography	MALDI-TOF MS QTRAP LC/MS/MS	No conclusions on expression changes
(66)	LNCaP Human serum: PCa(+) Human serum: BPH(+)	Lectin affinity	Lectin affinity ELISA Real-time PCR	(+) α1,2Fuc (+) GalNAc

(67)	Human serum: PCa(+)	Immunoaffinity	MALDI-TOF/TOF MS Electrophoresis	(-) Neu5Ac (-) Fuc **
(68)	PCa tissue	N/A	HPLC-TSQ-SRM MS	(+) Neu5Ac
(69)	Human serum: PCa(+) Human serum: BPH(+)	Immunoaffinity	Lectin western blot Lectin affinity chromatography	(+) α2,3Neu5Ac (-) Fuc
(70)	Human urine: PCa(+) Human urine: BPH(+)	Immunoaffinity	LC-MS	(±) Neu5Ac (±) Fuc

It is clear that a multitude of glycan biomarkers are produced as a result of abnormal cell growth however the complexity of biosynthetic routes and heterogeneity of expressed structures currently represses their clinical utility. Before discussion of current glycan detection methods, the structural configurations of carbohydrates will first be examined. This will elaborate the anomeric configurations saccharides may take providing background for subsequent sections and clarifying the complexity involved in synthetic detection methods.

1.2.4 Monosaccharides

Monosaccharides form the basic unit of all saccharide structures consisting of carbon, oxygen and hydrogen in the empirical formulae: $C_m(H_2O)_n$ where (n) are repeating saccharide

units and (*m*) being between 3 - 7. The Nomenclature of a carbohydrate depends on several elements that can be represented in several projections namely: Fischer, Haworth or chair (*Fig. 4*).

Experimentally, saccharides are recognised to be either reducing (containing aldehyde) or non-reducing (containing ketone) classifying them as either aldoses or ketoses respectively. The number of carbons present denotes the name (*Table. 2*) which contains a prefix designating stereochemical information; either (D) or (L) dependent on arrangement of hydroxyl furthest from aldehyde/ ketone and (α) or (β) derived from spatial arrangement of hydroxyl around the anomeric carbon in the cyclic monosaccharide form (*Fig. 4*). The remaining hydroxyl configuration along with carbon content are used to chemically define monosaccharides.

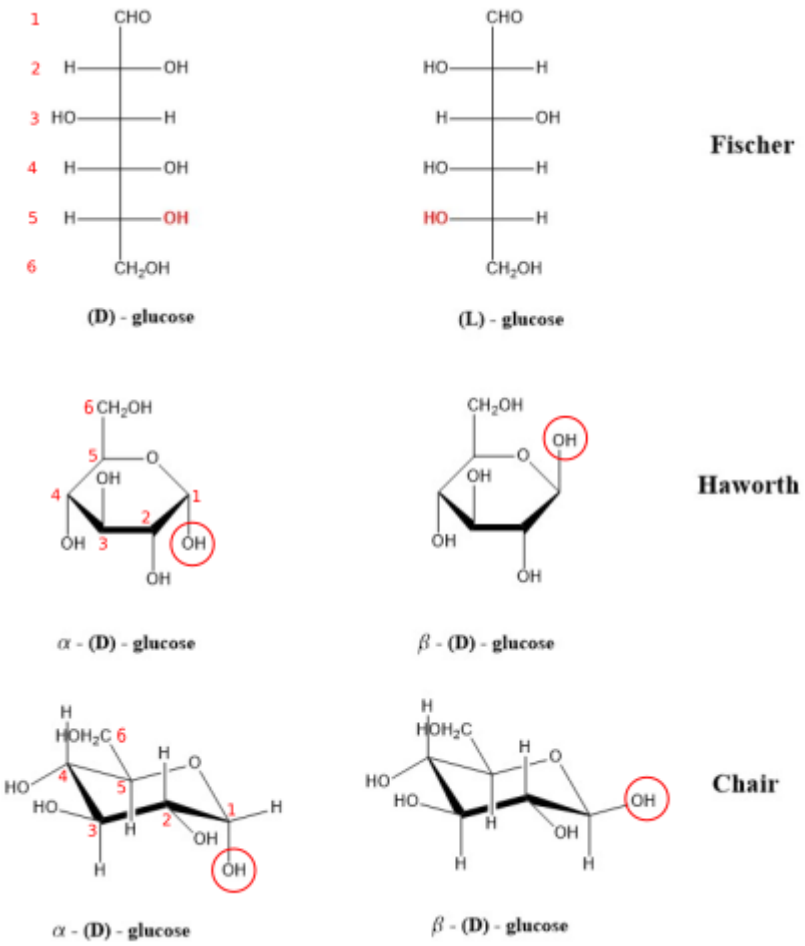


Fig. 4: Fischer, Haworth and chair projections of the monosaccharide glucose in (D)/ (L) configuration and (α)/ (β) configuration.

Table. 2: Carbon number, name and examples of common monosaccharides expressed as either aldose (blue) or ketose (red) (71).

(*n*) Carbons	Name	Example monosaccharide
3	Triose	Glyceraldehyde, dihydroxyacetone
4	Tetrose	Erythrose, erythulose
5	Pentose	Ribose, ribulose
6	Hexose	Glucose, fructose

In aqueous solution saccharides exist in equilibrium between linear and cyclic form albeit favouring cyclic. In taking this form, a hydroxyl reacts with the carbonyl forming a hemiacetal and producing an additional sterogenic centre at the anomeric carbon (72,73). Based on spatial arrangement of the hydroxyl at the anomeric carbon, stereogenic configuration will take either axial position in the α conformation or conversely, equatorial in the β when drawn in the Haworth projection (C1, *Fig. 4*). Both configurations are characterised by distinct melting points and exist in an equilibrium between rotations and the open chain formation in a process referred to as mutarotation (73).

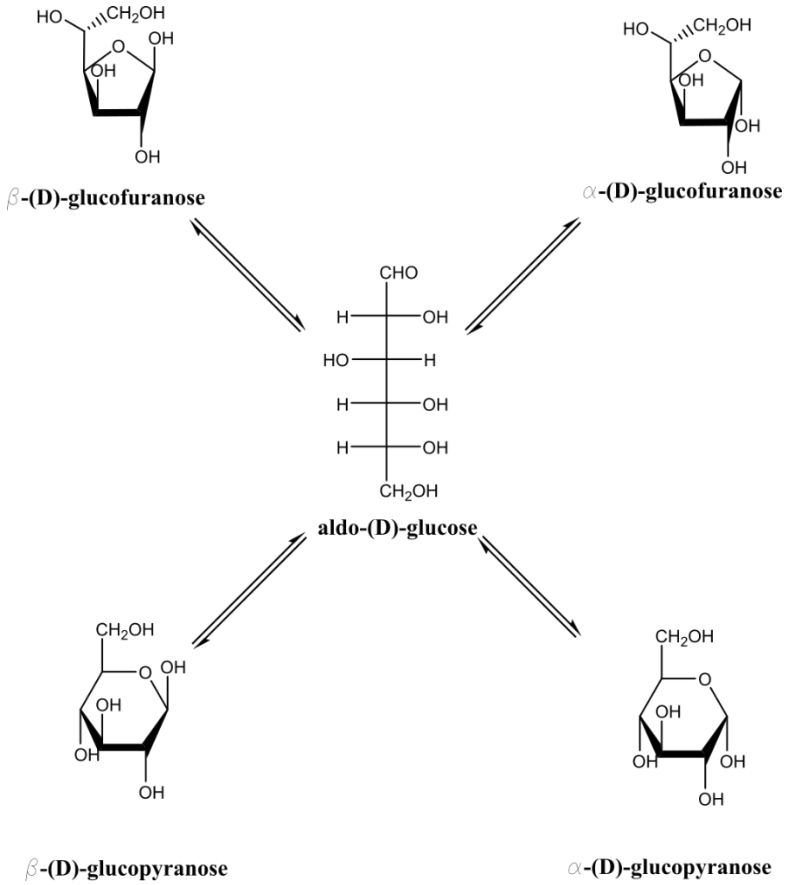


Fig. 5: Mutarotation of (D)-glucose showing possible transitions between (α) and (β) and between linear, pyranose and furanose configuration

Additionally, during cyclisation, pentose and hexose saccharides will take on either five or six membered rings designated furanose and pyranose, respectively. In conjunction with mutarotation this gives rise to five possible forms shown in *Fig. 5*. This rate of this process, while typically slow, can

be altered with the addition of organic solvents, acid-base or enzymatically (74,75). Furthermore, the proportion of these forms depends on the monosaccharide unit *i.e.* with increased percentage of furanose form of fructose observed compared to glucose which thermodynamically favours the pyranose form (*Table. 3*).

Table. 3: Proportion of configurations for two common monosaccharides: glucose and fructose arising from mutarotation.

Mono-saccharide	(%) α-pyranose	(%) β-pyranose	(%) α-furanose	(%) β-furanose	(%) linear	Ref
Glucose	**33**	**66**	**0.498**	**0.498**	**0.004**	(75)
Fructose	**3**	**57**	**9**	**31**	**1**	(76)

1.2.5 Di, oligo & polysaccharides

Glycosidic linkage between two monosaccharide units is achieved through condensation reaction between the anomeric carbon (glycoside) and a hydroxyl group on opposing saccharide (aglycone). In nature, this reaction is controlled enzymatically being capable of generating a variety of configurations dependent on bond formation (*Table. 4*). Typical notation of

glycosidic bonds states α/β configuration proceeded by bond linkage with glycoside appearing first *i.e.* for sucrose: α-D-glucopyranosyl-(1→2)-β-D-fructofuranoside (72,73).

Table. 4: Disaccharides produced from two glucose molecules.

Disaccharide	bond
Maltose	α(1-4)
Trehalose	α(1-1)α
Isomaltose	α(1-6)
Cellubiose	β(1-4)
Sophorose	β(1-2)
Qentiobiose	β(1-6)

While monosaccharides and disaccharides are typically more important nutritionally, on increasing size and complexity, as oligo and polysaccharides they become crucial regulatory elements. As discussed, the complexity of monosaccharides alone allows for numerous configurations of a simple sugar. On joining to form a disaccharide, a second layer of complexity is added where bonds determine the disaccharide product. As an oligosaccharide (3-10 monosaccharide units) and polysaccharide (>10 units) branching may occur presenting unique structural biomolecules (77–79).

Dependent on glycosidic bond location, mutarotation may still occur in oligo and polysaccharides dependent on availability of a free hydroxyl attached to the anomeric carbon. Where there is no free hydroxyl however *i.e.* in sucrose (α-D-glucopyranosyl-(1→2)-β-D-fructofuranoside) and trehelose (α-D-glucopyranosyl-(1→1)-α-D-glucopyranoside), mutarotation cannot occur (76).

1.3 Glycan & saccharide recognition methods

Not surprisingly, saccharide sensors have become ubiquitous in the biomedical industry since the first proposed enzymatic assay by Clark & Lyons in 1962 (80). With rapidly rising incidence of diabetes and the recognition of altered glycan expression in numerous diseases, the rapid quantification and saccharides is essential in disease management (81). Serum monosaccharide sensors commonly use enzymatic methods as seen in point of care glucose meters. Saccharide detection occurs the catalysed breakdown of a saccharide such as glucose or fucose and measurement of by-products via amperometric or spectroscopic methods (82–84). While simple quantitative methods are sufficient for simple sugars, quantification of complex carbohydrates requires more robust approaches. Anti-glycan antibodies (AGAs) and lectins has garnered significant use in

probing glycan structures and attempts at quantifying serum glycans but suffer with inherent poor immunogenicity.

1.3.1 Anti-glycan antibodies

A vast collection of AGAs are present in human sera and play critical functions in a diverse range of immune processes displaying highly specific immunogenicity to foreign glycan epitopes such as Neu5GC and α-Gal and to sequences of the 'self' *i.e.* blood group antigens (85–87). Interestingly, similar to saccharides, AGAs are useful biomarkers of disease seeing increased expression in inflammatory and autoimmune disease such as cancer, multiple sclerosis and Crohns (88–93). While promising as a diagnostic tool, therapeutic value of AGAs in tumour targeted treatment is limited due to poor immunogenicity of AGAs without modification such as glycan clustering (94,95).

Lower affinity is observed between AGAs and ligands displaying equilibrium dissociation constants (K_D) in the µM range for monovalent interactions compared to antibody-protein KD values in the nM range. This low K_D is typically compensated by multivalency of the protein-glycan interaction (96–98). Interactions mostly consist of hydrogen bonding within defined grooves alongside additional Van Der Waals interactions. While dependent on proximal amino acid functional groups *i.e.* methyl or carboxyl, ionic or hydrophobic interactions may also support

binding. The network of hydrogen bonding between an AGA and *Streptococccus pneumoniae* tetrasaccahride antigen TS14 (Galβ1-4Glcβ1-6[Galβ1-4]GlcNAcβ1) is shown in *Fig. 6* as resolved by X-ray crystallography (99). Building upon these structural studies, phage display technology has enabled screening and generation of highly specific AGAs and are providing a means to produce diagnostically and perhaps therapeutically important libraries of AGAs (100–103).

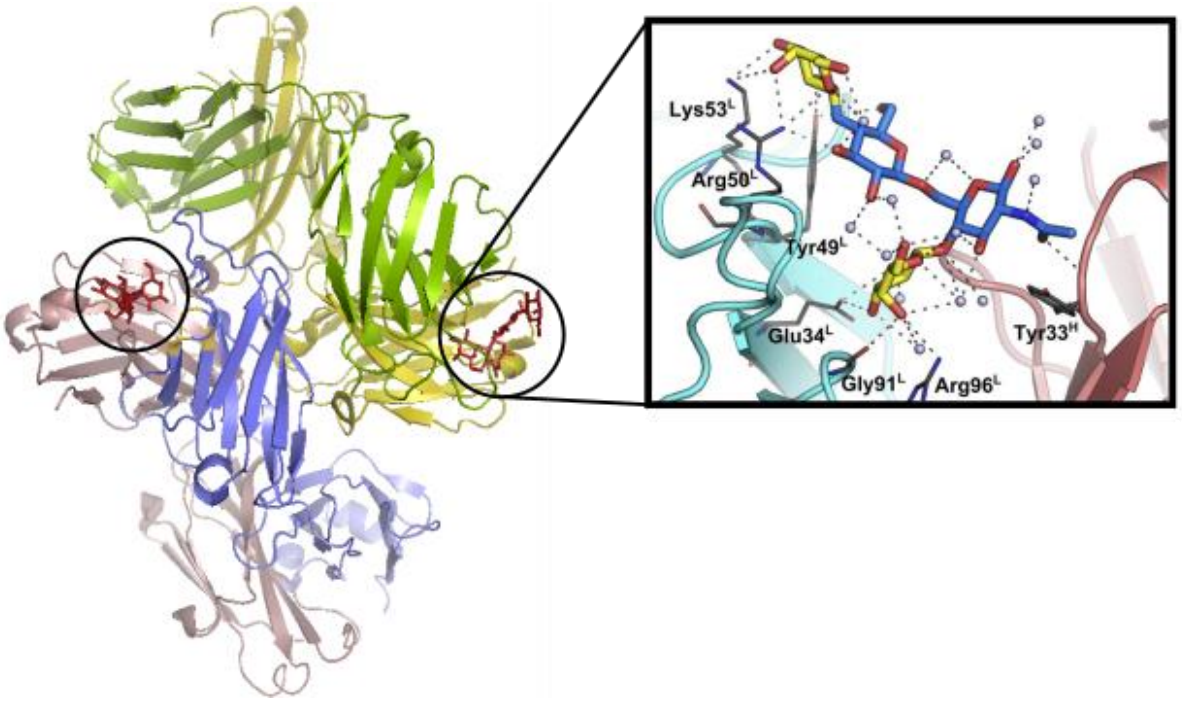


Fig. 6: Crystal structure of TS14 specific AGA in complex with tetrasaccharide TS14 ligand with network of hydrogen bonds in the binding pocket displayed (right). [image (*left*) produced using PyMol, version 2.2, image (*right*) taken from (99)].

Well-defined validated specificities are now possible due to, in particular, recent improvements in glycan microarray-based technology with new revelations of antibody requirements for interaction. For instance, for IgG anti-glycan immunoglobulins, glycan binding additionally depends on recognition of specific peptide motifs. Comparatively IgM anti-glycan immunoglobulins show glycan binding irrespective of peptide motifs demonstrating dependence on both glycan and

protein interactions depending on the antibody isotype (104–107).

Despite there being over 1000 AGAs discovered to date, only 247 glycan epitopes can be recognised through immunogenic means due to high cross-reactivity of AGAs for multiple glycan antigens (108). Finding selective AGA-glycan binding is therefore important in obtaining clinically relevant immunogenic glycan detection. Tumor-associated carbohydrates, such as the sLe^x, Thomsen-nouvelle (Tn) antigen, sTn, and the TF antigen, have been particularly targeted for AGA development as promising biomarkers of disease (58,109–115). There is also a significant number of AGAs for ABH blood group antigens, Lewis antigens and glycolipids *i.e.* CA19-9 (sLea), CA15-3 and CA125 (116–119). Amongst these are several clinically available assays, clinical trials for implementation and application to therapeutic use in cancer vaccines as seen with CA19-9 and its conjugation to keyhole limpet hemocyanin (119,120).

Despite considerable efforts, many current AGAs still lack high affinity for their target glycans and have broad specificity whereby families of structurally related glycans, rather than a single distinct glycan structure are recognised. Furthermore, considering the breadth of the glycoproteome, only a narrow set of glycans are currently targeted by AGAs.

1.3.2 Lectins

The superfamily of lectins represents a large class of glycan-binding proteins (GBP) and are found amongst all species class including bacteria, viruses, plants and animals. On discovery of the first lectin in 1887 the nature of the interaction was presumed immunogenic on observation of jack-bean haemagglutinin reaction with erythrocytes (121–123). These interactions are now known to be neither immunogenic or catalytic but may reversibly bind carbohydrates. Furthermore, lectin-carbohydrate interaction has demonstrated indispensable importance in a host of biological activities, including bacterial adhesion (124), tumorigenesis (125), inflammatory response (126), infection (127) and foetal development (128).

Dependent on carbohydrate-binding domain (CBD) sequence and origin, lectins are split into the 6 sub-classes: C-type, P-type, R-type, L-type, I-type and galectins. Of these, the L-type lectins have been extensively used in lectin based glycan assays imparted by their high concentrations in readily available legume seeds (1). Despite comprehensive use in glycan research and similar to application problems of AGAs, lectins suffer from weak affinities to saccharide ligands typically with K_D in the mM range whilst also cross-reactivity between individual saccharides. Similar to AGA, this is due to monovalency and nature of interaction sites with CBPs usually exhibiting shallow

grooves allowing heterogeneity in ligand binding. This may be circumvented in the oligomerisation of lectin binding pockets producing large multivalent binding sites (129–132).

Consistent with this similarity to AGA-carbohydrate binding, lectin-carbohydrate interaction depends on a network of hydrogen bonding, Van der Waals, CH-π and electrostatic interactions (for charged saccharides such as sialic acid) (133,134). An example of this multivalent bonding is shown in *Fig.* 7 in the resolved crystal structure of the *Platypodium elegans* lectin A in complex with trimannosidase saccharide (135). Strength of binding is influenced by length of oligosaccharide, flexibility and solvation alongside multivalency of interaction where monosaccharides show lower K_D values than large glycans (133,136–138).

Interestingly, lectins can also exhibit conformational and stereo selectivity as observed for the pertussis toxin lectin preference of terminal α2-3 sialic acid glycans or the plant lectins: *Maackia Amurensis* (MA) and *Sambucus Nigra* (SN) for α2-3 or α2-6 linked sialic acid respectively (139,140). Additionally, anomeric selectivity is observed amongst some C-type lectins with Ca^{+} ions co-ordinating hydrogen bonding differentiating axial or equatorial anomeric hydroxyl groups, whilst others such as *L*-arabinose binding protein (ABP) is selective for both α and β isomers of arabinose (133,141,142).

Despite relatively weak binding, high selectivity of lectins for differentiating saccharide units, linkage and anomeric configurations is highly desirable in assay development and has found application in various research and diagnostic technologies (143–145).

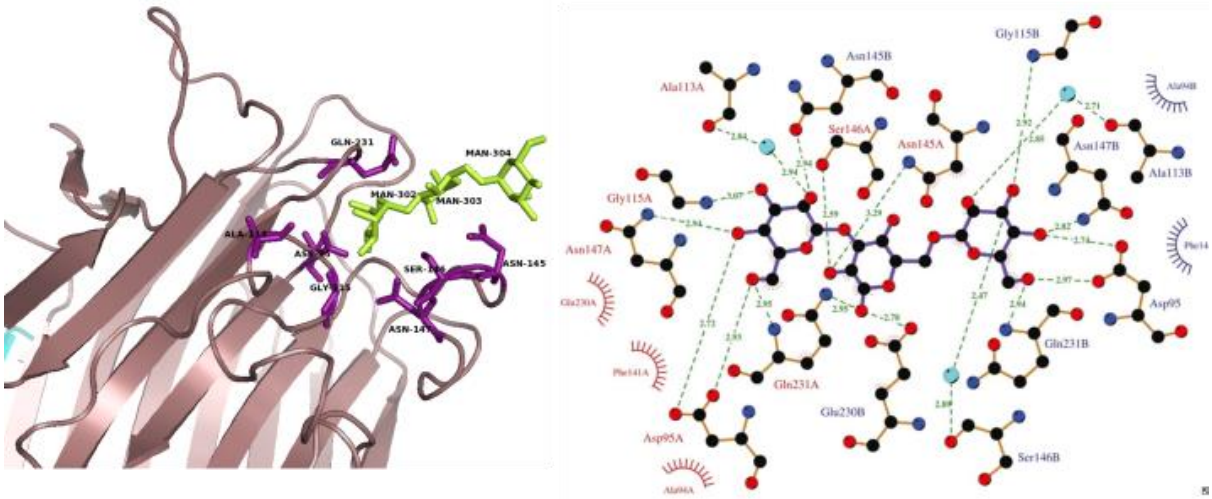


Fig. 7: (Left) crystal structure of *P. elegans* Lectin A complexed with trisaccharide (PDB ID: 3ZYR, image generated in PyMOL, version 2.0). (Right) network of bonds between trisaccharide and binding pocket. Green lines represent hydrogen bonding, curved lines represent Van der Waals contacts. [image taken from (135)].

To date, numerous lectin based assays for probing glycoprofile have been developed including lectin-affinity chromatography, western blotting, lectin-probed flow cytometry, enzyme-linked lectin assays (ELLA) and lectin microarrays (146–151). Of these, lectin microarray platforms have significant

economic advantage over AGA based platforms owing to the abundant library of readily available lectins capable of rapid glycoprofiling the biomaterial (152). Application of this technology to cancer diagnostics in particular has revealed a multitude of promising new biomarkers but has not yet found extensive use in the clinical laboratory (153–158). Unfortunately, consistent with all antibodies, lectins suffer from the same susceptibility to degradation from environmental factors such as heat or pH.

Additionally, while ELLAs can provide quantitative measurements of a narrow glycoprofile, they fail to capture the broad changes in glycan expression. With specific glycan changes recognised in tumour states *i.e.* increased core fucosylation or O-GlcNAcylation, as correlated with increased metastasis or proliferation through metabolic reprogramming respectively (159,160); screening for isolated glycan changes as produced by ELLAs fail would fail to derive a full image of tumour progression with only a small number of glycan changes quantified. Contrarily, screening for broad changes to the glycoprofile might reveal structures isolated to benign, aggressive, or metastatic outcomes thus providing valuable prognostic data. Conversely to ELLAs, lectin microarrays typical provide qualitative data on glycans giving an essential 'snapshot' of cellular changes but lacking crucial information

on extent of change. This provides prognostic value in the variety of glycans at the expense of quantitative data. Nevertheless, both AGAs and lectins have been indispensable in glycoprofiling but clearly, new approaches are needed to expand our range of glycan binding compounds with higher affinity, selectivity, and stability.

1.3.3 Boronic acids

The design of new glycan sensing probes is dependent on compounds that can successfully and strongly interact with saccharides; more-so than AGAs and lectins whilst being economically viable *i.e.* cheap, stable, abundant *etc.* Boronic acids (BA) have diverted attention in recent decades by virtue of their ability to covalently and reversibly bind saccharides through recognition of 1,2 or 1,3 *cis* diols forming 5 or 6 membered cyclic esters respectively (*Fig. 8*) (161). Individually and at neutral pH, BAs show relatively weak association constants (K_{eq})to saccharides such as glucose (K_{eq}= 4.6 M^{-1}). However, on increasing multivalency of interaction *i.e.* addition of multiple BA groups, binding increases significantly (K_{eq} up to 19000 M^{-1}) as demonstrated by various research groups (161–166). The stability and adaptability of BAs undoubtedly makes them a viable candidate for glycan sensing probes however, further conditions must be met to attain a feasible glycan selective platform.

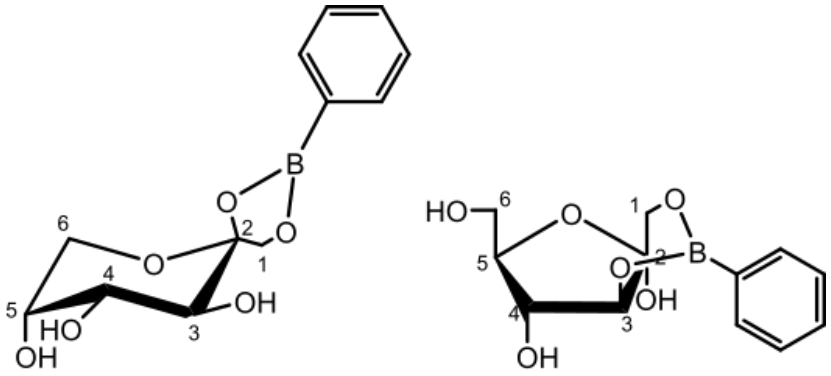


Fig. 8: Fructose recognition by PBA in (a) pyranose configuration forming 1,2 diol bond and (b) furanose configuration forming 1,3 diol bond (167).

The esterification of BA to diols while covalent, is a reversible and dynamic process observed to be dependent on pH. Acting as a Lewis acid, BA accepts electrons from a base forming an equilibrium between a hybridised sp^2 trigonal planar to an sp^3 tetrahedral boronate anion configuration (*Fig. 9*) (168,169). At lower pH, this equilibrium favours the former configuration while at higher pH it favours the latter. The tetrahedral configuration has demonstrated increased reactivity with diols thought to arise from proton transfer and hydroxide displacement within the coordinated boron (170). The consequence of this is requirement of BA sensors to operate at a pH above the pKa of BA

species therefore limiting its potential in clinical diagnostics that usually require settings at physiologically relevant pH.

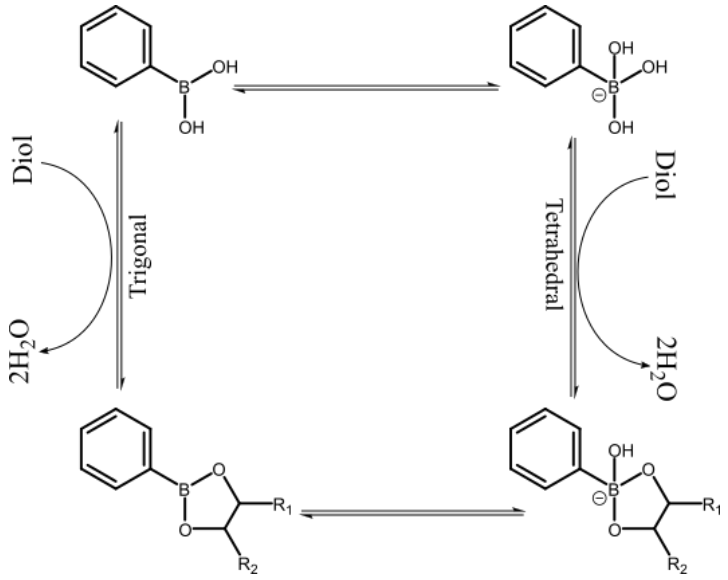


Fig. 9: Transition between trigonal and tetrahedral configuration of PBA with diol binding. [adapted from (171)]

The inclusion of functional groups proximal to the BA group has been shown to alter the pKa of the compound allowing for application of more useful pH ranges with BA sensors. Given the pKa of phenylboronic acid (PBA) is 8.7, pushing the equilibrium towards the tetrahedral configuration would require pH conditions damaging to fragile glycoprotein biomarkers. The development of benzoboroxoles (BBA) bypassed this problem whereby the incorporation of the boron into a 5 membered

oxoborole ring displayed a pKa around 7.3, significantly closer to physiological pH than PBA. This is believed to arise from relief of ring strain upon the BA on ionisation into its tetrahedral configuration (172,173).

Similarly, the Wulff-type BAs contain a proximal amino group that forms intramolecularly co-ordinated complex between boron and amine by acting as a Lewis base thereby facilitating a reduction in pKa (174–176). Alternatively, addition of an electron withdrawing group to the PBA such as sulfonyl or carbonyl groups increases Lewis acidity of the BA acting to decrease the pKa (177–179) (*Fig. 10*). In developing clinically relevant BA based sensors, manipulation of the chemical environment collectively with the multivalency of the BA-glycan interaction could provide the necessary foundation for sensor design.

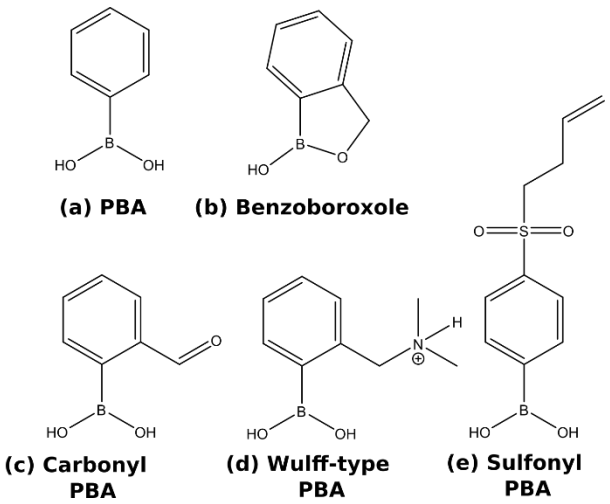


Fig. 10: Various chemical modifications made to PBA, altering the optimum binding pH of the BA-diol interaction.

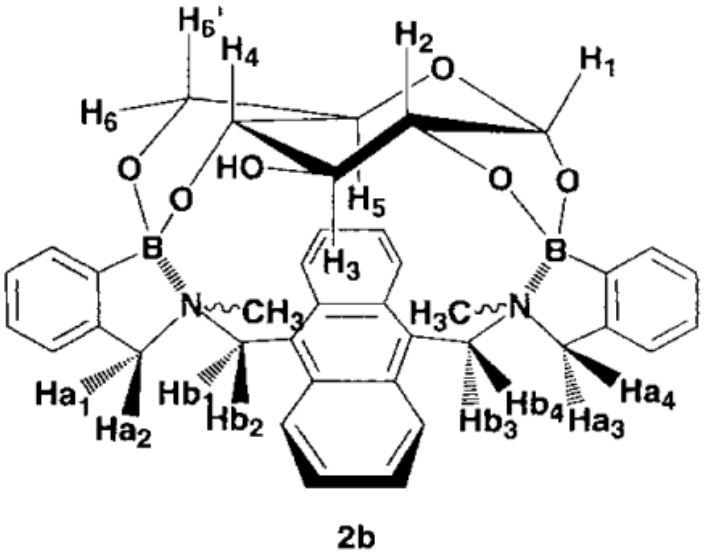
1.3.4 Boronic acids in carbohydrate sensing technology

The versatility of BA as a sensing moiety has seen numerous probes developed ranging from histopathological stains for the anionic compound peroxynitrite to glucose sensitive/ insulin releasing micelles (180–182). Aside from sensing application, BA has seen use in pharmaceuticals being a key component in the drug *bortexomib* used in treatment of multiple myeloma (183). Furthermore, its chemical stability and adaptability has allowed a variety of additional chemical modifications supporting its use on a range of substrates making it of particular interest in glycoprofling research.

As an additional benefit of PBA in biosensor design, BA can be used to modulate fluorescence in chemically grafted fluorophores provided there is an nearby electron donor such as an amine group (165,184). This modulation of fluorescence was originally explained through photoelectron transfer (PET) with BA esterification driving reduction in pKa thereby inducing PET between amine and fluorophore (165). More recently, Sun *et al* (2018) have proposed fluorescence occurs independent of amine-BA dative bond which is instead suggested solvent inserted in protic media. It is suggested fluorescence occurs through suppression of internal conversion on saccharide binding through removal of BA hydroxyl vibrational states referred to as 'loose bolt effect'. In essence, the fluorophore acts as the energy

donor while hydroxyl groups of the $B(OH)_3^-$ anion being in a high frequency vibrational state absorb this energy thus quenching fluorescence. Binding to saccharide sees suppression of this internal conversion thereby modulating fluorescence (185).

For mono-boronic acid (mBA) sensor designs, saccharide binding across a range of pH produced measurable fluorescence showing equivalent fructose and glucose binding (186). This research was expanded to include a di-boronic acid (dBA) connected to an anthracene fluorophore that showed selectivity for D-glucose. This was confirmed by ^1H NMR and mass spectroscopy to hold a 1:1 binding ratio between glucose and anthracene-dBA (*Fig.* 11) while fructose was in 2:1 ratio (187). On swapping the anthracene fluorophore for 1,1'-binapthyl, chiral discrimination of saccharides was also observed for *D* and *L* enantiomers of common monosaccharides (188). The impact of spatial modulation of BA moieties has on saccharide selectivity was later explored by Phillips and James (2004) who showed both fluorophore and linker modulate saccharide selectivity in PBA binding compounds (165).



2b

Fig.11: Glucose binding of dBA connected via anthracene fluorophore showing 1:1 binding as resolved by ^{1}H NMR and mass spectroscopy [taken from (187)].

It is observed then that while basic saccharide binding is dependent on the immediate BA moiety, selectivity is dependent on chemical adjuncts that can modulate spatial configuration of multiple BAs. Immobilisation of BA to a solid substrate can therefore provide a scaffold to induce this selectivity, foregoing 'designer BAs' in place for molecular imprinting of saccharides. Using modified poly(glycidyl methacrylate) microbeads, Wei *et al* (2016) recently developed a fluorescent sensor for glycated horseradish peroxidase (HRP) through imprinting a BA-HRP complex with aniline (189). While this only discriminated glycated from non-glycated glycoproteins, Jiang *et*

al (2019) later developed a less sensitive but more specific co-polymerised BA/ dopamine silica nanoparticle selective for HRP over other glycoproteins (190). Similarly, glycoprotein isolation has been achieved with BA capped magnetic nanoparticles in various groups. While this lacks direct quantification parameters, extraction of glycans or monosaccharides could be used as an enrichment step in saccharide characterisation (191,192).

The importance of steric placement of BA coordinated with saccharide is further shown by Zhou *et al* (2019) in sialic acid imprinted BA sensor on a carbon cloth electrode. Despite the lack of imprinting monomer, coordinating BA polymerisation through complexation with sialic acid produced a remarkably sensitive (LOD 0.5 µM) sensor even in presence of other monosaccharides (193). Additionally, chiral discrimination of monosaccharide enantiomers has been produced on Au nanoparticles and cross-linked micelles further highlighting the potential sensitivity of this technology (194,195).

Diverging from imprinting, simpler BA sensor designs have also provided selectivity for carbohydrates. The use of *bis*-BA immobilised on solid Au substrate showed increased affinity for glucose over other monosaccharides consistent with the early research of James *et al* (1994) (196). By increasing the BA content further, affinity for oligosaccharides can be induced

over monosaccharides as demonstrated by BA capped silver nanoparticles that display enhanced binding of the large polysaccharide dextran over glucose (197).

Alternatively, application of BAs to drug delivery systems has yielded novel approaches to treatment of diseases such as diabetes, cancer and infection. The development of glucose responsive insulin releasing structures has gained particular notoriety seeing numerous micellar and hydrogel polymers developed. For example, Jun Loh *et al* (2012) used the competitive binding of glucose to BA imbedded in micelles to disrupt structural integrity of the micelle allowing release of insulin (198). Comparatively, another system used the charge response of PBA to glucose binding to induce volumetric changes in amphiphilic gels thereby supporting timed diffusion of encapsulated insulin (199). Additionally, BA mediated cellular coordination shows potential in cancer treatment with several studies using PBA to modulate delivery of small interfering RNA (siRNA). In this, tumour cell sialic acid recognition by polymer bead displayed PBA moieties enables improved cellular uptake of siRNA consequently increasing siRNA dose received (200). More recently, a novel cholesterol modified siRNA delivery system was developed using the competitive binding of PBA between siRNA ribose and ATP thereby prompting timed release on delivery to cell cytoplasm (201).

The versatility of BAs has been extensively demonstrated by researchers in numerous fields showing potential as both a diagnostic and therapeutic agent. Of particular interest in this research is its value in diagnostics being verifiably capable of selectively differentiating saccharides and potentially glycan structures. As briefly discussed, this selectivity must be modulated by spatial arrangements being dependent on the immobilisation of BA units complimentary to saccharide hydroxyl groups. The self-arrangement of molecules on a substrate dubbed 'molecular self-assembly' is a phenomenon that may provide the naturally forming architecture to produce such complimentary shapes. By foregoing the designer BA based sensors such as those presented by Phillips and James (2004), larger more complex saccharide structures naturally forming their own BA templates in a system of self-assembly might produce a more elegant and sensitive sensor design.

1.4 Nanotechnology: self-assembled monolayers

Self-assembly describes the autonomous process of a disordered system arranging to form an ordered system dependent on internal components without manipulation. This is observed in many facets of nature seen at the nanoscale *i.e.* crystallisation and biological process such as the formation of phospholipid cell membranes (202,203). While the description of self-assembly remains broad, being also used to describe macro and mesoscopic

systems such as weather patterns and living processes, in the context of diagnostic development, it is molecular self-assembly that presents significant opportunity (204). In particular, intermolecular self-assembly, seeing spontaneous arrangement of molecules into supramolecular patterns provides a means of nanoscale manipulation. Thus, by observing transient interactions between chemical groups, nanostructures formed through resulting self-assembly can be predicted with examples provided in *Fig. 12*. Aside from hierarchal building of nanostructures, this process also informs formation of self-assembled monolayers on a molecule on a solid substrate. This enables molecular customisation of a surface providing the foundation layer for molecular imprinting and will be discussed in the following sub sections and used to inform our own biosensor design (202).

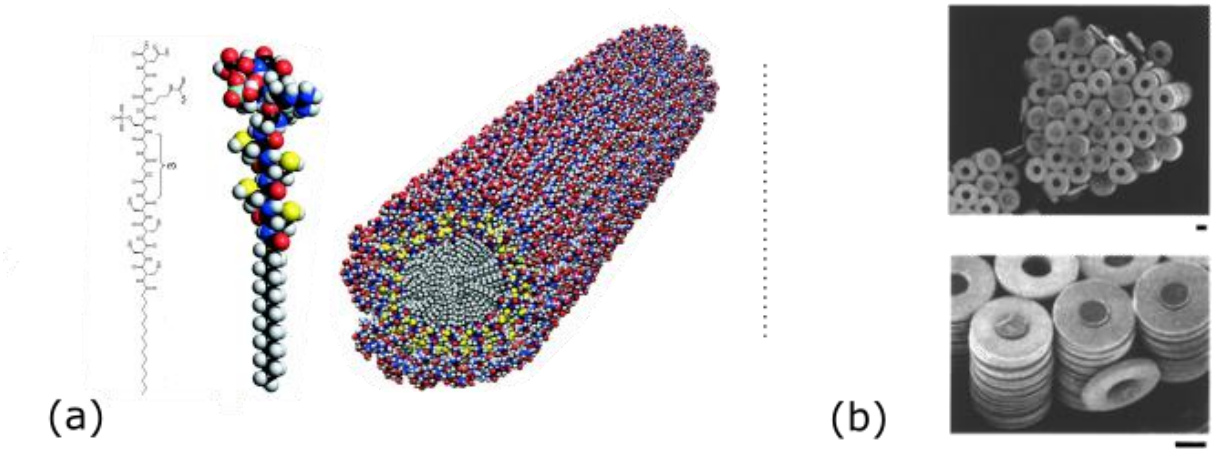


Fig. 12: Example of nano and microscale self-assembly. **(a)** Peptide-amphiphile nanofiber formed through pH dependent self-assembly of chemical structure shown *left* [Image from (205)] **(b)** Self-assembly of ≈10 µm sized metal plates into 3-dimensional aggregates by capillary forces dependent on plate surface functionalisation (scale bar µM) [Image from (206)]

1.4.1 Self-assembled monolayers

Taking inspiration from antibody-antigen interactions, in designing novel diagnostic sensors self-assembly can be used to build chemical scaffolds around a ligand producing a 'molecular imprint' (MIP). Naturally, the first step in building a structure is preparation of the foundations achieved through formation of a self-assembled monolayer (SAM).

The assembly of a well organised SAM is firstly dependent on spontaneous adsorption of a surfactant to a suitable solid

substrate. Ideally, this interaction should be non-covalent allowing a metastable organisation such that any inappropriate monomer arrangement can synchronise with the monolayer structure (202). Inorganic surfaces typically used for functionalisation include Au, Ag, Ti and silicon owing to their ease of surface characterisation and intrinsic properties *i.e.* biological compatibility of Au films (207–209). Alternatively, polymeric substrates such as poly(vinyl) alcohol (PVA) or polyethylene have biomedical applications where mechanical flexibility is required (210).

SAM monomer selection determines both the organisation on the substrate and functionalisation imbued at the surface and can be split into three distinct groups (*Fig. 13*). At the head group, substrate interaction occurs determining rate of association and orientation of monomer. The backbone forms the joining (typically aliphatic) carbon chain actuating molecular order *i.e.* density of the layer, while the terminal group presents the physiochemical properties (211). This directly changes certain parameters of the surface such as wettability and may also provide functional groups for further modification *i.e.* attachment of IgG (207).

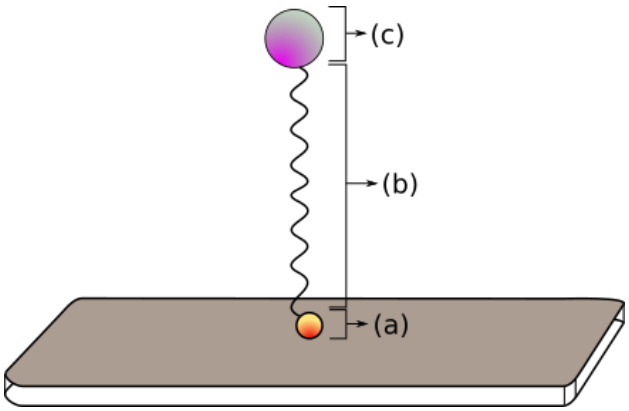


Fig. 13: Representation of basic SAM structure. **(a)** Head group associates with substrate. **(b)** Backbone forms lateral interactions regulating surface packing and organisation. **(c)** Terminal group modifying surface properties *i.e.* NH_2, COOH, CCH, biotin *etc.*

1.4.2 Alkanethiol SAMs on Au substrates

Considered one of the most important SAMs, alkanethiols have seen extensive research in recent years imparted by their stability and ease of preparation. While a number of metal substrates such as Cu, Ag and Pd have been used, Au substrates remain a more popular choice given the strong binding between Au-S (~160 kJ/mol) and Au surfaces being agreeably inert (212). Furthermore, the thiol-Au bond does not require chemically pure surface being strong enough to displace contaminants. Modulation of surface packing and functionalisation is achieved through backbone length and chemical groups allowing for a controllable

layer well suited to functionalisation/ modification and biomolecule immobilisation (213).

Both disulphides (R-S-S-R) and thiol (HS-R) adsorb strongly to Au however the nature of the event remains controversial. It is generally agreed that S-Au bonding occurs over two steps: rapid physiosorption of SAM compound to Au surface then slower chemisorption of S-Au bond formation (214) (*Fig. 14*). During physiosorption SAM backbone groups form interactions with Au surface via Van de Waals interaction thus rapidly producing a 'lying down' arrangement of monomers. With increasing surface coverage, SAM compounds transition from lying down to perpendicular 'standing up' arrangement while forming a covalent bond between Au-thiol species (215,216). Experimental scanning tunnelling microscopy (STM) evidence suggests however a more dynamic process seeing creation of a 2D AuS phase with Au lattice restructuring on thiol adsorption (217). This is contrary to X-ray photoelectron spectroscopy (XPS) and STM data provided by Lusteinberg *et al* (2008) who observe only small surface restructuring with no AuS phase but populations of mono and polymeric thiol species *i.e.* trimer and tetramers, chemisorbed to Au (218)

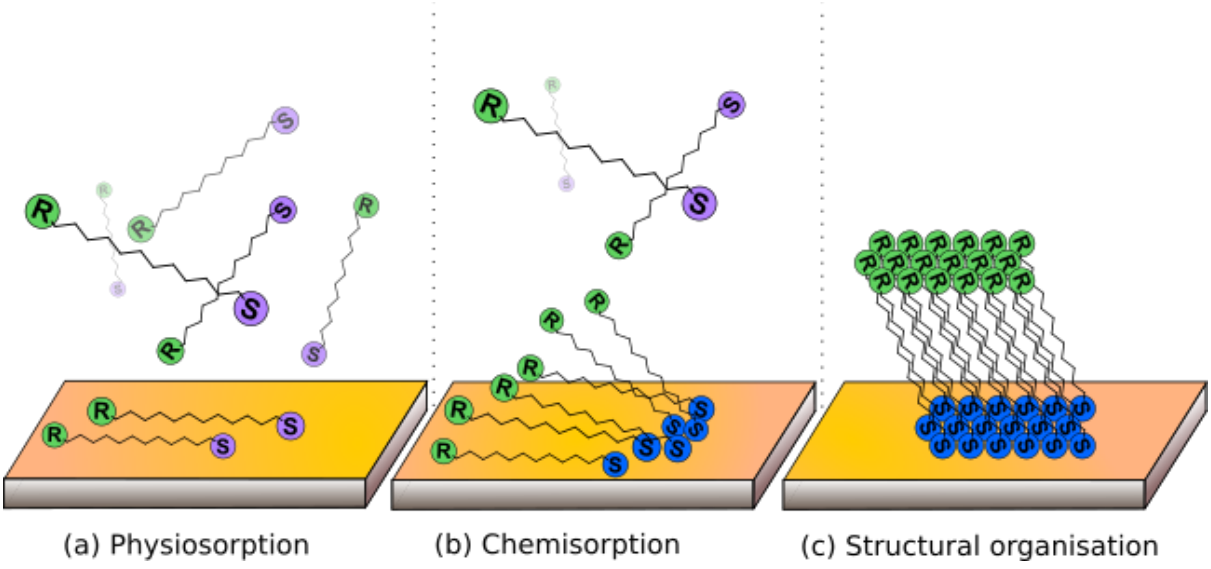


Fig. 14: Stages of alkanethiol organisation on Au. (a) Rapid physiosorption of SAM compound to surface through backbone groups. (b) Slower chemisorption of sulphur resulting in covalent Au-S bond. (c) gradual organisation of SAM transitioning from parallel to perpendicular orientation with dense packing of SAM compound.

Alternatively, disulphides also readily form organised SAMs through formation of two thiolate bonds. Unlike thiol chemisorption however the transition from lying down to standing up phase is sterically hindered. It has been suggested that disulphides break into separate thiol species favouring the S-Au bond. Contradictorily, oxidation of thiol groups thus forming disulphides at the Au interface has been observed at surface

defect boundaries being implied as a causative agent in SAM degradation (215,219). While disulphides provide several advantages over thiols for SAMs, notably, chemical stability, requiring no protecting groups during synthetic procedures and a resistance to oxidation, they additionally suffer from slow SAM formation time (220). Inclusion of thiol species as both head and terminal group (dithiol) has additionally been explored however 'biting-back' of the terminal thiol to the Au substrate presents a structural problem. Nonetheless, dithiol SAMs can form ordered SAMs with Millone *et al* (2009) suggesting a hydrogen exchange between free dithiol and chemisorbed dithiol. This enables liberation of one end of surface dithiol simultaneously chemisorbing the free dithiol thus producing typical substrate bound and free thiol groups at opposing terminus of the SAM monomer.

1.4.3 SAM surface defects

While initial surface adsorption occurs within minutes, formation of stable well-ordered monolayers may take several hours depending on SAM structure. Longer alkane chains are observed to adopt a crystalline like assembly with chains tilted 30-40° more rapidly than shorter counterparts (215,221). If a densely packed monolayer is required, the use of longer chain alkanethiols is preferred. However, all SAMs in practise suffer

from a number of defects. Common defects are shown in *fig. 15* including: (a) pinhole defects, (b) chemical defects, (c) domain defects and (d) vacancy islands.

Notwithstanding favourable surface coverage by long chain alkanethiols, all surfaces will present missing monomers in the monolayer called pinhole defects (*Fig. 15a*). These pinholes under STM also appear pronounced in instances of monomer collapse or gauche defects interrupting SAM organisation (*Fig. 15b*) (222,223). Interestingly, Chen *et al* (2017) found alkane backbone lengths $\geq C_4$ / $\leq C_9$ form a gauche defect dominated SAM in a liquid like state with quantity of defects reducing in longer alkanethiols (224). Larger surface anomalies occur under gradual growth of SAMs observed as domain defects (*Fig. 15c*). These arise during initial SAM nucleation with SAM monomers coalescing at domain interfaces. Naturally as surface coverage increases structural mismatching is observed where interfaces meet with heterogenous orientations. Vacancy islands unlike other defects mentioned, are not true SAM defects instead arising from Au remodelling on thiol adsorption. These present as mono or diatomic dips in the monolayer caused by local removal of Au possibly to solution and see increased occurrence with high concentrations of thiols (218,222).

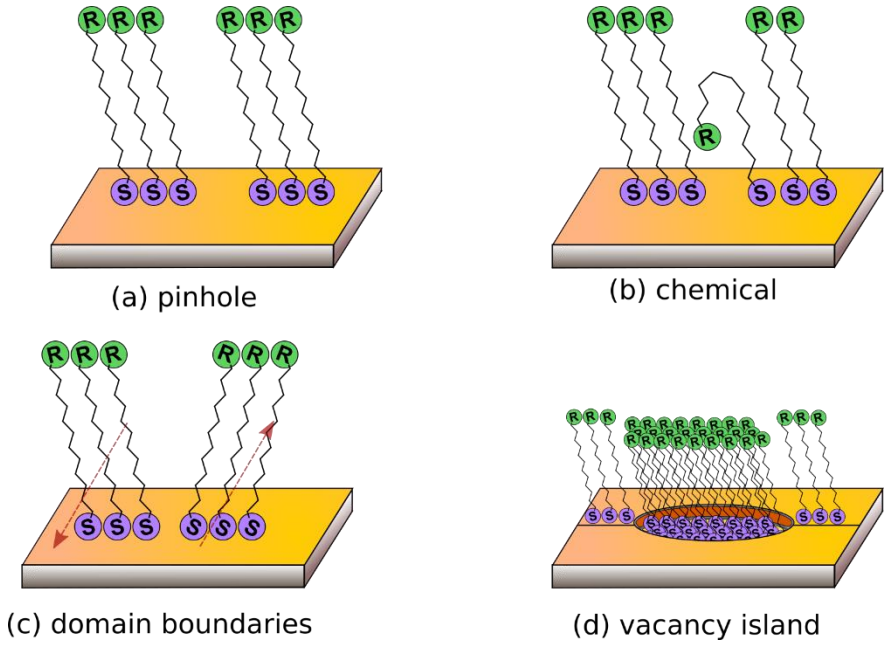


Fig. 15: Four common SAM defects (a) pinhole defects, (b) Chemical defects, (c) domain boundaries, (d) vacancy islands.

As noted, SAM organisation is significantly affected by chemical composition of the backbone, hence also impact surface defects. Increasing backbone length (minimum $\geq C_9$) with simple alkane thiols provides well organised/ densely packed surface structure owing to increased chain flexibility and Van de Waals between alkane chains (225).

Contrarily, in short chain alkanethiols ($\geq C_3$) lower packing density has been observed as calculated from a modified Young-Dupre equation from contact angle analysis. With this Chen *et al* (2017) suggest that short alkanethiol SAMs only pseudoform as

implied by calculated surface entropy due to lack of inter-monomer interactions and/ or inductive effects caused by proximity of surface to the thiol-Au bond (224). Furthermore, odd/ even carbon number has shown pronounced effect on SAM orientation where odd numbered alkanes displayed increased tilt coinciding with fewer gauche defects and decreased sensitivity to temperature (226).

1.4.4 Multi-component SAMs

As a modification to typical homogenous SAM design, multicomponent SAMs have a number of benefits and have become archetypal in biosensor design through SAM formation. As a common monomer inclusion, ethylene glycol terminated thiols used in solution with a functional thiol imparts dual function to a surface: a group capable of immobilisation and an anti-fouling layer resisting non-specific protein adsorption (227). By spacing functional monomers, steric hinderance in immobilisation of external groups is additionally minimised while also modifying wettability of the surface. In doing so, biomolecule immobilisation yield can be increased thus improving sensor sensitivity (228). This is exemplified in a ConA lectin sensing interface using immobilised maltoside developed by Sato *et al* (2014). In this significantly improved binding was observed only on inclusion of OH-terminated alkanethiols $>C_6$. On reducing

surface coverage of maltoside from 100% to 10% and modulation of spacer length, a multivalent recognition site for ConA was developed as opposed to the more rigid and homogenous maltoside monolayer (*Fig. 16*) (229).

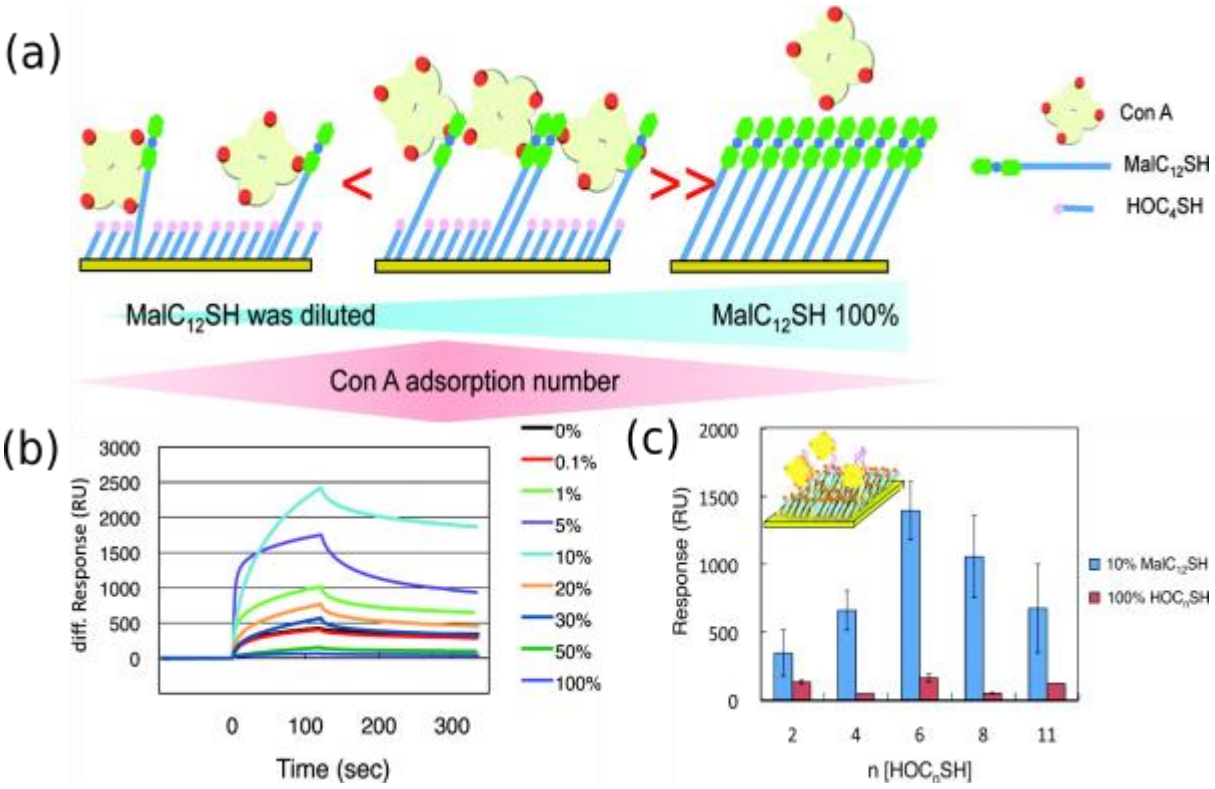


Fig. 16: ConA sensor design using mixed alkanethiol SAM. (a) SAM design showing maltoside terminated (functional) monomers with ConA capture efficiency at low and high maltoside monomer concentration (b) SPR response curve of 1 µM ConA binding against varying surface concentrations of maltoside terminated SAM. (c) SPR binding response displaying varying spacer alkane chain length with 5 µM ConA binding comparing 10% maltoside terminated SAM (blue) with 0% maltoside SAM (red). [image taken from (229)]

Further consideration must be given to solvent selection and relative size and chemical composition of each included monomer in the multi-component SAM. Selection of incompatibly sized units or with opposing chemical groups has shown domain segregation at the surface nullifying attempts at producing binding pockets while increasing potential surface defects (230). Equally, backbone length as discussed affects adsorption hence, competitive adsorption from a mixed monomer solution will be unsymmetrical generating uncertainty in the ratio of surface presented groups (231). Finally, solvent selection must be attuned with chemical composition of SAM monomers with several studies observing more densely packed alkanethiol structures in water/ ethanol systems including suggestions to the monomer solubility and hydrophobicity as a driving force of phase segregation alongside SAM monomer composition (228,231,232).

1.4.5 Monolayer functionalisation

In considering each element of SAM design to deliver an optimised densely packed and well organised monolayer, the stage is being set for a critical step in biosensor design: functionalisation of the surface, thus producing a practical use to the surface. Over the years a multitude of various surface reactions have been researched however, in bioassay design fragile biomolecules require more gentle immobilisation

techniques than typically available synthetic routes. This leads to two possible design paths: (1) use of biocompatible reaction or (2) pre-synthesis of the whole recognition monomer (the latter being far less frequently used given complex synthesis and purification methods). Several of these will be discussed further in the following chapters with emphasis given to the Cu(I) catalysed azide-alkyne cycloaddition (CuAAC).

While a multitude of surface reactions have been used in SAM functionalisation, there are several that have attracted considerable attention due to their ease of use and suitability for use with biomolecules such as DNA and proteins. Two such reactions, the Michael addition and thiolene reaction (*Fig. 17a, Fig. 17*b) are of particular interest given both make use of sulphur containing reactions hence could use a double sided alkanethiol, potentially reducing chance of improper surface association of the SAM monomers. These reactions also proceed rapidly with high yields and at neutral pH thus making them highly desirable reactions in biosensor design (233,234). This has been demonstrated across a number of maleimide-S reaction-based surface immobilisations of peptides, carbohydrates and DNA (235–238), while thiolene has been used in biotin and DNA immobilisation in microfluidic devices (239,240)and in both protein (241) and carbohydrate (242) based immunoassays.

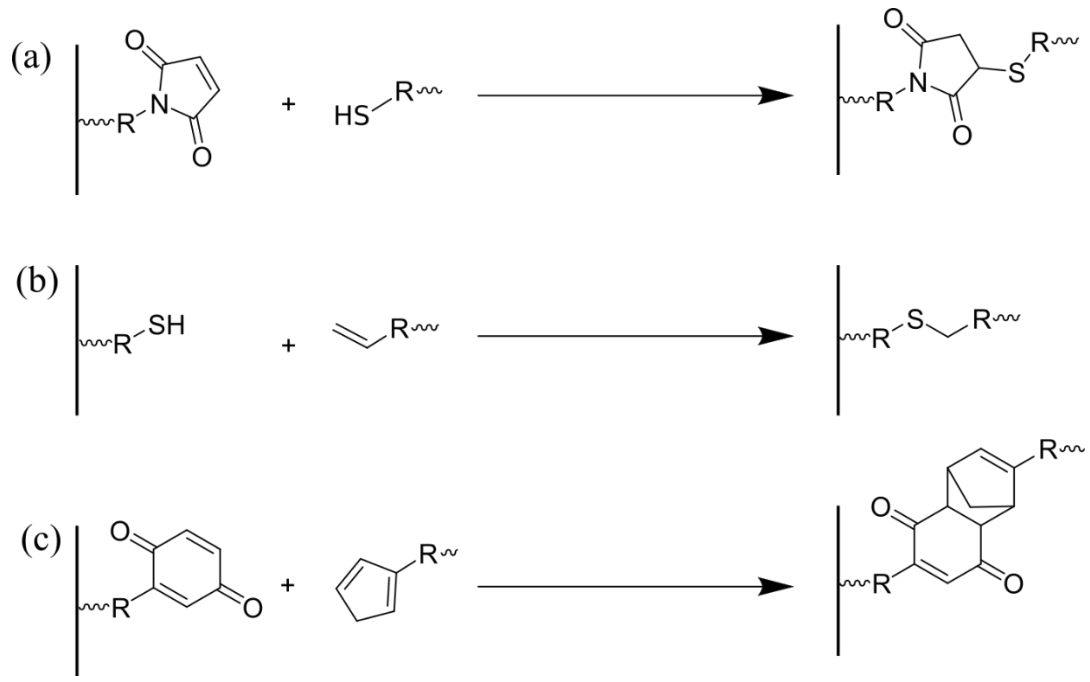


Fig. 17: (a) Michael addition. (b) Thiolene reaction. (c) Diels-Alder reaction (233,243).

Despite agreeable suitability, use of these reactions is limited by natural abundance of cysteine residues in some proteins potentially adding non-specific adsorption or improper orientation to immobilised ligands. Furthermore, monomer design with thiols at each terminus would require a rigid chemical structure *i.e.* phenyl ring to prevent chemical SAM defects with adsorption at both ends of the SAM. Dense packing of the SAM may also be interrupted by bulky terminal groups such as maleimide while use of radical initiators in thiolene reaction has

potential to introduce surface contaminants or damage to monolayer itself.

Alternatively, the Diels-Alder reaction (*Fig. 17c*) as introduced for surface reactions by Yousaf and Mrksich (1999) is a catalyst free rapid cycloaddition reaction between conjugated diene and dienophile *i.e.* alkene or alkyne (244). Being kinetically favourable, this reaction produces good yields even at low concentrations of reactants which, being coupled with its use in aqueous media makes this reaction highly compatible with biomolecules. This reaction has seen extensive use in peptide and protein immobilisation given reactivity can be imparted to nucleophilic side chains of amino acids: lysine, serine, threonine and tyrosine or through hexadienyl or maleimide conjugation (245). Whilst an excellent reaction for proteins and various chemical compounds, cross-reactivity can still occur as observed by Hammer *et al* (2014) who observed Michael additions between nucleophilic amino acids and maleimide commonly used in Diels-alder reactions (246). Furthermore, suitability to carbohydrate ligands is limited given the lack of reactive dienes on saccharides hence requiring complex further modification such as produced by Sun *et al* (2006) who used a Diels-Alder reaction to functionalise a surface before carbohydrate immobilisation via CuAAC reaction (247).

1.4.6 Cu(I)-catalysed azide-alkyne cycloaddition

Since Huisgen began his descriptions of 1,3 dipolar cycloadditions in 1963 much attention has been given to this set of reactions but none so much as from 2002 with the addition of a copper(I) catalyst introduced by Rostovtsev *et al* (2002) (248,249). In the addition of a Cu(I) catalyst, increased reaction rates and regioselectivity are imbued to alkyne-azide reactions yielding almost exclusively 1,4 disubstituted triazoles, a far more favourable regioisomer for surface chemistry compared to 1,5 disubstituted triazole counterpart (250) (*Fig. 18a*). The accepted reaction progression is shown in *Fig. 18b*.

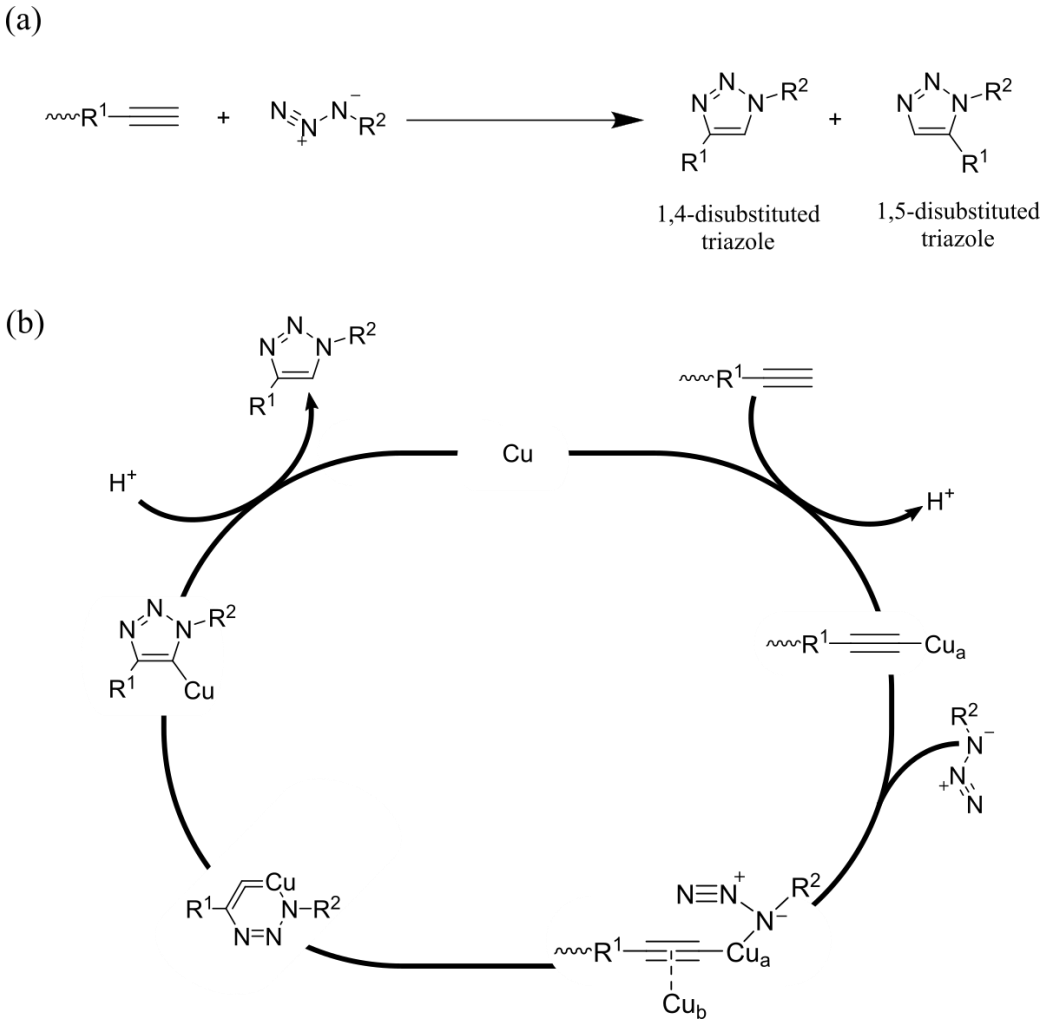


Fig. 18: (a) Reaction of alkyne and azide producing 1,4-disubstituted and 1,5-disubstituted triazoles respectively. (b) currently accepted CuAAC reaction scheme (251).

As proposed by Rostovstev *et al* (2002), the Cu(I) forms acetylide intermediates with alkyne species (249). This was later expanded by Worrell *et al* (2013) who used heat-flow calorimetry and isotopically enriched Cu^{63} in time-of-flight mass spectroscopy (TOF-MS) to study the reaction. From this, it was

proposed a second π-bound Cu was recruited to the complex (252). More recent computational DFT studies have confirmed the reaction progresses through enhanced nucleophilicity of Cu-acetylides enabling a transition from non-polar one step synthesis (uncatalyzed) to polar multi-step synthesis (Cu catalysed) (253). As shown in *fig. 18b,* the reaction starts with formation of Cu(I) acetylides through the alkyne which then associates with an azide species. A six-membered ring intermediate is then produced from β-carbon of alkyne-Cu(I)-acetylide and terminal nitrogen of the azide. The prototype triazole is then formed through reductive elimination of one Cu(I) before protonation of the final Cu(I) species thereby regenerating it for further reaction thus closing the cycle (253,254).

In achieving rapid reaction rates in aqueous media and lacking common biological ligands *i.e.* amino acid side chains, the CuAAC reaction has particularly high potential in biomolecule immobilisation. This is further emphasised in its application in neutral pH solvent systems and at ambient temperature thus has found widespread use in surface functionalisation. Significant amounts of research has been attributed to immobilisation of both alkyne or azide with varying degrees of success. An early study produced by Rohde *et al* (2006) adsorbing alkyne terminated SAM to silicon(111) surface with

CuAAC attachment of benzoquinone to the surface produced only 7% surface coverage. Successful CuAAC reaction was dominated at silicon step edges suggesting steric hinderance of the reaction preventing layer growth (*Fig. 19a*) (255). Surface coverage was markedly improved by Ciampi *et al* (2007) who saw 80& and 76% coverage for short azidoalkane and phenylazide compounds respectively via CuAAC reaction on alkyne terminated SAMs (*Fig. 19b*). Steric hinderance at the alkyne layer again was suggested to prevent CuAAC progression with mixed SAMs proposed to circumvent this issue (256).

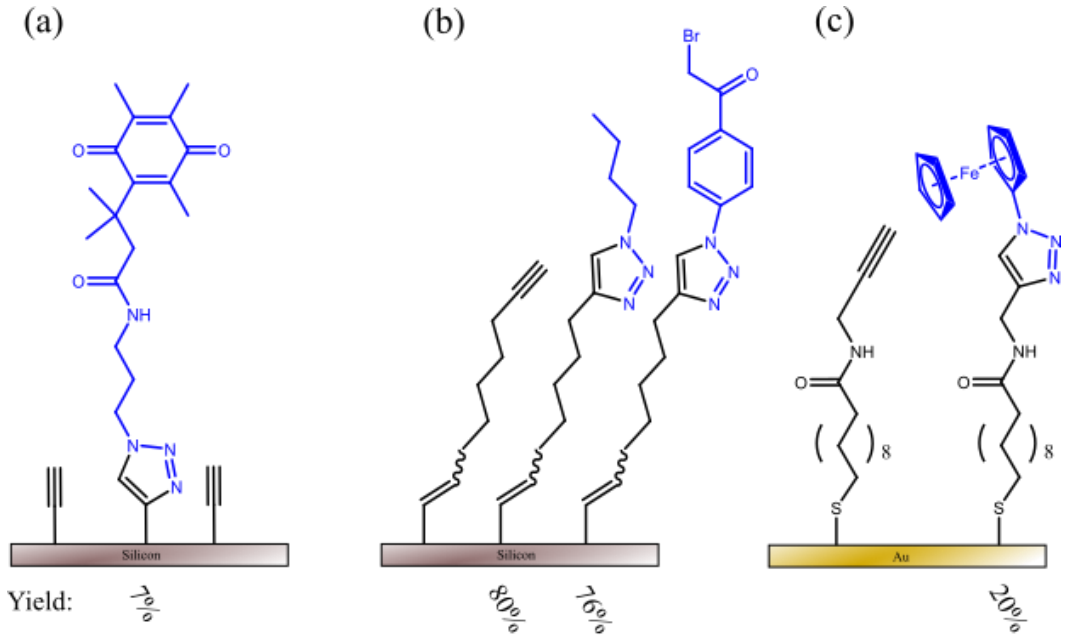


Fig. 19: Examples of CuAAC clicked SAMs (a) Short alkyne SAM with large azido ligand producing 7% yield (255). (b) Long alkyne with varying azido ligand size producing 80% and 76% yield respectively (256). (c) Long alkyne SAM with large ferrocene azido ligand with 20% yield (257).

Alternatively, several studies have used azide terminated monolayers and report higher yielding CuAAC surface reactions compared to similarly run alkyne terminated SAMs. A study produced by Chelmowski *et al* (2009) comparing alkyne Vs. azido terminated SAMs on Au (*Fig. 19c*) observed poor yields for CuAAC reaction between surface alkyne and solution azidoferrocene even with inclusion of up 90% mercaptoundecanol spacer monomer. Conversely, azido terminated SAMs produced significantly more ferrocene surface coverage further suggesting steric constraints of alkyne units can reduce CuAAC reaction rates. However, it should also be considered the size of the ferrocene ligand in this study potentially producing steric hinderance thus explaining conflicting results between alkyne terminated SAMs (257). Despite the steric constraints of alkyne functional SAMs, photolytic degradation of azide moieties has been reported elsewhere for peptidic alkyl azides at ambient laboratory light and temperature suggesting potential instability of this surface design (258).

The CuAAC reaction has become ubiquitous with bioconjugation in recent years as reviewed excellently by Pickens *et al* (2018). Extensive use has been sought in cell labelling, drug discovery and antibody/ protein conjugation emphasising the critical importance of this reaction in the biomedical industry (259). Amongst these, it’s utility in SAMs

has not gone unnoticed with a number of studies using CuAAC reaction to immobilise biologically significant compounds to a substrate providing a new generation of potential biosensors. These have included peptide terminated surfaces for stem cell recognition (260), DNA and drug presenting surfaces (261) and molecularly imprinted polymers for cancer diagnostics (262).

1.4.7 Molecular imprinting & artificial antibodies

If we reconsider the work of Sato *et al* (2012) as discussed in section 1.4.4 in producing a sensor for the lectin ConA, only on expression of multivalent interactions was the surface able to bind ConA. Likewise, in nature immunogenic interactions rely on a network of weak bonds working in synchronisation to deliver a strong association between antibody and ligand. Subsequently, biomimetic platforms using short oligonucleotide or peptide sequences (aptamers) or molecular imprinting rely on similar weak interaction networks. In producing this mesh of multivalent bonds, antibody-like ligand recognition can be designed and modulated offering stable and cheap alternatives to immunogenic detection.

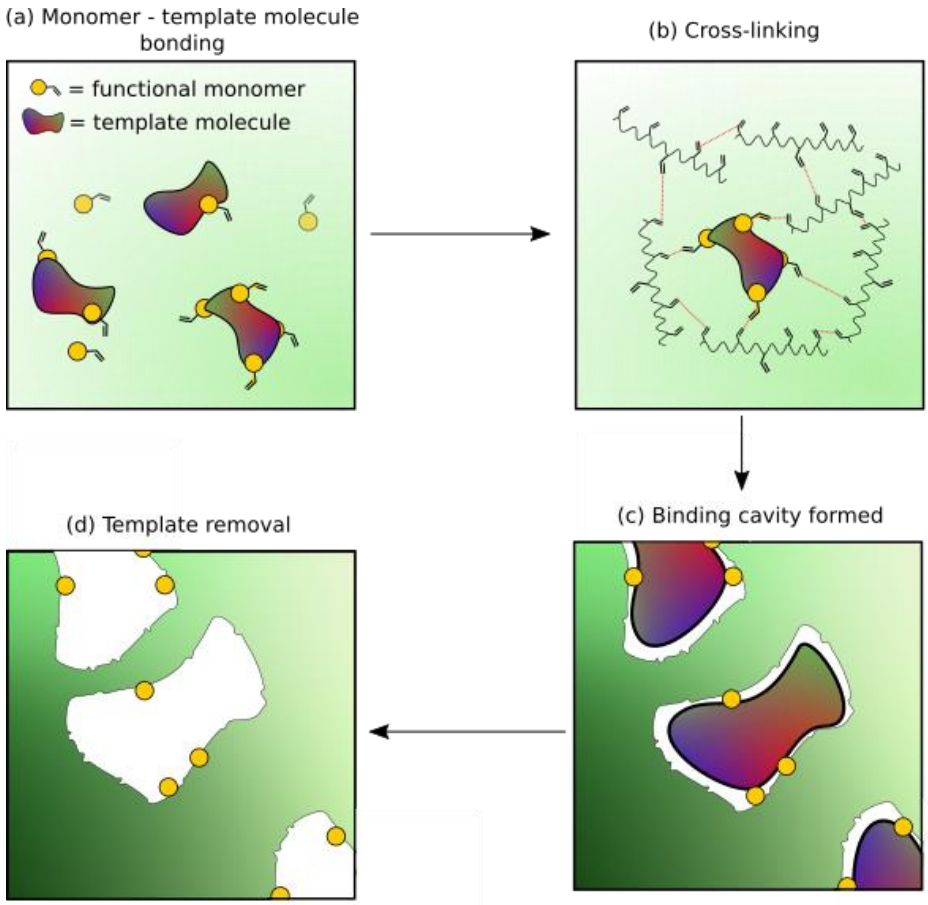


Fig. 20: Typical MIP polymerisation scheme. (a) Functional monomer and template molecule bonding. (b) Polymerisation of cross-linker monomer immobilising template molecule in matrix via functional monomers. (c) Binding cavity formed around template molecule by cross-linker with functional monomers complimentary to reactive groups. (d) Washing and removal of template molecule revealing empty functionalised binding cavity specific for template molecule.

Aptamers are formed from specific oligonucleotide or peptide sequences that hold high affinity and selectivity for target ligands and hold several advantages over biological antibodies, not dissimilar to molecular imprinting. Notably, the synthetic nature and ability to chemically modify sequences allow incorporation of functional moieties such as fluorophores (263). Referring specifically to oligonucleotide aptamers, synthesis requires enrichment of high affinity sequences from random DNA or RNA pools on exposure to target ligand through the process: systemic evolution of ligands by exponential enrichment (SELEX) (264). As each nucleotide sequence adopts specific conformations that enable ligand binding through various forces *i.e.* Van Der Waals, hydrogen bonding and electrostatic or hydrophobic interaction, only high affinity structures are captured on the target ligand allowing isolation (265). Inclusion of primers at each strand end allow amplification through polymerase chain reaction (PCR) thus producing a smaller library of high affinity sequences. Affinity determination and strand modification allows for identification of highly selective sequences for specific analytes as produced for small molecules, proteins and whole cells (266,267).

Alternatively, peptide aptamers are formed of short amino acid loops constrained within an inert scaffold protein *i.e.* inserted within catalytic domain of thioredoxin A (TrxA) thus

inactivating catalytic function (268). These function similarly to oligonucleotide aptamers using short conserved biomolecule sequences providing structurally distinct and selective binding domains. Synthesis of peptide aptamers typically relies on dihybrid yeast expression systems using a strategy of coupling target ligand and aptamer-scaffold to a DNA-binding yeast transcription factor and Yeast transcriptional activator. Only on conjoining these two factors will expression of a reporter gene be induced hence, only on interaction between peptide aptamer and target ligand will transcriptional factor be activated which can be detected through expression of reporter gene such as luciferase (269).

Once a suitable aptamer structure has been isolated and amplified, advantages over antibodies becomes abundant. The short simple structures associated with aptamers can be easily synthesised in bulk, hold higher stability, can be chemically modified without detriment to ligand binding and can have equivalent or improved dissociation constants to antibodies (270,271). A large library of aptamers have been developed against a number of protein and small molecule targets including PSA (272), dopamine (273) and several HIV expressed proteins (274). While fewer glycan targeting aptamers exist, charged saccharide residues such as sialic acid has been marked for development. High affinity RNA aptamers for sialic acid

providing nanomolar dissociation constants were produced by Cho *et al* (2013) using SELEX providing a promising cancer diagnostic probe (275). More recently, a DNA aptamer against *N*-glycolylneuraminic acid, a type of sialic acid, was developed into an immunochromatographic strip through conjugation of DNA aptamer onto gold nanoparticles. Offering high potential as a point of care device, these test strips produced semi-quantitative detection as low as 30 ng/mL under visual inspection reducing to 5.38 ng/mL with a scanning strip reader (276).

Aside from sialic acid, several aptamers have been synthesised against glycan structures including fibrinogen (277) and PSA (278). Directing aptamer selection against glycans is a major challenge however where cross-reactivity with the protein component of the glycoprotein is common. This was overcome by Li *et al* (2008) with the incorporation of boronic acid to direct aptamer selection towards the glycan moiety of fibrinogen. While successful, the resulting aptamer showed dependency on presence of boronic acid to induce high affinity binding. To prevent reliance on chemical modification, Díaz-Fernández *et al* (2019) adopted a rigorous counter-SELEX approach requiring challenging of the DNA library against both glycosylated followed by non-glycosylated PSA producing a high affinity anti-PSA glycan aptamer with K_D 177 ± 65 nm.

While promising, the application of aptamers to glycan sensor development is inhibited by several key challenges. As observed by Díaz-Fernández *et al* (2019), the selective anti-PSA glycan aptamer developed showed cross-reactivity to other glycoproteins notably, lipocalin-2. While this was overcome through incorporation of a sandwich aptamer assay targeting both protein and glycan units, the homology between some glycan structures may serve to reduce clinical specificity. Furthermore, affinity without chemical modification was shown to be lower than with additional chemical groups reflective of low availability of interaction sites on glycan structures as described by Li *et al* (2008). Nonetheless, overcoming these challenges with advances in counter selection and multiplexing of aptamer assays, this technology might offer a useful platform for glycan sensing (134).

The *in vitro* production of artificial antibodies using molecular imprinting was explored much earlier than aptamer technology beginning in 1942 by Pauling and Campbell. Using triphenylmethane methyl blue dye (TPMM) due as the ligand, the proposed the denaturing of γ-bovine globulin and subsequent refolding in presence of TPMM would allow complimentary refolding (279). While successful in creating a unique synthetic antiserum of non-immune origin, this process still suffered from the usual protein associated drawbacks notably: fragile

materials, complex production, time consuming and potentially costly. Nonetheless, research continued in artificial antibodies with some success around 1980 in producing wholly synthetic MIPs (280,281). Building on this early research, recent attempts at organically synthesising MIPs use a three-step approach. The antigen (template molecule) is first bound to functional monomers through either reversible, covalent or non-covalent associations to provide reversible binding. A 'binding pocket' is then produced through co-polymerisation of a cross-linking monomer with functional monomer-antigen complex thereby producing a polymer matrix. In the final step, template molecules are removed via washing yielding a complimentary binding cavity unique to the template molecule (*Fig. 20*) (282).

The benefits of using a polymer matrix include consistent control over binding cavity specificity achieved through careful choice of binding cavity functional group presentation. For instance, modification of a dopamine imprinted styrene-divinylbenzene (SdVB) polymer matrix with PBA and free sulphonic acid group demonstrated binding 400 times higher than just SdVB binding cavity alone (283). This research group later proceeded to construct a lysozyme specific MIP with binding cavities expressing various functional groups including amine, carboxyl and sulphonate groups that modulate re-binding of lysozyme (284). More recently in 2019, a PSA glycan specific MIP using

PBA groups to bind glycan structures was produced (*Fig. 21*). Whilst lacking sensitivity as demonstrated in SPR response curves, this imprint expressed selectivity against other proteins. Selectivity was increased through a dynamic protection method where post-imprinting, MIPs were exposed to PSA allowing binding of PSA within the high PSA affinity MIP pockets. Poly(ethylene) glycol (PEG) was then introduced to the MIP reacting with remaining low affinity binding pockets thereby capping them, preventing non-specific binding where the binding pocket failed to properly form. With observed higher selectivity of the capped MIP against non-capped MIPs this demonstrates importance in avoiding over expression of functional groups on a surface (285).

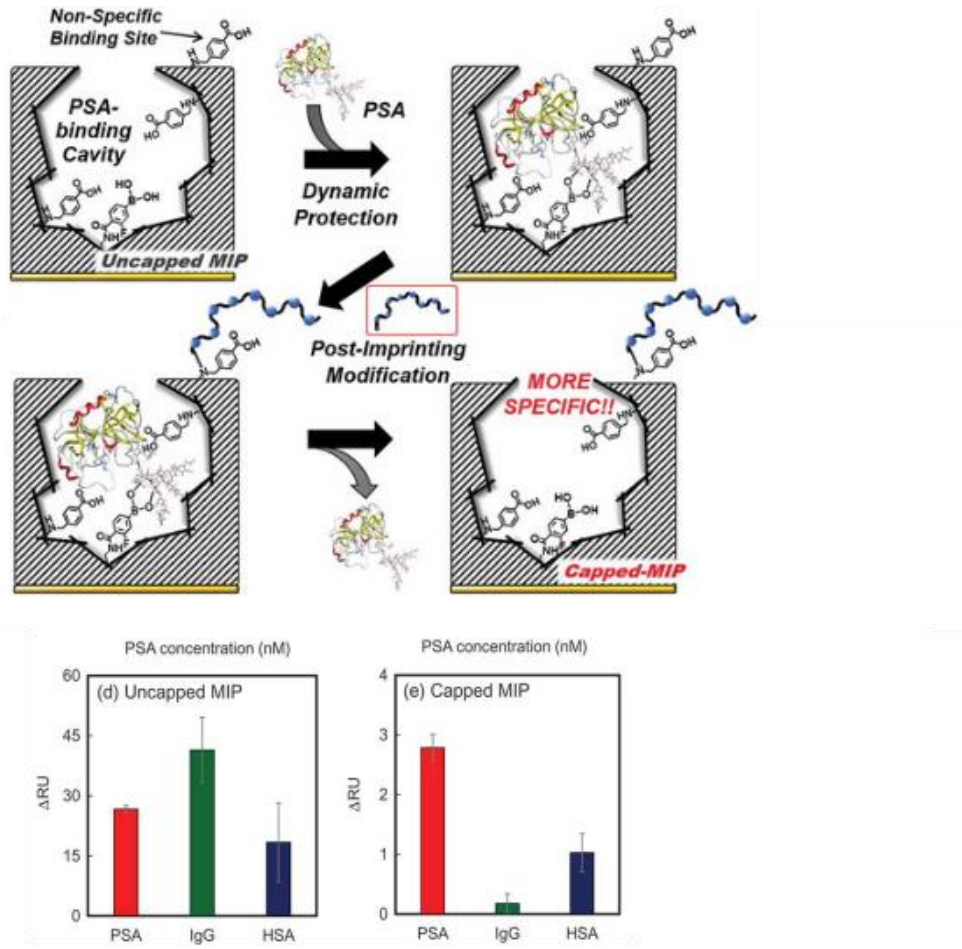


Fig. 21: MIP specific for PSA glycan structures as produced by Matsumoto *et al* (2019). SPR response (*bottom*) show specificity induced only on capping the cavities that lack PBA functionality. This was achieved through capping the MIP after incubation with PSA providing competitive binding between PSA and capping monomer. [image taken from (285)].

Attaining selectivity in MIPs has long been a challenge in the transfer of this technology to the biomedical industry particularly when using seemingly more flexible and functional

targets such as proteins. Nonetheless, recent publications in specific MIPs for CA-125 using a polypyrrole monomers to form binding cavities have been produced while also this year, another group published a carcinoembryonic antigen (CEA) specific MIP that acted as a pre-concentration step before CEA antibody binding and quantification via surface-enhanced Raman spectroscopy (SERS) (286,287). Interestingly, neither MIP used functionalised cavities instead relying on predominantly hydrophobic protein-polypyrrole interaction and gallic acid (monomer)– CEA hydrogen bonding respectively thereby only producing conformationally selective MIPs. Furthermore, in light of current research into glycans as potential biomarkers (section 1.2.3), it is surprising neither MIP were functionalised for glycan sensing.

Given the innocuously complex structural formations of glycans, generating MIPs selective for carbohydrates should provide a new set of challenges. One such challenge, the differentiating between glycosaminoglycan species has recently been explored by Zhang *et al* (2019) who produced MIP magnetic nanoparticles specific for heparin disaccharide (288). Similarly, to the above discussed MIPs however, these nanoparticles relied on a network of weak hydrogen bonds generated through functional acrylate monomers further emphasising the importance on provision of a multivalent mesh of

bonding. Imprinting of another glycosaminoglycan, hyaluronic acid (HA) was alternatively achieved through templating of the monosaccharide glucuronic acid (GlA) against a benzamidine bearing monomer which forms strong electrostatic interactions with COOH groups of the saccharide (*Fig. 22a*)(289). This complex was immobilised on glass beads via CuAAC reaction alongside a fluorophore, thermoresponsive monomer and cross-linking reagent. Despite only imprinting a monosaccharide unit of HA, comparative HA staining to traditional HA stains was observed in human keratinocytes (*Fig. 22b*) suggesting binding for the oligosaccharide thus providing a simpler method for biosensor design for complex glycan structures.

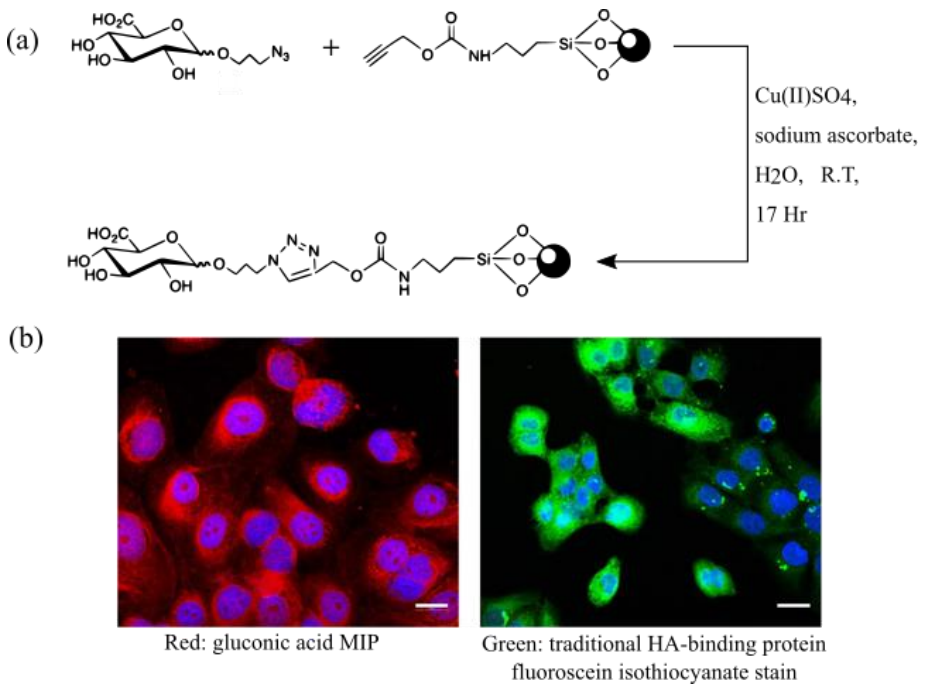


Fig. 22: (a) CuAAC reaction for immobilisation of GlA after which benzamidine, rhodamine B flurophore and cross-linking monomer were polymerised around template yielding GlA binding cavity. (b) GlA-MIP stain (left) versus HA-binding protein stain on human keratinocytes (scale bar 20 µM) [image taken from (289).

Alternatively, by utilising the stronger covalent bonds provided by PBA, a MIP specific for the trisaccharide kanamycin was produced by Zhang *et al* (2018) providing selectivity over other similar glycoside antibiotics (290). Despite this, non-specific binding was still present in MIPs with optimum binding pH surprisingly observed at pH 7.5. Being below the pKa of PBA and favouring trigonal BA configuration, this might suggest the

role of other interactions besides BA-diol esterification in producing binding. Further attempts with PBA functionalised MIPs have seen a unique glycoprotein imprinted polymer developed for ovalbumin by Saeki *et al* (2019). Their approach used dual functional monomers including fluorinated PBA with lower pKa value in conjunction with pyrrolidyl acrylate (PyA) as functional monomers thereby producing covalent PBA-glycan bonding with electrostatic interaction between PyA at the protein (*Fig. 23*). Control of polymer thickness was found to significantly impact MIP sensitivity to ovalbumin with suggestion of keeping thickness roughly double that the target glycoprotein (291). Consistent with this, Mitchel *et al* (2019) found polymer thickness and concentration of PBA functional groups determined both sensitivity and selectivity of the MIP to target glycoprotein. Using atom transfer radical polymerisation (ATRP), precise control over thickness was maintained during MIP formation. From this, sensor performance was optimised to 1:10 ratio of template glycoprotein to PBA and ATRP polymerised for 60 minutes showing significantly better sensor performance than at other PBA-template ratios and polymerisation time (292).

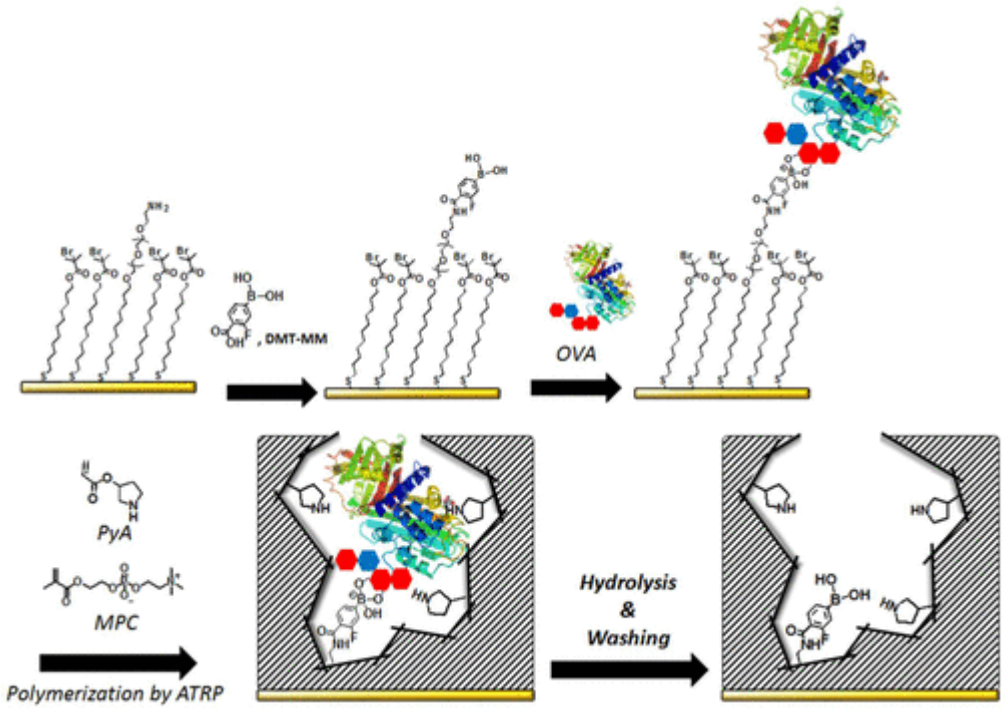


Fig. 23: Scheme for production of BA and PyA functional MIPs specific for ovalbumin. [image taken from (291)]

While the body of research on MIPs as diagnostic platforms is substantial, the transfer of this technology to clinical practise remains impeded. Long term stability and cost of synthesis make imprinting a desirable technology however, low sensitivity and specificity remains a major challenge in improving on current immunogenic sensor platforms (293). As discussed by Verheyen *et al* (2011), low reproducibility of imprints is common with suggestion that a significant number of published imprints do not withstand critical analysis (294). These issues are confounded further in development of glycan-

based imprints imparted by lack of available interaction sites compared with protein imprints. While careful selection of functional monomers such as boronic acids can overcome this, affinity is typically still within low millimolar range thus sensitivity must be markedly improved to produce a clinically relevant platform for glycan analysis (295).

Moving forward, a growing trend of inclusion of multivalent functionality in MIP structures imbuing MIPs with far greater sensitivity and selectivity is observed in recent publications. However, it is apparent more robust and carefully controlled methods are required to transfer this technology to biomarker detection to enable highly reproducible and clinically appropriate platforms. Alongside the imprinting process, careful choice of sensor technology will provide enhanced sensitivity. The growing use of SPR technology as a detection method with MIPs provides considerable benefits given the sensitivity of the technique. When used in conjunction with BA and MIPs could potentially provide a biosensor sufficiently sensitive to detect the small changes in glycoproteome expression.

1.5 Concluding remarks

Over the years, the role and prevalence of saccharide structures and protein glycosylation has come to be understood as an essential function both nutritionally and as regulatory biomolecules. Application of ultrasensitive detection methods such as mass spectroscopy and HPLC has begun to elucidate the minutiae of these regulatory functions and has revealed a complex picture of the glycoproteome. Aberration to the glycoproteome as a marker of cellular malignancy is an important discovery arising from these studies and has generated a new avenue for biomarker discovery for a range of diseases.

Of particular interest, disruption to glycosylation in cancer is a commonly observed trait and may uniquely provide both diagnostic and prognostic data on tumours. For hard to differentiate tumours such as BPH and aggressive PCa, this is a highly desirable function currently impossible by current techniques without invasive histopathological intervention. As discussed however, techniques to characterise glycan structures fail to usefully quantitate glycoproteome changes being reliant on the weak interactions provided by AGA or lectins. Moreover, these methods lack variety in glycans they can bind or lack specificity thus reducing clinical application. Conversely, sensitive physical methods of detection *i.e.* mass spectroscopy,

HPLC *etc.* require expensive and impractical equipment setup outside of specialist chemical laboratories.

In this review we have considered alternative routes of glycan detection namely, BA esterification with saccharides and their potential to be coupled with SAMs and molecular imprinting. This field of research has attracted significant attention in recent years given the commercial viability of a cheap reusable 'artificial antibody' and has seen a number of diagnostic applications produced. While various recent publications has attempted saccharide binding on MIPs, there is a distinct lack of biosensors using BA moieties as a glycan binding functional monomer despite the abundant evidence for its potential. Furthermore, whilst various surface reactions have been explored for biomolecule immobilisation, very few have used CuAAC in direct immobilisation of BA-saccharide complexes despite its suitability in physiologically relevant conditions. In keeping these conditions, perhaps glycan structures can be conserved during molecular imprinting given the highly dynamic nature of these structures thus producing a genuine saccharide imprint, an essential process if we hope to imbue selectivity to these new diagnostic platforms.

1.6 Aims & objectives

The aim of this PhD research is to synthesise a novel platform for selective binding of oligosaccharides. This will be produced using the well-established alkanethiol-Au SAM system which will provide the foundation layer for functionalisation with PBA. Response of the PBA terminated surface to saccharides will be probed with respect to inclusion of spacer monomers to establish effect of steric hinderance on saccharide binding. To imbue the surface with selectivity, we then intend to functionalise the surface via CuAAC reaction with a PBA-oligosaccharide complex thereby producing a complimentary PBA pattern on the surface. This research will be original in functionalisation of a surface with PBA via CuAAC reaction accounting for differences in SAM monomer composition.

This research can be broken down into three main objectives to achieve these aims as follows:

1. Chemical synthesis of all SAM compounds and functional monomers. Varying alkane chain length SAMs terminated in alkyne groups will be synthesised to assess impact on functionalisation. A corresponding azido PBA will be synthesised alongside an azido benzene compound to act as a control surface. A pre-synthesised thiol-PBA terminated SAM monomer consistent with alkanethiol

length will additionally be synthesised to provide a fully PBA terminated surface (*Fig. 24*).

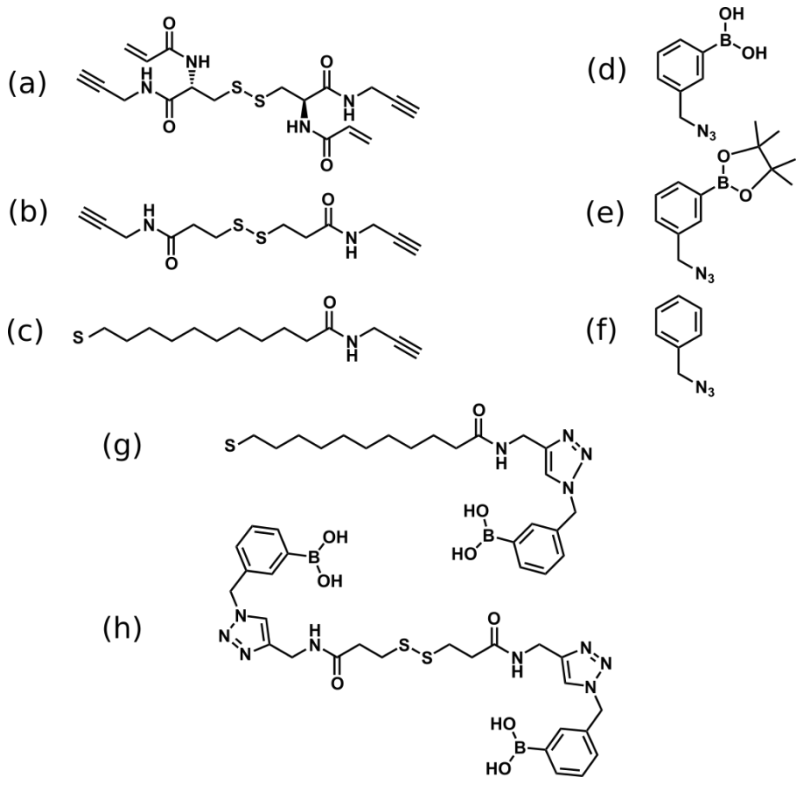


Fig. 24: Compounds to be synthesised for formation or functionalisation of SAMs. (a) Branched dithiol SAM monomer. (b) Linear short (C_2) dithiol SAM monomer. (c) Linear long (C_{10}) thiol SAM monomer. (d) Azide functional PBA. (e) Azide functional pinacol protected PBA. (f) Benzyl azide. (g) PBA functionalised long (C_{10}) thiol SAM monomer. (h) PBA functionalised short (C_2) dithiol SAM monomer.

2. Each SAM and PBA functionalised surface will then be characterised for film growth via a collection of contact angle goniometry, ellipsometry and X-ray electron spectroscopy (XPS). As an effective procedure is developed to produce well defined SAMs, we will then move to probe the surfaces for saccharide binding (*Fig. 25*).

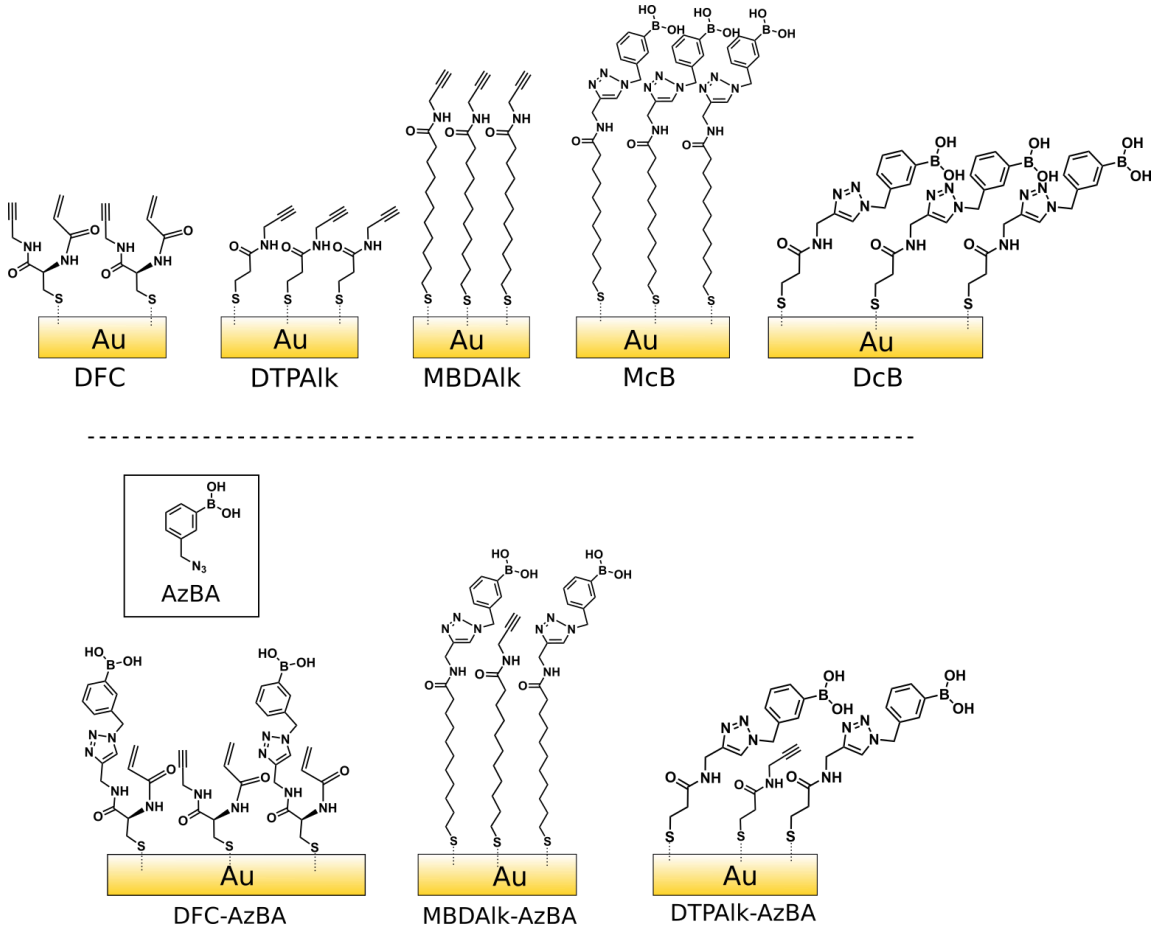


Fig. 25: (*Top*) SAMs produced from monomers (*left to right*) DFC, DTPAlk and MBDAlk expressing terminal alkyne groups. McB and DcB expressing terminal PBA groups. (*Bottom*) Alkyne SAMs surface functionalised with AzBA using the CuAAC reaction based on (*left to right*) DFC, MBDAlk and DTPAlk SAMs.

3. Once characterised, each developed protocol will be used to produce PBA functional SAMs for use with surface plasmon resonance (SPR). Through use of SPR we will establish saccharide binding of pure PBA and PBA functionalised SAMs and optimise this binding. From this we will then produce an oligosaccharide selective MIS using a pre-complexed PBA-saccharide compound to impart complimentary PBA motifs to the surface with binding pocket formation using azido-PEG (*Fig. 26*).

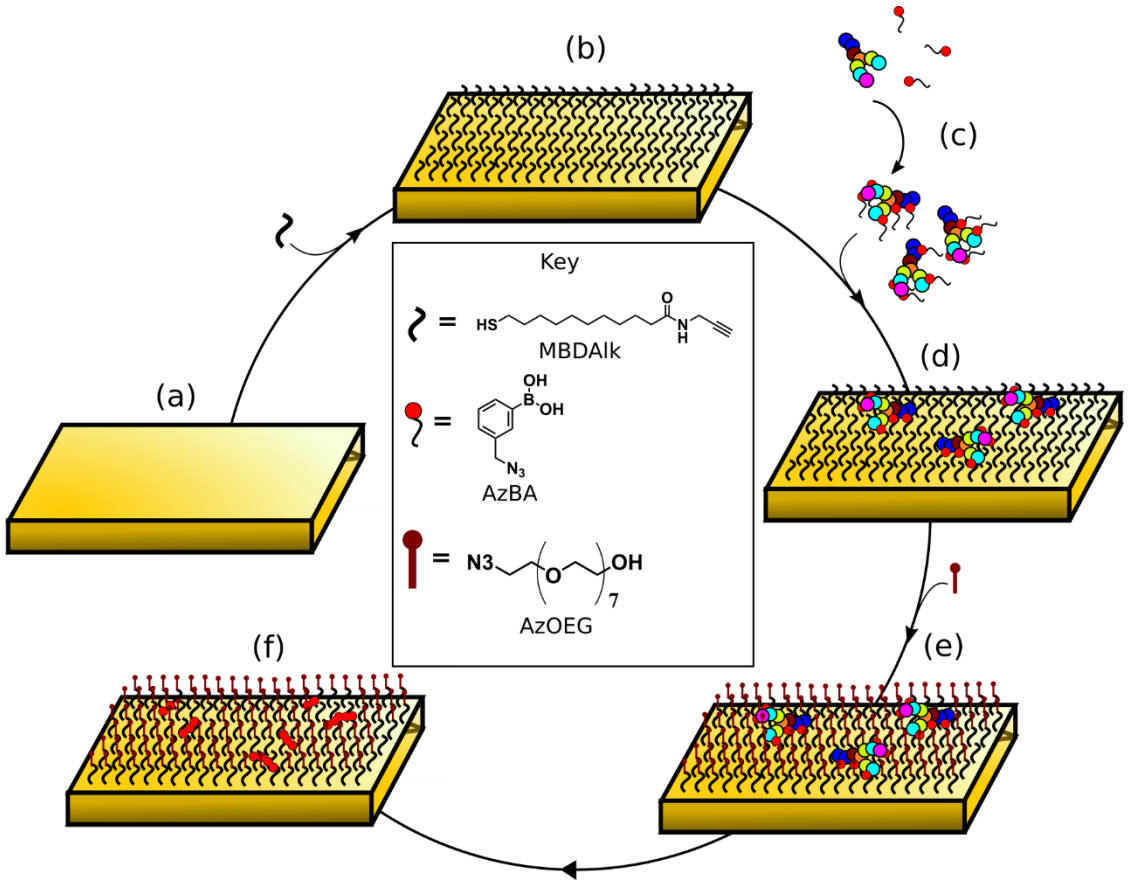


Fig. 26: Schematic for formation of oligosaccharide selective MIS. (a) Chemically clean Au substrate will be (b) functionalised with MBDAlk SAM. A pre-formed oligosaccharide-AzBA will then be (c) immobilised on the surface through CuAAC reaction between AzBA azide groups and MBDAlk alkyne groups. (e) Remaining alkyne groups will then be capped with azide functional PEG (AzOEG) followed by (f) oligosaccharide removal via washing revealing complimentary binding pocket with PBA motifs.

Chapter 2.

Surface characterisation techniques

Abstract: Alongside surface preparation and formation of our SAMs it is essential that growth and composition of each layer is monitored. To do so, we have employed several practical methods that will be discussed briefly in this chapter including contact angle, ellipsometry and X-ray photoelectron spectroscopy (XPS). These techniques were used to monitor wettability, surface thickness and elemental composition providing a means to study SAM organisation and growth. Following characterisation, surface plasmon resonance (SPR) will also be described as the method used to probe interaction between surface and ligand.

2.1 Chapter introduction

Understanding the spontaneous generation of monolayers through chemisorption is critical to the development of SAMs in the biomedical industry and has employed a variety of spectroscopic and physical methods in elucidating kinetics, growth and organisation. Characterisation of surface parameters have seen use of various analytical methods such as infrared spectroscopy to distinguish functional groups to atomic force microscopy to study surface defects and topography. Of this repertoire of methods, this project employed contact angle, ellipsometry and XPS to monitor to measure wettability, thickness, and elemental composition respectively. Following this, surface plasmon resonance (SPR) was used for *in situ* observation of saccharide binding to our surfaces (*Fig. 27*). A brief background of each technique will be discussed in this chapter to give the reader a better clarity of the choice of methods and surface preparation in later chapters.

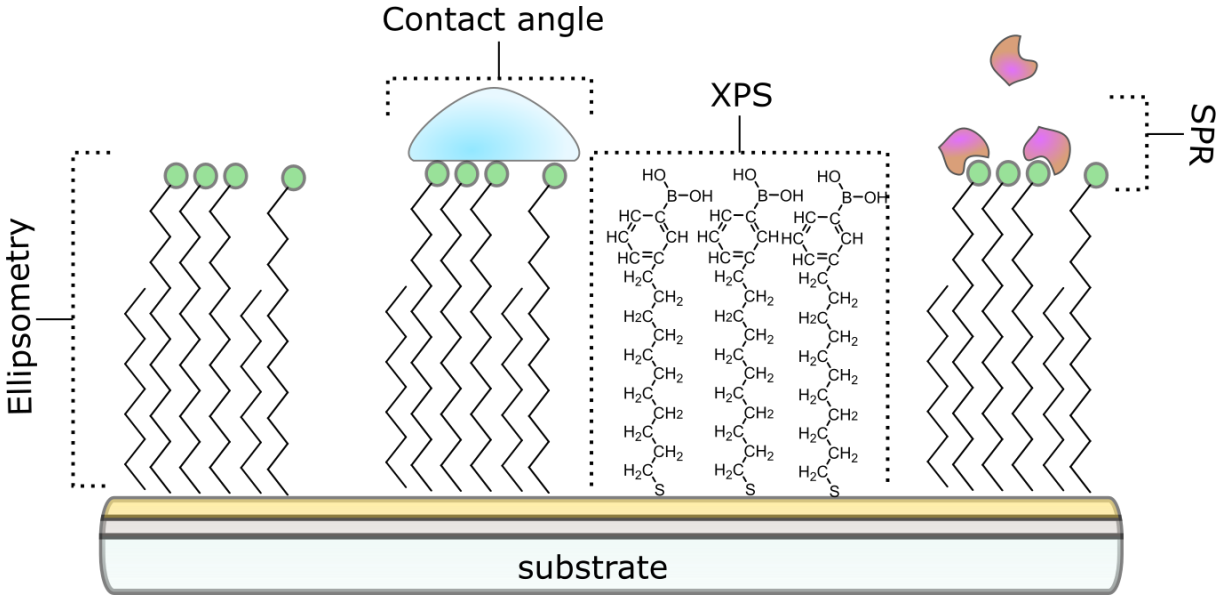


Fig. 27: Overview of methods used to study thickness (ellipsometry), wettability (contact angle), elemental composition (XPS) and ligand interaction respectively (SPR).

2.2 Contact angle goniometry

As identified by Thomas Young in 1805, the measurement of the angle between solid-liquid and liquid-air interface can be a useful determinant of the properties of a surface (296). This technique quantifies the wettability of a surface under certain conditions from which surface tension and free energies of a surface can be calculated (297). To measure this, a modern laboratory setup for measurement of contact angle typically uses a silhouetted sample stage facing a high-resolution camera for

optical measurement and calculation of drop angles against a surface (*Fig. 28*).

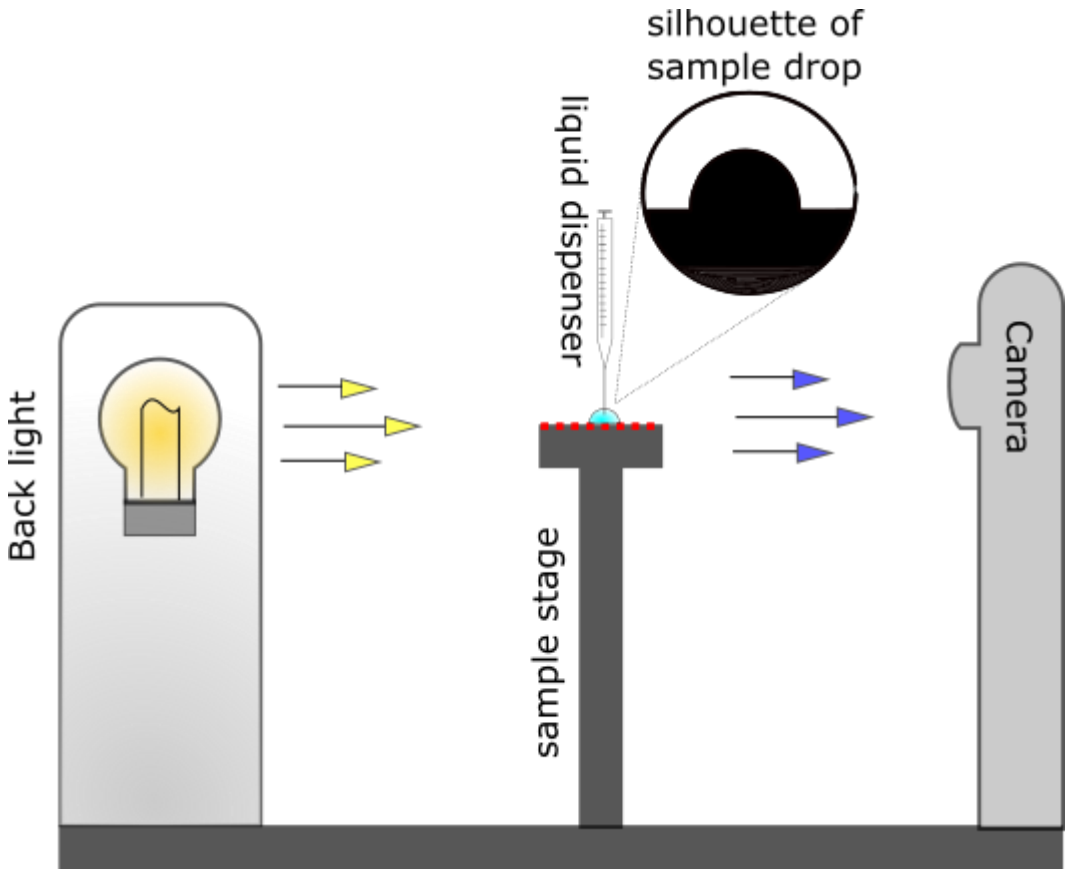


Fig. 28: Typical contact angle goniometry setup. The liquid drop is back-lit against a light source producing a silhouette. The camera is typically connected to a computer enabling automatic angle calculation.

On dispensing of a solvent drop against a surface there is an immediate reaction against the point of contact between solid-liquid and liquid-air interface dependent on atmospheric conditions, solvent and surface properties. Application of a

backlight against the sample enables generation of a silhouette through which a camera can capture real time dynamic angles generated at this interface forming the contact angle (θ)(298). The contact angle can theoretically be described based on the thermodynamic equilibrium between the three phases: solid, liquid and vapor. Youngs equation (*Eq. 1*), describes the shape of the droplet on the surface based on interfacial energies between these phases where γ_{sv} represents the solid-vapor interface, γ_{sl} represents the solid-liquid interface, γ_{lv} represents the liquid vapor interface (alternatively, surface tension) and θ_Y is the determined contact angle (299).

Eq. 1 $$\gamma_{lv}\cos\theta_Y = \gamma_{sv} - \gamma_{sl}$$

The calculated contact angle according to the Young equation can therefore be used to determine surface tension and free energy for γ_{sl} and γ_{sv}. Using water as the solvent drop, on contact with the surface, the drop will spread according to minimisation of total free energy; thus, dependent on surface parameters *i.e.* chemical group and topography, the drop will spread forming a high contact angle (>90°) demonstrating hydrophobicity (low surface energy) or a low contact angle (<90°)

showing hydrophilicity (high surface energy) (*Fig. 29*) (299-303).

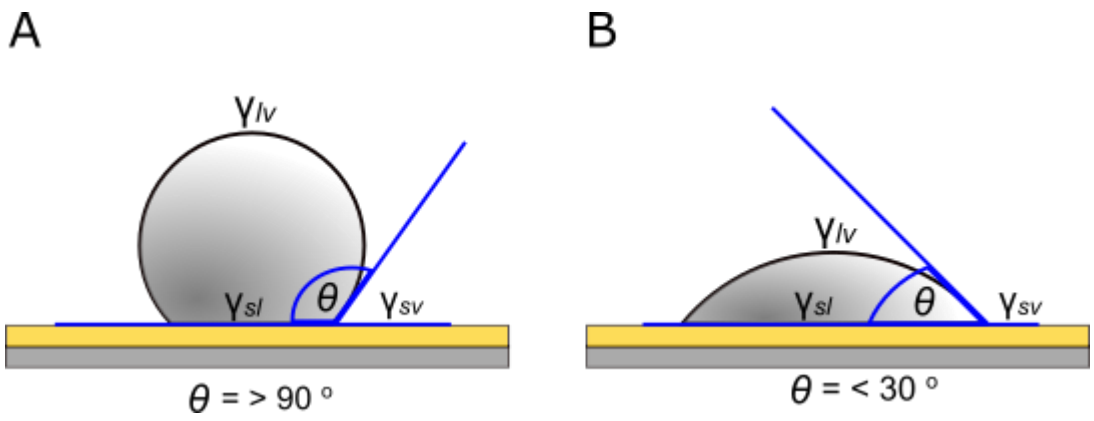


Fig. 29: solvent drop on substrate showing solid-liquid, liquid-vapor and solid-vapor interface. (A) hydrophobic surface with *θ* (B) hydrophilic surface with low *θ*.

A popular method for studying contact angle, the sessile drop experiment uses a solvent drop deposited on a surface to obtain either static (θ_S) or dynamic contact angle. For calculation of surface free energy from sessile drop, contact angle for two or more solvents with known polar and dispersive components must be obtained with surface free energy calculated from the sum of these. For calculation of contact angle from sessile drop , a single solvent *i.e.* water is typically used providing information on surface chemistry and homogeneity (304,305). In the static experiment, solvent deposition on a surface will spread to its final static angle. Conversely, in

its dynamic counterpart, the contact angle is studied during movement of the three phase interface; initially during solvent deposition and drop growth giving the advancing angle (θ_A) and then on solvent removal giving the receding angle (θ_R)(306,307).

From the difference between advancing and receding angles, the hysteresis (θ_H) can be calculated. Surface parameters such as roughness, chemical heterogeneity and contamination can be gauged from the hysteresis where a surface can be assumed smooth and homogenous where the hysteresis is <10 °. Despite the seemingly simple application of the hysteresis, it has still been observed on smooth homogeneous surfaces as well and can be assumed all surfaces will display one (298,299,308,309).

While surface parameters can be inferred from the sessile drop experiment, we must consider the accuracy of the measured hysteresis. Chemical interactions between each interface categorised as the kinetic hysteresis will influence the measured hysteresis (305). For instance, evaporation of the drop from the liquid-vapor interface with potential deposition and pre-wetting of surrounding substrate. Furthermore, any affinity between solvent and chemical groups of the substrate at the solid-liquid interface may introduce swelling, penetration or reorganisation of the chemical groups. For example, Good (1992) describes the behaviour of polar hydroxyl groups of polymer chains being buried at the solid-vapor interface but surfacing

forming hydrogen bonds with water in the solid-liquid interface thus introducing very different advancing and receding contact angles (310). Careful consideration of solvent choice and purity and efforts to minimise time-dependent sources of kinetic hysteresis must therefore be made for accurate collection of contact angle data. Consequently, inferring surface chemistry and homology using hysteresis cannot preclude sources of kinetic hysteresis from results unless ideal experimental conditions are met *i.e.* no sources of motion, no interaction between chemical groups and solvent and evaporation of solvent minimised (311).

2.3 Ellipsometry

Despite the principles of ellipsometry first being described in 1902 by Drude (312), the actual term was not coined until 1945 by Rothen who used elliptically reflected light to determine film deposition thickness on metal slides (313). Since 1990, this technique has received considerably more publications and is an essential tool in characterizing ultra-thin films (314). As a non-destructive technique, ellipsometry uses the change in light polarization on reflection from a surface measuring changes in surface properties. Furthermore, its ease of use, ability to work under ambient conditions and speed allow for *in situ* experiments providing a desirable technique for real time film growth studies (315,316).

In order to describe the principles of ellipsometry, it is necessary to briefly describe the components of light first. According to Maxwell's theory, light can be represented by two mutually perpendicular vectors: **E** (amplitude of the electric field) and **B** (amplitude of the magnetic field) both of which are perpendicular to **Z** (direction of propagation of light). In unpolarized light, **E** oscillates randomly on a plane perpendicular to **Z**. Where polarization occurs, light may become linearly, circularly or elliptically polarized where the parallel ($\mathbf{E_p}$) and perpendicular ($\mathbf{E_s}$) components of **E** are out of phase. For linear polarized light, **E** components: $\mathbf{E_p}$ and $\mathbf{E_s}$ are in phase with coinciding maximas. Conversely, when $\mathbf{E_p}$ and $\mathbf{E_s}$ become 90° out of phase the wave would appears to rotate circularly around **Z** if observed head on (*Fig. 30*). Where the amplitude of $\mathbf{E_p}$ and $\mathbf{E_s}$ are unequal, this produces an elliptical trace as opposed to circular (315,317).

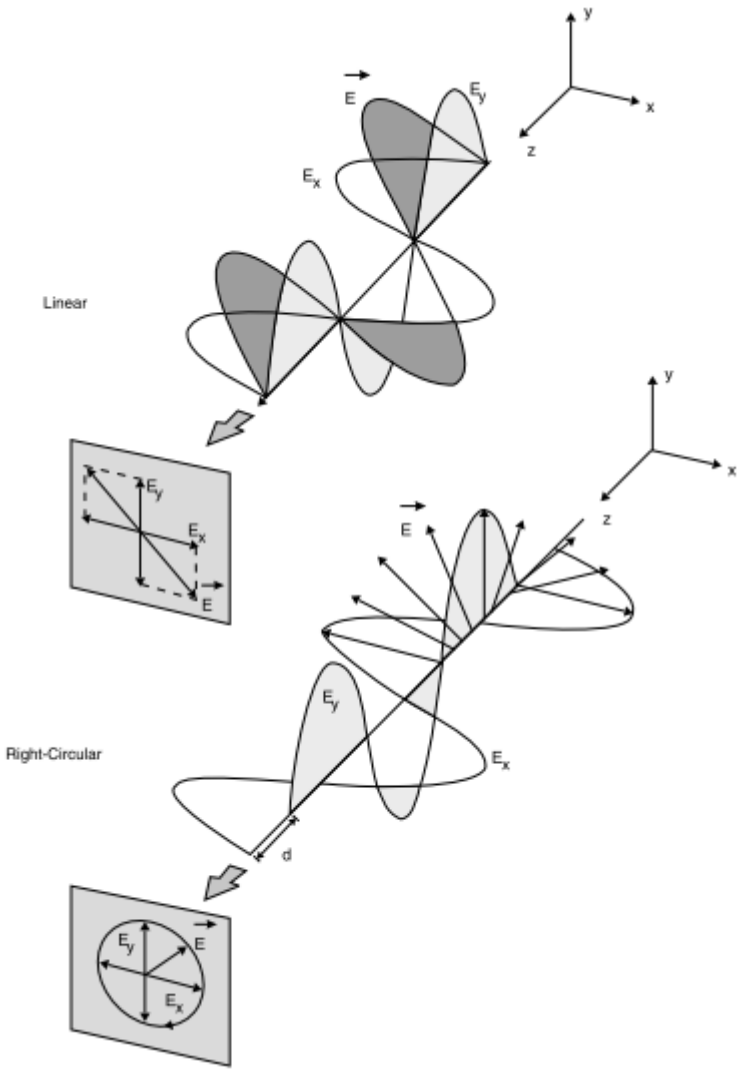


Fig. 30 (top) linearly polarized light with **E** parallel and perpendicular components in phase. (bottom) **E** components 90 ◦ out of phase displays circularly polarized light. Deviation from this becomes elliptical polarized [image taken from (318)].

The reflection of linearly polarised light from a surface will cause **E** to resolve its $\mathbf{E_p}$ and $\mathbf{E_s}$ components out of phase and amplitude dependent on surface characteristics. The result is elliptically polarized light reflected from the surface from which the ellipsometer can quantify changes and provide information such as film thickness (*Fig. 31*)

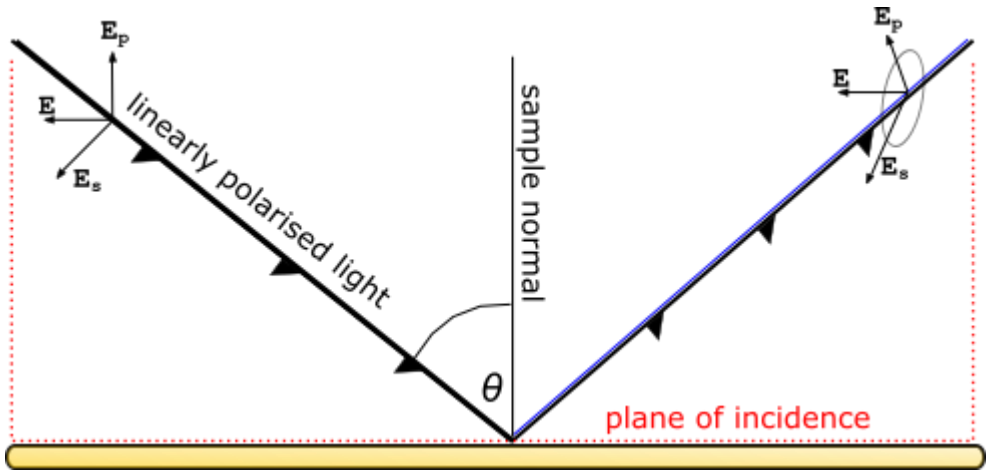


Fig. 31: Change in E components E_p and E_s on reflectance of linearly polarized light from a surface. Shift in amplitude and phase can be quantified allowing calculation of film thickness.

Shown in *Fig. 32* is a basic ellipsometer experiment. A source of collimated unpolarized light is passed along a set angle (close to the Brewster angle) through a polarizer and a compensator (*i.e.* quarter wave plate, retarder or phase

modulator) placed either before or after reflectance on a sample. This produces linearly polarized light that on interaction with optical properties of a surface, reflect elliptically polarized light. An analyser then manipulates the polarization of reflected light before being passed through a detector. (315,317)

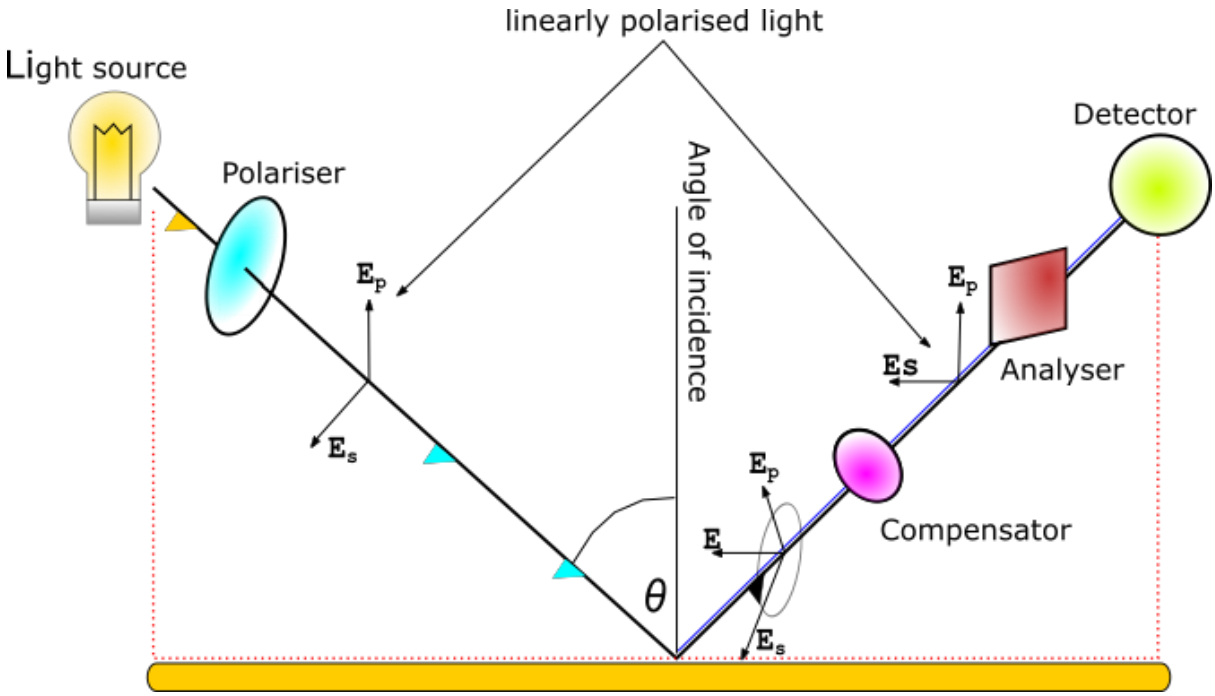


Fig. 32: basic ellipsometer setup showing transition from unpolarized light to linear and to elliptically polarized on reflectance from a surface. The change in phase and amplitude is used to calculate Ψ and Δ.

From the change to $\mathbf{E_p}$ and $\mathbf{E_s}$ amplitude and ratio, the reflection coefficient ρ can be calculated according to *Eq. 2* where ρ is equal to the ratio of $\mathbf{E_p}$ and $\mathbf{E_s}$ coefficients and can be expressed as angles Δ (phase difference) and Ψ (amplitude ratio). These angles are related to reflection coefficients derived by Fresnel expressed as r_s and r_p for s and p polarized light respectively.

Eq. 2 $$\rho = \frac{\mathbf{r_s}}{\mathbf{r_p}} = \tan(\Psi) e^{i\Delta}$$

The Ψ and Δ parameters obtained through measurement of optical constants are however abstract thus requiring an indirect method to measure surface parameters such as thickness. To derive useful surface parameters from Ψ and Δ, a model using least squares minimization is used to vary the optical constants n (refractive index) and k (extinction coefficient) and the Fresnel equations used to calculate Ψ and Δ forming a predictive surface parameter model. Matching predicted Ψ and Δ with experimental data Ψ and Δ is used to obtain experimentally derived n and k optical constants alongside varied parameters such as surface thickness (315,319).

Modern ellipsometers provide an impressive sensitivity to films with reported thickness as low as 0.1 nm with a precision of 0.002 nm across 30 measurements and measuring up to 10 μm for

transparent films (320,321). Despite this, measurement of ultra-thin film (<15 nm) however is complicated by inability to experimentally calculate refractive index due to correlation between film thickness and refractive index below the threshold thickness of <15 nm (322). To calculate thickness therefore we must assume refractive index with this commonly fixed at between 1.45 – 150 for ultra-thin transparent films. Consequently, we must always assume a small degree of error associated with varying the assumed refractive index in ultra-thin films (318,320,323–326).

Alongside refractive index, the optical constant k describes the change in parameters of the electromagnetic wave passing through a medium *i.e.* phase and amplitude. For transparent thin films, k is observed very close to zero in the visible light spectrum (~600 nm) however, for absorbing or films, k is coupled to thickness and unknown hence must be determined either from a wavelength region where k=0 or through inclusion of alternative parameter derived from alternative methods such as thickness in modelling procedures (315,327,328).

As previously stated, experimentally derived Ψ and Δ are abstract thus we cannot determine thickness from these alone. In addition, for ultra-thin transparent films, k is defined as zero and n cannot be determined due to correlation with the parameter, thickness. To calculate thickness therefore, an approach of

predicting Ψ and Δ through varying parameters such as thickness until uniformity between experimental and theoretical Ψ and Δ is observed with the goodness of fit quantified with root mean squared error (MSE). A commonly used predictive model for transparent films, the Cauchy dispersion relationship (equation. 3) provides a simple predictive model for Ψ and Δ where n is expressed as a function of wavelength (λ) forming nλ and A, B and C are the Cauchy coefficients determining nλ at different wavelengths. By varying parameters such as thickness, A, B and C, theoretical Ψ and Δ values can be produced and matched against experimental Ψ and Δ thus we achieve uniformity between observed and theoretical Ψ and Δ from which we can infer experimental thickness of our film from a predictive model (329,330).

Because thickness is not directly measured but instead, inferred from theoretical modelling we must always consider potential sources of inaccuracy as result of poor data fitting. For instance, Durgapal *et al* (2006) describes a discrepancy of 13% in calculated thickness of thin SiO_2 (<10 nm) when calculated with different models including Cauchy and Sellmeier dispersions. Interpretation of ellipsometry derived thickness must always therefore consider a source of innate error dependent on modelling procedures (327,329).

Eq. 3 $$n(\lambda) = A + \frac{B}{\lambda^2} + \frac{C}{\lambda^4}$$

In the context of this research, ultra-thin (<1 nm) films of alkanethiols on Au substrates were being studied. To obtain thickness we used a Cauchy model based on a three phase system of ambient/SAM/substrate where optical constants of ambient and substrate phases were known and SAMs were assumed homogenous and defect free (331). For optical constants of our SAMs we assume a refractive index of 1.5 as previously used for similar ultra-thin films (262,324). To determine if the film is transparent or absorbing, the relationship between experimental optical constants n and k must be observed for 'physical' shape that is, n must increase towards shorter wavelengths on the spectrum whereas n decreases towards shorter wavelengths in absorbing films (332). As the observed n and k relationship represented a transparent film for our SAMs, k was defined as zero. The three Cauchy model parameters A, B and C alongside thickness were then varied to calculate Ψ and Δ in our theoretical model until matching experimentally derived Ψ and Δ thus providing our reported thickness values with goodness of fit determined from MSE (322,333,334).

2.4 X-ray photoelectron spectroscopy

One of the major challenges in surface chemistry remains studying ultra-thin film deposition where ellipsometry and contact angle lacks sensitivity and ability to derive compositional information. To circumvent this, X-ray photoelectron spectroscopy (XPS) is a technique that uses X-ray irradiation of a surface up to 10 nm to cause ejection of photoelectrons. Energy of ejected electrons are characteristic of both the atom and of chemical environment *i.e.* bonds and nearby atoms. Elemental composition of ultra-thin films can be derived from this emission spectra providing data on surface characters such as chemical composition and contamination (335).

A typical XPS setup sees a sample mounted and placed under ultra-high vacuum. A source of monochromatic X-rays generated from a metallic anode such as Mg or Al *K*α providing X-ray energies of 1253.6 or 1486.6 eV respectively, is aimed at fixed angle towards the sample. An electron collection lens connected to a hemispherical electron energy analyser which is placed adjacent for capture of ejected photoelectrons. The electron energy analyser is connected to a detection device and computer peripherals through which binding energy of the ejected photoelectrons can be calculated (*Fig. 33*)(336–338).

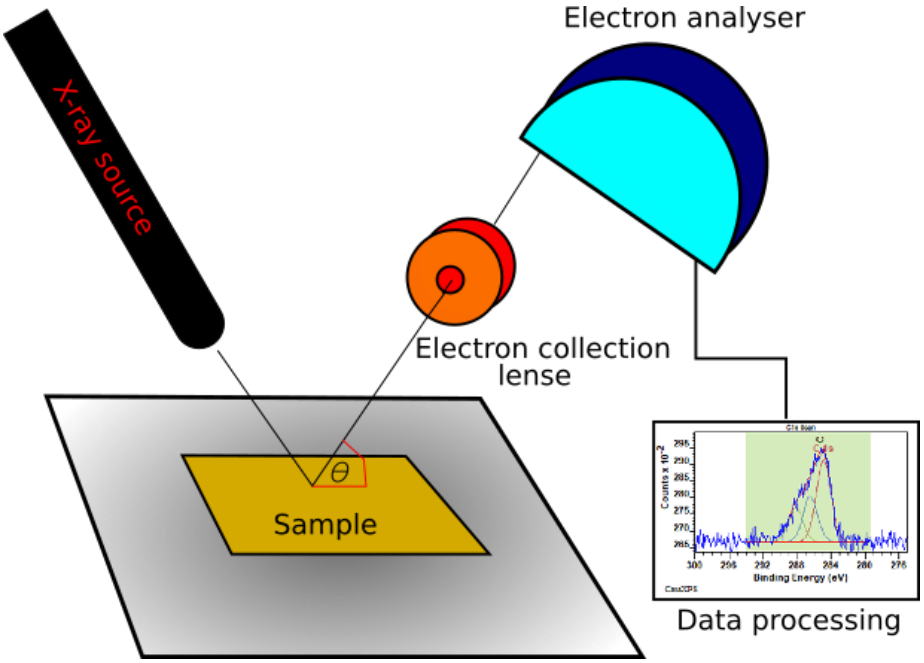


Fig. 33: Schematic of experimental XPS setup. Sample irradiation occurs in ultra-high vacuum chamber. Ejected photoelectrons are detected and used to generate XPS spectra plotting intensity against electron binding energy.

The characteristic elemental peaks provided by XPS are produced from ejected photoelectrons. On irradiation of an atom with an X-ray beam, inner core-level electrons will absorb the X-ray photon energy which, if sufficiently large will cause ejection of a core electron as a result of ionisation (*Fig. 34*). In addition peaks attributed to outermost valence band electrons are typically observed at weak binding energy (up to 30 eV) however low resolution using typical Al Kα X-ray sources prevent useful resolving of peaks spectra in this region (339,340).

Following photoelectron ejection, a relaxation process occurs with two possibilities: an electron from a higher energy level fills the vacancy emitting an X-ray photon or an additional auger electron is ejected from an outer low energy shell (335,337,339). The measured quantity in this process is the electron kinetic energy (E_k). However, this does not account for X-ray photon energy used in the experiment. A more useful parameter is the electron binding energy accounting for this relationship and shown in equation. 4.

Eq. 4 $$E_B = hv - E_k - W$$

In this, the photon energy (hv) and work function of the spectrometer (W) are known quantities while E_k is derived from the experiment allowing easy calculation of binding energy (E_B)(339,341). Given the different chemical environments and binding strengths of electron configurations, this transcribes to a series of discrete binding energy peaks and chemical shifts between 0.1 eV to 10 eV unique to irradiated atoms and associated auger peaks (341).

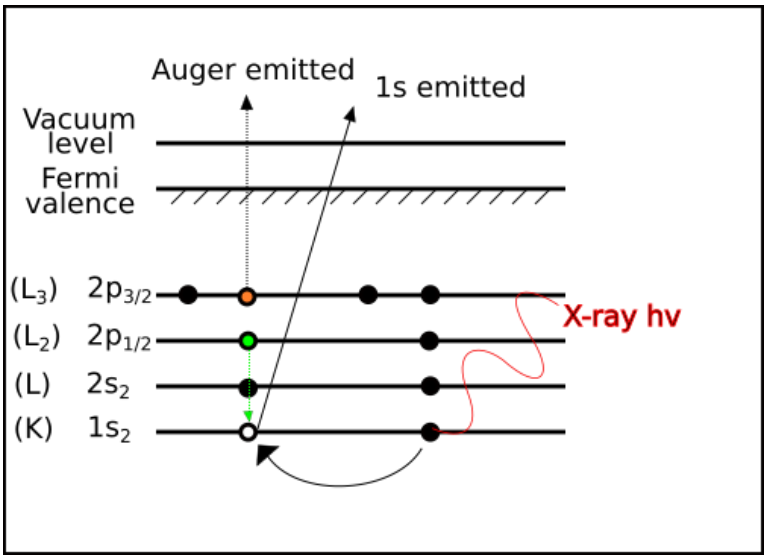


Fig. 34: illustration of electron ejection during X-ray irradiation. During relaxation, an electron from lower energy state can fill the vacancy or an outer shell auger electron can be lost.

For each element, electron subshell peak positions are determined by the chemical environment it originated from. In addition, elemental quantification can be provided through peak areas as calculated from curve fitting the XPS spectrum using Gaussian/ Lorentzian line shapes with the background subtracted. Peak intensity is however dependent on a number of factors including: cross section of the orbital *i.e.* increased emission is observed at higher subshell number such as 1s, 2p, 3s *etc.*, electron escape depth as related to sample thickness, electron location and kinetic energy of the electron, and instrument

dependent parameters such as detector efficiency (339,342). We can nonetheless account for these factors for instance, applying relative sensitivity factors (RSF) to scale quantified peaks and through depth profiling of sample layers. Accurate quantification however relies on defined separation of peaks as observed in the full width half maxima (FWHM) of peaks which is determined by the energy resolution of the instrument (342,343).

The energy resolution depends on instrument specific parameters but is commonly modulated through varying of pass energy. Typical pass energies range from 5-50 eV with lower pass energy producing high resolution but decreased signal strength. Conversely, high pass energy provides reduced resolution but increased peak intensity thus suiting it to elemental survey scans where accurate quantification is not required (339,342). At high pass energy, increased peak intensity results from rejection of lower energy inelastically scattered electrons that serve to increase signal to noise ratio while diminished resolution is a consequence of reduced angular deviation of higher energy electrons in the hemispherical analyser (344).

In effect, a trade-off is observed between peak intensity and peak separation. Instrument parameters must therefore be set according to the chemical configuration and requirements of the experiment *i.e.* low pass energy for accurate elemental quantification (345–347). Accurate quantification therefore

rests on achieving high resolution with peak separations above the energy resolution of the instrument, hence clarifying individual chemical environments. In practise, ejected electrons can be close in binding energy thus providing broad peaks representing multiple environments. Unless the chemical configuration of the sample is known and the sample is homogenous, we cannot reliably assign peaks with less separation than the energy resolution. Consequently the accuracy of XPS is limited with energy resolution of the instrument (348). In addition, decomposition of organic surfaces under the X-ray beam has been observed hence sample degradation may also artefactually reduce peak intensity (349).

Despite this limitation, XPS provides a highly sensitive elemental quantification typically within ±10% of elemental composition (350). As this technique is sensitive to depths of <10 nm, XPS is well suited for the study of ultra-thin films such as SAMs. In addition, subsurface profiling can be achieved with sputtering techniques while thickness and composition parameters can be attained through angle resolved XPS (351–353).

2.5 Surface plasmon resonance

Providing a real time, label-free and adaptable analysis procedure, surface plasmon resonance (SPR) has become a desirable technique in the bio-assay industry. The phenomena of SPR was first observed by Wood in 1902 (354) where he viewed anomalous diffraction of light through diffraction gratings. This was expanded into practical procedures by incorporation of attenuated total reflection allowing for development of modern SPR spectrometers using the Kretschmann configuration (355,356).

To understand the typical setup of an SPR spectrometer it is necessary to describe surface plasmon wave (SPW) generation. If we consider again the components of light described in section 2.3, the polarisation state of light is represented in the parallel (E_p) and perpendicular (E_s) components of the vector E (amplitude of the electric field) (*Fig. 30*) (315). Isolation of either polarisation state provides p-polarised and s-polarised light respectively. While s-polarised light is incapable of exciting plasmons, p-polarised light on striking a thin metal film interfaced with a dielectric media can produce delocalised charge-density oscillations called a surface plasmon wave at the metal-dielectric interface (357–359).

For stable SPW generation however, momentum conditions must be synchronised between incident light and the propagated SPW *i.e.* wave vector of the surface plasmon must match the wave

vector of the incidence light. Therefore, the SPW cannot be produced simply at the planar metal-dielectric interfaces with direct light but requires tuning of incident light wave vector to match the surface plasmon wave vector. Surface plasmon excitation can be achieved by inclusion of a prism with incident light angled under total internal reflection (TIR) conditions. At a fixed angle above the critical angle of TIR, excitation of surface plasmons occurs where a decrease in intensity of reflected light is seen thus providing the SPR angle (θ_{spr}) where minimal reflectivity is observed (360,361). The SPW is propagated along the metal-dielectric interface while evanescently decaying approximately 200 nm into the dielectric media (362,363). The propagation constant of this wave is shown in equation. 5.

Eq. 5 $$\beta = \frac{\omega}{c}\sqrt{\frac{\varepsilon_m \varepsilon_d}{\varepsilon_m + \varepsilon_d}}$$

In this, ω is the angular frequency, c is the speed of light in a vacuum, ε_m is the dielectric constant of the metal and ε_d is the dielectric constant of the dielectric media. This model establishes connection between incident light wavelength and SPR oscillation decay penetration in media (364).

The Kretschmann configuration is a common experimental setup relying on directly coupling a thin metal film (typically

Au or Ag) to a glass prism with high refractive index (RI). This allows coordination of incident light with surface plasmon wave vectors thus providing generation of the SPW under TIR conditions with the metal film subsequently interfaced with a dielectric media (*Fig. 35*). In this configuration, changes in the dielectric media RI are measured equating to changes in the propagation constant. This in turn impacts interaction between surface plasmon (SP) and optical wave which is subsequently measured via reflected light parameters such as phase, intensity and polarization. Alternatively, decaying SP oscillations in media manifest as sensitivity of θ_{spr} to changes in media RI that can be quantified as changes in intensity, phase and angle of reflected light (364–366).

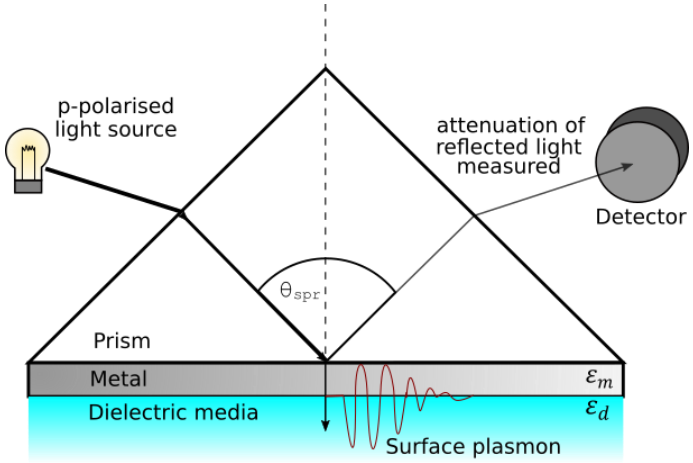


Fig. 35: Kretschmann configuration measuring attenuation of p-polarised light resulting from disturbance in SPW at metal and dielectric media interface.

As the evanescent field of the SPW only penetrates within approximately 200 nm of the propagating media, this technique is highly sensitive to real time events occurring at a surface (*Fig. 36*). While θ_{spr} sensitivity to changes in RI is useful in detecting binding events on a surface this also means SPR is unable to distinguish between different types of interaction. In effect, any change to the RI can be mistaken for binding including non-specific interactions or differences in buffer solutions forming the dielectric media (367). For actual representation of binding then we must either select a region of the SPR sensogram where we expect stable binding and free from excess ligand (*Fig. 36d*) or provide a null-binding control surface for determination of bulk refractive index. Comparison then of binding and non-binding surfaces will provide actual binding response free from RI change caused by analyte presence in the dielectric media. In addition, the intensity of θ_{spr} change is mass sensitive with larger molecules producing increased response. While suitable for bioassays using large proteins, sensitivity is reduced for smaller molecules such as metabolites or saccharides (368).

For example, if we consider a standard immunoassay: an antibody is immobilised on an SPR suitable substrate (*i.e.* Au sputtered-on glass). On passing the ligand over antibody we expect binding to occur disturbing the stable SPW evanescent

field and in turn disturbing the propagation constant which then changes the $\theta_{spr.}$ This is quantified in reflected light attenuation parameters *i.e.* phase and intensity, which is translated to response units (RU). During injection of our ligand however, a significant increase in RI is associated with solution concentration of the ligand (*Fig. 36c*). On exchange of ligand solution for the original dielectric media, only bound ligand immobilised on the surface will remain producing a stable change in the θ_{spr} which is converted to response units (RU). Plotted RU against time, this shows real time binding events and dissociation at a surface making this an excellent technique for quantification and binding kinetics study where a rule of thumb is signal accumulation of 1000 RU ≈ 1 ng mm^{-2} (*Fig. 36*)(366,369).

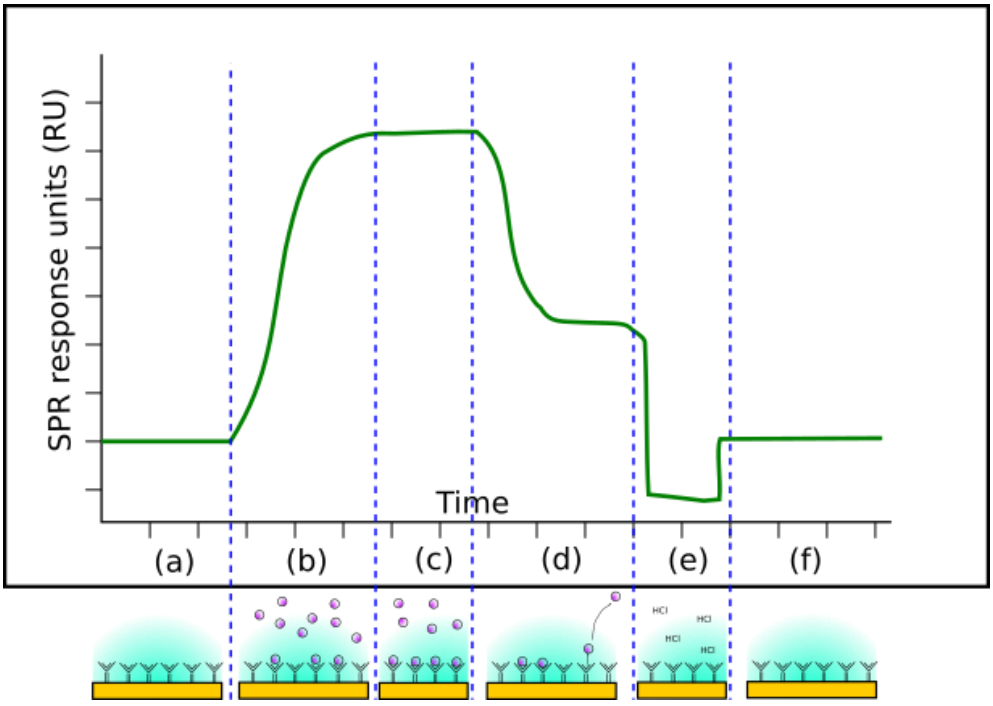


Fig. 36: SPR response curve for basic immunoassay binding pattern. (a) only buffer in contact with immobilised antibody, RI is stable (b) introduction of ligand. Binding event occurs at surface translating change in SPW to θ_{spr} to accumulation of RU. (c) antibody-ligand interaction saturated, response curve stabilises. (d) surface washed with buffer leaving strongly bound ligand at the interface. (e) regeneration of surface with cleaning agent reduces bulk shift response from buffer and removes tightly bound ligand. (f) no ligand bound, and buffer equilibrates surface RI back to baseline

Chapter 3.

SYNTHESIS OF SAM COMPONENTS

Abstract: In this chapter we describe the selection and synthesis of compounds for immobilisation on our surfaces producing SAMs expressing terminal alkyne or PBA functional groups. In the first stage of synthesis, three SAM forming compounds were synthesised to examine effect of branching and alkane backbone length impact on SAM organisation with each presenting alkyne groups for CuAAC reaction. Azide functionalised PBA was then synthesised alongside a similar azido benzene compound and a pinacol protected Azido-PBA for producing surfaces resisting saccharide binding. In the final synthesis set, short and long linear SAMs DTPAlk (C_2) and MBDAlk (C_{10}) were functionalised with PBA in solution allowing optimisation of the synthesis and to provide a defined terminal PBA expressing surface for future saccharide binding studies.

3.1 Introduction

Despite their recognised importance in disease diagnosis, the detection and quantification of carbohydrates still lacks suitable clinical tests. While a small number of clinically relevant assays exist (*i.e.* CA125 ELISA for ovarian cancer or aPTT for monitoring heparin therapy), demand is currently outstripping supply with the myriad of new glycan disease markers now available (38,370,371). While anti-glycan antibodies and lectins exist, the difficulties in production and inherently weak affinities of these biomolecules prevents mass implementation in assay design (121,134,372). In addition, being biomolecules, these suffer from typical susceptibility to environmental degradation *i.e.* temperature, pH, solvation etc., impeaching their designation to point-of-care (POCT) testing facilities (373,374). As potential diagnostic and prognostic markers of disease, bringing anti-carbohydrate assays to community physicians as POCT assays would enable extensive population screening for malignancy such as PCa (375,376). To meet anti-glycan assay demand therefore, new strategies must be developed for generation of assay supply.

The development of chemically stable SAMs and MIPs has attracted attention in recent years as a means to produce highly sensitive and selective synthetic biosensors. With a range of substrates including silica, gold and nanoparticles and a

variety of functional groups and surface reactions available, this technology presents a fully customisable template for biosensor design (282). As discussed in Chapter 1 (section 1.4) selective SAMs and MIPs have been developed for several biomolecules including ConA (229), dopamine (283), lysozyme (284) and estrone (377) each using unique chemical imprinting procedures. Additionally, through functionalisation with PBA, several glycoprotein and saccharide biosensors have been developed hence confirming its potential utility in diagnostics (194,262,292,378). Having found extensive use in bioconjugations, click chemistry is a genre of reactions that provide high yield, stereospecific and easily purifiable products from abundant precursors produced through simple synthesis (379). Given the biocompatibility of click reactions, this provides an excellent library for immobilisation of biomolecules to a synthetic platform thus has been explored in regards to our MIS design.

In the design of these MISs and SAMs, careful consideration must be given to the chemical composition of components with surface organisation being highly influenced by SAM characteristics *i.e.* alkane backbone length and terminal group. In selection of certain parameters such as length, surface organisation can be modulated allowing for more or less packing thus, concentration of terminal groups can be altered, steric

hinderance from dense packing of SAM monomers reduced and unique structural patterns developed on the substrate (216,219,222,226,380).

It is with these considerations that informed the synthesis of our saccharide sensor design where length and branching of the SAM monomer could be changed to alter SAM organisation. Typically, MIPs are produced as either 2D or 3D systems where imprints are developed on solid substrates or within 3D polymer matrixes respectively. Limitations of 3D MIPs include poor suitability to large heterovalent binding complexes seeing ligand trapping and poor reusability however (262,381). To overcome this, a 2D imprinting system is proposed based on simple hierarchal construction of an alkyne functional SAM and subsequent functionalisation providing PBA expression within a binding pocket. Free from trapping effects observed with 3D MIPs, this system would allow free binding and regeneration providing a reusable and stable molecularly imprinted surface (MIS).

Having seen use in previous SAM designs, the CuAAC reaction as discussed in Chapter 1 (*Section 1.4.6*) uses Cu(I) to catalyse stereospecific reaction between alkyne and azide producing 1,4 disubstituted triazoles (382,383). With a significant number of studies describing optimisation and accelerating ligands, we will address the functional utility of the CuAAC reaction in producing saccharide sensing surfaces. Given the contradictions

regarding surface yield of the CuAAC reaction, using various SAM monomer designs will allow examination of SAM composition impact on the reaction yield (255–257). Given the biocompatibility of the CuAAC reaction, our intention will be to design an imprinted surface for selective saccharide detection thus preparing the foundation for an adaptable glycan sensor design. Given the commercial abundance of azide functional ligands, preparing clickable surfaces will not be limited to saccharide biosensors allowing for a customisable platform depending on the target biomarker (259).

To this end, we will describe in this chapter the synthesis of three alkanethiol SAM monomers for production of SAMs on gold appropriate for use with SPR analysis in addition to azide functional PBA and a null saccharide binding compound. Additionally, the synthesis of preformed PBA terminated monomers will be described thus providing a reference PBA terminated surface. This can therefore be broken down into the following objectives.

3.1.1 Objectives

1. Synthesis of three alkyne terminated SAM monomers including Branched design (**1**), short chain (C_2) (**2**) and long chain (C_{10}) (**3**) providing distinct SAM structural characteristics to be assessed for reaction CuAAC yield (*Fig. 37*).

2. Synthesis of azide functionalised CuAAC reaction ligands including PBA terminated (**4**), pinacol protected (**5**) and benzene terminated (**6**) providing glycan sensing component through PBA and two non-glycan binding control CuAAC reaction ligands (*Fig. 37*).

3. Synthesis of PBA terminated SAM monomers via solution CuAAC reaction of long chain (**7**) and short (**8**) monomers with azide functionalised PBA (*Fig. 37*) to provide defined PBA terminated SAMs for glycan binding and structural characterisation studies.

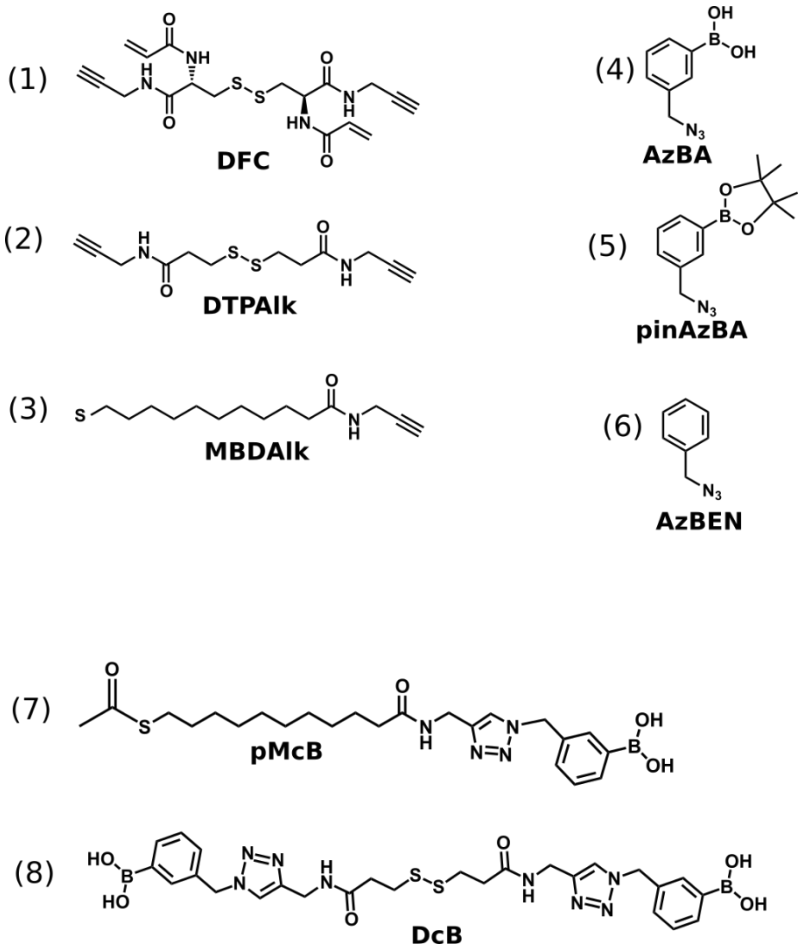


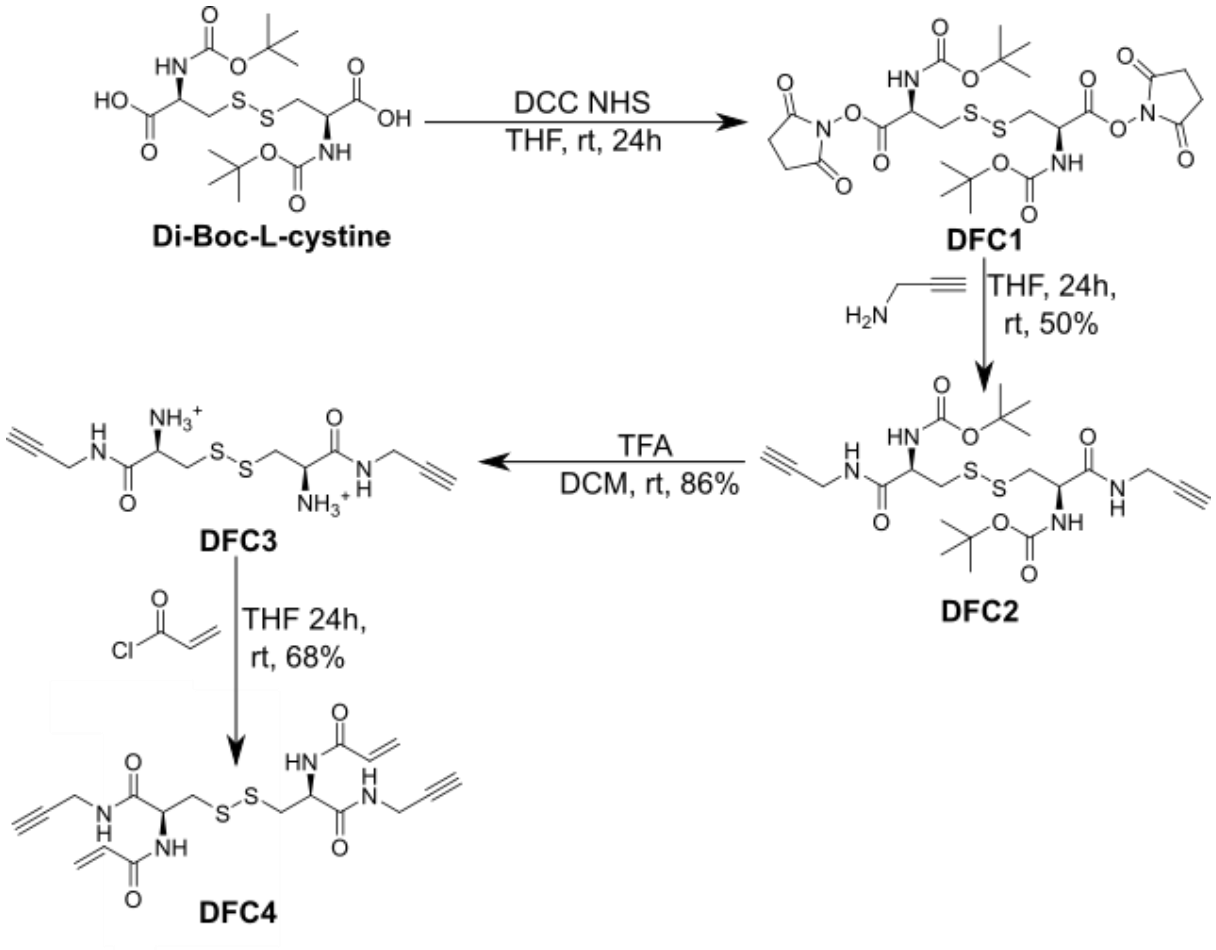
Fig. 37: SAM monomer configurations (1) branched dithiol, (2) short dithiol and (3) long thiol. Azide CuAAC ligands with functional groups (4) PBA, (5) pinacol protected PBA and (6) benzene. Solution PBA functionalised monomers (7) long thiol and (8) short dithiol.

3.2 Synthesis of SAM monomers

Forming the foundation of our MISs, three monomer configurations were selected to explore SAM organisation induced by branched monomers, short alkanethiols and long alkanethiols (*Fig. 37,1-3*). On increasing alkane chain length, increased SAM organisation has been observed imparted by Van der Waals interactions along the carbon backbone. Conversely, short ($<C_7$) alkanethiol SAMs while more rapidly forming SAMs, exhibit lower organisation with a fluid-like behaviour around the orientation angle resulting from lack of backbone interactions (226). For branched monomers, conflicting reports of changes in surface organisation exist depending on polarity of branched groups however both studies observe lower concentration of branched monomers on the substrate (384,385). Alongside backbone configuration all monomers must incorporate both a substrate anchoring and terminal functional group. Given the high affinity of the thiol-gold interaction, all selected monomers contained either thiol or dithiol groups enabling self-assembly on gold substrates (386). To provide route for surface functionalisation, SAM monomers were modified with terminal alkynes to provide site for CuAAC reaction between surface and azide functionalised PBA or control benzene.

3.2.1 Branched monomer: DFC

To produce a branched dithiol SAM monomer, we followed the synthesis for a di-functionalised cysteine (DFC) described by Stephenson-Brown *et al* (2015). With DFC, a PSA selective MIP was previously reported using two surface reactions: the CuAAC reaction and free radical polymerisation. Whilst we only intend to approach click chemistry, the inclusion of alternative functional groups provides additional routes for more complex MIP generation in future studies. Given the previous success in imprinting achieved with this SAM, this design was included in our selection for comparison to linear SAMs for development of saccharide sensors. The synthesis of this compound can be broken down into four stages as shown in *Scheme. 1*.



Scheme. 1: Synthetic route to functionalise cystine with alkyne and acryloyl functional groups. Detailed synthetic methodology is available in Chapter 7 (section 7.2.1.1 – 7.2.1.4).

In the first stage of this reaction, Addition of alkyne groups to terminal carboxylic acids was achieved through activation of these groups with dicyclohexylcarbodiimide (DCC) followed by addition of N-hydroxysuccinimide (NHS). The reaction mixture was stirred over 24 hours at room temperature to produce **DFC1**. With no purification of DFC1, the reaction mixture was cooled to 0 °C and reacted with propargylamine over 24 hours in

THF liberating NHS groups and forming amide to produce **DFC2** which was purified by silica chromatography. Boc deprotection of amine groups was achieved by adding trifluoroacetic acid (TFA) to a DCM solution of DFC2 to yield **DFC3**. Acryloyl group attachment to deprotected amines was achieved through reaction of DFC3 with acryloyl chloride in THF for 24 hours producing the final product **DFC**. This was characterised by ^{1}H NMR with the spectrum and proton assignment shown in *Fig. 38*.

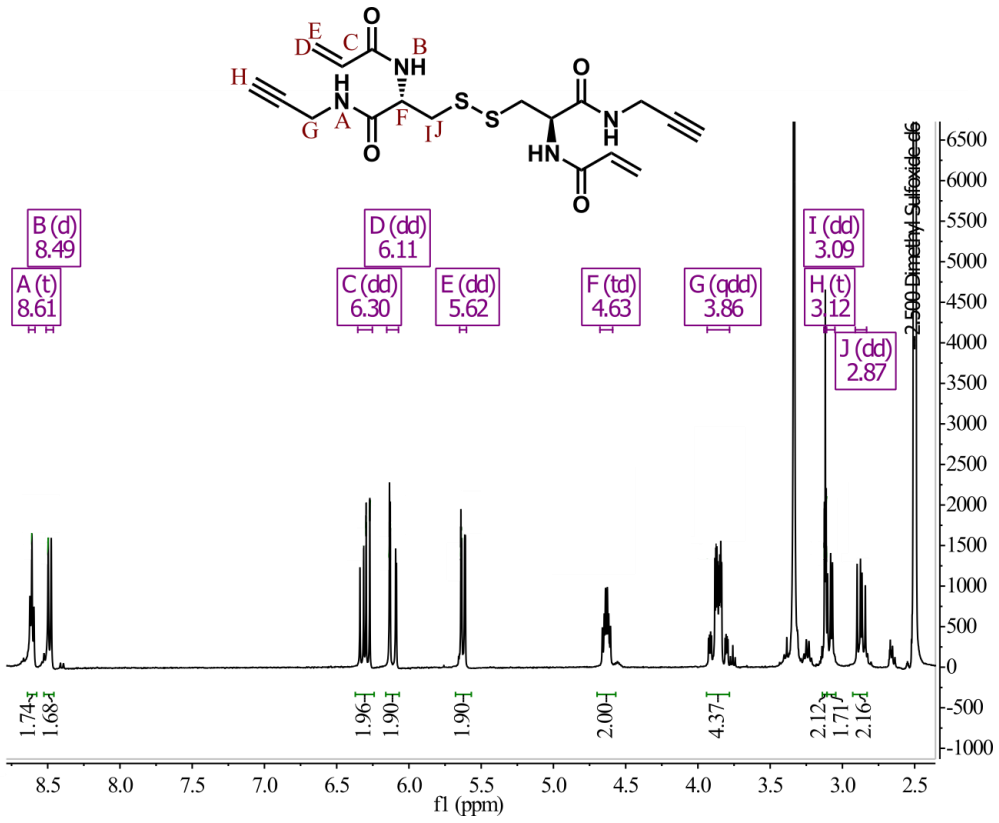


Fig. 38: ^{1}H NMR spectra of DFC (D6-DMSO, 298K, 400 MHz) with proton assignments.

Interpretation of ^{1}H NMR spectra of the final DFC compound in *Fig. 38* shows several interesting peak splittings notably protons ‘G’ and ‘F’. Long range coupling is observed for alkyne group proton ‘H’ with a J = 2.5 Hz manifesting as a triplet due to coupling with ‘G’. This is also seen in proton ‘G’ coupling to protons of both amide ‘A’ and alkyne ‘H’ exhibiting a quadruple double doublet resulting from diastereotopic configuration of DFC. Due to this configuration, geminal coupling is observed for protons ‘D’ and ‘E’ with peak roofing suggestive of coupling to ‘C’. This geminal coupling is additionally seen in protons ‘I’ and ‘J’ showing similar peak splitting between these protons while exhibiting a double doublet from coupling to ‘f’ with J = 13.5 for both ‘I' and ‘J’. Peak splitting for ‘F’ is influenced by the *cys-trans* amide groups showing coupling to ‘B’, ‘I' and ‘J’ as a triple doublet. Confirmation of coupling relationships between protons was achieved with COSY NMR shown in *Fig. 39*.

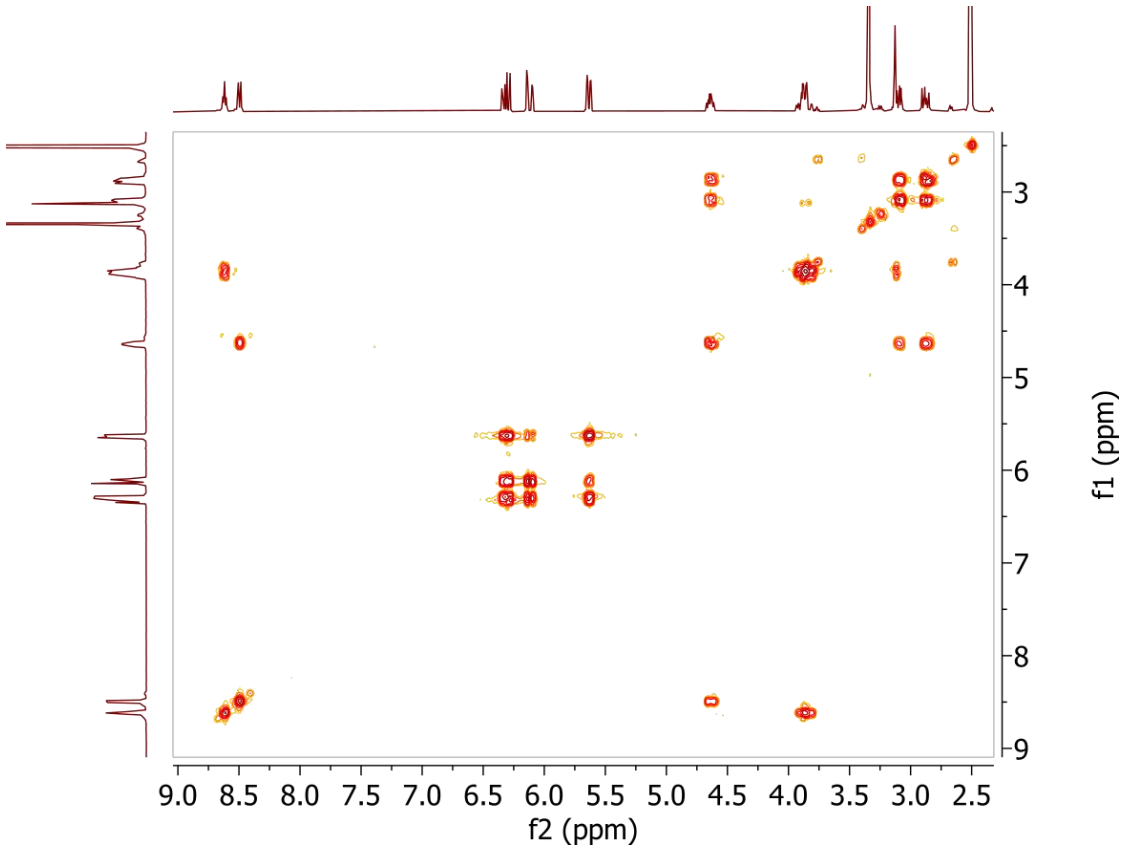


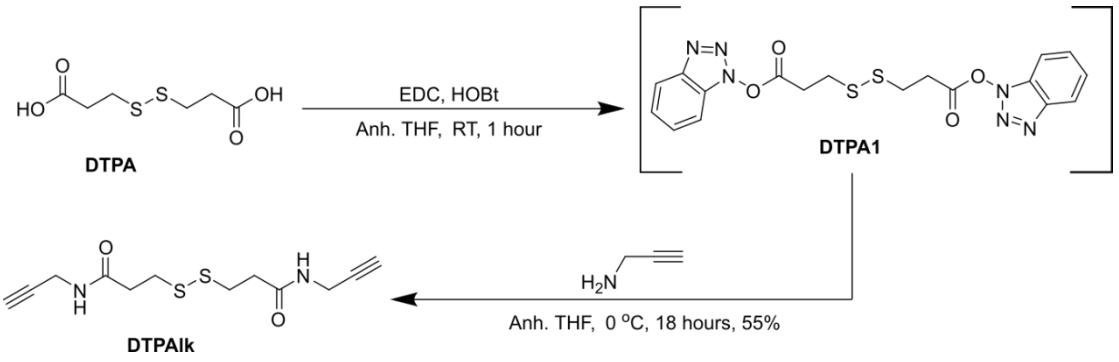
Fig. 39: 2D COSY NMR spectra of DFC (D6-DMSO, 298K, 400 MHz)

In addition to NMR spectroscopy the isolation of DFC was confirmed via mass spectroscopy (ESI-(+)MS) analysis. In this, two peaks at *m/z* 445.10 and 461.07 were observed corresponding to sodium ($[M+Na]^+$) and potassium ($[M+K]^+$) adducts respectively as calculated from expected DFC mass of 422.52.

3.2.2 Short (C_2) monomer: DTPAlk

For comparison between linear and branched SAMs we synthesised a linear short alkane chain monomer with similar structure to DFC but lacking acryloyl groups. With similar

chemical composition along the backbone group this synthesis used the commercially available 3’3-dithiopropionic acid (DTPA). While a similar DCC/NHS coupling chemistry could be used as in DFC synthesis, an alternative (but analogous in principle) coupling strategy was used to avoid time consuming silica chromatography. In place of DCC, N-(3-Dimethylaminopropyl)-N′-ethylcarbodiimide hydrochloride (EDC) was used to form an O-acylisourea intermediate. Addition of 1-hydroxybenzotriazole (HOBt) then displaces EDC as 1-(3-dimethylaminopropyl)-3-ethylurea (EDU) while forming a stable ester between carboxylic acid and alcohol on HOBt. Similar to the NHS ester, this is susceptible to attack by nucleophilic amines hence on exposure to free amine this ester is cleaved forming a stable amide (387). This reaction to functionalise DTPA with alkyne groups is shown in *Scheme. 2.*



Scheme. 2: Synthetic route to functionalise DTPA with alkyne groups producing DTPAlk. Detailed synthetic methodology is available in Chapter 7 (section 7.2.5).

To produce DTPAlk, carboxylic acid groups on **DTPA** were first activated by EDC followed by HOBt over 1 hour producing **DTPA1.** The reaction was then cooled to 0 °C and propargylamine added and allowed to react over 18 hours forming **DTPAlk.** This was easily purified by precipitation in ultra-pure H_2O (UHP) as both EDC and HOBt were soluble in water while DTPAlk readily precipitates. DTPAlk was characterised by NMR spectroscopy as shown with proton assignments in *Fig. 40*.

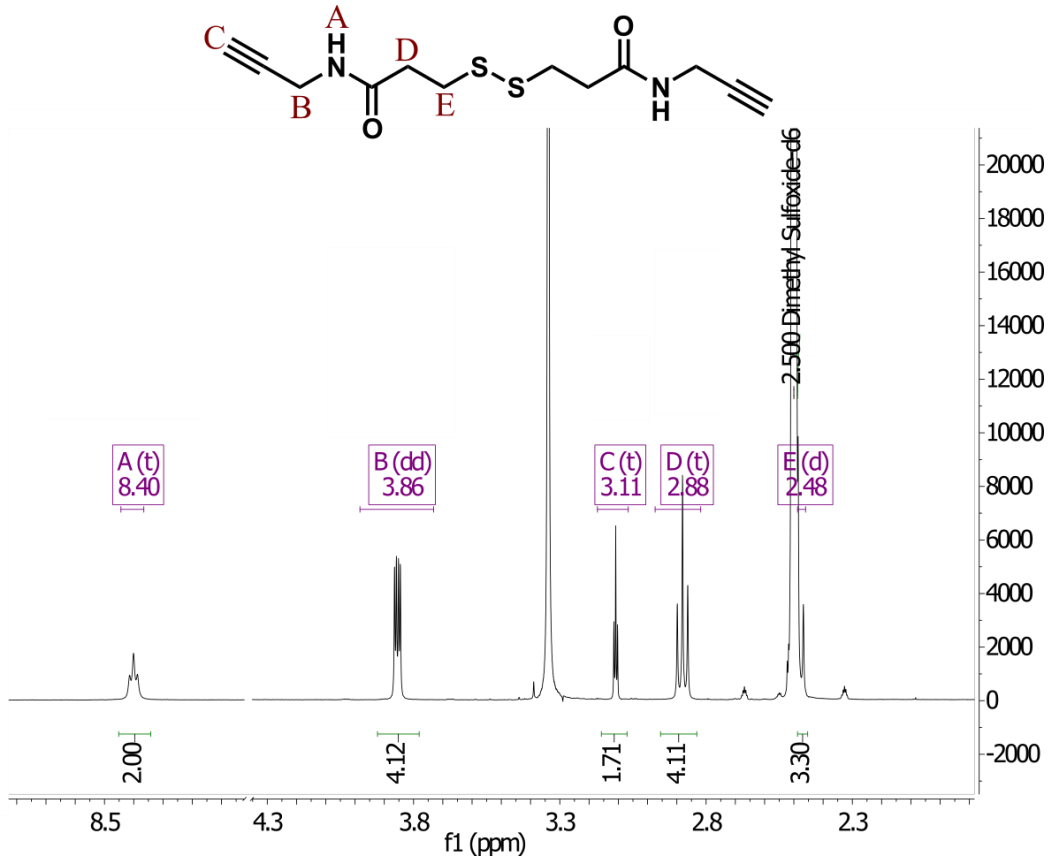


Fig. 40: ^{1}H NMR spectra of DTPAlk (D6-DMSO, 298K, 400 MHz) with proton assignments.

^{1}H NMR spectra of DTPAlk shows similar peak locations for common groups between DFC and DTPAlk with protons ‘C’ and ‘B’ occurring at 3.12 and 3.87 ppm respectively while for DFC similar protons appeared at 3.12 and 3.86 ppm. Proton ‘B’ occurs as a double doublet with long range coupling to alkyne proton ‘C’ with J = 2.4 Hz and coupling to amide ‘A’ while in DFC this occurred as a quadruple doublet. Protons vicinal to dithiol are unfortunately partially masked by D6-DMSO solvent peak however clear coupling to protons ‘D’ is observed in COSY spectra. All coupling between protons is confirmed in COSY NMR spectra shown in *Fig. 41* showing clear coupling between CH_2 ‘B’ and amide ‘A’ and alkyne ‘C’.

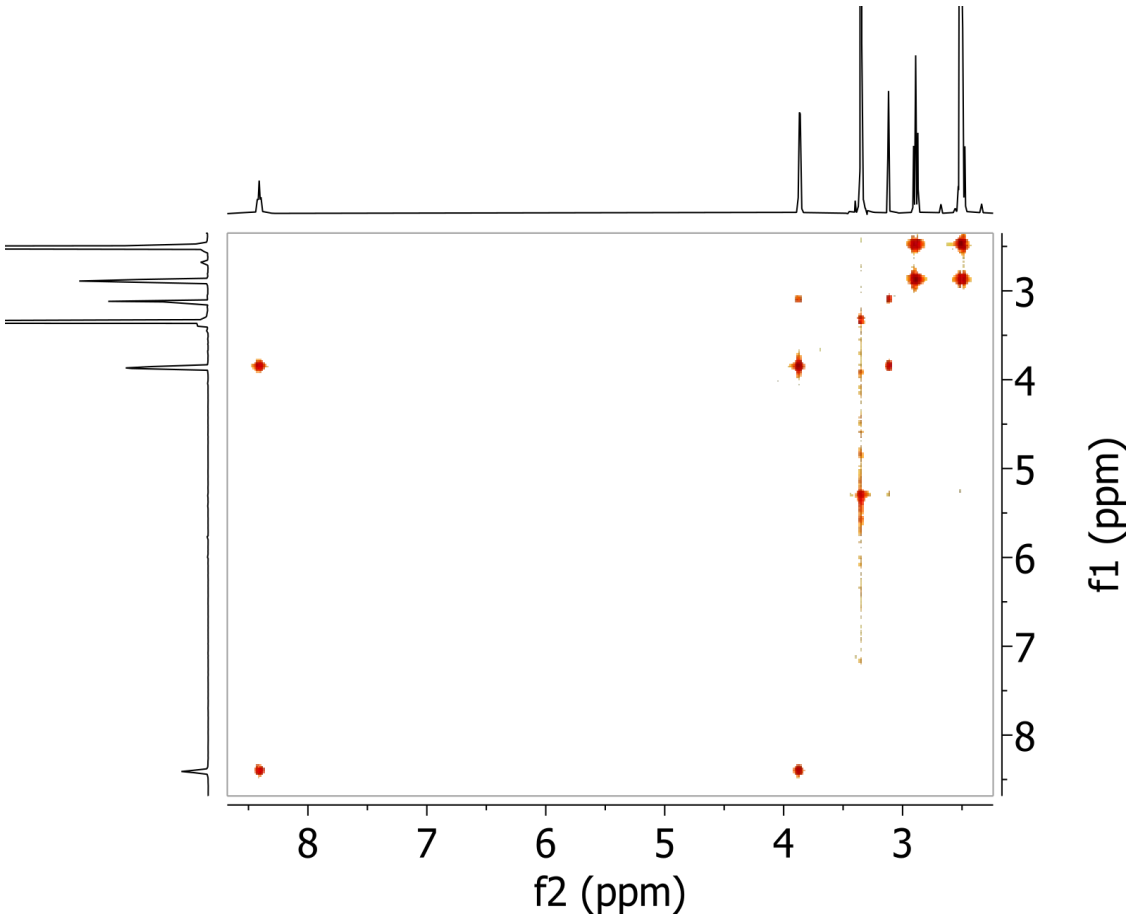
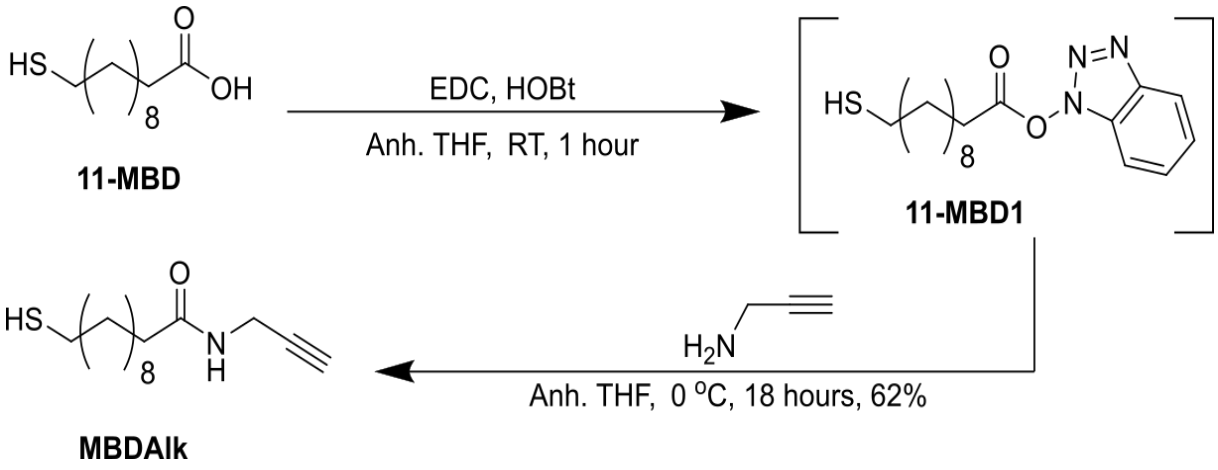


Fig. 41: 2D COSY NMR spectra of DTPAlk (D6-DMSO, 298K, 400 MHz)

The isolation of DTPAlk was confirmed via ESI-(+)MS in positive ion mode producing three observed species. The peak at *m/z* 285.07 was ascribed to DTPAlk ($[M]^+$) having a calculated mass of 284.39. At higher mass, the peak at 307.06 was assigned to a sodium adduct ($[M+Na]^+$).

3.2.3 Long (C_{10}) monomer: MBDAlk

To increase availability of alkane chain interactions during SAM formation we synthesised a linear SAM monomer containing higher carbon content than DTPAlk similar to a previously published alkyne terminated SAM design (257,388). In providing inter-chain interactions higher SAM organisation with dense packing of monomers should be observed compared to SAMs formed with DTPAlk (224). The same approach for the synthesis of DTPAlk was used in this synthesis employing EDC/ HOBt coupling. The synthetic pathway for this reaction is shown in *Scheme. 3* using the commercially available 11-mercaptoundecanoic acid (11-MBD) as starting material.



Scheme. 3: Synthetic route to functionalise 11-MBD with alkyne groups producing MBDAlk. Detailed synthetic methodology is available in Chapter 7 (section 7.2.7).

Similar to DTPAlk synthesis, carboxylic acid groups on 11-MBD are activated with EDC followed by HOBt producing **11-MBD1.** Propargylamine was then added directly to the reaction vessel cleaving the HOBt ester and forming and amide with the propargylamine forming **MBDAlk.** MBDAlk was precipitated in UHP leaving the by-product EDU and HOBt in solution. MBDAlk was then characterised by ^{1}H NMR with assigned protons shown in *Fig. 42*.

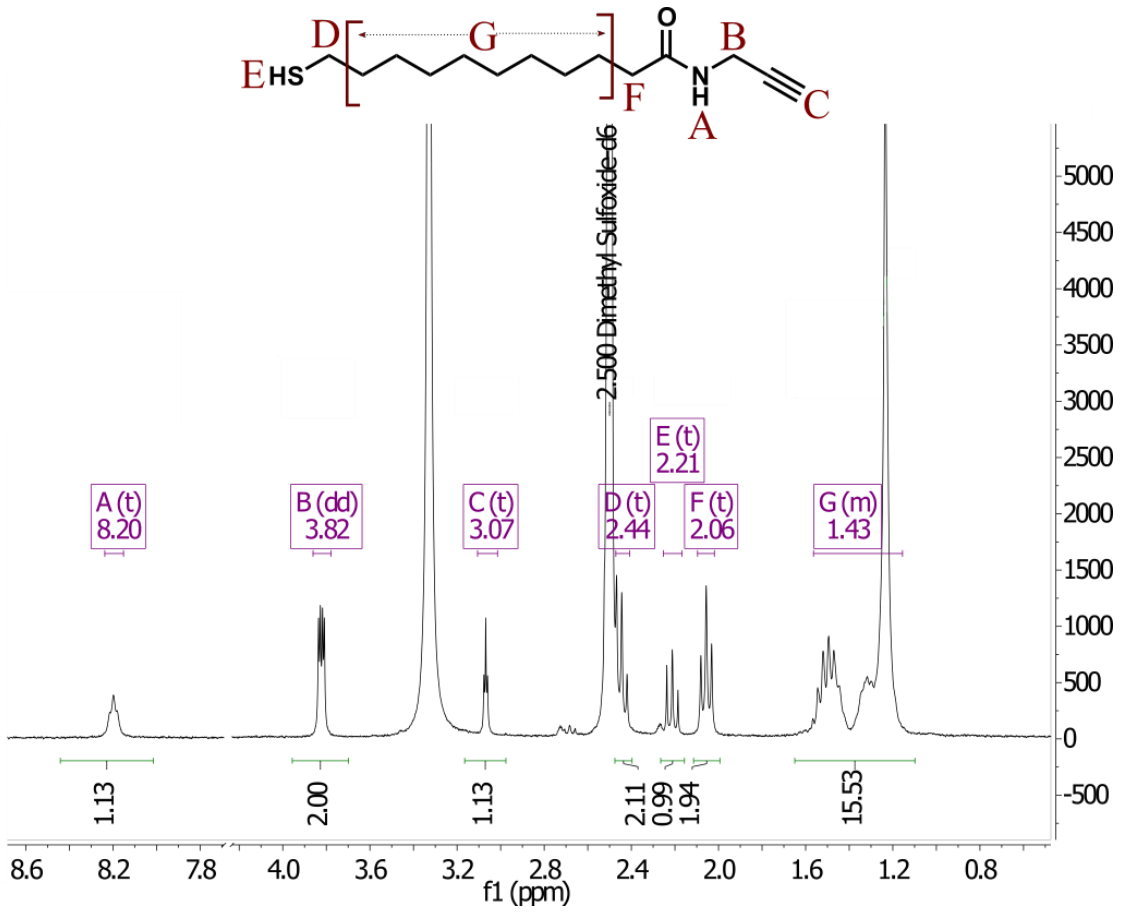


Fig. 42: ^{1}H NMR spectra of MBDAlk (D6-DMSO, 298K, 300 MHz) with proton assignments.

Proton assignment of MBDAlk reveals similar peak splitting pattern for alkyne group to both DFC and DTPAlk as expected. Proton ‘B’ occurs as a double doublet coupling to both amide ‘A’ and with long range coupling to alkyne ‘C’ (J = 2.4 Hz). A large multiplet assigned to alkane chain ‘G’ shows convoluted splitting due to unsymmetrical configuration of MBDAlk being chemically inequivalent at each end of the alkane backbone. Being adjacent to distinct functional groups, peaks ‘D’ and ‘F’ are assigned to CH_2 neighbouring thiol and carbonyl respectively with thiol proton assigned to ‘E’. Coupling was confirmed between CH_2 ‘B’ with amide and alkyne and between thiol ‘E’ with adjacent CH_2 ‘D’ with COSY NMR shown in *Fig. 43*. Coupling between ‘D’ and ‘F’ is also observed with the alkane chain ‘G’.

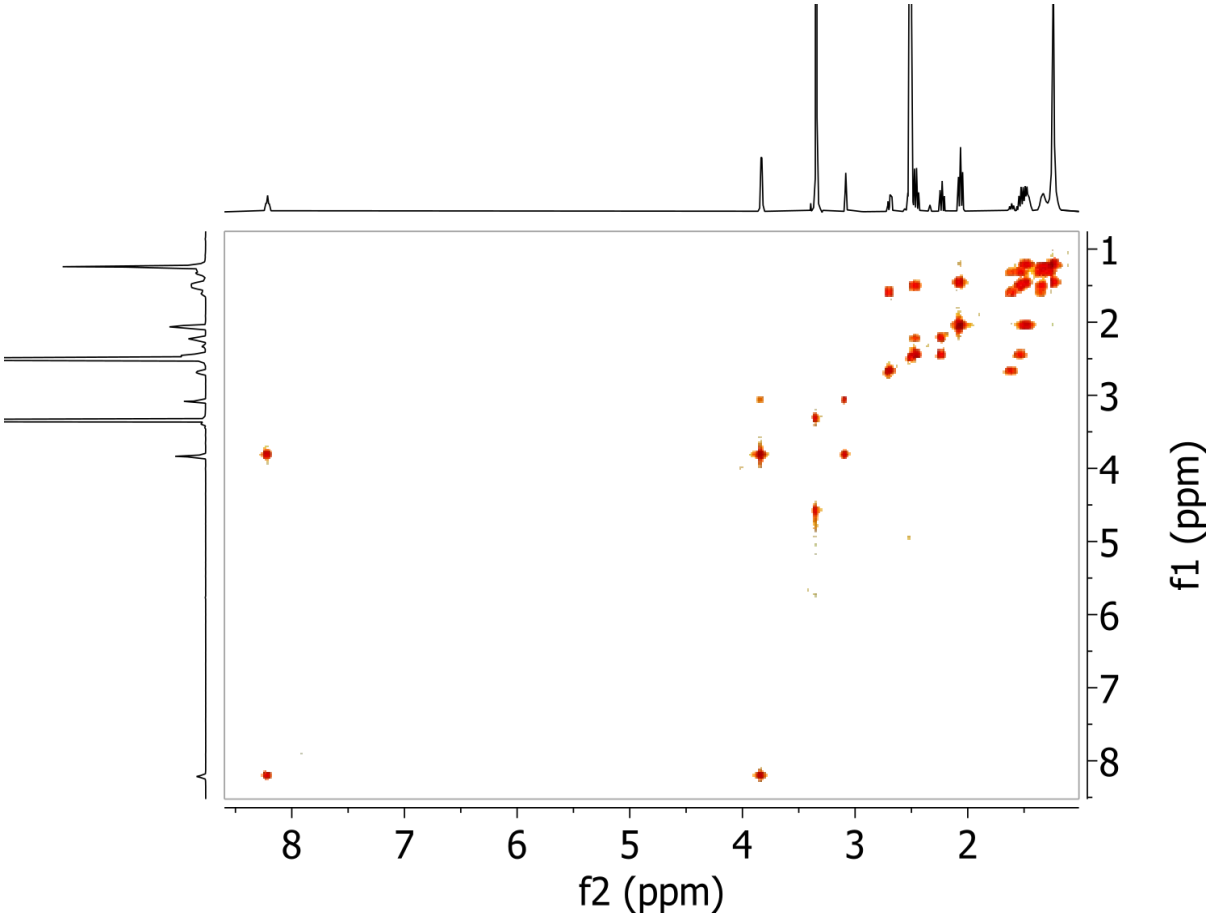


Fig. 43: 2D COSY NMR spectra of MBDAlk (D6-DMSO, 298K, 400 MHz)

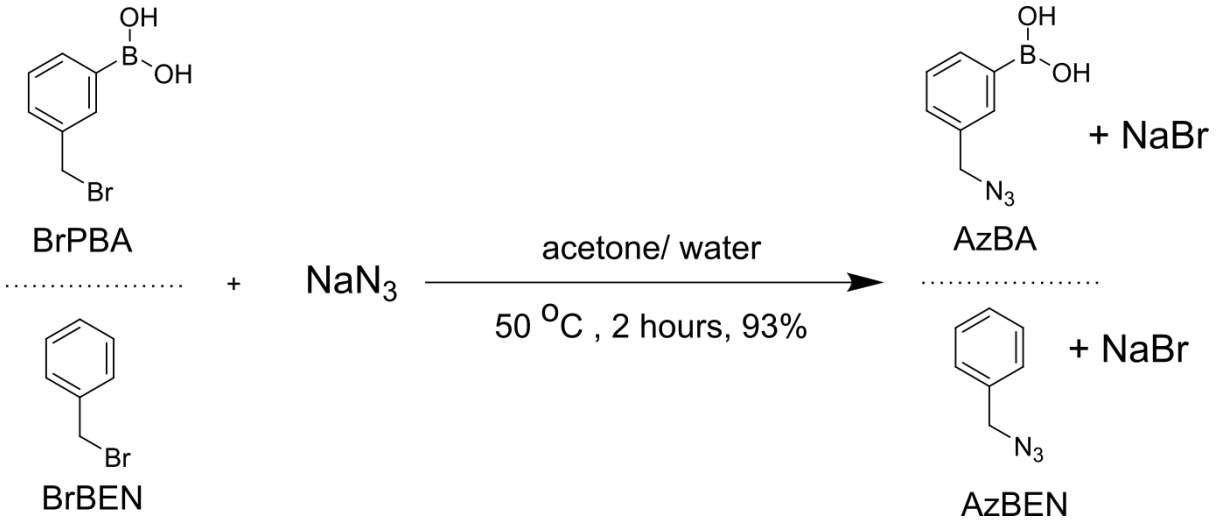
The isolation of MBDAlk was confirmed by ESI-(+)MS showing two observed chemical species. With calculated weight of 255.42, the peak observed at *m/z* 256.18 ($[M]^+$) was assigned to MBDAlk while with a higher mass, 278.16 was assigned to MBDAlk with sodium adduct ($[M+Na]^+$).

3.3 Synthesis of azide functionalised CuAAC ligands

With the successful synthesis and characterisation of three alkyne terminated SAM monomers we then sought to synthesise azide functionalised CuAAC ligands. While various configurations of BA exist as discussed in Chapter. 1 (section 1.3.3) exhibiting differences in pKa and saccharide affinities, we used a standard PBA given its extensive use in previous research (169,196,262,292,389–391). By inclusion of an azide group, alkyne terminated SAMs can be functionalised *in situ* with a Cu(I) catalyst enabling generation of PBA terminated SAMs. Furthermore, as this reaction is compatible with aqueous media with no side reactions reported with biomolecules, this process will be compatible with molecular imprinting of oligosaccharides in future experiments (392). Coinciding, we additionally synthesised two similar compounds providing no saccharide binding sites namely, benzyl azide and a pinacol protected PBA. These serve as a control surface for SPR analysis enabling calculation of binding affinity between PBA terminated SAMs and saccharides and will be discussed in more detail in Chapter. 5 (section 5.2.2).

3.3.1 Synthesis of benzyl azide and 3-(azidomethyl)phenyl boronic acid

For synthesis of our azide functionalised PBA 3-(azidomethyl)phenyl boronic acid (AzBA) and control benzyl azide (AzBEN) we used the synthetic strategy shown in *Scheme. 4*. This simple reaction uses nucleophilic substitution (S_N2) between the nucleophile (azide) and electrophile (bromide) thereby substituting the bromide for azide producing sodium bromide as a by-product (393).



Scheme. 4: Synthetic route to functionalise BrPBA and BrBEN with azide group producing AzBA and AzBEN respectively. Detailed synthetic methodology is available in Chapter 7 (section 7.2.2, 7.2.4).

Both AzBA and AzBEN followed identical synthetic routes using a single step reaction with sodium azide. In each synthesis commercially available benzyl bromide (BrBEN) or 3-(bromomethyl)phenyl boronic acid (BrPBA) was dissolved in an acetone water mixture with sodium azide and allowed to react for 2 hours at 50 ^{o}C producing azide functionalised counterparts **AzBEN** or **AzBA** respectively. Both compounds were characterised by ^{1}H NMR alongside respective starting material as only discreet changes to CH_2 chemical shift were expected shown in *fig. 44*c.

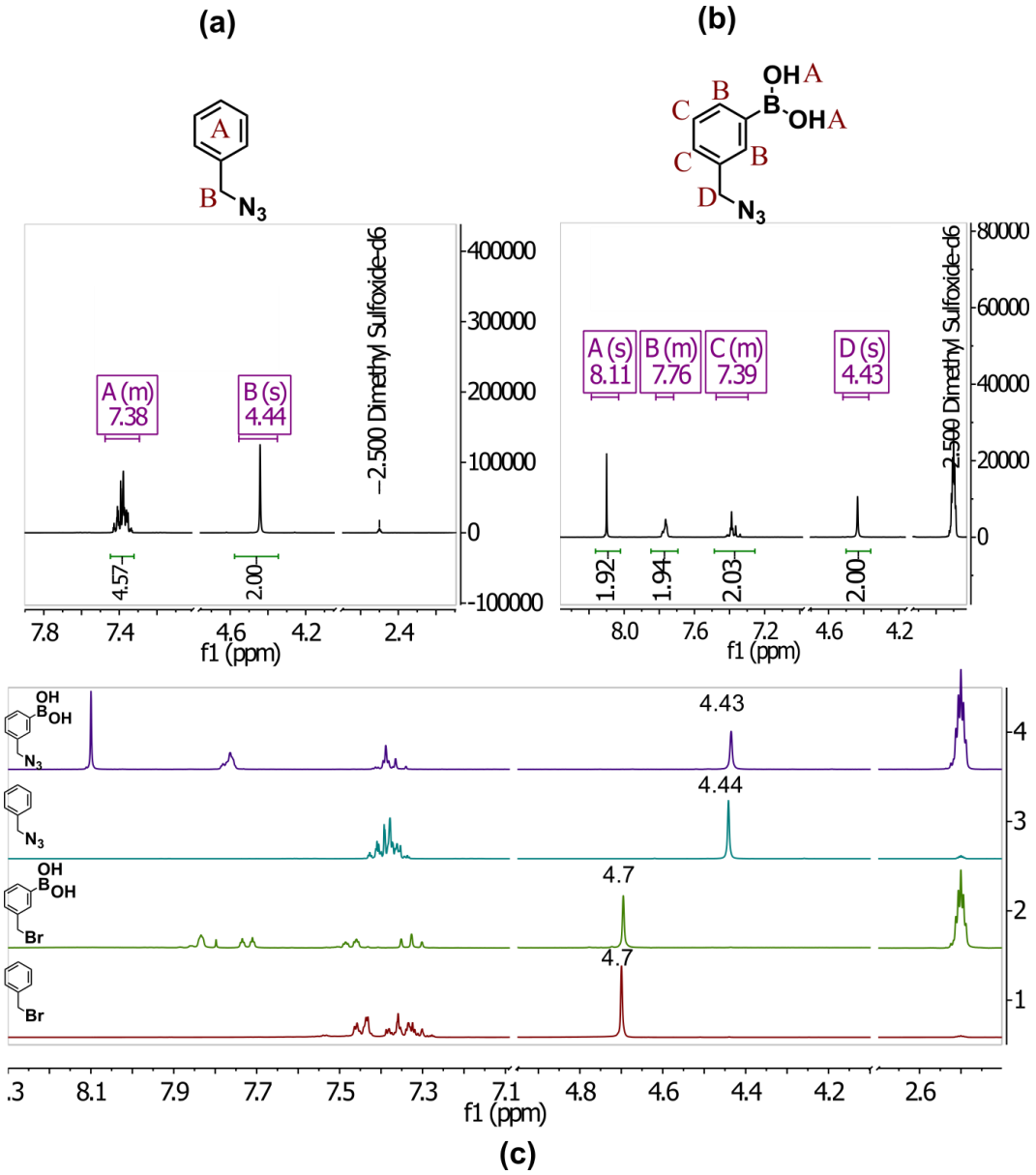


Fig. 44: (a) ^{1}H NMR spectra of AzBEN with proton assignments. (b) ^{1}H NMR spectra of AzBA with proton assignments. (c) Stacked spectra of AzBEN and AzBA with starting material BrBEN and BRPBA showing decrease in chemical shift of CH_2 group on exchange of bromide for azide group.

^{1}H NMR spectra for AzBEN (*Fig. 44a*) shows two isolated chemical environments with the aromatic ring 'A' assigned to the multiplet at 7.38 ppm due to adjacent CH_2 imparting chemical inequivalency to the phenyl group. Being unable to couple to the aromatic ring however, the CH_2 group 'B' appears as a singlet being shifted upfield from 4.7 ppm to 4.44 ppm on exchange of bromide for azide group (*Fig. 44c*). As AzBEN has full characterisation previously reported and proton assignment reported here is in agreement, no further characterisation was pursued (394).

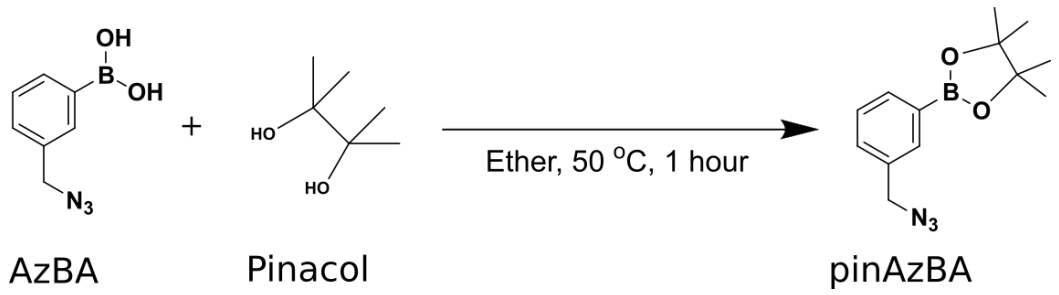
For AzBA a similar single peak corresponding to CH_2 group 'd' is observed being shifted from 4.7 ppm in BrBA to 4.43 ppm in AzBA (*Fig. 44c*). With the inclusion of the BA group, additional hydroxyl signals 'A' are assigned to the isolated singlet at 8.11 ppm not seen in the BrBA spectra due to presence of water solvent impurity causing deuterium exchange (395,396). Aromatic ring peaks are further split to two multiplets 'B' *ortho* to BA at 7.76 ppm and 'C' *meta* and *para* at 7.39 ppm.

The isolation of AzBA was confirmed using ESI-(+)MS however significant fragmentation of the azide occurred consistent with previous reports (397,398). With a predicted mass of 176.97, the peak at *m/z* 179.11 was assigned to AzBA ($[M]^+$). Displaying graduated lower masses, peaks at *m/z* 164.11 ($[M-N]^+$), 150.08 ($[M-N_2]^+$) and 135.01 ($[M-N_3]^+$) were assigned to incremental

fragmentation of the azide group. Fragmentation of the BA group was additionally observed as peaks with mass of 105.99 ([M-N_3, BO_2]$^+$) and 94.05 ([M-N_2, BO_2]$^+$) corresponding to total loss of BA and partial or total loss of azide group respectively.

3.3.2 Pinacol protection of AzBA

Commonly used in Suzuki-Miyaura coupling, esterification of BA with pinacol produces a highly stable boronate ester (399). To provide an alternative control to AzBEN while maintaining similar chemical configuration to AzBA we synthesised a pinacol protected counterpart to AzBA as outlined in *Scheme. 6.*



Scheme. 6: Synthetic route for pinacol protection of AzBA producing pinAzBA. Detailed synthetic methodology is available in Chapter 7 (section 7.2.3).

PinAzBA was synthesised by reaction of pinacol with **AzBA** in diethyl ether at 50 °C over 1 hour yielding **pinAzBA.** PinAzBA was characterised by ^{1}H NMR with proton assignments shown in *Fig. 45*.

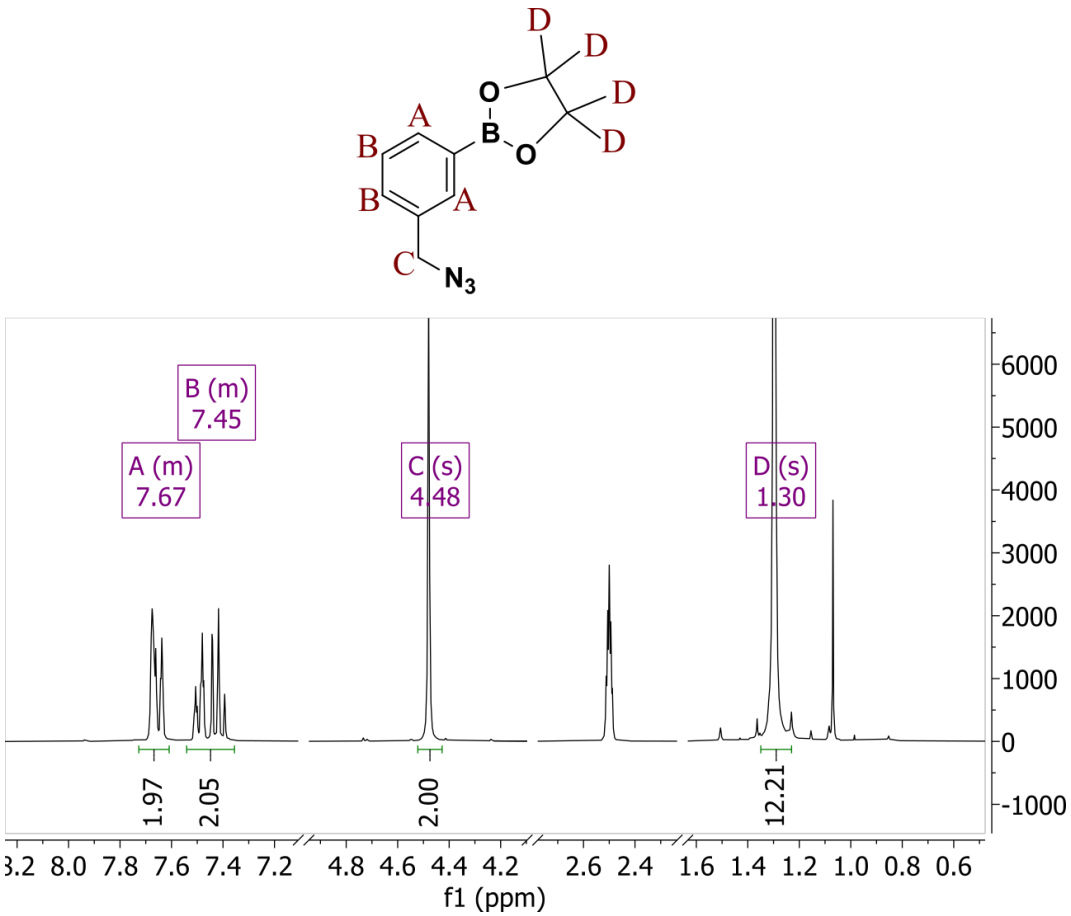


Fig. 45: ^{1}H NMR spectra of pinAzBA (D6-DMSO, 298K, 300 MHz) with proton assignments

Proton assignment for ^{1}H NMR spectra of pinAzBA (*Fig.* 45) shows similar multiplet peaks for *ortho* aromatic protons 'A' and *para* and *meta* aromatic protons 'B' to AzBA as expected.

Consistent with this, CH_2 group 'C' is assigned to the single peak at 4.48 ppm in similar location to CH_2 group on AzBA ^1H NMR spectra (*Fig. 44b*). Confirmation of successful pinacol protection can be seen in loss of hydroxyl protons previously at 8.11 ppm for AzBA and gain of large single peak at 1.30 ppm which integrates to 12 protons 'D' corresponding to the 4 methyl groups of the pinacol ester.

Isolation of pinAzBA was confirmed by ESI-(+)MS and showed less fragmentation of the azide than previously with AzBA. With a predicted mass of 259.12, the peak corresponding at *m/z* 232.2 was assigned to pinAzBA with loss of azide group ($[M-N_3]^+$). At lower mass, the peak at *m/z* 217.19 was assigned to loss of both azide and adjacent CH_2 ($[M-CH_2N_3]^+$).

3.3 Synthesis of PBA terminated SAM monomers

With alkyne terminated SAMs and azide functional PBA ligands synthesised we then optimised the CuAAC reaction in solution prior to application on our SAMs. Coinciding, with the pre-synthesis of PBA terminated monomers these would also serve as defined PBA terminated SAMs for future surface characterisation and saccharide binding studies. Referring back to Chapter. 1 (section 1.4.6) we discussed the CuAAC reaction progressing through formation of multiple Cu(I) acetylide intermediates with

alkyne species. Alkynes then associate with azide groups which then converts to 6-membered ring intermediate from β-carbon of alkyne-Cu(I)-acetylide and terminal nitrogen of the azide. Reductive elimination of one Cu(I) then forms a prototype triazole before protonation of the remaining Cu(I) thereby regenerating Cu(I) catalytic function (*Fig. 46*) (254).

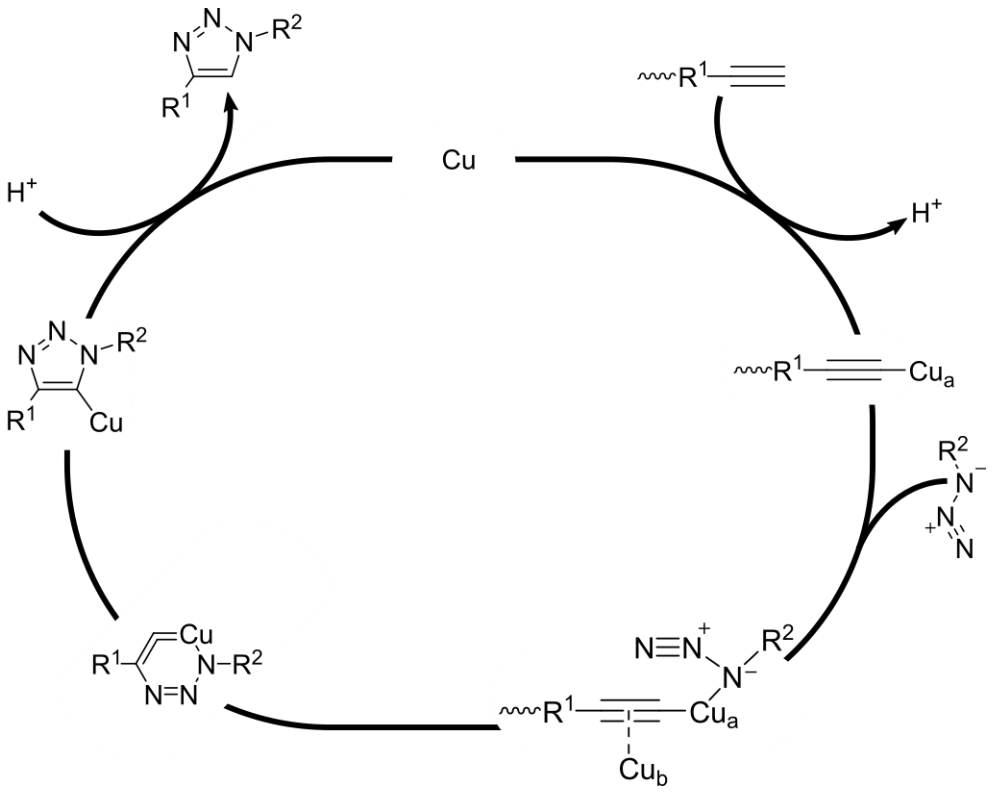
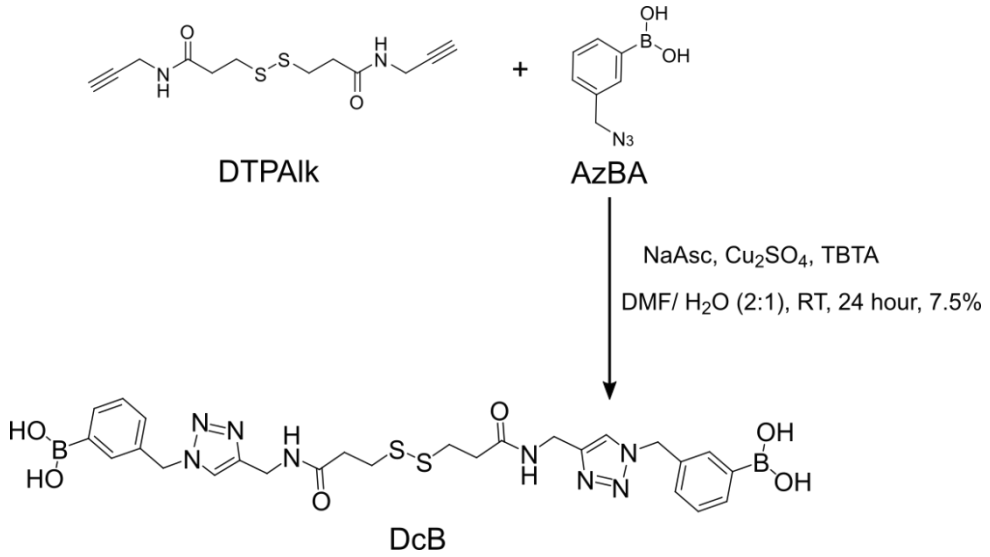


Fig. 46: Progression of the CuAAC reaction forming 1,4-disubstituted triazoles (254)

3.3.1 Synthesis of PBA terminated C_2 SAM monomer from DTPAlk and AzBA

Whilst the CuAAC reaction is well characterised, initial attempts at CuAAC reaction of AzBA with DTPAlk showed slow reaction times showing incomplete reactions by thin-chromatography (TLC) after three days. To increase reaction rate we included the rate accelerating ligand tris[(1-benzyl-1H-1,2,3-triazol-4-yl)methyl]amine (TBTA) as previously described (400,401). On inclusion of TBTA reaction times shortened to 24 hours consistent with previous reports. The reaction scheme for synthesis of PBA terminated dithiol from AzBA and DTPAlk is shown in *Scheme.* 7.



Scheme. 7: Synthetic route for CuAAC reaction of DTPAlk with AzBA producing DcB. Detailed synthetic methodology is available in Chapter 7 (section 7.2.6).

To synthesise DcB, a catalyst prepared by stepwise addition of Cu(II)SO_4, sodium-L-ascorbate (NaASC) and TBTA was prepared in a DMF UHP water mixture thereby reducing Cu(II) to Cu(I). **DTPAlk** and **AzBA** were added to this catalyst solution and reacted over 24 hours protected from light to prevent NaASC degradation (402) producing **DcB**. Only low yields of DcB were able to be produced from this reaction due to complications in purification. Attempts at column chromatography produced poor separation in standard dichloromethane (DCM)/ methanol (MeOH) or hexane (hex)/ ethyl acetate (EtOAC) solvent systems attributed to interaction between PBA and silica (403). Further precipitation or crystallisation trials yielded impure products and failed to crystallise DcB. Basifying the silica with trimethylamine showed small improvement in the column chromatography separation in DCM/ MeOH however, only on basifying with ammonium hydroxide we were able to recover a small amount of pure DcB. This was characterised by ^{1}H NMR spectroscopy with proton assignments shown in *Fig. 47*.

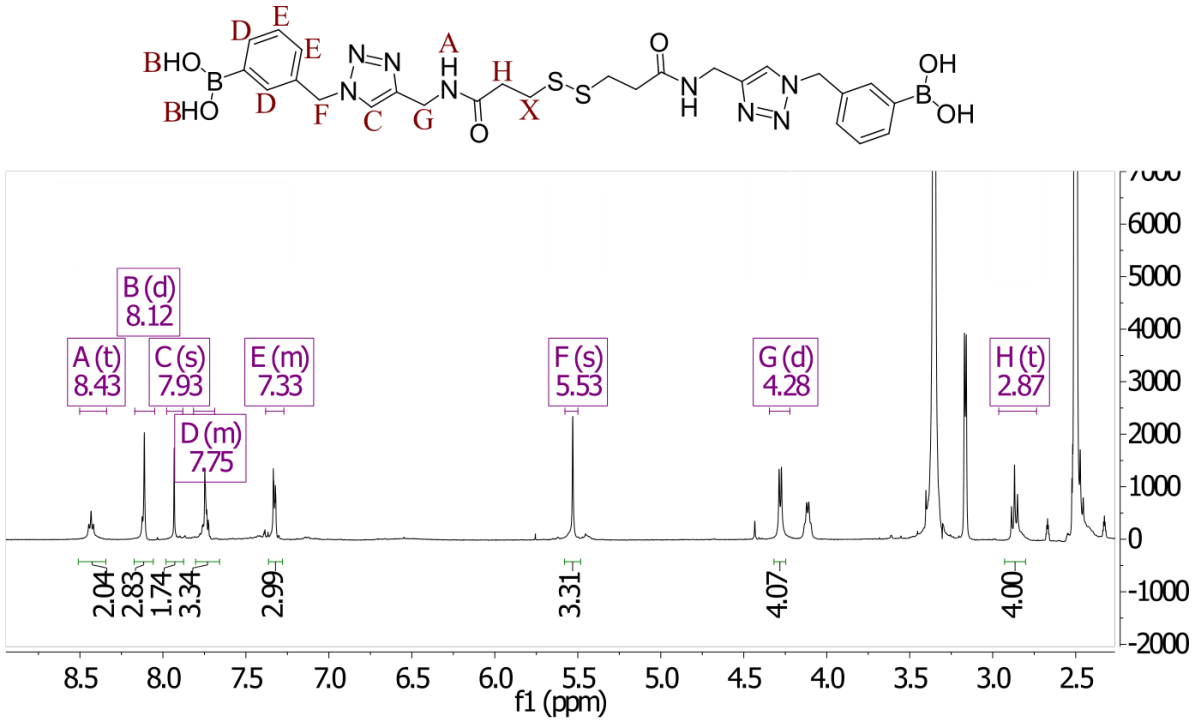


Fig. 47: ^{1}H NMR spectra of DcB (D6-DMSO, 298K, 400 MHz) with proton assignments.

Proton assignment for ^{1}H NMR spectra of DcB in D6-DMSO (*Fig. 47*) shows similar peak distribution to both AzBA and DTPAlk with downfield peaks (8.12 – 7.33 ppm) corresponding to aromatic ring of AzBA and upfield showing CH_2 adjacent to carboxyl (2.87 ppm). Several differences in peak distribution are observed however notably the appearance of the singlet 'C' at 7.93 attributed to triazole proton close to previously reported shift of 7.91 ppm (404). The conversion of alkyne to triazole sees double doublet of DTPAlk (proton 'B', *Fig. 40*) converted to doublet for proton 'G' that couples to amide 'A' occurring as a triplet. Hydroxyl

protons 'B' on DcB are observed in similar location to AzBA hydroxyl protons (8.12 and 8.11 ppm respectively) as are peaks assigned to aromatic ring (7.75, 7.33 ppm and 7.76, 7.39 ppm respectively). A shift is observed in adjacent CH_2 peaks from 4.43 ppm for AzBA to 5.53 ppm on DcB with incorporation of neighbouring triazole. Similarly, to DTPAlk, CH_2 protons adjacent to thiol are masked by D6-DMSO solvent signal thus, ^1H NMR was additionally provided in MeOD shown in *Fig. 48*.

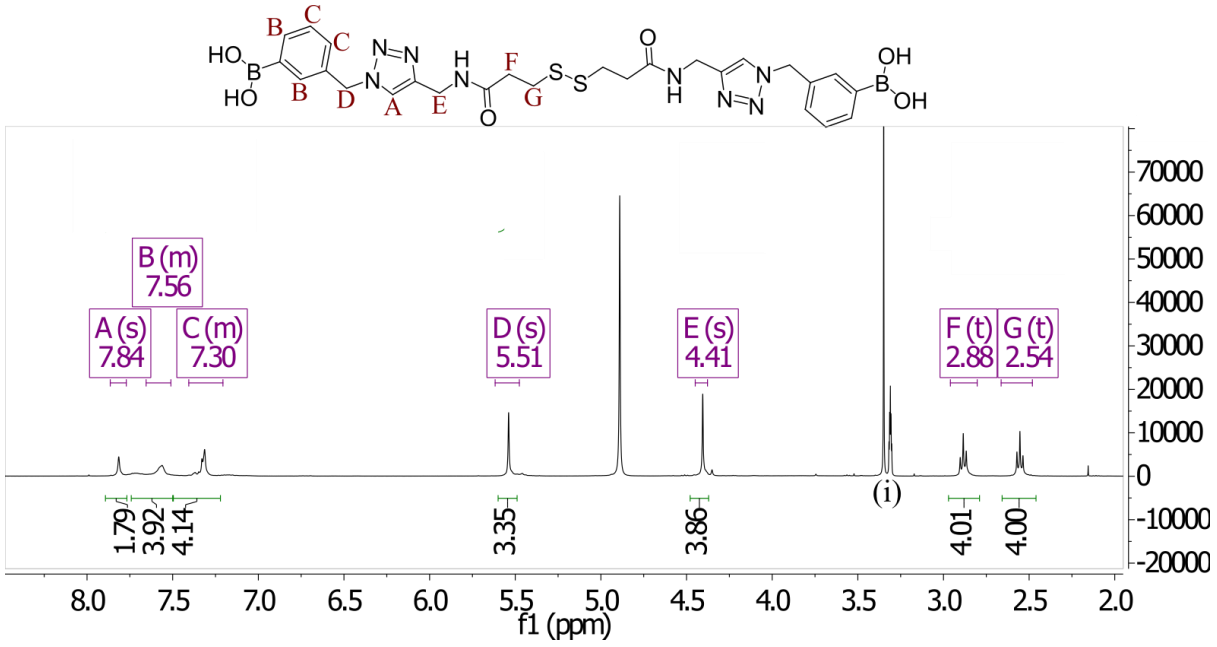


Fig. 48: ^1H NMR spectra of DcB (MeOD, 298K, 400 MHz) with proton assignment

On exchanging NMR solvent from D6-DMSO to MeOD peaks corresponding to CH_2 protons 'g' adjacent to thiol are observed at 2.54 ppm coupling to 'f' protons as suggested by roofing of

both triplets (393). Peaks corresponding to amide and hydroxyl protons on BA are lost however due to deuterium exchange with the NMR solvent MeOD (393). With deuterium exchange at the amide, proton 'e' no longer couples to the amide occurring now as a singlet as opposed to the doublet observed when in D6-DMSO (*Fig. 47*). Proton 'd' as with previous AzBA and DcB in D6-DMSO spectra occurs as a singlet having no coupling while triazole proton 'a' is similarly observed as a singlet at 7.84 ppm close to literature value (404). Coupling was confirmed with COSY NMR in D6-DMSO to ensure visible amide peaks. Coupling is observed between protons 'H' and 'X' and between amide 'A' and 'G' (*Fig. 49*). Due to low solubility, ^{13}C NMR was unable to be obtained for DcB where increasing concentration of DcB in the NMR solvent D6-DMSO or MeOD caused precipitation.

The isolation of DcB was confirmed by ESI-(+)MS showing three distinct masses. The peak at *m/z* 639.29 was assigned to DcB ($[M]^+$) having predicted mass of 638.33. A small peak corresponding to mass of 140.01 was assigned to fragmentation of DcB constituting a sodium adduct of phenyl boronic acid ($[pheBO_2+Na]^+$) consistent with previous fragmentation around the CH_2N_3 group.

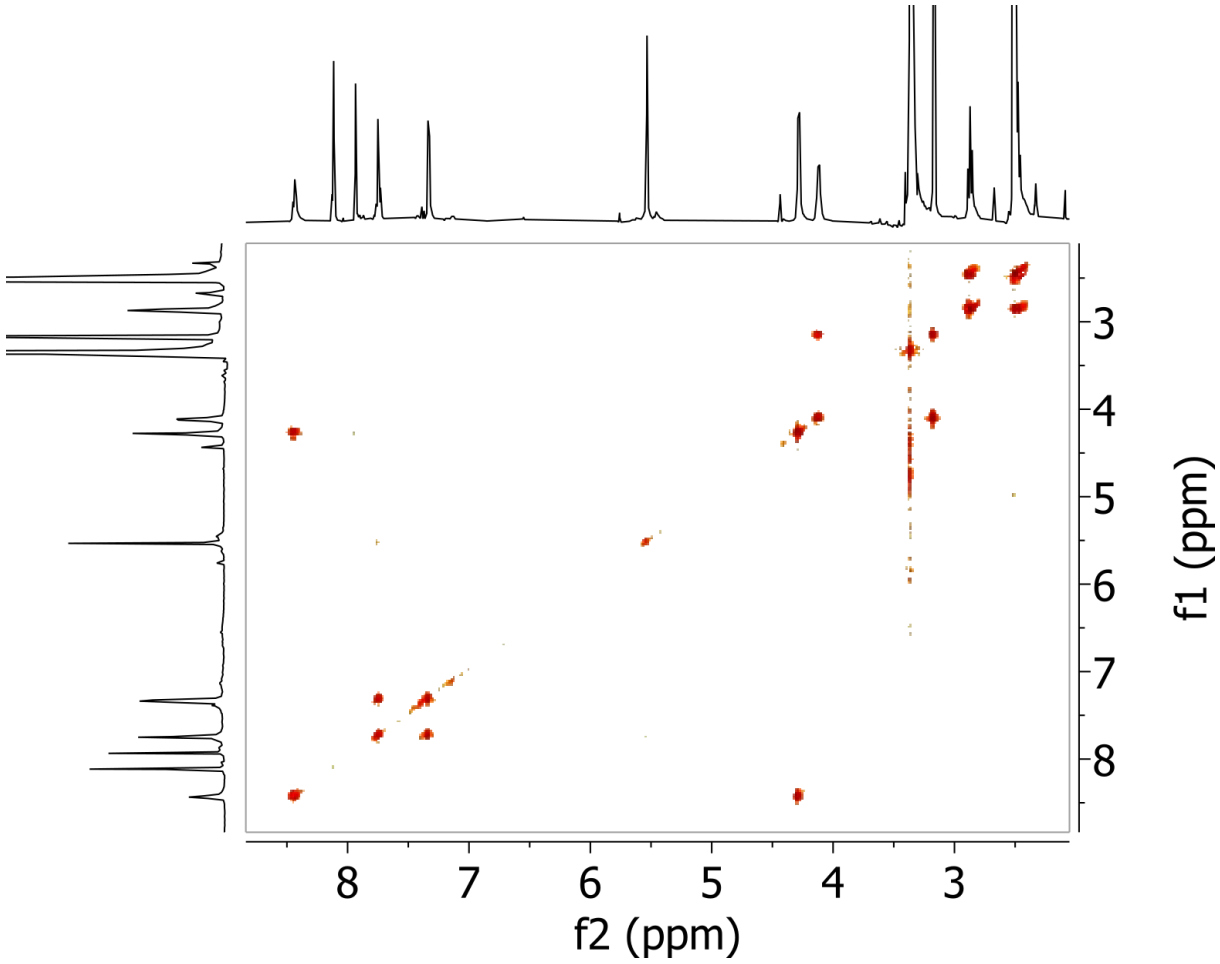
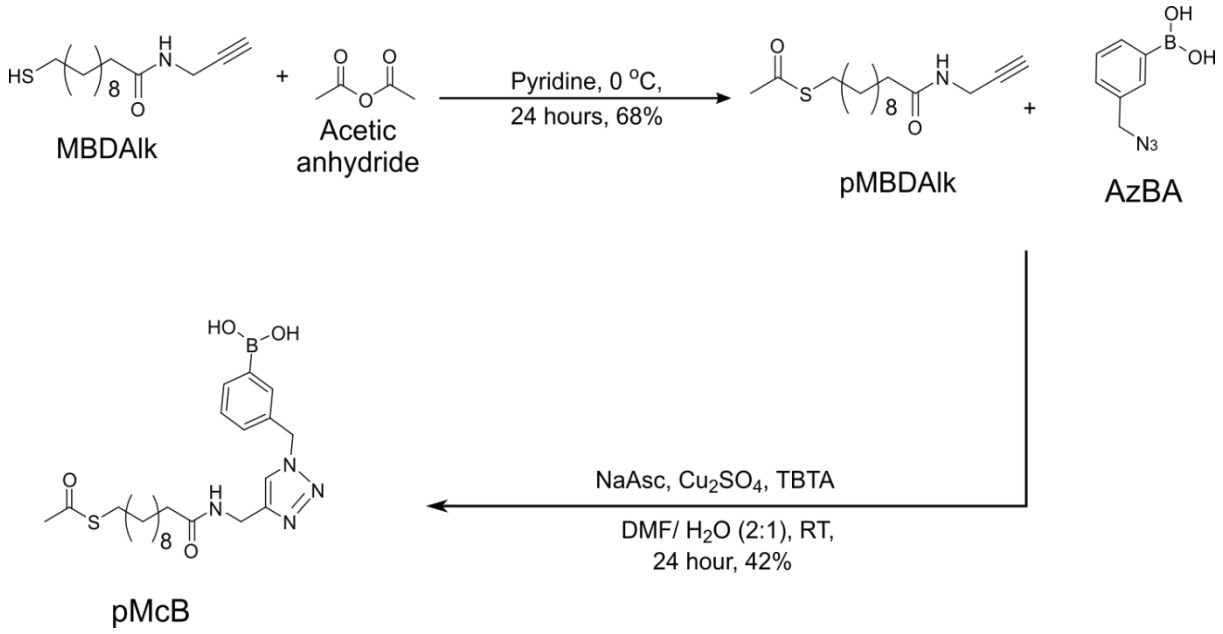


Fig. 49: 2D COSY NMR spectra of DcB (D6-DMSO, 298K, 400 MHz).

3.3.2 Synthesis of PBA terminated C_{10} SAM monomer from MBDAlk and AzBA

Synthesised alongside the short chain (C_2) DcB, we additionally produced a long chain (C_{10}) PBA terminated SAM monomer using the developed CuAAC reaction from *Scheme. 7.* The synthetic pathway to produce the PBA terminated long chain (C_{10}) SAM monomer (pMcB) is shown in *Scheme. 8*.



Scheme. 8: Synthetic route to produce pMcB through CuAAC reaction of MBDAlk and AzBA. Detailed synthesis methodology is available in Chapter 7 (section 7.2.9).

Initial attempts at CuAAC reaction between our MBDAlk and AzBA evidently produced several unknown side-products (observed by TLC) attributed to oxidation of the thiol by NaASC and reactions between boronic acid and thiol groups (405–407). To prevent this, we first acylated the thiol group on MBDAlk producing **pMBDAlk** which was then reacted with AzBA using the Cu(I) catalyst as described in *section 3.3.1* producing pMcB. pMcB was characterised by ^{1}H NMR spectroscopy with proton assignments shown in *Fig. 50*.

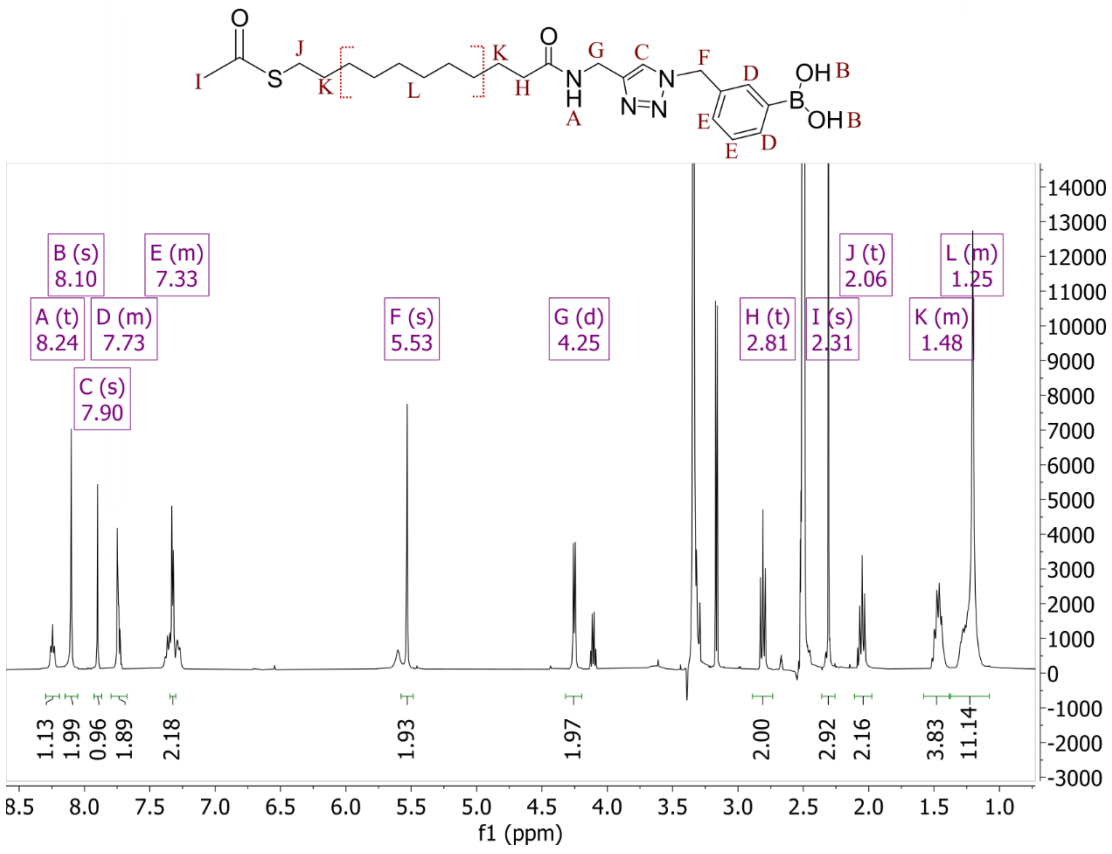


Fig. 50: ^{1}H NMR spectra of pMcB (d6-DMSO, 298K, 400 MHz) with proton assignment.

Consistent with proton assignments for DcB (*Fig. 47*), Confirmation of successful CuAAC reaction between pMBDAlk and AzBA producing pMcB is providing in several changes to peak distribution. Disappearance of alkyne triplet (3.07 ppm, MBDAlk ^{1}H NMR spectra, *Fig. 5*) and occurrence of singlet assigned to triazole at 7.90 ppm confirms pMcB synthesis. Additional downfield shift of protons 'F' to 5.53 ppm are assigned to aromatic adjacent CH_2 observed in similar position to corresponding protons in ^{1}H NMR DcB spectra (5.51 ppm). With loss of long-range alkyne coupling to neighbouring CH_2 protons 'G', this now presents a doublet coupling only to amide protons 'A'. PBA group hydroxyl protons 'B' occur as a single peak while aromatic *ortho* protons 'D' couple to *para* and *meta* protons 'E' as confirmed in COSY NMR spectra (*Fig. 51*). Coinciding, protons 'H' are assigned to CH_2 neighbouring the carboxyl group and 'J' to thiol neighbouring CH_2 showing coupling to alkane chain 'K' as observed in COSY NMR spectra. Protons 'K' show clear coupling to the large peak at 1.25 ppm assigned to homogenous alkane backbone 'L' while the acetyl protecting group 'I' shows an isolated peak at 2.31 ppm. Due to low reaction yield and complications in scaling up this reaction, no ^{13}C NMR was acquired for pMcB.

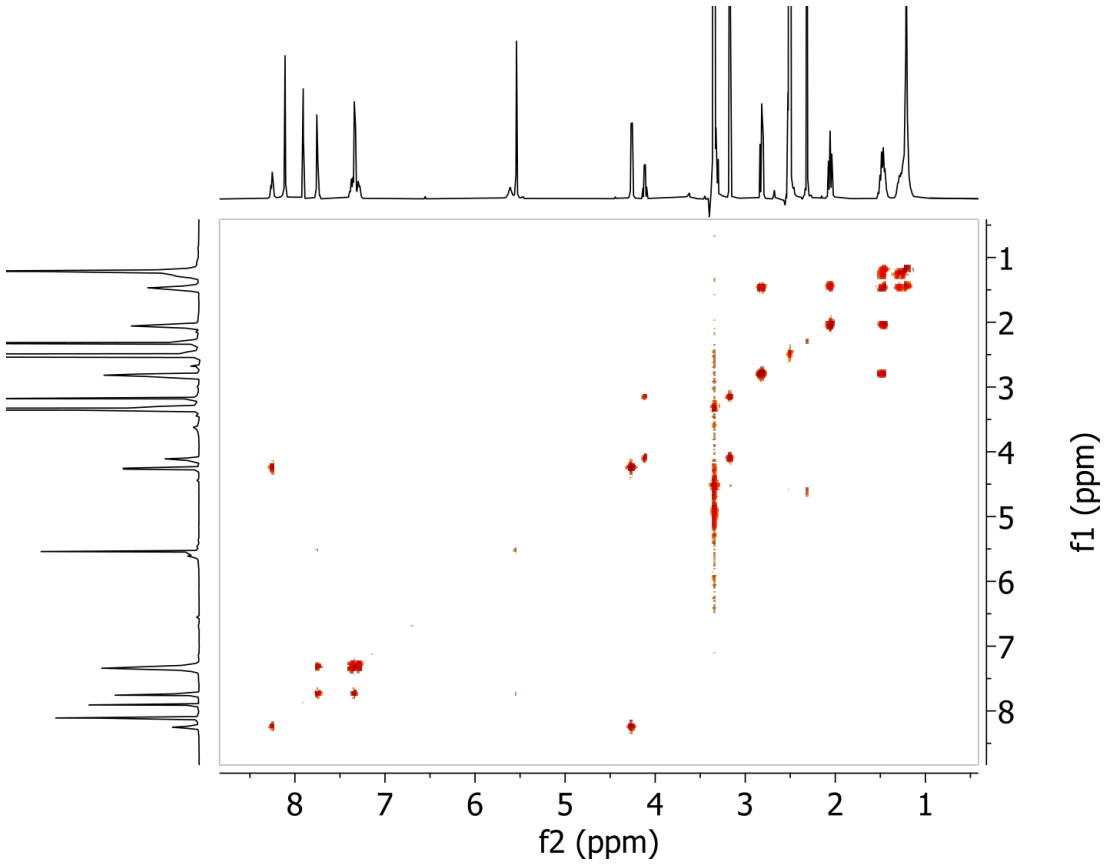


Fig. 51: 2D COSY NMR spectra of pMcB (D6-DMSO, 298K, 400 MHz).

The isolation of pMcB was confirmed using ESI-(+)MS showing significant fragmentation of pMcB. With predicted mass of 474.43, the peak at *m/z* 475.26 is assigned to pMcB ($[M]^+$). Additional major peaks are seen at *m/z* 333.11 assigned to fragmentation of acetyl group and PBA with sodium adduct ($[M-C_8H_9O_3B+Na]^+$), *m/z* 239.16 assigned to fragmentation at carbonyl group with sodium adduct $[M-C_{12}H_{13}N_4O_3B+Na]^+$ and 185.11 assigned to fragmentation within the triazole ($[M-C_{16}H_{26}O_2SN_2+Na]^+$).

3.5 Conclusion

In this chapter we have described the design rationale and synthesis of three compounds for generation of alkyne terminated SAMs. The synthesis of a further three azide functionalised compounds has been described thereby providing CuAAC ligands for alkyne terminated SAMs. Finally, we have optimised the CuAAC reaction in solution producing two distinct PBA terminated SAM monomers. With the developed CuAAC method, rapid reaction time between monomer and azide ensure suitability with surface functionalisation with the reaction proceeding to completion within 24 hours. With the SAM monomers, azide functionalised ligands and methodology developed in this chapter we will now proceed to generate alkyne functional SAMs and optimise the procedure for PBA functionalisation using the various surface characterisation techniques described in Chapter. 2.

Chapter 4.

Formation and characterisation of alkyne and PBA terminated SAMs

Abstract: In this chapter we will examine the SAMs produced by compounds synthesised in chapter 3 through various surface characterisation techniques. In this we will explore the effect of alkane backbone and branching on SAM organisation to establish procedures for producing organised alkyne terminated SAMs. Following this, pre-clicked PBA terminated monomers will be used to produce SAMs with defined BA-saccharide binding surfaces, serving as a comparative surface to our CuAAC reacted AzBA functionalised SAMs. Once surface parameters are established, the CuAAC reaction between our alkyne terminated SAMs and AzBA will be examined for yield and speed of reaction thus producing an effective surface functionalisation procedure.

4.1 Chapter introduction

The spontaneous adsorption of chemical groups to a substrate producing SAMs provides a simple route of surface functionalisation and a method by which to impart unique chemical properties. This has seen use across a number of fields including biomedical implants (408,409), corrosion inhibition (410,411) and of concern to this research, biosensors (412,413). Given the vast library of research on various substrates and self-adsorbing chemical groups, complex molecular imprinting technology-based biosensors has surged in recent years seeing development of synthetic multivalent binding pockets producing remarkable selectivity in biomarker discrimination (193,285,291).

The chemical composition of the SAM monomer has demonstrated remarkable effect on quality and formation rate of the final monolayer being regulated by the length of alkane chain, terminal groups and elemental composition throughout the compound (222,224,225). By increasing backbone length more densely packed monolayers are produced suggesting benefits to use of long simple alkanethiols for monomers. Contrary to this, high packing density imparts steric hindrance to further surface reactions and potentially imparts more dramatic boundary defects given the adopted tilt by long alkanethiols and chain

flexibility. The use of mixed thiolate SAMs has been used to alleviate steric hinderance effects thus in an ideal monolayer, terminal functional groups must be sufficiently spaced (228,414,415). Alternatively, use of a pre-functionalised SAM monomer provides a route for complete functionalisation being unrestrained by reaction yields. Quality of the produced SAM however will be affected given the inclusion of bulky groups inhibits dense packing and increases time taken for full SAM organisation (416).

Selection of a high yield, rapid and physiologically suitable surface reaction is essential for sufficient surface functionalisation and has seen development of several well suited reactions (235,242,246). Being stable under atmospheric conditions and soluble in aqueous buffer, the CuAAC reaction has seen extensive use in biomolecule functionalisation since its inception by Rostovtsev *et al* in 2002. It's application to SAM functionalisation has been explored across a number of studies providing compelling evidence to its suitability in surface reactions (262,417,418). While high CuAAC reaction yields are attained in solution, careful consideration to SAM monomer design must be given in adapting this reaction to a solid substrate however. During CuAAC reaction progression, the formation of Cu(I)-alkyne intermediates are essential thus, in

densely packed SAMs with limited access to alkyne groups, steric effects would serve to inhibit the CuAAC reaction (380).

In this chapter, we will investigate the formation of SAMs from previously synthesised compounds in chapter 3 through characterisation of SAM growth. Our optimised CuAAC reaction will be applied to alkyne terminated surfaces for optimisation of surface reaction procedure. This will be compared to SAM formation of pre-functionalised PBA-alkanethiol monomers to establish intensity of PBA functionalisation with CuAAC surface reaction. Through this an optimised SAM and surface CuAAC reaction will be developed for application to PBA-oligosaccharide complex immobilisation to our surface. The objectives of this work can be broken down as follows:

4.2 Objectives

1. Produce and characterise alkyne terminated SAMs (MBDAlk, DTPAlk and DFC) synthesised in chapter. 3 and evaluate SAM packing and organisation based on chemical composition (*Fig. 52a*).

2. Produce and characterise SAMs of PBA terminated monomers (DcB and pMcB) for comparison between alkyne terminated and AzBA functionalised surfaces (*Fig. 52b*).

3. Using the optimised CuAAC reaction, functionalise alkyne terminated SAMs with AzBA and characterise the reacted surface

to establish changes in surface properties and surface reaction yield (*Fig. 52c*).

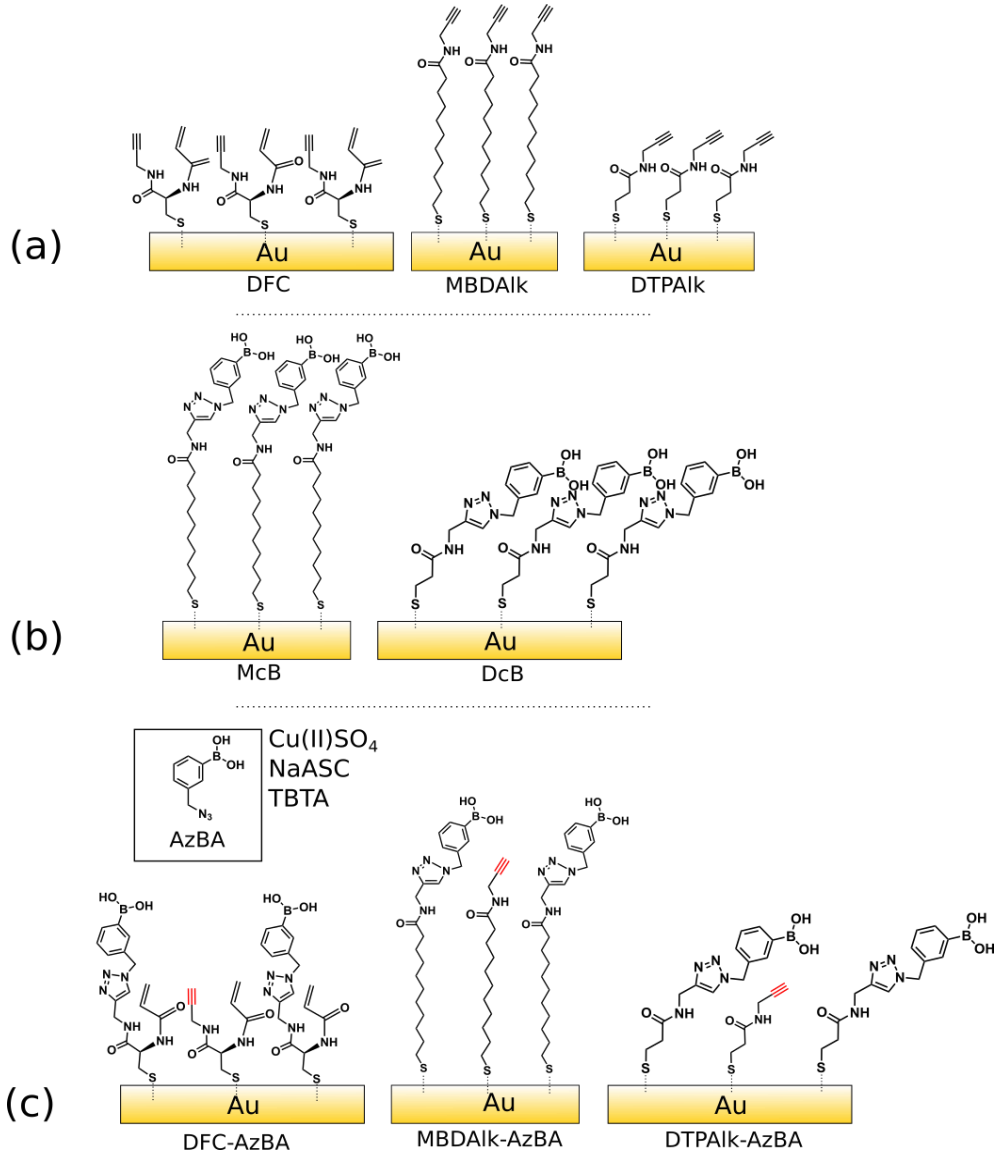


Fig. 52: (a) Alkyne terminated SAMs showing branched DFC, long chain (C_{10}) MBDAlk and short chain (C_2) DTPAlk. (b) PBA-terminated SAMs long chain (C_{10}) McB and short chain (C_2) monomers. (c) AzBA functionalisation of alkyne terminated SAMs.

4.2 Formation and characterisation of alkyne-terminated SAMs on gold surfaces

All SAMs characterised by ellipsometry, contact angle and XPS were formed on polycrystalline gold substrates purchased from George Albert PVD., Germany consisting of a 100 nm gold layer on silicon. Monomers were incubated with clean gold substrates for 24 hours to allow sufficient monolayer organisation whilst preventing excessive desorption as previously reported (419). Prior to incubation, gold substrates were chemically cleaned by immersion in piranha solution (H_2SO_4: H_2O_2, 7:3) for 7 minutes before extensive washing with ultra-pure MilliQ H_2O (UHPW) followed by HPLC grade methanol. Solutions of SAM monomers were sonicated for 3 minutes and then purged by argon bubbling for 1 minute. Immediately following piranha treatment, clean substrates were immersed in 1 mL methanolic solutions of either 0.1 mM DTPAlk, 0.1 mM DFC or 0.2 mM MBDAlk and reaction vial sealed under argon. These were incubated for 24 hours on a rotary mixer after which time SAM adsorption was quenched by liberal rinsing of substrates with HPLC grade methanol with drying of SAMs under argon stream. To minimise atmospheric contamination, all SAMs were immediately used in characterisation techniques and stored under argon for transport. An associated error of 0.05 ± 0.04 nm was observed on varying refractive index (n) between 1.45 and 1.5 in ellipsometry modelling for DTPAlk, DFC

and MBDAlk SAMs with thickness reported calculated from n=1.5. All SAMs were synthesised in duplicate with four measurement spots per sample for contact angle and ellipsometry analysis. Reported error was calculated from standard deviation between measurement spots of all samples.

4.2.1 DTPAlk short chain SAM generation and characterisation

Examination of SAMs formed by DTPAlk (*fig. 53a*) by ellipsometry (*Table. 5*) shows a thickness (0.4 ± 0.03 nm) roughly half of the theoretical value (0.7 nm). While tilting of monomers is commonly reported (215,226), a folded conformation of structurally similar cysteine based SAMs was reported by Stephenson-Brown *et al* (2015) (*Fig. 53b*) (420). Assuming a prescribed tilt of 30 ^{o} as suggested by Vericat *et al* (2010) we expect a thickness of 0.65 nm, still higher than experimentally derived thickness of 0.4 ± 0.03 nm. Alongside thickness values consistent with SAM formation presenting low surface organisation, advancing contact angle (78.6 ± 1.0^{o}) (*Table. 5*) reports lower value than previously reported (≈ 84^{o}) (421). Exposure of polar carbonyl and amide groups thereby providing polar sites amongst exposed non-polar alkyne groups might explain lower experimental advancing contact angle consistent with low derived thickness of the DTPAlk SAM. (420). This is

further confirmed in calculation of contact angle hysteresis (θ_{adv}- θ_{rec}) of 13.6^{o} being consistent with low surface organisation suggested at hysteresis >10^{o} (422). As the CuAAC reaction requires Cu(I) acetylide intermediate formation, in presenting buried alkyne groups we expect significantly reduced reaction yield thus functional capability. This will be explored in *section 4.4* in comparison of reaction yields between structurally different SAMs.

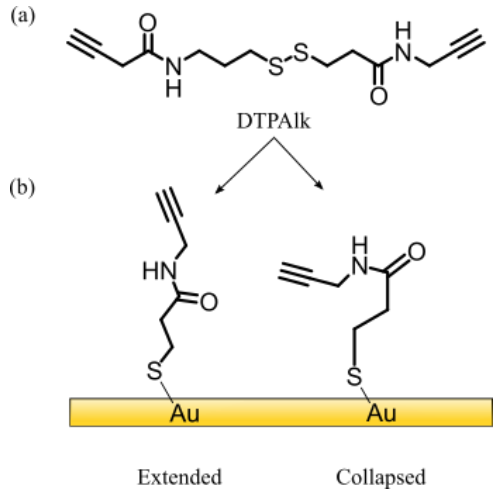


Fig. 53: (a) DTPAlk short chain SAM monomer. (b) Extended and folded conformation that can be adopted by DTPAlk.

Table. 5: ellipsometry and contact angle measurements for DTPAlk SAMs.

Contact angle (^{o})		**Ellipsometry thickness (nm)**	
Advancing	Receding	Theoretical	Experimental
78.6 ± 1.0	65.0 ± 2.0	0.73	0.40 ± 0.03

To confirm DTPAlk SAM formation, XPS was used to examine elemental composition of the surface (*Fig. 54*). The C, N, O, S and Au elements were observed in XPS survey scans suggesting monomer adsorption to Au surface. Adventitious carbon and oxygen contamination are common artefacts produced under XPS and are seen in high-resolution (HR) scans for C1s and O1s hence will not be accounted for in elemental ratios. Providing confirmation of SAM formation, S, N and Au ratios are shown in *Table. 6*. The ratio of S/N is lower than expected value of 1:1 attributed to nitrogen contamination (423).

Table. 6: Elemental ratio of S to N and Au derived from HR spectra.

	Theoretical	Experimental
S/N	1.00	0.77 ± 0.06
Au/S	n/a	24.91 ± 0.80

Interpretation of the C1s HR scan observes three chemical species. The peak at 288.2 eV can be attributed to C=O preceded by C-S/C-N at 286.7 eV while alkyne and C-C are located within the large adventitious carbon peak arising from atmospheric

contamination at 284.8 eV (345). This contamination is further confirmed in O1s HR scans with an observed peak at 533.3 eV corresponding to atmospheric C-O species while O=CN of DTPAlk is defined at 531.6 eV. N1s scans reveal a singular peak at 399.8 eV ascribed to N-C. Confirmation of thiol-Au adsorption is shown in S2p spectra displaying a doublet corresponding to S2p3/2 (162.5 eV) and S2p1/2 (163.7 eV) split 1.2 eV in a distinct 2:1 ratio consistent with literature values (424). At 163.6 eV a smaller doublet is ascribed to unbound sulphur suggested to arise from insufficient rinsing of SAMs (424). As SAMs were liberally rinsed with HPLC methanol prior to analysis and to prevent further desorption of thiol species, no further methods were employed to remove unbound sulphur. Peak separation between bound S2p1/2 and unbound S2p3/2 (separation 0.1 eV) is below the energy resolution of the XPS instrument (0.5 eV) thus we cannot confirm reliably this species. Despite this, presence of unbound S2p1/2 provides sufficient evidence for presence of the unbound S2p3/2 peak given the expected S2p3/2 and S2p1/2 separation of 1.2 eV. High resolution XPS spectra were charge corrected to adventitious carbon peak at 284.8 eV.

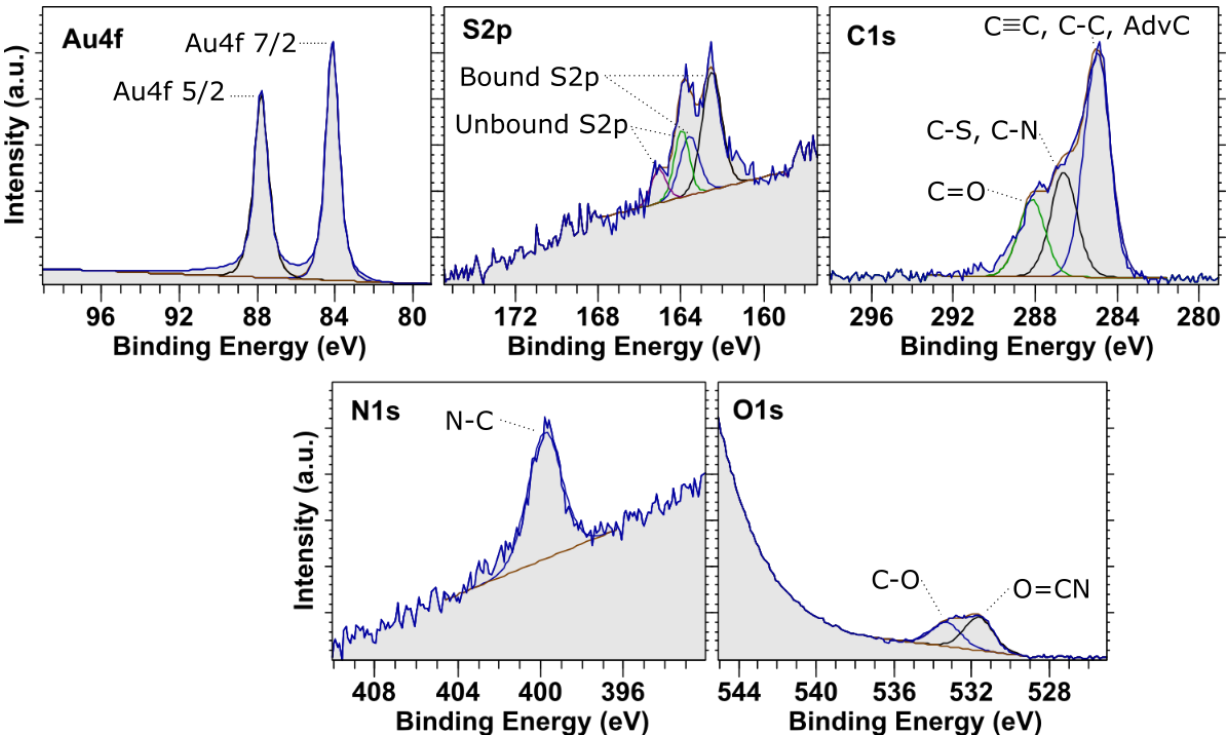


Fig. 54: HR XPS spectra of S2p, C1s, N1s and O1s from DTPAlk SAMs with peak regions.

4.2.2 MBDALk long chain SAM generation and characterisation

To investigate effect of alkane backbone length on SAM formation, monolayers of MBDALk (*Fig. 55*) were produced as per method outlined in section 4.2. In increasing the length of the alkane chain, significantly more opportunity for Van der Waals interaction is presented during adsorption allowing more densely packed and stable structures as previously reported (225,380). Thickness value of the MBDAlk SAM (1.81 ± 0.04 nm) is close to

theoretical thickness of 1.85 nm confirming formation of a densely packed SAM (*Table.* 7). Advancing contact angle (82.6 ± 2.3^{o}) confirms this showing close to literature values of ≈84^{o} while hysteresis (θ_{hys} 5.7^{o}) is consistent with high surface organisation (421,422,425).

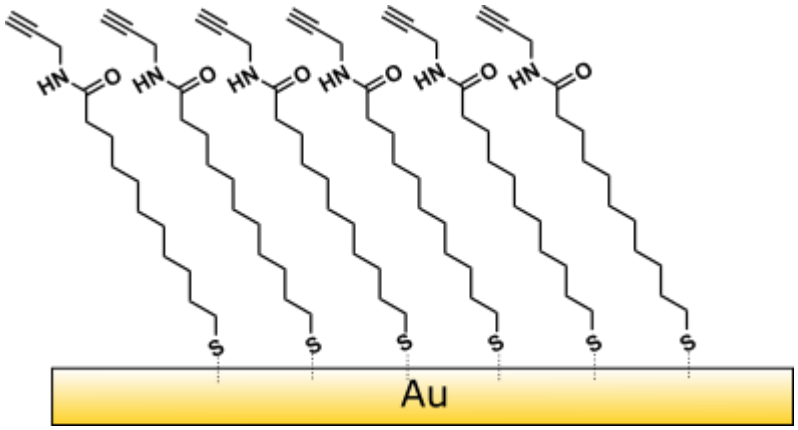


Fig. 55: SAM formed by MBDALk monomer.

Table. 7: Contact angle and ellipsometry measurements for MBDALk SAMs.

Contact angle (^{o})		**Ellipsometry thickness (nm)**	
Advancing	Receding	Theoretical	Experimental
82.6 ± 2.3	76.9 ± 1.9	1.85	1.81 ± 0.04

XPS analysis was conducted on MBDALk SAMs to confirm elemental composition and adsorption of thiol to Au substrate. Survey scan of the MBDAlk SAM shows a similar composition to

DTPAlk with presence of C, N, O, S and Au as expected. Contrary to the DTPAlk SAM however, no adventitious carbon or oxygen contamination is observed in HR spectra with ratio values shown in *Table. 8.* As previously described, ellipsometry and contact angle data suggests MBDAlk forms densely packed SAMs lacking the folded conformation provided by DTPAlk SAMs. As previously reported by Wieliczka & Dubowski (2006), exposed polar groups might facilitate increased C-O contamination further confirming low surface organisation of the DTPAlk SAM. Conversely, as no contamination is observed on MBDAlk SAMs, this suggests polar amide and carbonyl are likely embedded within the SAM presented alkyne groups at the SAM interface (426).

Table 8: Elemental composition of MBDAlk SAMs.

	Theoretical	Experimental
N/S	1.00	1.44 ± 0.11
N/O	1.00	1.09 ± 0.10
N/C	0.07	0.07 ± <0.01
Au/S	n/a	19.24 ± 1.53

Agreement in theoretical and observed ratios for MBDAlk SAMs are consistent with successful SAM formation displaying similar attenuated S2p signals to DTPAlk attributed to shielding

of thiol species by the hydrocarbon chain (*Table. 8*) (427). Unbound sulphur is again observed comprising 37% of total sulphur despite extensive rinsing of SAMs prior to XPS analysis. Despite this, comparison of Au/S ratios shows increased thiol adsorption compared to DTPAlk emphasising higher surface organisation imparted by inclusion of a longer alkane backbone in the monomer.

Being of similar chemical design to DTPAlk, HR spectra of Au, C, O, N and S reveal a highly similar pattern of peak integration with two doublets of bound and unbound S 2p at 162.5 eV/ 163.7 eV and 163.8 eV/ 165.0 eV (S 2p3/2 and S 2p1/2) respectively and a singular N1s peak at 400.2 eV for N-C species. Increased carbon content of alkane backbone manifests as a large C-C peak at 285.2 eV masking the C≡CH species. At higher binding energies C-S/C-N are present at 286.6 eV with C=O species at 288.4 eV. A single peak is observed in O1s HR spectra ascribed to C=O species at 531.9 eV (*Fig. 56*) consistent with no atmospheric contamination (256,345). Peak separation between bound S2p1/2 and unbound S2p3/2 (separation 0.1 eV) is below the energy resolution of the XPS instrument (0.5 eV) thus we cannot confirm reliably this species. Despite this, presence of unbound S2p1/2 provides sufficient evidence for presence of the unbound S2p3/2 peak given the expected S2p3/2 and S2p1/2 separation of 1.2 eV.

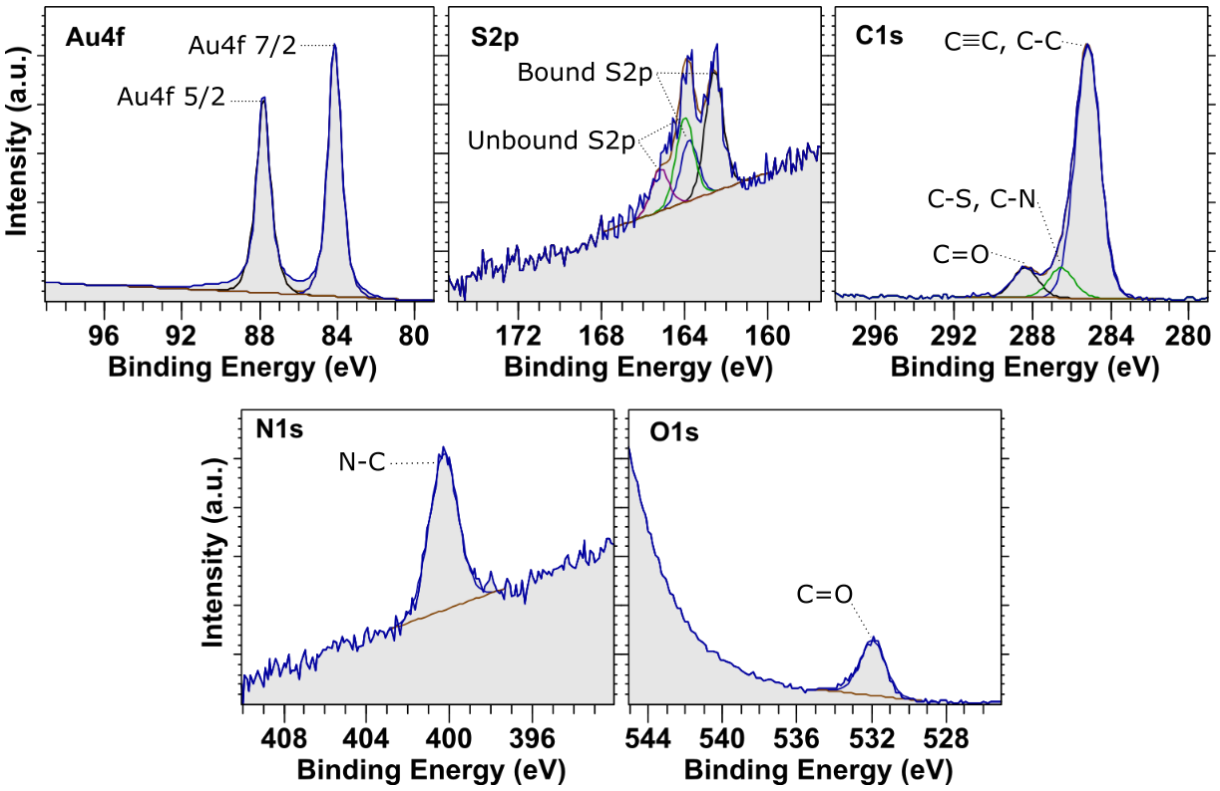


Fig. 56: HR XPS spectra of MBDAlk SAM for elements: S2p, C1s, N1s, O1s and Au 4f displayed with peak regions.

4.2.3 DFC branched SAM generation and characterisation

A common theme across surface functionalisation is the inhibition of surface reactions and ligand interaction by steric hindrance arising from densely packed SAM structures. Inclusion of mixed SAM monomers has been reported previously to counter this by providing spacing between SAM terminal groups from shorter monomers (228,229). Alternatively, packing of SAM monomers can be modulated directly at the substrate interface by

incorporation of branched groups preventing the tightly packed structures observed for linear alkanes (225). Several groups have reported SAMs of branched monomers with Zhang *et al* using methyl branched propanethiol to produce unique monomer packing patterns (428). Alternatively, a PSA specific MIP was produced by Stephenson-Brown *et al* (2015) using the monomer shown in *Fig. 57*. Through inclusion of two functional groups both ligand immobilisation and templating was achieved through separate surface reactions producing complimentary binding pockets to PSA (262).

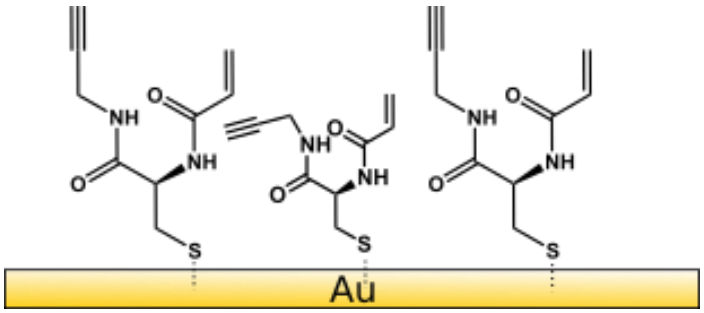


Fig. 57: SAM formed by DFC monomers showing potential folded configuration similar to DTPAlk.

To investigate effect of packing density by branched SAMs we produced SAMs of the previously reported alkyne/ acryloyl modified cystine (*Fig. 57*) (420). Surfaces were characterised by ellipsometry and contact angle (*Table. 9*) for comparison to DTPAlk where we expect a more hydrophilic surface imparted by

additional polar groups on DFC. In addition, we expect reduction in thickness to DTPAlk arising from lower organisation imparted by branched groups preventing dense packing of the monomer (429).

Table. 9: Ellipsometry and contact angle measurements of DFC SAM.

Contact angle (^{O})		**Ellipsometry thickness (nm)**	
Advancing	Receding	Theoretical	Experimental
70.5 ± 3.0	56.4 ± 7.0	0.73	0.49 ± 0.04

Contact angle measurements confirm increased hydrophilicity of DFC compared to DTPAlk seeing a reduction in both advancing and receding angles. Additionally, while the hysteresis of DFC (θ_{hys} 14.1^{O}) appears similar to that of DTPAlk (θ_{hys} 13.6^{O}), heterogeneity was observed across receding angle data collection surmounting to large error. Accounting for this, the DFC SAM might be considered less homogenous than DTPAlk SAMs as predicted. Thickness of DFC (0.49 ± 0.04 nm) retains similarity to DTPAlk (0.40 ± 0.03 nm) albeit still showing slight increase in thickness. Given the branched composition of DFC, this can be attributed to either higher surface organisation or reduction in monomer tilt due to steric constraints between branched groups and the substrate.

Table. 10: Elemental composition of DFC SAMs.

	Theoretical	Experimental
N/S	2.00	2.98 ± 0.04
N/O	1.00	2.92 ± 0.11
Au/S	n/a	77.70 ± 15.29

XPS survey spectrum shows elemental composition consistent with chemistry of the DFC compound with peaks corresponding to C, N, O, S and Au species. Examination of HR spectra for all elements shows low resolution suggesting low concentration of DFC on the surface. This is confirmed in the Au/S ratio (77.7 ± 15.29) showing lower surface coverage of DFC (*Table. 10*) compared to DTPAlk (24.91 ± 0.80) and MBDAlk (Au/S 19.24 ± 1.53) SAMs. This is additionally shown in the S2p spectrum where little sulphur was detected at 162.5 / 163.7 eV with unbound sulphur at 163.8 / 165 eV. Peak separation between bound S2p1/2 and unbound S2p3/2 (separation 0.1 eV) is below the energy resolution of the XPS instrument (0.5 eV) thus we cannot confirm reliably this species. Despite this, presence of unbound S2p1/2 provides sufficient evidence for presence of the unbound S2p3/2 peak given the expected S2p3/2 and S2p1/2 separation of 1.2 eV. N1s HR spectrum shows a single sharp peak at 399.6 eV while for O1s, a small peak at 531.8 eV consistent with amide and C-O species

(430). Similar to DTPAlk, a large adventitious carbon peak is present at 284.8 eV preventing extensive peak deconvolution. Coinciding, elemental ratios of nitrogen to sulphur and oxygen (*Table.* 10) show increased nitrogen content consistent with contamination similarly seen for DTPAlk (423). Two further peaks on the C1s spectrum are presented at 288.5 eV and 286.8 eV which are assigned to C=O and C-N species respectively (345). Together with the observed large contact angle hysteresis (14.1^{O}), XPS analysis suggests low surface organisation with sparsely packed monomers. This can be attributed to branched acryloyl groups disturbing SAM formation seeing inhibition of inter-monomer interaction thus preventing dense packing. In addition both DTPAlk and DFC display a propensity for surface contamination compared to MBDAlk showing large adventitious carbon peaks on both SAMs. This was attributed to low surface organisation of DFC and DTPAlk enabling contamination through exposed polar carboxyl groups (420).

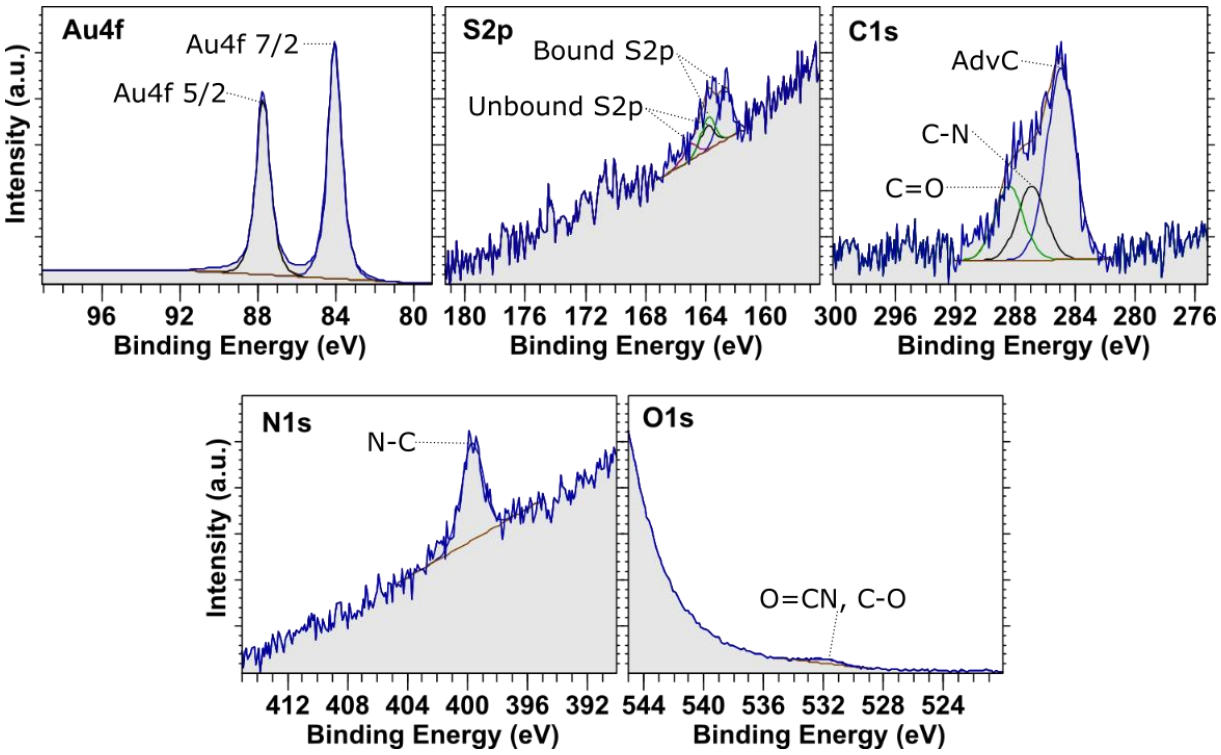


Fig. 58: HR XPS spectra of DFC SAM for elements: S 2p, C1s, N1s, O1s and Au 4f displayed with peak regions.

4.2.4 Comparison of DTPAlk, MBDALk and DFC SAMs and effect of backbone composition on SAM organisation

Based on ellipsometry measurements of DTPAlk, MBDALk and DFC we can confirm each compound was capable of SAM formation on gold substrates. Thickness measurements of 1.81 ± 0.4 nm for MBDALk being close to the theoretical value of 1.85 nm suggests reduction in adopted monomer tilt contrary to reports of 30-40^{o} tilt adopted by long alkanethiol SAMs (431). Conversely, with a theoretical thickness of 0.73 nm, both DTPAlk and DFC

demonstrated lower thickness at 0.40 ± 0.03 and 0.49 ± 0.04 nm respectively. This is attributed to folded conformation of SAM monomers supported by increased hydrophilicity of the SAM (DFC θ_{adv} 70.5 ± 3.0^{o}, DTPAlk θ_{adv} 78.6 ± 1.0^{o}) compared to MBDAlk (θ_{adv} 82.6 ± 2.3^{o}) through exposure of polar C=O groups. While comprehensive structural characterisation of potential defects is outside the remit of this thesis, pursuing either DTPAlk or DFC SAMs for sensor development might require additional structural analysis. Quantification of defects such as pinholes, vacancy islands and domain boundaries alongside surface topography through scanning tunnelling and atomic force microscopy would confirm low organisation of DTPAlk and DFC SAMs as previously used in alkanethiol SAM characterisation studies (432–434).

Comparison of Au/S ratios derived from XPS analysis further suggests higher SAM organisation of MBDAlk showing a densely packed monolayer (Au/S 19.24 ± 1.53) with lower packing of DTPAlk (Au/S 24.91 ± 0.80) and significantly lower packing of DFC (Au/S 77.7 ± 15.29). Given that a low hysteresis suggests higher surface organisation, MBDAlk again demonstrates a more homogenous surface (θ_{hys} 5.7^{o}) than both DTPAlk (θ_{hys} 13.6^{o}) and DFC (θ_{hys} 14.1^{o}). While we expect more sparsely packed DFC given its branched configuration translating to lower SAM organisation, the linear composition of DTPAlk, while improving

monomer packing, does not improve organisation. Given the comparative thickness and contact angle values between DFC and DTPAlk but increased density of DTPAlk packing, this implies there is increased surface heterogeneity regardless of packing density. Instead, SAM disorder translates from lack of inter-monomer interactions consistent with short monomer SAMs presenting increased fluidity and surface defects (226,435). If pursuing

4.3 Formation and characterisation of PBA-terminated SAMs on gold surfaces

As the CuAAC reaction is not guaranteed to achieve complete surface functionalisation, we synthesised PBA terminated monomers via solution CuAAC reaction of azido-PBA (AzBA) with DTPAlk and MBDALk. These compounds were used to produce the SAMs shown in *Fig. 59* exhibiting 1:1 ratio of thiol to PBA thus providing a defined saccharide binding surface. Prior to SAM formation of McB, deprotection of acetate group from terminal thiol was first required. To do so, 0.2 mM pMcB in HPLC grade ethanol was mixed 1:1 with aqueous KOH and sonicated for 5 minutes. This was incubated for 2 hours on a rotary mixer under ambient conditions after which time clean gold substrates were immersed in 1 mL of McB-KOH solution for 24 hours under argon

before liberal rinsing with HPLC ethanol and drying under argon stream. DcB SAMs were produced with 0.1 mM DcB in HPLC grade methanol as described in section 4.2.

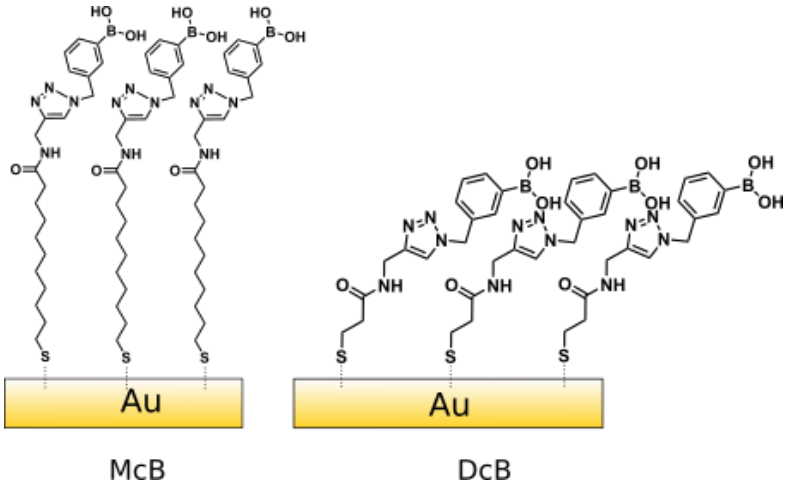


Fig. 59: SAMs formed by McB (*left*) and DcB (*right*).

4.3.1 Characterisation of DcB and McB PBA-terminated monolayers by ellipsometry, contact angle and XPS

SAMs of McB and DcB were subjected to ellipsometry and contact angle analysis to determine thickness and wettability with the experimental data shown in *Table. 11*. Ellipsometry measurements for SAMs formed from acetyl protected thiol are shown alongside McB for justification of deprotection procedure. An associated error of 0.09 ± 0.03 nm was observed on varying refractive index (n) between 1.45 and 1.5 in ellipsometry modelling for DcB and McB SAMs with thickness reported calculated

from n=1.5. All SAMs were synthesised in duplicate with four measurement spots per sample for contact angle and ellipsometry analysis. Reported error was calculated from standard deviation between measurement spots of all samples.

Table. 11: Ellipsometry and contact angle measurements of DcB, pMcB and McB SAM.

SAM	**Contact angle (^{O})**		**Ellipsometry thickness (nm)**	
	Advancing	Receding	Theoretical	Experimental
DcB	64.7 ± 1.5	55.0 ± 2.4	1.77	0.7 ± <0.01
pMcB	-	-	2.64	0.9 ± 0.09
McB	74.5 ± 2.0	63.5 ± 2.8	2.64	2.2 ± 0.10

Increased thickness is observed on inclusion of PBA terminal groups for DcB (0.7 ± <0.01 nm) compared to alkyne counterpart DTPAlk (0.40 ± 0.03 nm). This is significantly lower than expected thickness (1.77 nm) however suggesting either adoption of increased monomer tilt or increased prevalence of folded monomer configurations. While previously, increased hydrophilicity of DTPAlk SAMs was attributed to this folded conformation, contact angle of DcB SAMs is expected at ≈60^{O} as previously reported for PBA terminated surfaces (425,436). This

is confirmed in reported DcB θ_{adv} (64.7 ± 1.5^{o}) showing significantly more hydrophilic nature compared to DTPAlk (θ_{adv} 78.6 ± 1.0^{o}) close to literature value. Examination of hysteresis additionally suggests a more homogenous SAM for DcB (θ_{hys} 9.7^{o}) than produced by DTPAlk (θ_{hys} 13.6^{o}) attributed to availability of inter-monomer interactions through π-π stacking across aromatic rings (437). With consideration for contact angle data, this implies the folded conformation is not likely as prevalent on the DcB SAM with θ_{adv} suggesting presentation of terminal PBA groups. Interestingly, Zareie *et al* (2002) in producing phenyl terminated SAMs reported a stacking of terminal phenyl groups similar to graphite construction lying parallel to SAM interface whilst being dependent on SAM packing density. As the DcB SAM lacks sufficient inter-chain interactions we can assume phenyl stacking is responsible for decreased contact angle hysteresis thus increased SAM organisation. Accounting for phenyl groups of the PBA unit stacking parallel to the SAM interface, we would expect a thickness reduction of 0.65 nm. As we expect the DcB SAM to additionally adopt tilt, the conformation of the phenyl group would further serve to reduce the observed thickness thus providing the pronounced decrease in thickness for DcB SAMs (226,438,439).

Review of ellipsometry data for McB SAMs reports a thickness of 2.2 ± 0.10 nm demonstrating increased deviation from the

theoretical thickness (2.64 nm) than previously seen for alkyne counterpart MBDAlk (theoretical 1.85 nm, experimental 1.81 ± 0.04 nm). From this we can assume increased adoption of tilt with the McB monomer on inclusion of terminal PBA group. In addition, requirement for pMcB deprotection is confirmed in comparison of pMcB thickness (0.9 ± 0.09 nm) to McB (2.2 ± 0.10 nm) showing significantly lower thickness where thiols were protected with acetyl groups. Verifying change in surface organisation with contact angle analysis showed a reduction in advancing angle (θ_{adv} 74.5 ± 2.0) and increase in hysteresis (θ_{hys} 11^{O}) compared to MBDAlk (θ_{adv} 82.6 ± 2.3, θ_{hys} 5.7^{O}). While this is consistent with expression of terminal PBA, advancing angle remains higher than expected value (≈60^{O}) while increased hysteresis implies reduction in SAM organisation. Taken together, inclusion of large terminal functional groups appears to interrupt SAM formation through disturbance to alkane chain interaction that assist in assembling densely packed monolayers. To confirm elemental composition of the DcB and McB SAMs, XPS analysis was provided with elemental ratios shown in *Table. 12.*

Table. 12: elemental composition of DcB (*left*) and McB (*right*) SAMs

	DcB		McB	
	Theoretical	Experimental	Theoretical	Experimental
N/S	4.00	4.08 ± 0.29	4.00	3.97 ± 0.62
N/O	1.33	1.25 ± 0.07	1.33	1.34 ± 0.13
N/B	4.00	11.55 ± 2.40	4.00	0.00 ± 0.00
Au/S	n/a	31.19 ± 1.78	n/a	87.58 ± 16.9

Elemental composition of DcB SAM shows close to expected ratios of N/S and N/O confirming SAM formation. However, lower surface coverage is observed (Au/S 31.19 ± 1.78) than DTPAlk (Au/S 24.91 ± 0.80) as derived from the increase in Au/S ratio of DcB compared to DTPAlk (*Table. 12*). Despite running an increased number of scans for boron detection, sensitivity appears low with significantly lower than expected values for B1s. Nonetheless, agreeable ratios of nitrogen to oxygen are in agreement with presence of triazole and terminal PBA hydroxyl groups.

HR spectra of DcB C1s can be interpreted with four distinct peaks. At higher binding energy of 287.9 eV is C=O species preceded by C-B species at 287.0 eV consistent with previous reports (440). At 286.0 eV, C=C is attributed to triazole ring while at 284.8 eV two peaks correspond to aromatic, C-C, C-S and

C-N species (*Fig. 60, C1s, blue*) and adventitious carbon from atmospheric contamination (*Fig. 60, C1s, yellow*). Two peaks are observed for N1s spectra in clear 1:3 ratio at 401.5 eV attributed to N=N from triazole and 399.7 eV encompassing C-N and N-N species (441). O1s HR spectrum is divided between two peaks with C=O species assigned to 531.4 eV. At higher binding energy, both PBA hydroxyl groups and atmospheric contamination C-O are assigned to 532.7 eV (430). S2p HR spectrum shows typical doublet pattern for S2p3/2 at 162.5 eV and S2p1/2 at 163.7 eV with no presence of unbound sulphur while B1s presents as a single peak at 192.3 eV consistent with literature values (425) (*Fig. 60*).

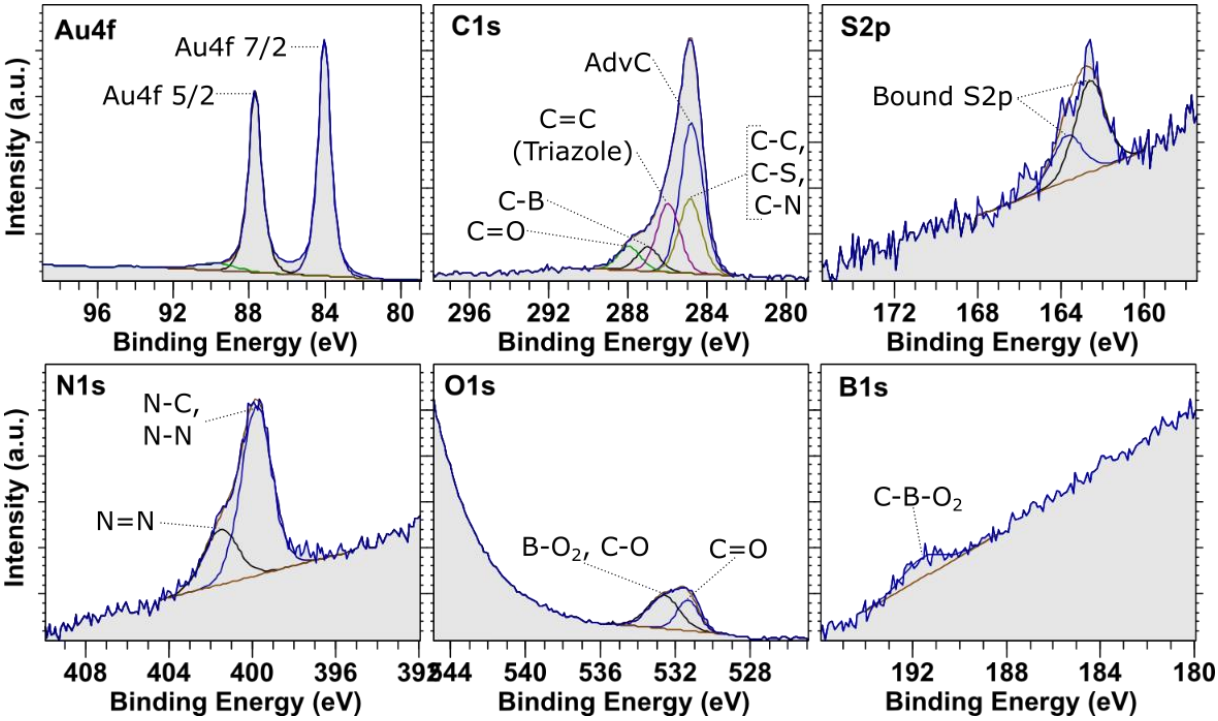


Fig. 60: HR XPS spectra of elements Au4f, C1s, S2p, N1s, O1s and B1s for DcB SAM with displayed peak regions.

For McB SAMs, elemental composition of the surface shows experimental N/S (3.97 ± 0.62) and N/O (1.34 ± 0.13) ratios are in good agreement with theoretical value (N/S 4.00, N/O 1.33) (*Table. 12*). Despite this, no boron was detected on the McB SAM and a significant reduction in SAM packing was observed (Au/S 87.58 ± 16.9) compared to the MBDAlk SAMs (Au/S 19.24 ± 1.53). Further to our earlier observation of decreased surface organisation demonstrated with low thickness and high hysteresis for the McB SAM, this confirms reduction in surface organisation on exchanging alkyne for aromatic functional groups. Given the low sensitivity of XPS for boron, low concentration of McB on the surface would provide limited PBA hence we would expect a significantly diminished signal (345).

Analysis of McB HR spectra reveals similar peak distribution to DcB as expected. For C1s HR spectra, at 288.1 eV, C=O peaks are visible with C-B at 286.1 eV and C=C of the triazole group at 285.7 eV. Peak separation Between C-B and triazole C=C (0.4 eV) is below the energy resolution of the instrument hence we cannot reliably confirm this chemical species. Similar peak distribution to the DcB SAM is observed however thus providing sufficient justification to the peak fitting. At 284.8 eV, a large peak is attributed to aromatic groups, C-C, C-S and C-N. Triazole N=N is shown in N1s HR spectra at 401.6 eV at 1:3 ratio with N-C and N-N peak at 399.9 eV. For

O1s, two peaks are observed corresponding to PBA hydroxyl groups at 532.9 eV and C=O at 531.5 eV. Weak signal is observed for S2p due to low concentration of McB on the surface similarly seen for DFC SAMs (*Fig. 58*). Unbound sulphur forms 34% of total sulphur species showing typical doublet at 162.5 eV (bound S2p2/3) and 163.7 eV (bound S2p1/2) and for unbound sulphur at 163.8 eV (S2p3/2) and 164.0 eV (S2p1/2) respectively (*Fig. 61*). Peak separation between bound S2p1/2 and unbound S2p3/2 (separation 0.1 eV) is below the energy resolution of the XPS instrument (0.5 eV) thus we cannot confirm reliably this species. Despite this, presence of unbound S2p1/2 provides sufficient evidence for presence of the unbound S2p3/2 peak given the expected S2p3/2 and S2p1/2 separation of 1.2 eV.

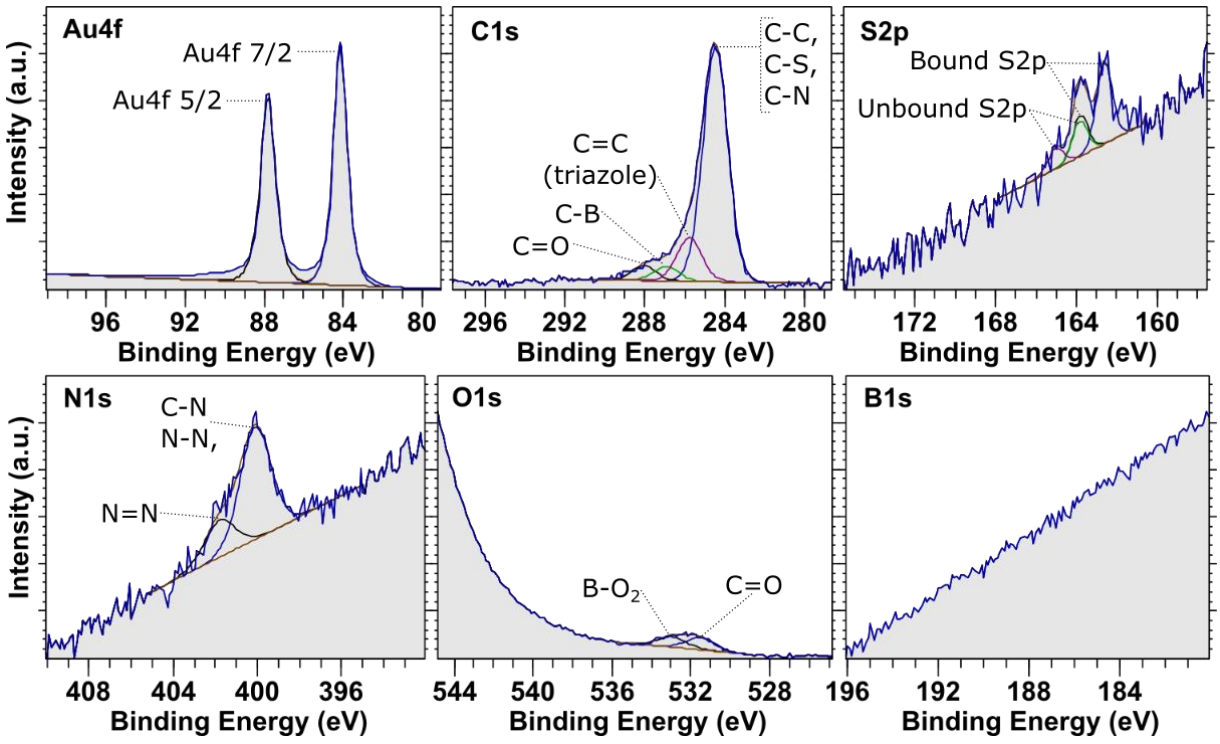


Fig. 61: HR XPS spectra of elements Au4f, C1s, S2p, N1s, O1s and B1s for McB SAM with displayed peak regions.

Comparatively, both DcB and McB are capable of SAM formation however, inclusion of terminal PBA groups reduces surface organisation for long chain (C_{10}) monomers seeing decrease in SAM packing from Au/S ratio 19.24 ± 1.53 for MBDAlk to 87.58 ± 16.9 for McB SAMs. With a significant drop in surface concentration of PBA we expect lower sensitivity of the McB SAM to glycan sensing given the 1:1 binding between PBA and saccharide unit. Furthermore, as the advancing angle shows a more hydrophobic angle (74.5 ± 2.0^{o}) than expected (≈60^{o}), we cannot confirm PBA hydroxyl groups are located at the SAM interface thus further

reducing potential glycan sensitivity. Interestingly, packing was only slightly reduced for DcB SAMs (Au/S 31.19 ± 1.78) compared to DTPAlk (Au/S 24.91 ± 0.80) with evidence for increased surface organisation provided by reduction in contact angle hysteresis (DTPAlk θ_{hys} 13.6^{O}, DcB θ_{hys} 9.7^{O}). For short chain (C_2) SAMs therefore, absence of alkane chain interactions can be accounted for by inclusion of terminal groups capable of providing inter-monomer association thus stabilising SAM formation. Conversely, inclusion of similar groups on long chain (C_{10}) SAMs disturbs chain interactions reducing surface organisation. Consideration should therefore be given to antagonistic chain-chain and terminal-terminal group interactions in the selection of SAM monomers for forming densely packed monolayers.

4.4 AzBA functionalisation of alkyne terminated SAMs via CuAAC reaction

As we have now established a method of producing SAMs of alkyne terminated monomers and developed a working CuAAC reaction in solution, we transferred this reaction to our alkyne SAMs DTPAlk, MBDAlk and DFC where we functionalised the surface with PBA via CuAAC reaction producing SAMs shown in *Fig. 62*. To produce PBA surface CuAAC reaction, alkyne terminated SAMs were

produced according to the method described in section 4.2. The CuAAC catalyst was prepared in DMF/ UHP H_2O (2:1) containing 0.1 mM Cu(II)SO_4, 0.2 mM (+)-sodium (L)-ascorbate (NaASC), 0.1mM Tris(benzyltriazolylmethyl)amine (TBTA) and 1 mM AzBA. This was produced by stepwise addition of 10 mM stock of Cu(II)SO_4 to 20 mM stock of NaASC in UHP H_2O producing a brown precipitate of Cu(I). On formation of this, TBTA was added from a 1 mM stock in DMF stabilising Cu(I) oxidation state after which AzBA was added from a 10 mM stock in DMF (400). This solution was degassed by sonication and purged with argon for 3 minutes before use. Alkyne-terminated SAMs were then immersed in 1 mL of this solution and protected from light before incubation for 24 hours on a rotary mixer under argon. The reaction was quenched and excess PBA and catalyst solution were removed from SAMs by sonication in HPLC grade methanol/ UHP H_2O (1:1) for 20 seconds followed by liberal rinsing with HPLC grade methanol. SAMs were then dried under argon stream and characterised by contact angle, ellipsometry and XPS. An associated error of 0.04 ± <0.01 nm was observed on varying refractive index (n) between 1.45 and 1.5 in ellipsometry modelling for DTPALk-AzBA and DFC-AzBA SAMs. For MBDAlk-AzBA SAMs associated error was 0.14 ± <0.01 nm for similar n variance of 1.45 – 1.5. Reported thickness was calculated using n=1.5. All SAMs were synthesised in duplicate with four measurement spots per sample for contact angle and ellipsometry

analysis. Reported error was calculated from standard deviation between measurement spots of all samples.

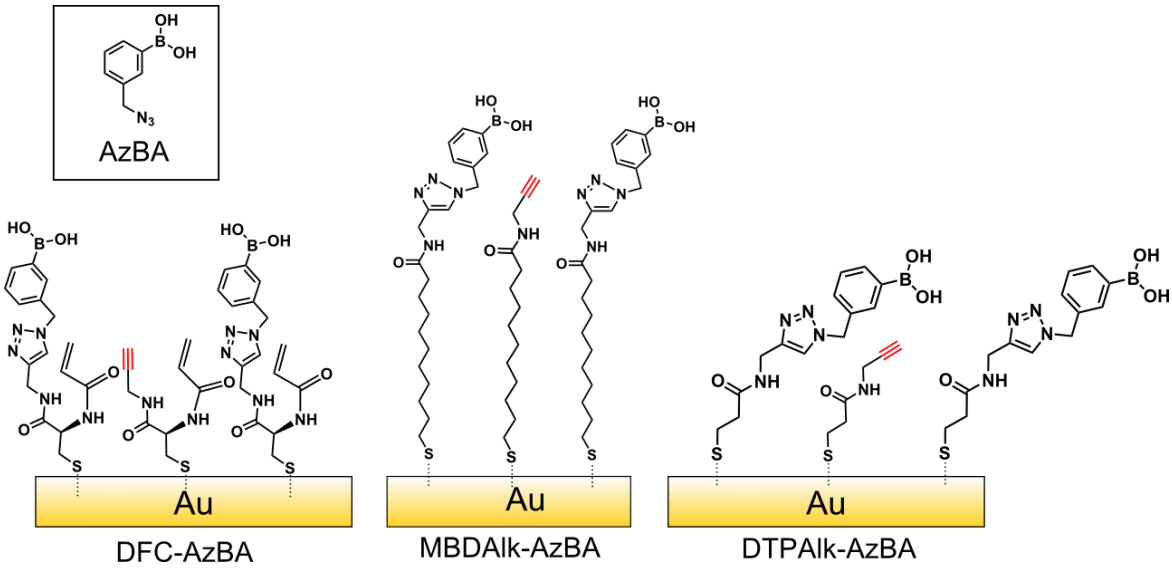


Fig. 62: Surface functionalisation of DFC, MBDAlk and DTPAlk with AzBA by CuAAC reaction. Unreacted alkynes are shown in red.

4.4.1 Surface characterisation of AzBA functionalised DTPAlk, MBDAlk and DFC SAMs via surface CuAAC reaction

Consistent with our earlier surface characterisation of alkyne and PBA terminated SAMs, ellipsometry, contact angle and XPS was used to establish surface properties including wetting, thickness and elemental composition. From ellipsometry derived thickness values shown in *Table. 13*, growth is observed from precursor monomers DTPAlk (0.40 ± 0.03 nm) and DFC (0.49 ± 0.04 nm) to 0.63 ± 0.03 nm and 0.69 ± 0.06 nm respectively. While

theoretical thickness is 1.77 nm for both SAMs, experimental thickness is closer to that observed for DcB SAMs (0.7 ± <0.01 nm) thus is consistent with a PBA expressing surface. As described for DcB, low observed thickness is ascribed to a combination of monomer tilt and parallel configuration of the aromatic PBA ring on the surface as previously reported (226,439). In addition, measurement of both unreacted alkynes and PBA groups averaged over a 1 mM light beam diameter in ellipsometry would serve to artefactually lower observed thickness (442). Furthermore, a reduction in advancing contact angle and hysteresis is observed between DTPAlk (θ_{adv} 78.6 ± 1.0^{o}, θ_{hys} 13.6^{o}) and post-AzBA functionalised DTPAlk-AzBA SAMs (θ_{adv} 71.4 ± 1.4^{o}, θ_{hys} 9.2^{o}). This is consistent with both terminal expression of PBA and surprisingly, an increase in surface organisation. However despite decrease, θ_{adv} remains higher than literature value of ≈60^{o} suggesting incomplete functionalisation (425,436). Coinciding with similar thickness growth to DTPALk-AzBA, DFC-AzBA additionally showed a similar advancing angle (θ_{adv} 73.3 ± 3.0^{o}) but increased hysteresis (θ_{hys} 16.9^{o}). While this again implies incomplete functionalisation it additionally shows increased surface disorder post-CuAAC reaction.

Table. 13: Contact angle and ellipsometry results for DTPAlk-AzBA, MBDAlk-AzBA and DFC-AzBA PBA functionalised surfaces by surface CuAAC reaction.

SAM	**Contact angle (°)**		**Ellipsometry thickness (nm)**	
	Advancing	Receding	Theoretical	Experimental
DTPAlk-AzBA	71.4 ± 1.4	62.2 ± 1.0	1.77	0.63 ± 0.03
MBDAlk-AzBA	67.2 ± 2.7	58.7 ± 2.3	2.64	2.54 ± 0.04
DFC-AzBA	73.1 ± 3.7	61.8 ± 3.0	1.77	0.69 ± 0.06

For MBDAlk-AzBA reacted surfaces, observed thickness (2.54 ± 0.04 nm) close to theoretical (2.64 nm) suggest successful AzBA functionalisation. This is also confirmed in the increased hydrophilicity (θ_{adv} 67.2 ± 3.0°) of the surface compared to MBDAlk SAMs (θ_{adv} 82.6 ± 2.3°) consistent with terminal PBA (425). Furthermore, while the hysteresis of MBDAlk-AzBA (θ_{hys} 8.5°) increased from the precursor SAM MBDAlk (θ_{hys} 5.7°), this value is still consistent with a homogenous surface (422).

To establish yield of surface CuAAC reaction over time, XPS analysis was performed on DTPAlk-AzBA, DFC-AzBA and MBDAlk-AzBA SAMs with timed reactions conducted for MBDAlk-AzBA. Unfortunately, DTPAlk-AzBA and DFC-AzBA were unable to quantitated due to a combination of contamination peaks on C1s,

O1s and N1s spectra. In addition DTPAlk SAMs show significant Cu2p emission at 932.2 eV and 951.9 eV (Cu2p3/2 and Cu2p1/2 respectively) attributed to strong copper contamination forming during CuAAC reaction (345,443). Unexpectedly, DFC showed far smaller Cu2p peaks at similar binding energy despite apparent lower surface organisation. Nonetheless survey spectra showed peaks corresponding to C1s, O1s, S2p, N1s and Au4f for both DTPAlk and DFC SAMs however no B1s was detected on either SAM.

If we consider our earlier observation of similar thickness between DTPAlk-AzBA (0.63 ± 0.03 nm) and DFC-AzBA (0.69 ± 0.06 nm) SAMs alongside similar advancing angle (DTPAlk-AzBA (θ_{adv} 71.4 ± 1.4^{O})(DFC θ_{adv} 73.3 ± 3.0^{O}) but significantly less SAM packing on DFC SAMs than DTPAlk (DTPAlk Au/S 24.91 ± 0.80) (DFC Au/S 77.70 ± 15.29). This might suggest a similar level of SAM organisation between DTPAlk and DFC but lower concentration of alkyne groups on DFC with these being spaced by adjacent acryloyl groups. The propensity to contaminate due to exposure of polar carbonyl groups was earlier proposed however this does not explain capacity of the DTPAlk SAM to chelate the Cu(I) catalyst compared to DFC nor MBDAlk that do not chelate Cu(I). From this we can assume the Cu(I) does not strongly bind to alkyne or alkene groups as a contaminating agent. Instead this suggests that despite high concentration of DTPAlk on the surface, this monolayer is loosely formed consistent with previous reports of

short alkanethiol SAMs (222,226). Through low organisation it is likely the Cu(I) is associating with the substrate therefore inhibiting the CuAAC reaction. For DFC however, branched groups prevent access to the substrate but presents lower concentration of functional alkyne groups thus limiting the reaction yield on the surface.

Given the agreeable thickness of the MBDAlk-AzBA SAM (2.54 ± 0.04 nm), this reaction was assumed successful thus was produced at 1, 4- and 18-hour intervals to establish the rate and yield of reaction on the surface. Reaction yields for MBDAlk-AzBA SAMs are shown in *Table. 14* as calculated from N/S ratios assuming 100% yield provides N/S ratio of 4:1. From this, the reaction demonstrated rapid progression reaching 45 ± 5% yield at 1 hour and plateauing at 4 hours (58 ± 4%) with negligible difference observed following 18 hours (56 ± 5%) reaction time with both yields within error limits.

Elemental composition was confirmed using XPS with survey spectra reporting C, N, O, S and Au peaks as expected with additional small Cu2p doublet at 932.2 eV and 951.9 eV Similar to Cu2p peaks observed on DFC XPS survey spectrum. All SAMs underwent liberal rinsing with UHP H_2O and HPLC methanol however, complete removal of residual Cu(I) appears difficult with Ciampi *et al* (2007) reporting similar Cu(I) trace issues on alkyne terminated SAMs. Washing samples with a basic solution of 0.05%

(w/v) ethylenediaminetetraacetic acid (EDTA) was suggested however this failed to remove all traces of Cu(I) (444). Examination of bound and unbound sulphur for MBDAlk-AzBA SAMs shows 24.1 ± 0.4% after 1 hour reaction increasing to 46.1 ± 3.4% at 4 hour reaction. To preserve SAM integrity and reduce thiol desorption, this washing step was not integrated to our method.

Table. 14: Observed yield of surface CuAAC reaction between AzBA and MBDAlk derived from N/S ratio.

CuAAC reaction time	N/S observed ratio	Yield (%)
1 Hr	1.80 ± 0.19	45 ± 5
4 Hr	2.33 ± 0.17	58 ± 4
18 Hr	2.25 ± 0.18	56 ± 5

Peak fitting for HR spectra of 18 hour reaction MBDAlk-AzBA C1s shows C=O species assigned to 288.4 eV with C-B as a small peak at 287.4 eV. At lower binding energy, the peak at 286.5 eV is assigned to triazole C=C and large peak at 285.2 assigned to C-C, unreacted C≡C and the aromatic ring (445). N=N species are ascribed to a small peak at 402.2 eV with C-N and N-N species assigned to 399.9 eV on N1s spectra. For O1s spectra, PBA hydroxyl groups are assigned to peak at 532.9 eV and C=O species

at 531.5 eV. Similarly to DcB SAMs, attenuation of boron is observed with only a small peak occurring at 192.2 eV assigned to PBA boron (345). Thiol species are observed as two doublets on S2p spectra corresponding to bound sulphur at 162.5 eV (S2p3/2) and 163.7 eV (S2p1/2) and unbound sulphur at 163.8 eV (S2p3/2) and 165 eV (S2p1/2) forming 45% of total sulphur. Peak separation between bound S2p1/2 and unbound S2p3/2 (separation 0.1 eV) is below the energy resolution of the XPS instrument (0.5 eV) thus we cannot confirm reliably this species. Despite this, presence of unbound S2p1/2 provides sufficient evidence for presence of the unbound S2p3/2 peak given the expected S2p3/2 and S2p1/2 separation of 1.2 eV. HR spectra for 18-hour reaction for MBDAlk with AzBA are shown in *Fig. 63*.

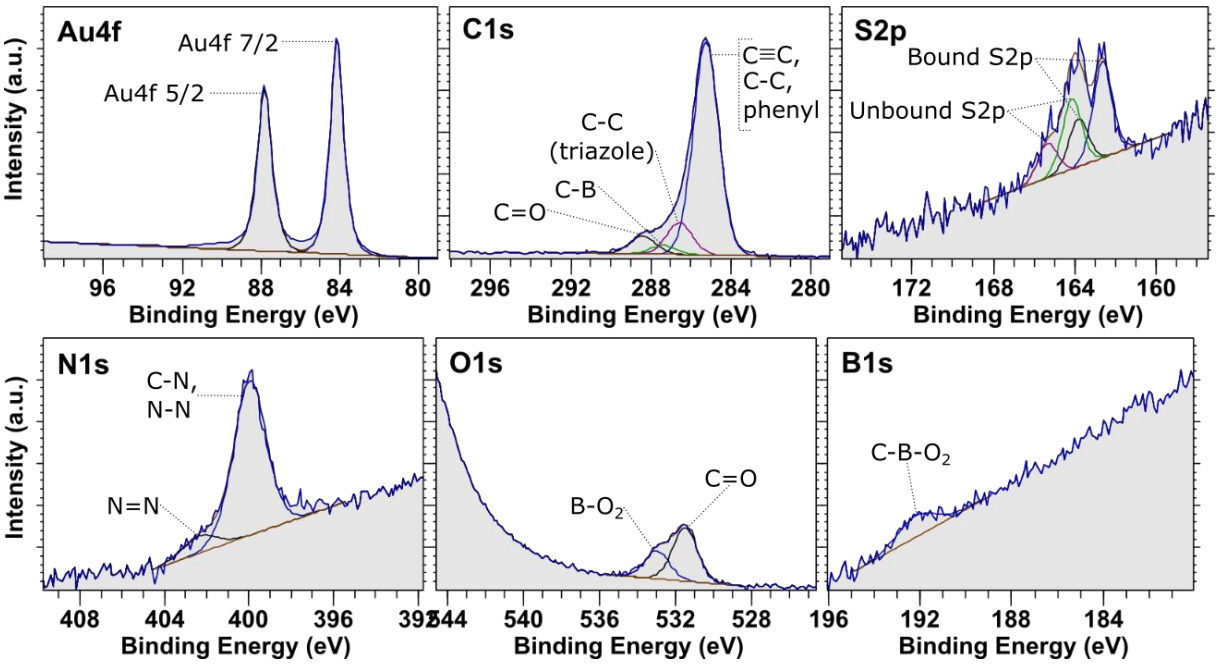


Fig. 63: HR XPS spectra of elements S2p, C1s, Au4f, N1s, B1s and O1s for 18-hour CuAAC reaction of MBDAlk SAM with AzBA with displayed peak regions.

4.5 Conclusion

As the foundation of molecular imprinting, production of highly organised and high density SAMs is an essential first step in surface functionalisation. In development and characterisation of various alkyne and PBA terminated SAMs we have shown that structure of backbone length and terminal groups significantly affects SAM organisation. Furthermore, we have demonstrated utility of the CuAAC reaction in functionalisation

of these surfaces as a rapid high yield reaction suitable for ligand immobilisation.

Comparison of our DTPAlk, MBDAlk and DFC SAMs shows that while each monomer will form SAMs, significant differences in surface organisation occur in both DFC and DTPAlk with DFC exhibiting low organisation and with lower surface concentration than DTPAlk. On the contrary, MBDAlk as expected produces densely packed SAMs as suggested by contact angle and ellipsometry thickness values. Furthermore, MBDAlk SAMs demonstrated high yield for surface CuAAC reaction with surface yield shown at 58 ± 0.04%. As yield was shown to plateau at 4 hours with no increase after 18 hours reaction time, this confirms the maximum practical yield of the surface CuAAC reaction for MBDAlk SAMs. Given the requirement for Cu(I)-alkyne intermediates to form for reaction progression, it is unlikely this can be improved where we expect reaction inhibition arising from loss of access between catalyst and reacting alkyne groups (251).

For preparation of defined saccharide binding surfaces, we have additionally described here the characterisation of two novel PBA-terminated monomers McB and DcB. Examination of these SAMs through ellipsometry, contact angle and XPS has shown increased surface organisation and packing of DcB over its unreacted counterpart DTPAlk imparted by addition of aromatic groups providing inter-monomer interaction. Conversely, McB SAMs

found their organisation interrupted by inclusion of PBA groups thus we have found modulation of both alkane backbone and terminal group to be an important consideration in the use of pre-functionalised SAM formation. With effective alkyne and PBA terminated SAM formation procedures developed, saccharide binding and surface imprinting of oligosaccharides can now be explored.

Chapter 5.

Saccharide probing of PBA-terminated SAMs and molecular imprinting of stachyose

Abstract: Continuing with our synthesised and characterised functional SAMs, in this chapter we will examine the application of these surfaces in saccharide binding and molecular imprinting. Providing sensitive real-time data collection, SPR analysis will be used to monitor binding events of mono and oligosaccharides thus confirming PBA-saccharide surface interaction. The application of alkyne-terminated SAMs to molecular imprinting will then be examined through development of a stachyose specific MIS. This will act as a proof of concept study for the utility of these clickable surfaces to oligosaccharide biosensor design.

5.1 Introduction

With the recognition of the importance of glycosylation in disease and its potential utility in biomarker discovery, there is a pressing need to develop increasingly sensitive and specific diagnostic technology for these complex biomolecules. As we have discussed in Chapter. 1, changes in the glycoproteome provide accurate reflections of cellular malignancy and disease however, current glycan profiling methods rely on clinically impractical or insensitive techniques such as mass spectroscopy (12,54), HPLC (60) or lectin affinity (153,156).

Providing real-time and label free monitoring of interaction kinetics, SPR is a highly suitable analytical platform for SAM biosensors. As discussed in Chapter 2 (section 2.5), SPR detects changes in produced surface plasmons of a metal film on total reflectance of *p*-polarised light in media of differing dielectric constants (364–366). A typical setup for analysis of alkanethiol SAM binding kinetics would see propagation of a stable surface plasmon on the SAM-Au substrate interrupted by binding of a ligand changing this plasmon wave hence producing a quantitative change shown in response units (RU) (*Fig. 64*)(446). Therefore, if we produce BA decorated binding pockets, on exposure to saccharide ligands, the dynamic BA-saccharide esterification would be witnessed *in-situ* with SPR, seeing ligand association followed by SAM regeneration as

the saccharide dissociates. Given the reported femtomolar sensitivity of SPR as described by Zhang *et al* (2013) in microRNA detection, SPR has the potential for ultrasensitive biomarker detection and has previously seen use in a number of sensitive glycan binding biosensor designs thus demonstrating its utility in saccharide detection (196,262,292,447).

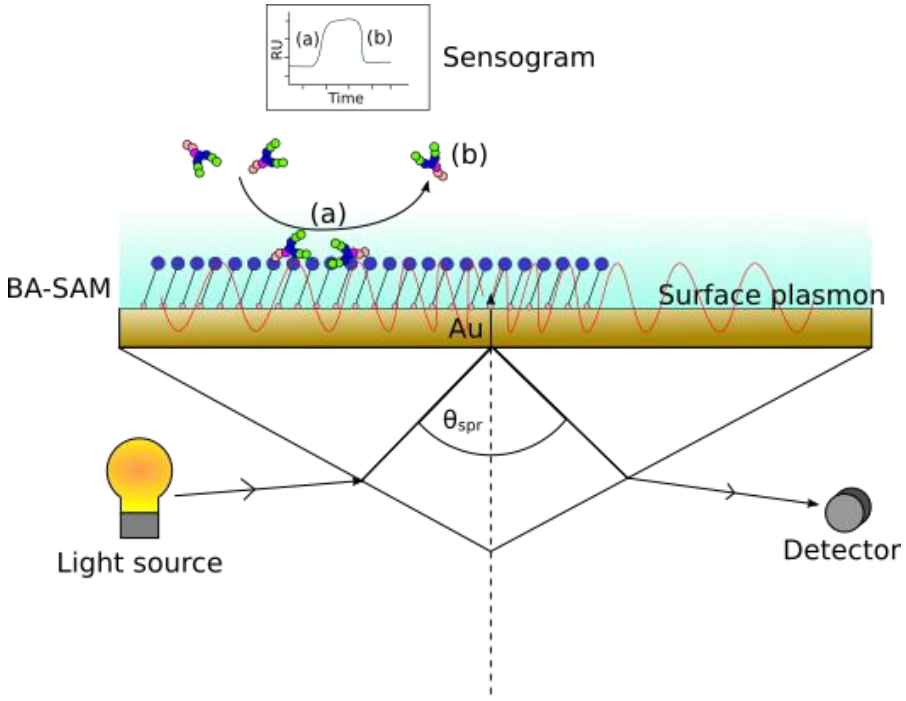


Fig. 64: Overview of SPR analysis of BA functionalised SAMs showing (a) saccharide binding producing increase in response units of SPR sensorgram and (b) dissociation of saccharide returning RU to baseline. Interruption to stable surface plasmon (red line) by saccharide binding produces quantitative changes in wave parameters *i.e.* intensity or phase of internally reflected light (366).

As we have now synthesised our various alkyne and PBA terminated SAM monomers and characterised these surfaces confirming their terminal functionality, our intention in this chapter now moves to attest their saccharide binding capability. Examination of XPS data of DcB and McB SAMs in chapter. 4 certifies PBA functionality thereby providing a defined saccharide binding surface for comparison to surface functionalised alkyne SAMs. Using DcB and McB SAMs we can determine dissociation constants (K_d) of PBA for simple monosaccharides and optimise pH requirements for BA-saccharide binding. Using this to inform following binding studies, binding can be examined for our AzBA CuAAC reacted SAMs confirming practicality of the CuAAC reaction in producing saccharide binding surfaces. As the final step, the utility of alkyne terminated SAMs for molecular imprinting will be examined as outlined in *Fig. 65*. To produce imprints, a pre-formed complex of stachyose with AzBA will be immobilised on our MBDAlk SAM via CuAAC reaction. After a set time interval, unreacted alkyne groups will be capped with addition of O-(2-Azidoethyl)heptaethylene glycol (AzOEG) forming an inert anti-fouling surface while templating immobilised stachyose. On removal of stachyose, a defined binding pocket will be left displaying a complimentary BA configuration specific for stachyose thus producing an imprinted surface.

5.1.1 Objectives

1. Optimise binding buffer for AzBA-saccharide complexation through pre-functionalised SAM McB with SPR.

2. Determine differences in saccharide binding depending on chemical composition of pre-functionalised and surface functionalised SAM monomers with SPR.

3. Characterise thickness growth of MIS formation using an AzBA-stachyose complex on MBDAlk SAMs by ellipsometry.

4. Probe for specificity of MIS for stachyose against structurally different and similar oligosaccharides using SPR.

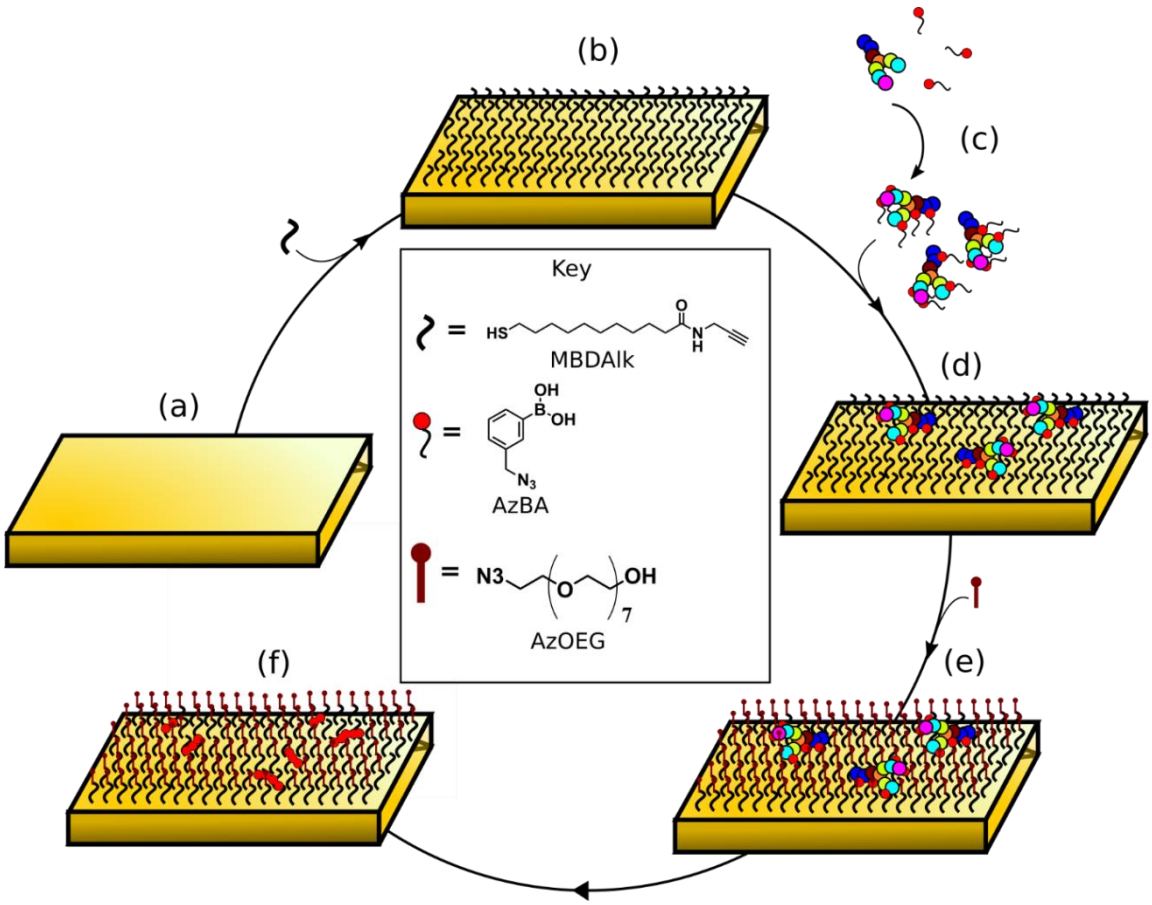


Fig. 65: Schematic of MIS preparation for stachyose. (a) Chemically clean Au substrate. (b) Formation of MBDAlk SAM. (c) Complexation of stachyose to AzBA. (d) CuAAC reaction immobilising AzBA-stachyose complex to MBDAlk SAM. (e) CuAAC reaction capping remaining alkyne groups with AzOEG. (f) Washing to remove stachyose revealing stachyose binding pocket decorated with complimentary BA moieties.

5.2 Saccharide binding of McB and DcB PBA terminated SAMs

While the affinity of PBA for monosaccharides in solution is well established, few studies have examined this interaction on a surface taking into account SAM chemical composition effect on PBA-saccharide esterification. A group of chemically similar short SAMs (C_1 – C_3 backbone length) have previously been studied however these failed to demonstrate the common binding pattern of fructose>galactose>glucose (161,389,448). Despite this, Chen *et al* (2007) observed significantly higher fructose binding on increasing carbon content of the SAM backbone from C_2 to C_3 attributed to reduction in SAM disorder with longer monomers. Similarly, we have discussed in Chapter 2 the impact of backbone length on SAM formation showing increased disorder in short (C_2) alkyne terminated SAMs and in long (C_{10}) PBA terminated SAMs.

In developing PBA functionalised MIPs, we first examined these differences in monosaccharide binding on our McB and DcB surfaces serving two functions. First, monosaccharide binding response of PBA SAMs confirms terminal functionality and provides opportunity for pH optimisation of the binding buffer. Second, comparison between PBA terminated and AzBA functionalised SAMs will allow observation of steric effects of dense packing of PBA groups on saccharide binding as we have established ≈50% CuAAC surface reaction yield of MBDAlk-AzBA

compared to full PBA coverage of McB and DcB SAMs. Given the evidence that mixed SAMs phase segregate to form islands of monomer species hence not truly mixing, using our surface functionalised SAMs might therefore provide a more accurate PBA spaced SAM where we expect more random expression of PBA groups (449–451).

5.2.1 Non-specific adsorption of monosaccharides to gold substrate or SAMs

Prior to undertaking saccharide binding studies, it was necessary to first establish non-specific saccharide adsorption to substrates at each stage of development and to produce an accurate control SAM. To do so, concentrations (3.125, 6.25, 12.5, 25 and 50 mM) fructose was injected (100 µL over 2.5 minutes) over four substrates: chemically clean gold substrate, MBDAlk and CuAAC functionalised MBDAlk with either benzyl azide (AzBEN) or pinacol protected AzBA (pinAzBA) (*Fig. 66*). Chemically clean Au surfaces and MBDAlk SAMs were prepared as per Chapter. 4 (section 3.2). AzBEN and pinAzBA functionalised SAMs were formed on MBDAlk SAMs via surface CuAAC reaction with 1 mM AzBEN or pinAzBA with CuAAC catalyst described in Chapter. 4 (section 4.4) as per similar method for AzBA CuAAC reaction. SPR running buffer and all saccharides were produced in 0.1 M ammonium acetate (AmAc) buffer pH 10.

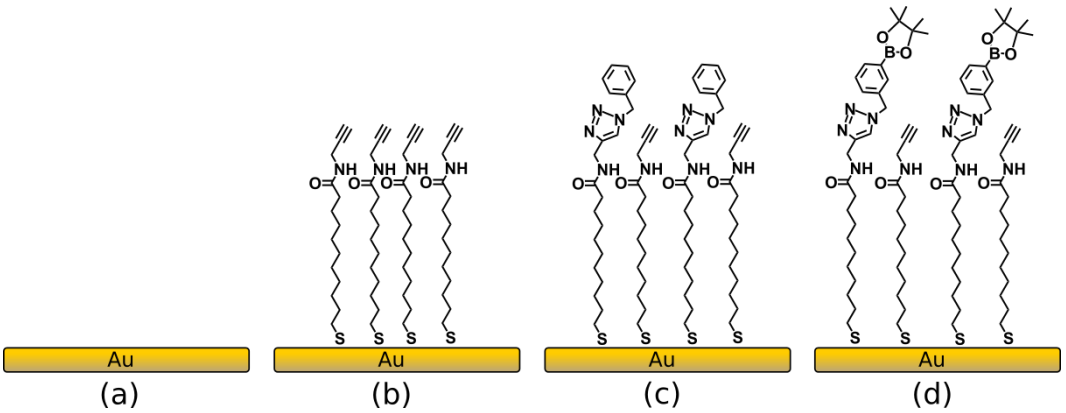


Fig. 66: Non-saccharide binding SAMs to establish non-specific adsorption. (a) Clean Au, (b) MBDAlk, (c) AzBEN and (d) pinAzBA. Surface CuAAC reaction assumed yield of ≈50% (based on AzBA CuAAC reaction yield, Chapter. 4, section 4.4.1) is reflected in AzBEN and pinAzBA.

To distinguish non-specific adsorption (NSA) from actual saccharide-PBA binding, the SPR response (RU) of both clean Au substrate and alkyne terminated SAMs was determined for fructose. While our XPS data (Chapter. 4) shows good surface organisation for DTPAlk and MBDAlk SAMs, less organisation was observed for McB and DFC SAMs. If we consider this alongside presence of potential surface defects *i.e.* domain boundaries, we cannot assume there is no exposed Au on the surface thus potential NSA sites (452). Furthermore, with the CuAAC surface reaction yield of ≈50%, exposed alkyne groups are inevitable in functionalised SAMs alongside benzene species provided by PBA.

To confirm interactions between saccharide and these groups are negligible, AzBEN and pinAzBA comparison to clean Au and MBDAlk will clarify any present NSA where we see a raised response (453,454). SPR response is shown in *Table. 15* with 50 mM fructose concentration shown in *Fig. 67*.

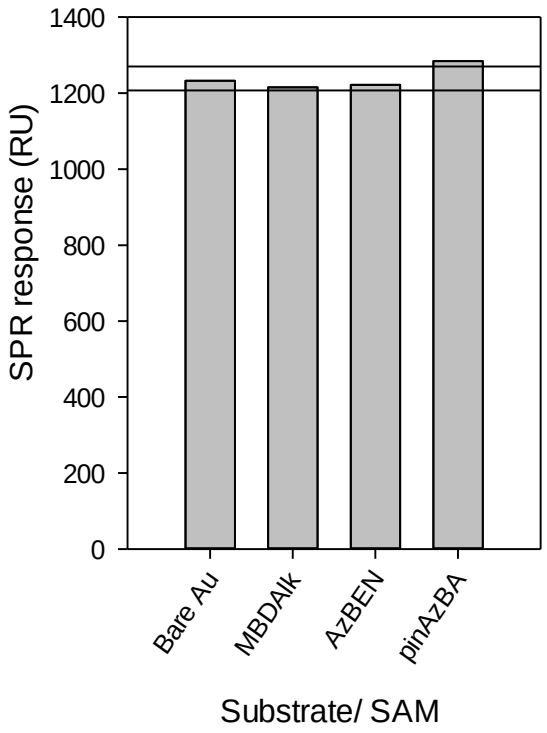


Fig. 67: SPR response of Substrate/ SAMs: bare Au, MBDAlk, AzBEN and pinAzBA to 50 mM fructose.

Table. 15: SPR response of Substrate/ SAMs: bare Au, MBDAlk, AzBEN and pinAzBA to fructose at varying concentrations.

Fructose concentration (mM)	**Bare Au**	**MBDAlk**	**AzBEN**	**PinAzBA**
3.125	82	78	77	94
6.25	160	153	154	174
12.5	314	303	306	337
25	616	609	607	651
50	1233	1216	1222	1285

Analysis of the SPR RU shown in *Table. 15* confirms no apparent NSA is occurring on MBDAlk or AzBEN functionalised SAMs with only bulk refractive index observed as indicated by linear growth of RU consistent with no binding. For the clean gold substrate, a small increase in RU compared to MBDAlk and AzBEN is observed corresponding to low NSA and within acceptable quantities even at high fructose concentrations (*Fig. 67*). Contrarily, pinAzBA demonstrates higher RU across all injections which, granted the high affinity of PBA for fructose, can be attributed to exchange between pinacol and fructose given the lability of PBA-pinacol in presence of fructose as previously described by Lee *et al* (2019) (455). With homogeneity in fructose binding between MBDAlk and AzBEN SAMs confirming low NSA, and to maintain similarity in our control surface compared to AzBA

functionalised, the AzBEN functionalised SAM was selected to act as our control for calculation of binding free from bulk refractive index.

As observed with data presented in *Table. 15*, irrespective of binding a change in response occurs caused by change in solution surrounding the surface referred to as bulk refractive index. In this case, the running buffer is replaced by buffer containing incrementally more concentrated fructose following injections manifesting large increase in bulk refractive index. For calculation of actual binding bulk refractive index must be accounted for achieved through synchronised running of both functional 'binding' surface and null 'non-binding' surface. Given only bulk refractive index is observed on null binding surfaces, deduction of this from functional surfaces allows calculation of binding exclusive of bulk refractive index.

5.2.2 pH optimisation of McB SAM for fructose binding

Following examination of NSA and selection of our control surface we then examined buffer pH requirements to improve the esterification between PBA and ligand. To study pH effect on surface PBA-saccharide esterification, an McB SAM was prepared in duplicate by incubation of a chemically clean gold substrate with 0.2 mM deprotected McB solution for 24 hours as per the method detailed in Chapter. 4 (section 4.3). To calculate binding

between SAM and saccharide void of bulk refractive change, an AzBEN SAM was prepared as outlined in section 5.2.1. and subjected to identical SPR run parameters.

SAMs of McB and AzBEN were subjected to SPR analysis where 100 µL of a series of fructose concentrations (3.125, 6.25, 12.5. 25 and 50 mM) in 0.1 M AmAc buffer at pH 7.4, 8.5 or 10 were injected over the SAM for 2.5 minutes producing SPR sensograms with an example shown in *Fig. 68*. As these experiments sole intention was to determine optimal pH binding, we did not explore low saccharide concentration (<3.125 mM) as all relevant conclusions could be extrapolated from higher fructose concentration SPR response. As discussed in section 1.3.3, boronic acids form a reversible covalent bond with saccharides which, unlike traditional immunoassay designs, will allow complete dissociation of the saccharide providing a re-usable sensor. Consequently however, no region of stable saccharide binding from which we can quantify binding will be observed post saccharide injection. Binding is instead only observed during injection of the saccharide over the surface with complete dissociation observed on exchange of saccharide solution for the original buffer (*Fig. 68*). During injection therefore, both saccharide binding and bulk refractive index will contribute to the observed RU. To isolate binding response, we must deduct bulk refractive index from the total response as produced by

exposure of a saccharide null binding surface to identical saccharide solutions.

To calculate dissociation constants for saccharide binding, SPR response at equilibrium (R_{equil}) of the AzBEN control SAM was deducted from R_{equil} of PBA functional SAM and plotted against concentration (C_s) of injected saccharide. This was then fit to a 1:1 Langmuir isotherm model by non-linear least squares regression (*Eq. 1*) using Sigmaplot, version 13.0 where R_{max} is maximum possible RU and K_d is the dissociation constant.

Eq. 1 $$R_{equil} = \frac{R_{max}[C_s]}{K_d + C_s}$$

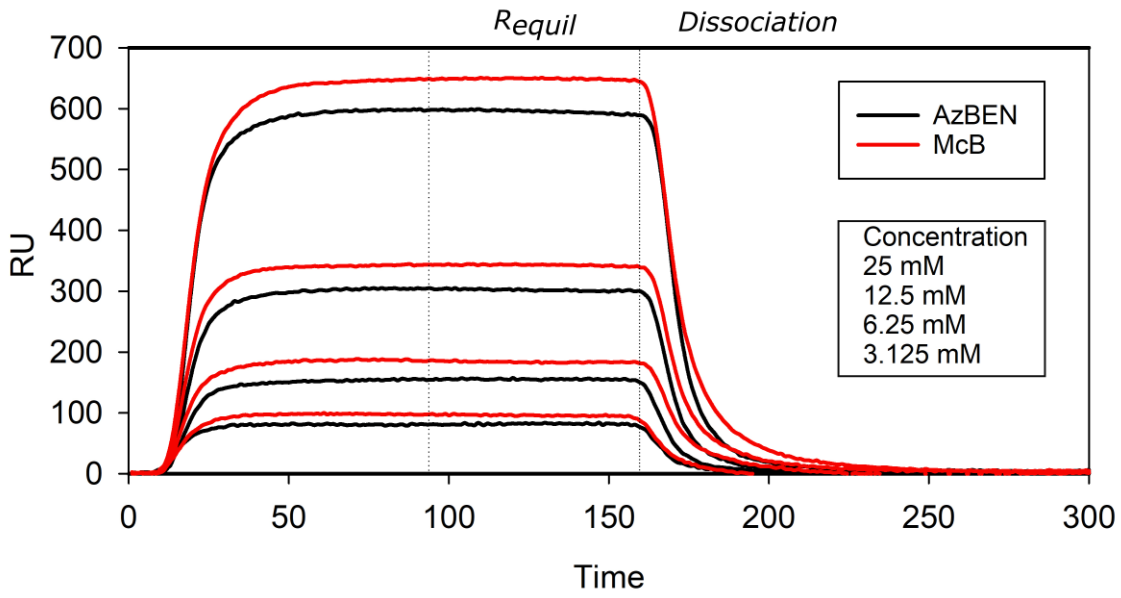


Fig. 68: Fructose SPR sensogram on the McB (black) and AzBEN control surface (red) using pH 10 AmAc buffer. No stable binding is observed during the dissociation phase of the sensogram. Binding is therefore quantified and K_D calculated from the stable region at equilibrium (Requil) where the number of association and dissociation events occurring are equivalent (456).

As observed in both AzBEN and McB SPR sensograms R_{equil} is achieved between 50-100 seconds during fructose injection. Deduction of AzBEN R_{equil} from McB R_{equil} produces binding response shown in *Fig. 69*. At pH 7.4 and 8.5, only small increases are observed at high concentrations of fructose while pH 10 shows markedly higher binding across low and high concentrations. With a pKa of 8.5, PBA is expected to transition to tetrahedral

anionic configuration over pH 8.5 increasing affinity for saccharides hence we expect increase in RU (457). Surprisingly, only negligible binding increase was seen on transition to pH 8.5 from 7.4 despite several studies reporting using pH between 7.4 and 8.5 for their binding buffers (196,262,389,458,459) and with optimal PBA-fructose binding being previously determined at pH 10.4 (460).

Counter to this however, XPS analysis has previously shown buffers at pH >9 slowly deplete surface boron through cleavage of B-C bonds with rapid cleavage observed at pH 12, a process not seen in free PBA in solution (425). As derived from binding response shown in *Fig. 69*, K_d and R_{max} values for fructose binding are shown in *Table. 16* showing increased affinity of McB for fructose at pH 10 (K_d 4.96 ± 0.4 mM, R_{max} 76.10 ± 1.6 RU) compared to pH 8.5 (K_d 18.05 ± 6.4 mM, R_{max} 43.44 ± 6.6 RU) and pH 7.4 (K_d 9.90 ± 4.3 mM, R_{max} 25.62 ± 3.9 RU).

Lower affinity of McB for fructose at pH 8.5 with K_d 18.05 ± 6.4 mM compared to pH 7.4 (K_d 9.90 ± 4.3 mM) is attributed to poor curve fitting (R^2 0.87) arising from low sensitivity of McB SAM to fructose at pH 7.4. Despite poor fitting for calculation of K_d, the higher R_{max} of pH 8.5 more accurately reflects higher affinity of McB for fructose at pH 8.5 over pH 7.4. Significantly higher binding occurred at pH 10 consistent with previous affinity studies (460). These findings are however contradictory

to the numerous studies employing pH 7-8.5 buffer in PBA based sensors as previously discussed. To preserve surface boron and given the higher K_d and R_{max} values, pH 10 was determined suitable for further saccharide binding experiments where we expect minimal boron depletion given the short exposure time of the surface to the buffer.

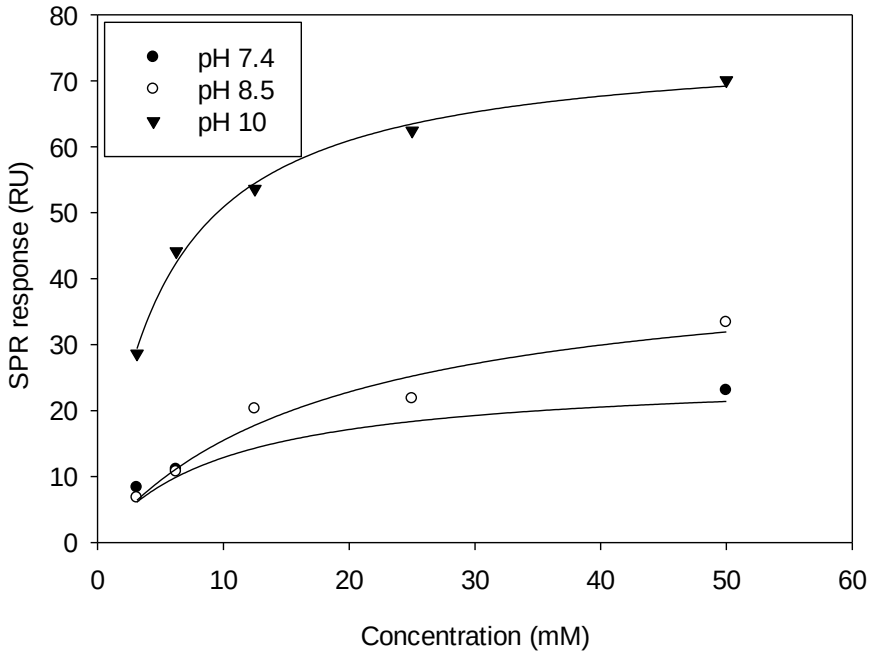


Fig. 69: Binding response of McB SAM to fructose at varying buffer pH.

Table. 16: Binding kinetics of McB to fructose at varying pH.

pH value	K_d (mM)	R_{max} (RU)	R^2
7.4	9.90 ± 4.3	25.62 ± 3.9	0.87
8.5	18.05 ± 6.4	43.44 ± 6.6	0.94
10	4.96 ± 0.4	76.10 ± 1.6	0.99

5.2.3 Comparison of DcB and McB SAMs for monosaccharide binding

With an established working binding pH, we then examined the difference in saccharide binding between McB and DcB SAMs. As discussed in Chapter 4, surface organisation is increased in DcB SAMs as compared to McB as observed with contact angle hysteresis of 9.7^{O} and 11^{O} and XPS derived Au/S ratios of 31.19 ± 1.78 and 87.58 ± 16.9 respectively. From this we might presume increased affinity of the DcB SAM for saccharides over McB given less PBA presence on the McB SAM. To investigate chemical composition of SAM monomer impact on saccharide binding we prepared SAMs of McB and DcB as per methods described in Chapter. 4 (section 4.3) and an AzBEN functionalised MBDAlk SAM as per section 5.2.1. SAMs were subject to SPR analysis as described in section 5.2.1 in AmAc buffer pH 10 (0.1 mM). Three monosaccharides: glucose, galactose and fructose were injected at concentrations: 3.125, 6.25, 12.5, 25 and 50 mM and binding

response at R_{equil} of AzBEN SAM deducted from PBA functional SAM. This was plotted against monosaccharide concentration to produce graphs shown in *Fig. 70*.

Table. 17: Monosaccharide binding kinetics for McB and DcB SAMs

	Saccharide	**K_d (mM)**	**R_{max} (RU)**	**R^2**
McB	Glucose	3.5 ± 1.4	53.3 ± 4.9	0.82
	Galactose	9.9 ± 2.1	99.4 ± 7.4	0.97
	Fructose	2.8 ± 0.6	150.7 ± 6.4	0.95
DcB	Glucose	2.2 ± 1.3	64.4 ± 7.1	0.60
	Galactose	3.3 ± 1.3	83.3 ± 7.8	0.81
	Fructose	8.5 ± 1.5	226.1 ± 12.9	0.98

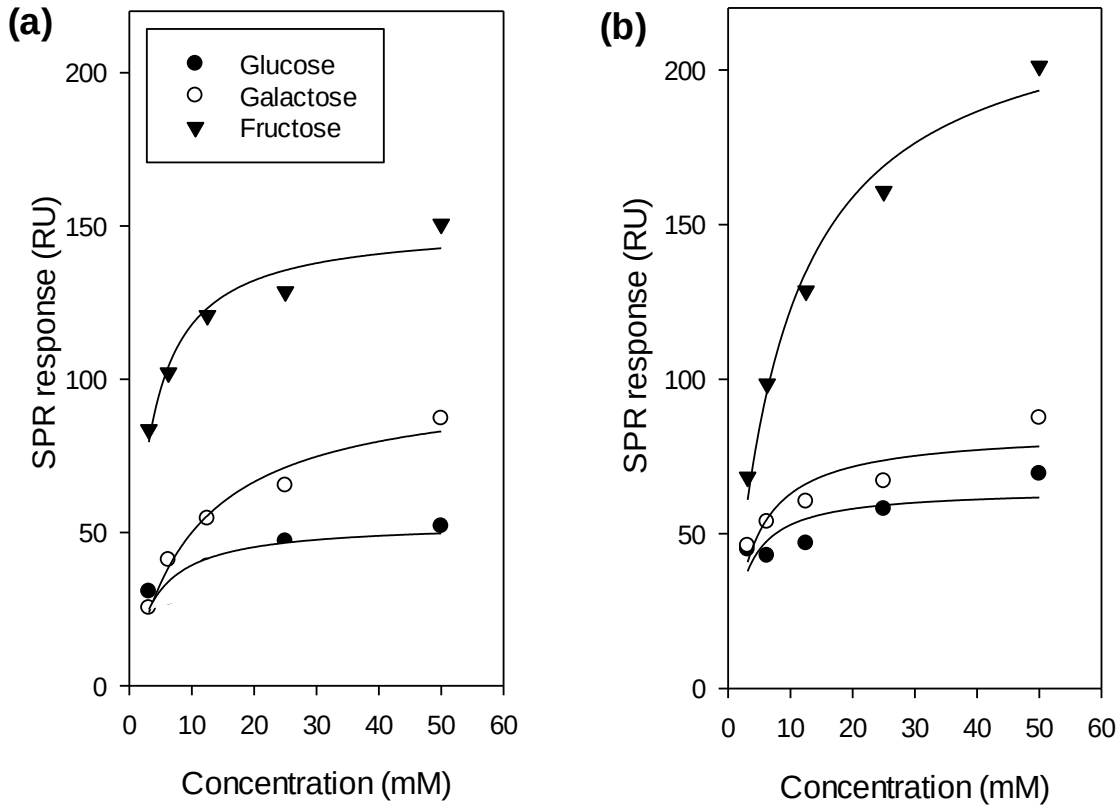


Fig. 70: SPR monosaccharide binding response curves for (a) McB and (b) DcB SAMs.

Examination of binding curves shown in *Fig. 70* shows similar binding response between glucose and galactose at concentrations between 3.125 mM and 50 mM. Alternatively, higher fructose binding is observed for McB over DcB until 12.5 mM where DcB binding is higher than McB. Consistent with PBA-monosaccharide affinity following the order fructose>galactose>glucose, this trend is seen across both McB and DcB SAMs however, this trend is not reflected in K_d values attributed to low sensitivity of McB and DcB SAMs to low concentrations of glucose and galactose.

With low R_2 values for DcB glucose (R^2 0.60) and galactose (R^2 0.81) and for McB glucose (R^2 0.82), we must consider the inaccurate calculation of K_d from these binding curves (*Table. 17*). As we expect consistent low sensitivity to glucose and galactose we can presume also consistent inaccuracy of curve fitting for these saccharides thus repeating these experiments was deemed unnecessary. Nonetheless, galactose R_{max} for DcB and McB suggest higher capacity of both SAMs for galactose (R_{max} ≈91.4 ± 8.1 RU) over glucose (R_{max} ≈58.9 ± 5.5 RU) attributed to higher furanose content of galactose providing increased availability of PBA binding sites (461,462).

Comparison of fructose binding between McB and DcB SAMs shows an interesting difference notably, the higher affinity of the McB SAM (K_d 2.8 ± 0.6 mM) over DcB (K_d 8.5 ± 1.5 mM). However, a reversal of this trend is observed for R_{max} with McB (R_{max} 150.7 ± 6.4 RU) showing lower capacity than DcB (R_{max} 226.1 ± 12.9 RU). Returning to XPS analysis in Chapter. 4 (section 4.3.1), McB (Au/S ratio 87.58 ± 16.9) was shown to form less packed monolayers than DcB (Au/S ratio 31.19 ± 1.78). We therefore expect a higher concentration of PBA on the DcB surface which translates here as higher fructose binding capacity as expected. Notwithstanding, McB shows higher affinity suggesting lower PBA surface concentration enhances affinity. Given the inhibitory effects of dense packing of functional groups on ligand binding

as previously reported, this implies steric hinderance arising from dense packing of PBA groups of DcB reduces affinity for fructose while the sterically free PBA groups on McB more readily bind fructose (414,457,463)

To compensate for steric hinderance inhibiting binding between SAM and ligand, mixed SAMs are typically designed to provide spacing between functional groups. For larger ligands such as antibodies, lectins or glycoproteins, inclusion of spacer monomers markedly improves sensitivity and specificity (229,464,465). As determined by Bonanno & DeLouise (2006), in biotin-streptavidin biomolecule surface functionalisation, biotin surface coverage >57% presents steric crowding effects reducing streptavidin immobilisation. In doing so, potential sensitivity of the final biosensor is reduced thus emphasising the requirement to minimise steric hinderance to improve ligand binding (466). For PBA terminated surfaces, Matsumoto *et al* (2013) found inclusion of 1:1 alkanethiol spacer: functional monomers showed highest sensitivity to glucose in their biosensor design however no comparison was made to pure PBA terminated surfaces instead relying on 1:1, 1:4 and 1:25 SAM mixtures (467). Alternatively, several groups have examined pure PBA monolayers finding good sensitivity but ignore steric effects on ligand binding despite the potential for sensitivity improvement (389,468,469). Comparing our results, this data

suggests a trade-off in SAM organisation where densely packed SAMs reduce affinity but compensate for this in increased binding capacity. Conversely, approaching less organised SAMs reduces binding capacity but sees an increase in affinity. Regarding biosensor design, careful control of SAM organisation is therefore a necessary step in optimisation depending on the target biomarker. For instance, quantifying a prognostic marker for disease at high concentration would benefit from high binding capacity. Detection of diagnostic biomarkers at low concentration would however, require less capacity but requires markedly higher affinity sensors to detect low levels of biomarker.

5.3 AzBA surface functionalised DTPAlk and MBDAlk response to monosaccharide and oligosaccharide binding

For development of our molecular imprinting technique, we must first ensure the CuAAC reaction produces saccharide responsive PBA surfaces. As examined in Chapter. 4 (section 4.4), ellipsometry and contact angle data suggest successful AzBA functionalisation of our DFC, DTPAlk and MBDAlk SAMs seeing increase in surface thickness and decrease in contact angle consistent with PBA presence. XPS interpretation however was

only able to be completed on MBDAlk-AzBA SAMs due to contamination peaks convoluting spectra on AzBA functionalised DTPAlk and DFC SAMs. Furthermore, in XPS analysis no boron was detected on any DTPAlk-AzBA or DFC-AzBA functionalised SAMs suggesting excessively low surface reaction yield. Given the propensity of smaller alkanethiol SAMs to hold lower surface organisation and consistently high atmospheric contamination for DFC and DTPAlk SAMs described in Chapter. 4, we therefore expect significant difference in functional capability between MBDAlk and DTPAlk or DFC based SAMs (225,226,230,470). As DFC consistently showed excessively low surface organisation (contact angle hysteresis 14.1^{O}, XPS Au:S ratio 77.7 ± 15.29), this SAM was not used in our monosaccharide binding studies. As this study will be used for comparison to our imprinting, glucose, galactose, and fructose will be used to determine binding of AzBA functionalised SAMs alongside two oligosaccharides stachyose and melezitose (*Fig. 71*.).

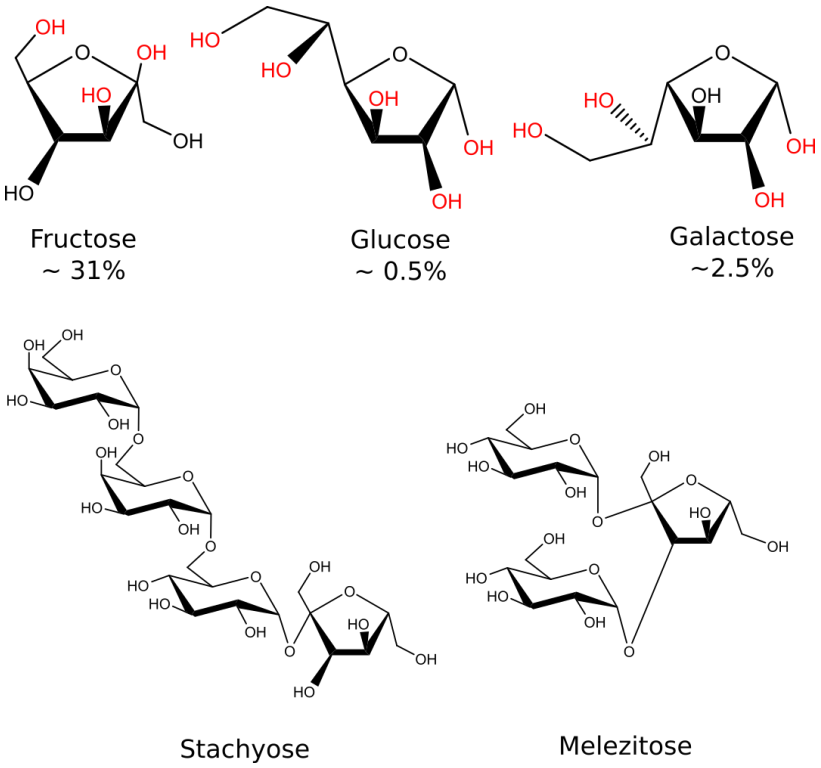


Fig. 71: (*top*) Furanose configurations of monosaccharides used in binding studies. Hydroxyls participating in BA esterification are shown in red with relative percentage furanose given beneath structures. (*bottom*) structures of oligosaccharides stachyose and melezitose used in binding studies. Pyranose and furanose configurations of saccharide units are assumed according to previous saccharide conformational studies. Stachyose composition Gal(α1-6)Gal(α1-6)Glc(α1-2β)Fru. Melezitose composition Glc(α1-3)Fru(β2-1α)Glc. (75,76,161).

To investigate DTPAlk and MBDAlk AzBA functionalised SAMs for saccharide binding we first produced SAMs of DTPAlk and MBDAlk on chemically clean gold substrates as described in Chapter. 4 (section 3.2). These were then subject to surface CuAAC reaction with AzBA via method described in Chapter. 4 (section 4.4) yielding SAMs shown in *Fig. 72.*

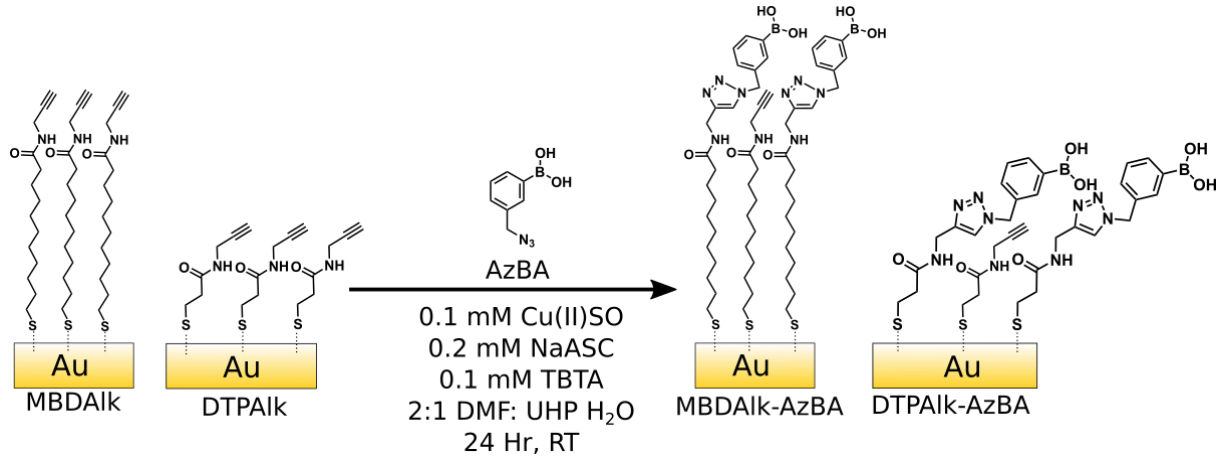


Fig. 72: Surface CuAAC reaction scheme for AzBA functionalisation of DTPAlk and MBDAlk SAMs assuming incomplete surface functionalisation.

AzBA functionalised DTPAlk and MBDAlk SAMs were then analysed for saccharide binding with SPR where 100 µL of monosaccharide glucose, galactose and fructose (concentrations: 3.125, 6.25, 12.5, 25 and 50 mM) and oligosaccharides stachyose and melezitose (concentrations: 1.56, 3.125, 6.25, 12.5 and 25 mM) were injected over 2.5 minutes in 0.1 AmAc buffer, pH 10.

Binding response was produced by deduction of R_{equil} from AzBEN control of equivalent saccharides from R_{equil} of functionalised DTPAlk and MBDAlk SAMs producing binding response void of bulk refractive change. Binding response was then plotted against saccharide concentration producing SPR response curve shown in *Fig. 73* with which K_d was calculated for the AzBA functionalised MBDAlk SAM. As response was either too low or not reflecting the 1:1 Langmuir isotherm used to calculate K_d, fitting was not provided for the AzBA-functionalised DTPAlk SAM.

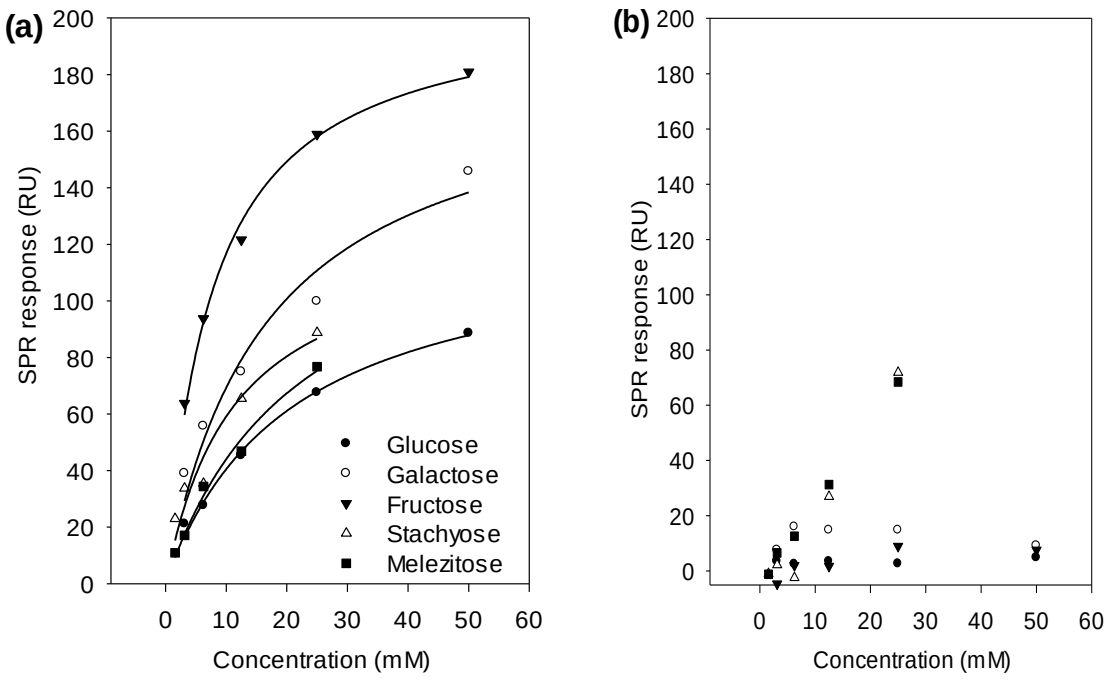


Fig. 73: SPR binding RU for (a) AzBA functionalised MBDAlk SAM and (b) AzBA functionalised DTPAlk SAM.

Initial examination of MBDAlk-AzBA and DTPAlk-AzBA SAMs presents a stark difference in saccharide binding capacity between these surfaces in that DTPAlk-AzBA shows a markedly low affinity for saccharide binding compared to MBDAlk-AzBA. Consistently low monosaccharide binding RU for AzBA-DTPAlk SAM suggests exceptionally low PBA surface presence with binding only observed at high concentrations of stachyose (12.5 mM, 65.4 RU, 25 mM, 88.7 RU) and melezitose (12.5 mM, 46.8 RU, 25 mM, 76.7 RU). Given the higher concentration of potential PBA binding sites on larger saccharides we can expect a low surface concentration of PBA groups to produce higher relative RU than for monosaccharide counterparts explaining response seen for these oligosaccharides, but low response seen for monosaccharides.

As previously discussed in Chapter 4.2.1, the low surface organisation of DTPAlk as derived from contact angle hysteresis (13.6^{O}) and low thickness 0.4 ± 0.03, theoretical 0.73 nm) was expected to affect functional capability through inhibition of Cu(I) acetylide intermediate formation. XPS analysis confirmed low functional capability demonstrated by excessive atmospheric contamination, no detected boron and a large copper contamination in survey spectra for AzBA functionalised DTPAlk SAMs thus verifying low CuAAC surface reaction yield. Furthermore, low thickness (0.63 nm ± 0.03, theoretical 1.77 nm)

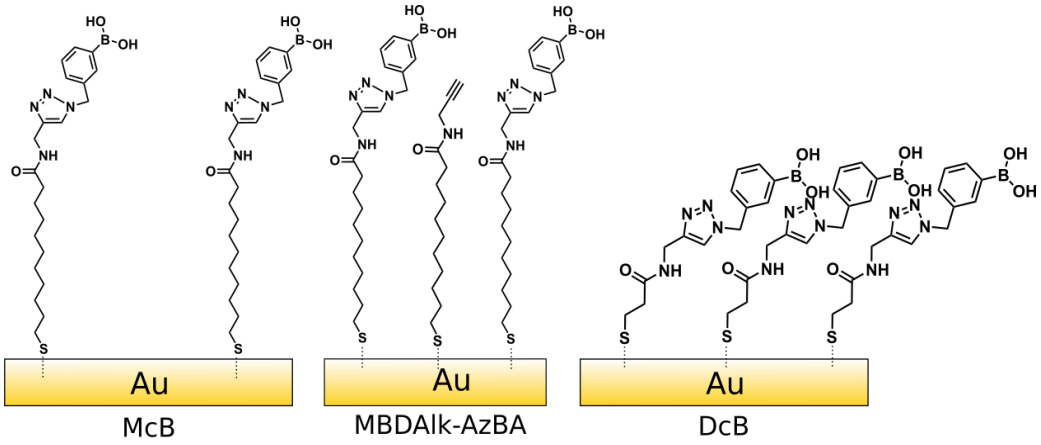
was also observed while an improvement in contact angle hysteresis (9.2^{O}) was attained suggesting growth and small improvement in surface organisation. However, lack of B1s emissions and apparent insensitivity to saccharide binding seen in SPR response confirms low functionality of this AzBA-DTPAlk SAM suggesting poor response to the surface CuAAC reaction. If we consider short alkanethiol SAMs propensity for atmospheric contamination and low surface organisation (216,222,380) coupled with significant copper chelation, this low reaction yield might arise from predisposition of Cu(I) to associate between SAM monomers preferentially over alkyne groups thus providing source of surface contamination and inhibiting CuAAC reaction (471,472). From this we can conclude unsuitability of our short alkanethiol SAM for surface CuAAC reaction.

Table. 18: Saccharide binding kinetics for AzBA functionalised MBDAlk and DTPAlk SAMs

	Saccharide	K_d (mM)	R_{max} (RU)	R^2
MBDAlk-AzBA	Glucose	20.7 ± 3.2	124.2 ± 8.7	0.99
	Galactose	16.6 ± 5.2	184.2 ± 24.2	0.94
	Fructose	7.7 ± 0.7	206.8 ± 6.4	0.99
	Stachyose	11.3 ± 4.9	125.8 ± 25.1	0.91
	Melezitose	22.6 ± 6.2	143.5 ± 23.0	0.98
DTPAlk-AzBA	Unable to calculate			

Contrary to the DTPAlk SAM, AzBA functionalised MBDAlk produced well-formed binding curves across all saccharides in *Fig. 73a*. These follow the typical fructose (K_d 7.7 ± 0.7 mM) >galactose (K_d 16.6 ± 5.2 mM) >glucose (K_d 20.7 ± 3.2 mM) pattern as expected (161). Additionally, the MBDAlk-AzBA SAM displays significantly higher R_{max} values (with the exception of fructose) than McB (R_{max} glucose 53.3 ± 4.9, galactose 99.4 ± 7.4) and DcB (R_{max} glucose 64.4 ± 7.1, galactose 83.3 ± 7.8) (*Table. 18, Table. 17*). The observed higher affinity of the MBDAlk-AzBA SAM for fructose over galactose and glucose stems from the higher affinity of PBA for furanose saccharide configurations over pyranose. Referring back to *Fig. 71*, fructose exists in furanose

form (~31%) in significantly higher concentration than galactose (furanose ~2.5%) and glucose (~0.5%) thus producing the affinity pattern fructose>galactose>glucose (473-475).



	McB	MBDAlk-AzBA	DcB
XPS ratio Au/S	87.58 ± 16.9	16.63 ± 0.83	31.19 ± 1.78
Fructose K_d	2.8 ± 0.6	7.7 ± 0.7	8.5 ± 1.5
Fructose R_{max}	150.7 ± 6.4	206.8 ± 6.4	226.1 ± 12.9
PBA/ thiol coverage	100%	56%	100%

Fig. 74: (top) Comparison of McB, MBDAlk-AzBA and DcB SAMs assuming (*left to right*) low to high concentration of surface PBA with increased packing of surface groups. (*bottom*) Elemental Au/S ratios for each SAM as derived from XPS with affinity and capacity for fructose binding shown below.

Further to our earlier observation that densely packed SAMs show lower affinity but higher binding capacity than loosely

packed SAMs arising from steric hinderance, as observed for fructose binding between DcB and McB SAMs; Affinity and capacity of the MBDAlk-AzBA (K_d 7.7 mM ± 0.7, R_{max} 206.8 ± 6.4) is consistent with values seen for DcB (K_d 8.5 mM ± 1.5, R_{max} 226.1 ± 12.9) suggesting similar PBA surface concentration of MBDAlk-AzBA with DcB (*Fig. 74*). If we consider the MBDAlk-AzBA SAM has approximately double the concentration of monomers than DcB (Au/S ratios MBDAlk-AzBA 16.63 ± 0.83, DcB 31.19 ± 1.78) but only 56% AzBA functionalisation, this confirms similar concentration of surface PBA.

Despite having similar PBA concentration to DcB, the MBDAlk-AzBA SAM shows significantly higher binding capacity of glucose (R_{max} 124.2 ± 8.7) and galactose (R_{max} 184.2 ± 24.2) than both DcB (R_{max} glucose 64.4 ± 7.1, galactose 83.3 ± 7.8) and McB (R_{max} glucose 53.3 ± 4.9, galactose 99.4 ± 7.4) SAMs. If we consider the spatial arrangement of PBA on the MBDAlk-AzBA SAM, organisation of the AzBA at the surface might take two routes: random distribution with even spacing between PBA groups or island formation of concentrated regions of PBA. In the first instance, steric hinderance is reduced through even spacing between PBA groups while in the second, PBA islands will present sterically free edges. Conversely, for DcB a more uniform packing is expected providing an abundance of PBA binding sites but restricting conformationally unfavourable binding.

While we have demonstrated steric hinderance affects fructose affinity for PBA, this effect is observably more pronounced for glucose and galactose. We can therefore assume a requirement for a degree of freedom in the target PBA group to allow inexpedient saccharide conformation binding as found in glucose and galactose. Alleviation of dense packing of PBA groups in MBDAlk-AzBA SAM (whether through even spacing or island formation) demonstrates this well producing significantly higher binding capacity than for similarly organised DcB. The use of mixed SAMs has been pursued elsewhere to reduce steric hinderance at the surface however, phase segregation of monomers reduces effectiveness of these methods. Alternatively, the CuAAC reaction presented here achieves reduction in steric effects with the potential for further modification to improve saccharide affinity (228,467,476,477).

In addition to monosaccharide binding, stachyose and melezitose binding to AzBA functionalised MBDAlk SAM is shown in *Fig. 73a* with binding affinity shown in *Table. 18*. Affinity for stachyose was observably higher than for melezitose with respective K_d values at 11.3 ± 4.9 and 22.6 ± 6.2 mM while the R_{max} remained similar (stachyose 125.8 mM ± 25.1 RU, melezitose 143.5 ± 23.0). This higher affinity is expected given the increased multivalency of the PBA-stachyose binding arising from additional participatory diols along the stachyose chain.

As the composition of these oligosaccharides contain an abundance of PBA binding sites, we expect increased affinity compared to monosaccharides. The majority of saccharide units however remain in pyranose configuration aside from stachyose reducing end fructose while melezitose would present pyranose configuration of reducing glucose thus reducing affinity (478). Furthermore, while pyranose-PBA binding for galactose and cellobiose (Glc(b1-4)b-Glc) has previously been described (*Fig. 75a*), this interaction depends on specific stereochemical configurations of saccharide units. In addition, α1-6 glycosidic linkage between galactose units on stachyose inhibit PBA esterification at 1,2 position leaving only 3,4 position. Esterification of PBA at fructose 2,3 will also be inhibited leaving space for 1,3 *cis*-diol formation only (*Fig. 75b*)(167,479).

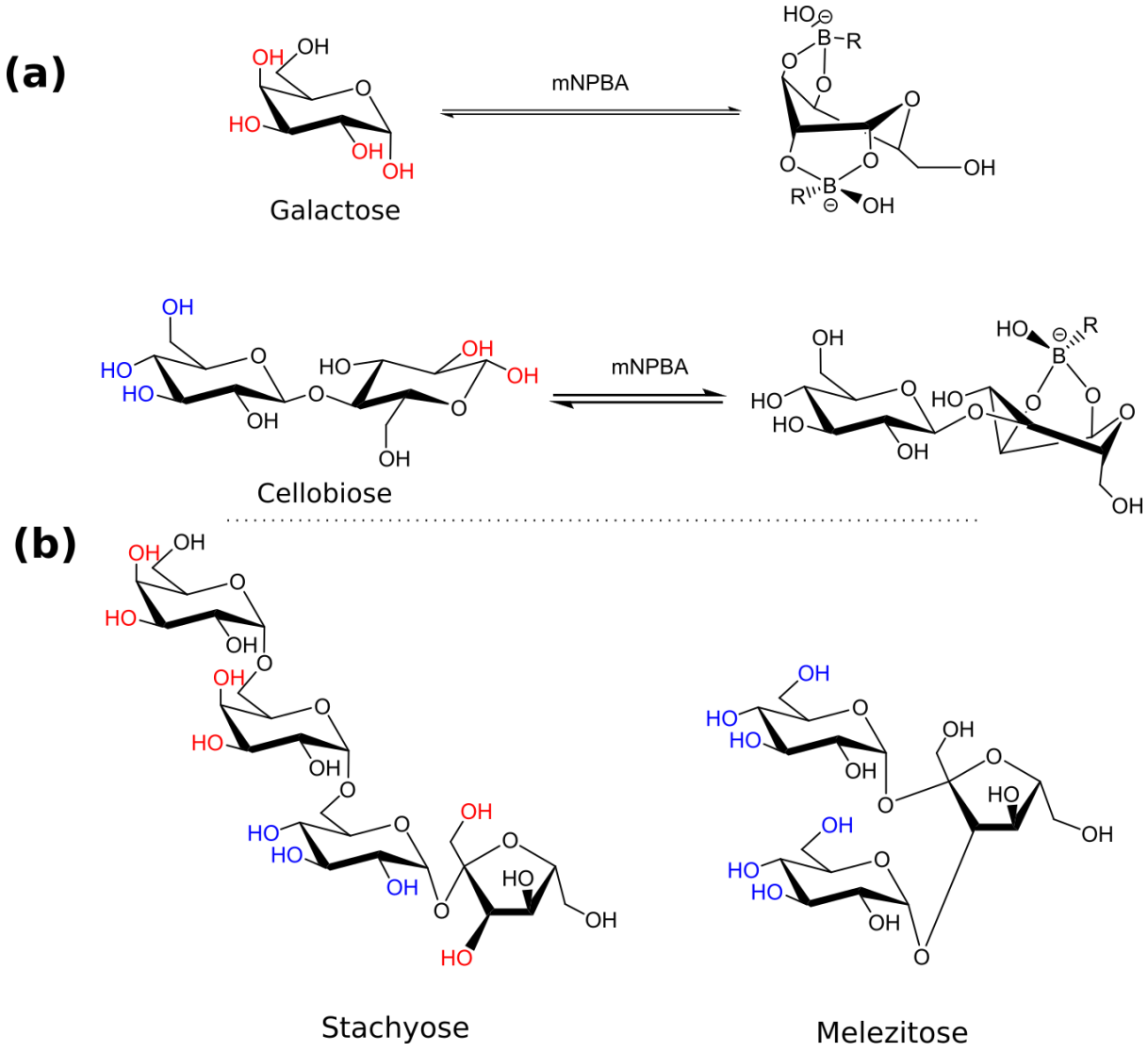


Fig. 75: (a) Interaction of nitro(phenyl) boronic acid (mNPBA) with pyranose configurations of galactose and cellobiose with involved hydroxyls shown in red. Possible hydroxyl interactions with benzoboroxole are shown blue. [image adapted from (479)]. (b) Structures of stachyose and melezitose with expected PBA interacting hydroxyls shown in red as derived from (167,479). Benzoboroxole binding sites are shown in blue (480).

Interruption of PBA esterification is particularly pronounced for melezitose seeing both 2 and 3 position hydroxyls occupied by glycosidic bond for fructose and 1 position hydroxyl on both glucose units. If we consider the expected PBA-cellobiose interaction determined by Nicholls & Paul (2004) (*Fig. 75a*), free hydroxyl is essential at the 1 position for PBA binding thus lowering affinity of melezitose hence we can assume the majority of PBA interaction likely arises from glucofuranose 3,4 hydroxyl groups. Alternatively, benzoboroxoles have demonstrated binding at the 3,4 and 4,6 diol positions through which we might assume limited binding at these positions with PBA.

With consideration for potential PBA binding sites, K_d of stachyose and melezitose (22.6 mM ± 6.2) reflect the loss of specific hydroxyl groups to glycosidic linkage. If we compare the K_d of fructose (7.7 ± 0.7 mM) and galactose (16.6 ± 5.2 mM) to stachyose (11.3 ± 4.9 mM), despite stachyose containing one fructose and two galactose units we see lower affinity than for fructose but higher affinity than seen for galactose on the AzBA-MBDAlk SAM. Further to this, the comparable affinity of melezitose (22.6 ± 6.2 mM) to glucose (20.7 ± 3.2 mM) despite increased multivalency of binding sites reflects loss of participating diols in the SAM-saccharide interaction.

Through comparison of both AzBA functionalised short DTPAlk and long MBDAlk SAMs, a clear distinction is drawn in the

functional capability hence usability in MIS design. Excessively low monosaccharide binding was observed for the DTPAlk-AzBA SAM attributed to copper chelation and rapid contamination as observed for both DTPAlk and DTPAlk-AzBA SAMs. Conversely, MBDAlk-AzBA responds well to the surface CuAAC reaction reaching high yields after 1 hour and producing strong saccharide binding for both mono and oligosaccharides despite stereochemical inhibition with larger saccharides. Following this we will now examine molecular imprinting based on our MBDAlk SAM to induce selectivity for stachyose in SPR analysis and to improve sensitivity where we develop multivalent stachyose binding pockets.

5.4 Development of stachyose specific MIS

Following our saccharide binding studies on AzBA surface functionalised SAMs, our next objective was to develop a molecular imprint for stachyose. In doing so, this serves as a proof of concept for this technology in selective oligosaccharide detection for future glycan biosensor adaption. As discussed in Chapter 1, section 1.2.3, with aberrant glycosylation recognised as a diagnostic and prognostic cancer biomarker, we must develop new selective glycan recognition platforms to appropriately provide clinical application. As we

have now developed a saccharide sensing surface in our AzBA functionalised MBDAlk SAM, we now move to produce selectivity in our surfaces as required by any clinical applications. As the MBDAlk SAM showed higher surface organisation, functional capability and saccharide response, our imprinting procedure will use only the MBDAlk SAM and exclude DTPAlk and DFC from further study. Our design can be broken down according to four main steps. In the first, standard MBDAlk SAMs expressing terminal alkyne groups will be produced (*Fig. 76a*). In the second step, a stachyose-AzBA complex kindly provided by Dr Stefano Tommasone will be immobilised to these MBDAlk surfaces via the CuAAC reaction (*Fig. 10b*). Following this an inert anti-fouling layer will polymerised to remaining alkyne by addition of Az-OEG to the reaction vial utilising the available CuAAC catalyst from earlier AzBA CuAAC reaction (*Fig. 76c*). In the fourth step, removal of the stachyose template via washing will reveal complimentary pocket to stachyose decorated with reciprocal PBA groups thus producing a stachyose specific binding pocket.

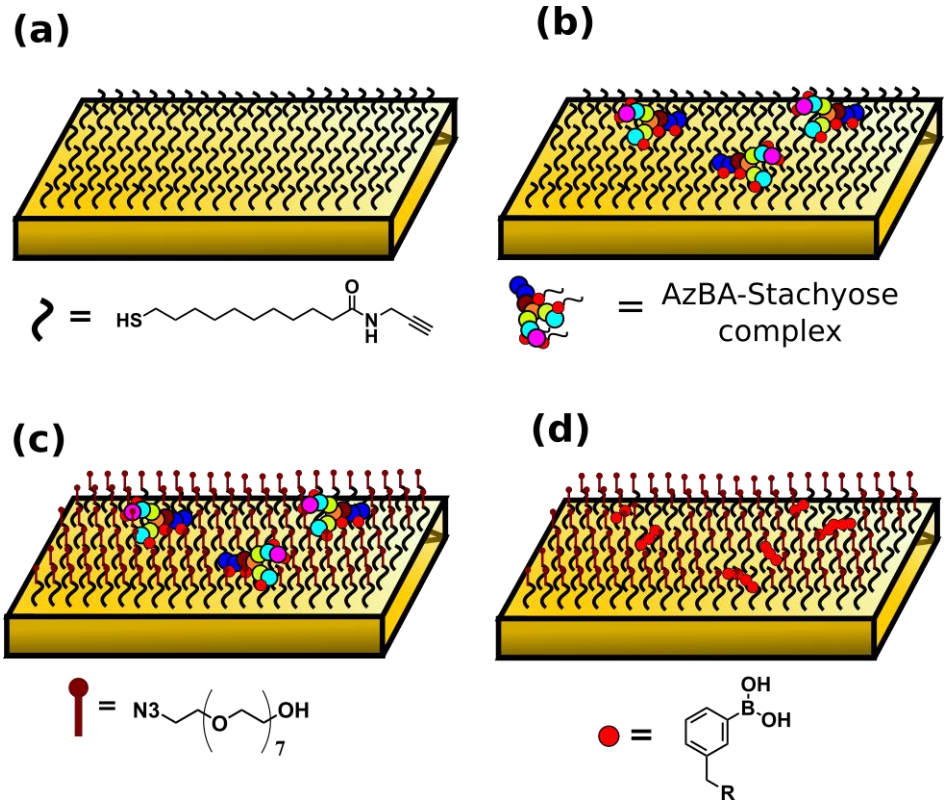


Fig. 76: Schematic for stachyose selective MIS design. (a) MBDAlk SAM presenting terminal alkynes. (b) CuAAC reaction immobilising AzBA-stachyose complex on MBDAlk SAM forming complimentary PBA-stachyose motif. (c) CuAAC reaction of remaining alkyne groups with Az-OEG providing both pocket shape and an anti-fouling surface. (d) Removal of template stachyose yielding complimentary PBA-stachyose selective binding pocket.

5.4.1 AzOEG functionalisation of MBDAlk SAM via CuAAC reaction

As a prerequisite to development of this MIS for use with biological media and as a clinically relevant biosensor, NSA of other biological constituents *i.e.* protein, nucleic acid, metabolites *etc* must be minimised. A common approach to prevent this is to coat a surface in polyethylene glycol (PEG), a well characterised protein-resistant compound thereby imparting biocompatibility to a surface and resisting NSA (262,409,481). Prior to application with our MIS design, we prepared a heptaethylene glycol-terminated monolayer by surface CuAAC reaction of MBDAlk SAM with AzOEG producing the SAM shown in *Fig.* 77. MBDAlk SAMs were prepared as per method described in Chapter. 4 (section 4.2.2). AzOEG functionalisation was completed by immersion of MBDALk SAM in 1 mL pre-made AzOEG/ CuAAC catalyst solution containing AzOEG (1 mM), Cu(II)SO_4 (0.1 mM), NaASC (0.2 mM) and TBTA (0.1 mM) in DMF/ UHP H_2O (2:1).

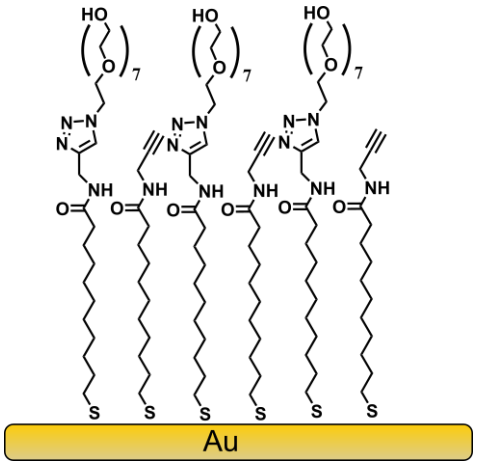


Fig. 77: AzOEG functionalised MBDAlk SAM via CuAAC reaction assuming similar ≈57% yield to AzBA functionalisation.

To study the NSA of saccharides to the AzOEG SAM, SPR analysis was used to plot response of stachyose and melezitose (concentrations 1.56, 3.125, 6.25, 12.5, 25 mM) and mono and disaccharides: fructose, cellubiose and palatinose (6.25 mM only) to the AzOEG SAM using SPR run parameters described in section 5.2.1. Shown in *Fig. 78* is the binding response of the AzOEG monolayer calculated by deduction of the AzBEN R_{equil} control SAM from the R_{equil} of AzOEG-MBDAlk SAM.

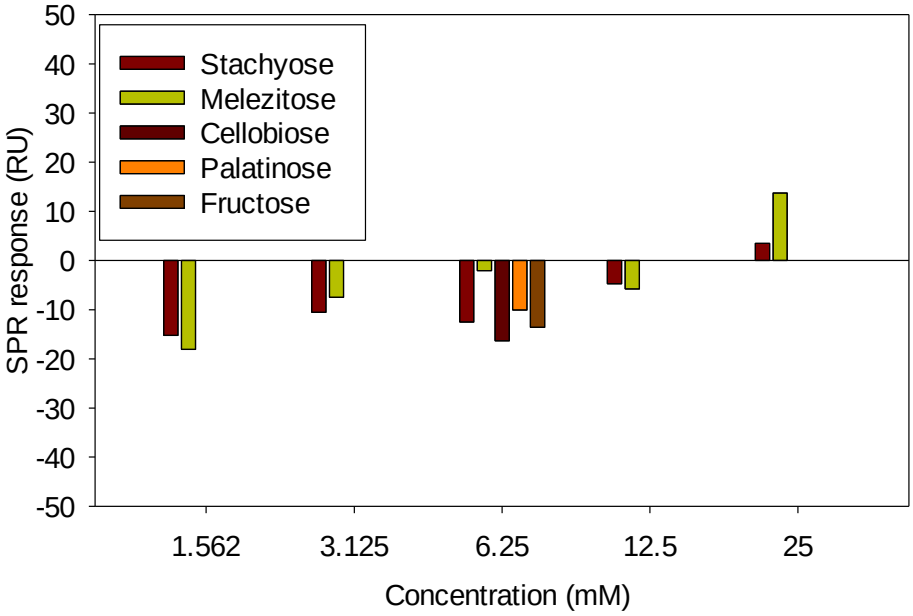


Fig. 78: Binding response of the AzOEG-MBDAlk SAM to different mono and oligosaccharides.

At concentrations between 1.56 mM and 12.5 mM a negative binding response is observed with concentrations 1.56 – 6.25 mM averaging -12.9 ± 3.5 RU. This increases to -5.2 ± 0.8 RU at 12.5 mM and returns a positive binding response at 25 mM for both stachyose and melezitose. Accounting for the accepted limit of detection for SPR at <5 RU, the negative binding response unexpectedly suggests low binding to the AzBEN SAM (482). This suggests low level NSA of saccharides to our control SAM which is reduced on exchange of terminal benzene groups for heptaethylene glycol. As we expect heptaethylene glycol to prevent NSA hence, we expect no SPR response to saccharides on

this surface, this confirms suitability of the AzOEG layer for capping remaining alkyne groups following AzBA-stachyose complex immobilisation. Being resistant to saccharide binding, this molecule is suitable for producing the binding pocket to induce saccharide selectivity in our MIS (409,481).

5.4.2 Proof of concept: Molecular imprinting of stachyose

With an NSA resistant monolayer and evidence for saccharide binding by AzBA functionalised SAMs established, we then sought to produce a molecular imprint of the oligosaccharide stachyose. If we review all SPR studies so far, it is evident that saccharide discrimination is impossible by random expression of PBA groups thus to achieve saccharide discrimination, we must design our SAMs around the target ligand. Several groups have approached saccharide selectivity via molecular imprinting seeing selective MIPs produced for various mono and di saccharides (195,483–486), oligosaccharides (487,488) and glycoproteins (292,489) on various substrates. While a significant number of selective saccharide MIPs have been produced, none have so extensively used the CuAAC reaction for both PBA functionalisation and binding pocket formation. In only using this reaction, our MIS would allow for a fully customisable surface (provided azide functional ligands are available) and producing high yield reaction between SAM and target ligand.

Furthermore, while we only explored BA functional groups, additional binding partners could easily be integrated to this design given the simplicity of the MIS schematic and stability and biocompatibility of the CuAAC reaction.

To produce our MIS, we followed the strategy outlined in *Fig. 76* using the MBDAlk SAM as an alkyne expressing monolayer further to our earlier discussion in section 5.3. Complexation of stachyose with AzBA was performed by Dr Stefano Tommasone through suspension of AzBA and stachyose in anhydrous dioxane/ acetonitrile (6:1) which was stirred at 90 ^{O}C for 24 hours with molecular sieves (3Å) to remove H_2O formed during this condensation reaction producing the AzBA-stachyose complex. In immobilisation of the stachyose-AzBA complex, a complimentary PBA motif specific for stachyose would be layered onto the MBDAlk SAM imparting selective binding for the saccharide pattern: Gal(α1-6)Gal(α1-6)Glc(α1-2β)Fru. Increased selectivity could then be attained by reacting remaining alkyne terminal groups with AzOEG thereby surrounding the immobilised AzBA-stachyose complex. On removal of the stachyose, a unique PBA decorated print would remain surrounded by AzOEG chains forming a binding pocket.

Prior to saccharide binding studies, we first optimised the incubation time of the AzBA-stachyose complex immobilisation on the SAM before proceeding into AzOEG capping. MBDAlk SAMs were

prepared as per Chapter. 4 (section 4.2.2) which were then immersed in 1 mL pre-made CuAAC catalyst solution (0.05 mM $Cu(II)SO_4$, 0.1 mM NaASC, 0.05 mM TBTA, 2:1 DMF/ UHP H_2O) containing 0.5 mM stachyose-AzBA complex provided by Dr Stefano Tommasone. Prior to use, CuAAC catalyst/ stachyose-AzBA complex solution was purged with argon for 3 minutes. Following immersion of MBDAlk SAMs in CuAAC/ complex solution, reaction vials were purged with argon and covered from light to prevent degradation of the NaASC and oxidation of the Cu(I) to non-catalytic Cu(II). SAMs were then incubated on a rotary mixer for timed intervals of 1, 4, 8 and 24 hours at room temperature. At these intervals, SAMs were rinsed briefly with HPLC grade methanol to preserve stachyose-AzBA complex and the thickness was measured by ellipsometry. Following ellipsometry and with complex still immobilised on the surface, these SAMs were then immersed in 1 mL AzOEG solution containing AzOEG (0.5 mM), $Cu(II)SO_4$ (0.05 mM), NaASC (0.1 mM) and TBTA (0.05 mM) in 2:1 DMF/ UHP H_2O, argon purged for 3 minutes. These were protected from light and allowed to react for 24 hours on a rotary mixer at room temperature. Post incubation, all SAMs were briefly rinsed with HPLC methanol before taking thickness measurements by ellipsometry thus confirming AzOEG addition to the surface. SAMs were then sonicated in 2 mL UHP H_2O for 30 seconds before placing in fresh 2 mL UHP H_2O and placing on a rotary mixer for 30 minutes allowing stachyose-AzBA complex to dissociate. These were then rinsed

liberally with UHP H_2O before taking final post-wash thickness measurements by ellipsometry. For each SAM therefore, three ellipsometry measurement sets, taken at each stage of MIS formation were produced allowing direct observation of layer growth following subsequent surface reactions. Thickness values are shown in *Table. 19*. An associated error of 0.16 ± 0.03 nm was observed on varying refractive index (n) between 1.45 and 1.5 in ellipsometry modelling for each stage of imprinting with thickness reported calculated from n=1.5. Reported error is calculated from standard deviation between measurement sets.

Table. 19: Thickness measurements of each stage of imprinting: complex only (pre-AzOEG), pre-wash (stachyose present) and post-wash (stachyose removed). Thickness values produced from ellipsometry.

surface reaction time	**Theoretical thickness: 2.64 – 3.12 nm**	**Theoretical thickness: 4.72 nm**	
	Complex only (nm)	MIS pre-wash (nm)	MIS post-wash (nm)
1 Hour	1.96 ± 0.06	3.04 ± 0.10	2.87 ± 0.16
4 Hour	2.04 ± 0.12	2.91 ± 0.28	2.78 ± 0.13
8 Hour	2.09 ± 0.07	2.45 ± 0.02	2.28 ± 0.05
24 Hour	2.24 ± 0.02	2.71 ±0.07	2.55 ± 0.05

Dependent on the orientation the oligosaccharide takes on immobilisation to the surface we can expect the thickness to vary between 2.64 and 3.12 nm (*Fig. 79*). Low thickness of complex only SAMs was observed averaging 2.08 ± 0.11 nm. Being lower than expected, several factors *i.e.* monomer tilt, low CuAAC reaction yield, averaging of thickness within the light beam *etc.* have likely served to artefactually reduce the measured thickness thus, all measured ellipsometry is suggestive of successful immobilisation but cannot be used to definitively

prove it. Nonetheless, the measured ellipsometry thickness values provide valuable insights to the monolayer growth which, interpreted together with SPR saccharide probing studies will provide compelling evidence to successful AzBA-stachyose immobilisation.

Despite low thickness, monolayer growth is observed over precursor MBDAlk SAMs previously shown at 1.81 ± 0.04 nm but lower than for previous MBDAlk-AzBA SAMs at 2.54 ± 0.04 nm. Thickness growth suggests successful CuAAC reaction however the lower than MBDAlk-AzBA thickness suggests lower yield. Given the lower concentration of AzBA-stachyose used (0.5 mM) compared to AzBA (1 mM) this was expected. In addition, as thickness measurements are taken as an average over a 1 mm diameter spot, unreacted alkynes will serve to artefactually reduce measured values (442). As we expect PBA groups to be grouped around immobilised stachyose instead of spaced out as assumed for AzBA-MBDAlk SAMs, thickness of complex only SAMs would be reduced further. Nonetheless, growth is observed at longer time intervals confirming reaction progression.

To form a complimentary binding pocket to stachyose, AzOEG was added to the reaction mixture with the complex still immobilised to the surface ensuring only surrounding free alkyne groups participate. Ellipsometry measurements taken before washing removal of stachyose from the complex encompass

thickness of SAM, complex and AzOEG. For pre-washed MISs, thickness is again lower than expected given the addition of the long AzOEG chain however it is well established that polyethylene glycol chains can adopt collapsed conformations explaining low thickness (481,490). Addition of AzOEG after 1 hour of complex immobilisation displays highest thickness (3.04 ± 0.10 nm) compared to other intervals suggesting little complex was bound to the surface. On addition of AzOEG, competition for alkyne units would likely favour AzOEG being smaller and more flexible than AzBA-stachyose thus well inhibiting further complex immobilisation. Small decrease at 4 hours to thickness 2.91 ± 0.28 nm suggests small increase in complex yield at the surface. At 8 hours the lowest thickness values (2.45 ± 0.02 nm) compared to other intervals are attributed again to increased complex immobilisation confirmed by higher thickness of respective complex only SAM. The increase in thickness at 24 hours is ascribed to dissociation of the AzBA-stachyose complex prematurely revealing the binding pocket and allowing AzOEG immobilisation within this pocket.

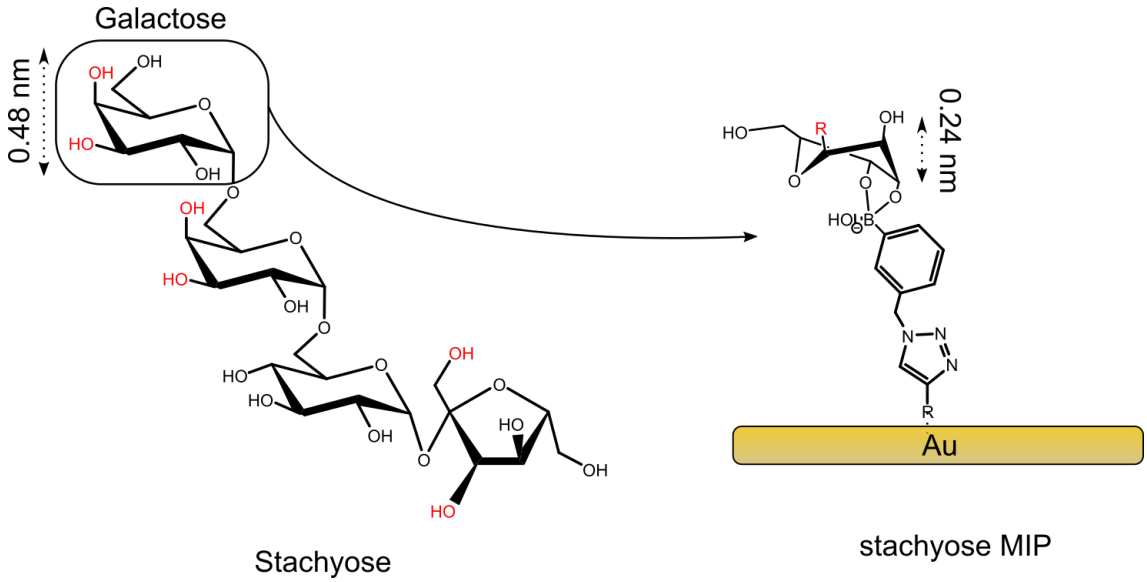


Fig. 79: Expected thickness of galactose unit if orientated parallel to the surface on immobilisation providing thickness of 0.24 nm. If Saccharide units are orientated perpendicular thickness increase is expected to be 0.48 nm. Parallel thickness is based on assuming complex takes PBA configuration described in (479).

Following washing of MISs to remove bound stachyose, thickness measurements were again taken to determine successful template removal. Overall time intervals on average decrease in thickness of 0.16 ± 0.02 nm confirming stachyose removal. Considering the thickness of galactose measuring C_1 to C_6 is 0.48 nm if bound perpendicular to the surface, decrease in thickness post washing is lower than expected. However, spatial

orientation of saccharide units may be orientated parallel to the surface (*Fig. 79*) which, coupled with averaging over 1 mm light beam diameter may serve to limit measured difference in thickness. Furthermore, given the reversible nature of the BA-saccharide interaction, dissociation during complex immobilisation would occur again, reducing observed change in thickness post-wash.

With successful multi-step functionalisation suggested by ellipsometry we then examined these imprints for saccharide binding of stachyose and melezitose being two structural distinct oligosaccharides. Based on thickness values, having the lowest thickness hence highest concentration of immobilised complex we can assume 8 hours should provide larger SPR response than 1-, 4- and 24-hour intervals. Furthermore, given the excessive thickness at 24 hours, suggestive of increased AzOEG surface concentration, it is likely this surface will perform poorly in saccharide binding. SPR experiments on timed MISs were run by injection of 100 µL of stachyose or melezitose (concentrations 1.56, 3.12, 6.25, 12.5 and 25 mM) over 2.5 minutes in 0.1 M AmAc buffer, pH 10. SPR RU at R_{equil} of the AzOEG monolayer was then deducted from R_{equil} of MISs thereby removing bulk refractive change of SPR RU. This was plotted against concentration producing chart shown in *Fig. 80*.

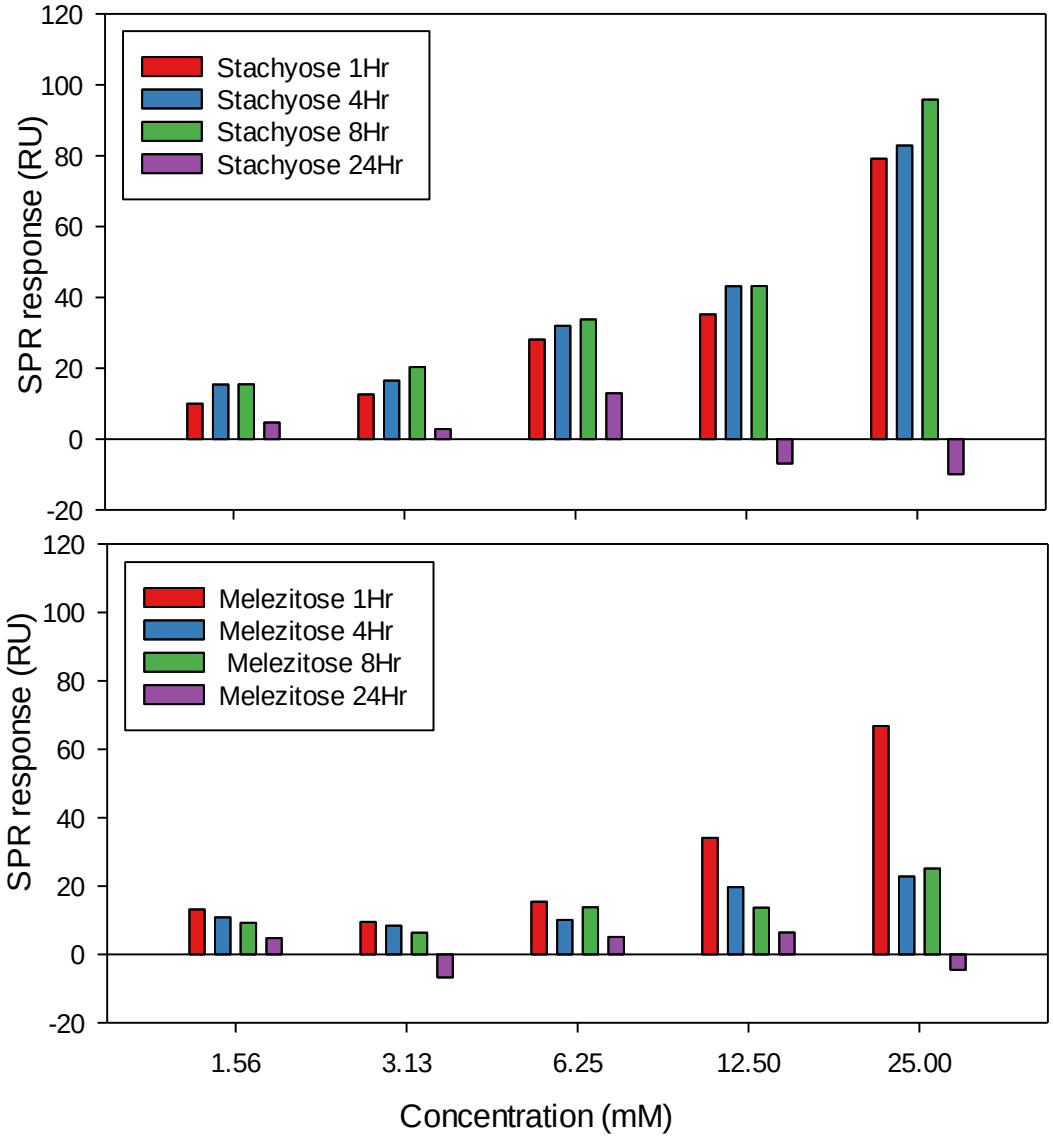


Fig. 80: Binding response of timed interval MISs to (a) stachyose and (b) melezitose.

If we compare both stachyose (*Fig. 80a*) and melezitose (*Fig. 80b*) congruity is seen between the two oligosaccharides SPR response where increasing stachyose-AzBA complex reaction time

from 1 hour up to 8 hours produces increased response of the MIS to stachyose while decreasing response to melezitose. This pattern is suggestive of increased selectivity of the MIS for stachyose up to 8 hours confirming our earlier prediction of higher response to stachyose for the 8-hour SAM. At 1-hour reaction time no selectivity is observed for MISs seeing slightly lower stachyose response than 4- and 8-hour reaction time while melezitose maintains similar binding to stachyose at 12.5 mM and 25 mM at 1-hour reaction time. Despite thickness values suggesting low yield after 1-hour reaction, earlier XPS data of AzBA functionalisation of MBDAlk (Chapter. 4, section 4.4.1) suggests 45% yield after this reaction time. Given the lack of selectivity, this suggests partial AzBA-stachyose complex immobilisation on the surface thereby providing sporadically placed PBA groups within a binding pocket thus reducing selectivity but allowing binding, nonetheless.

Subsequent increases to complex reaction time would allow further reaction of each AzBA in the stachyose complex thereby producing the complimentary stachyose-PBA motif on the surface. This is observed as consistently low melezitose RU while stachyose RU increases at 4- and 8-hour reaction times. Contrary to this, at 24 hours, negligible binding was seen for both stachyose and melezitose with slightly negative response at 12.5 and 25 mM attributed to no binding (491). With consideration for

thickness values at 24 hours being indicative of excessive AzOEG presence, low saccharide response following 24-hour complex reaction time confirms earlier hypothesis of binding pocket disruption by stachyose dissociation enabling AzOEG to fill the redundant space.

With the confirmation of 8-hours AzBA-stachyose complex reaction time with the MBDAlk SAM producing the most selective surface, we repeated this process of 8-hour reaction time to explore both reproducibility of this MIS and selectivity of the MIS without AzOEG addition. To this end, two MISs were prepared as described using 8 hour reaction time for complex immobilisation to the SAM proceeded by addition of AzOEG for 24 hours. Alongside this, two further surfaces were prepared using an 8 hour reaction time between complex and surface but with no addition of AzOEG thereby producing a SAM expressing a stachyose specific PBA motif without binding pocket formation.

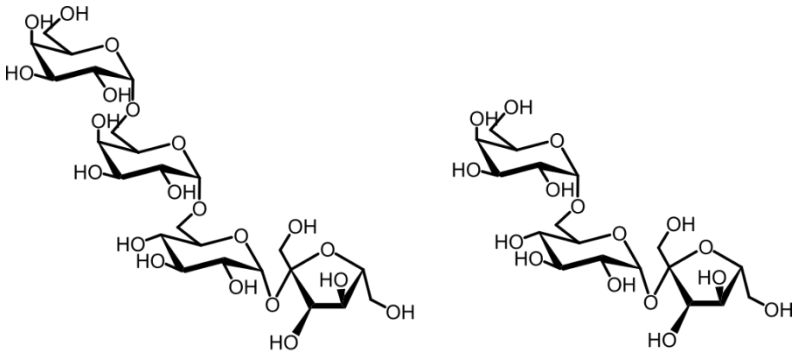


Fig. 81: Chemical structures of stachyose (Gal(α1-6)Gal(α1-6)Glc(α1-2β)Fru) and similar oligosaccharide raffinose (Gal(α1-6)Glc(α1-2β)Fru).

SPR experiments were performed using 100 µL injections stachyose, melezitose and raffinose, an oligosaccharide sharing structural similarity to stachyose (*Fig. 81*) at concentrations 1.56, 3.12, 6.25, 12.5 and 25 mM over 2.5 minutes. SPR RU at R_{equil} of the AzOEG monolayer was then deducted from R_{equil} of both MISs and AzBA-stachyose complex only SAMs thereby removing bulk refractive change of SPR RU. This was plotted against concentration producing chart shown in *Fig. 82* with error bars derived from standard deviation between replicates.

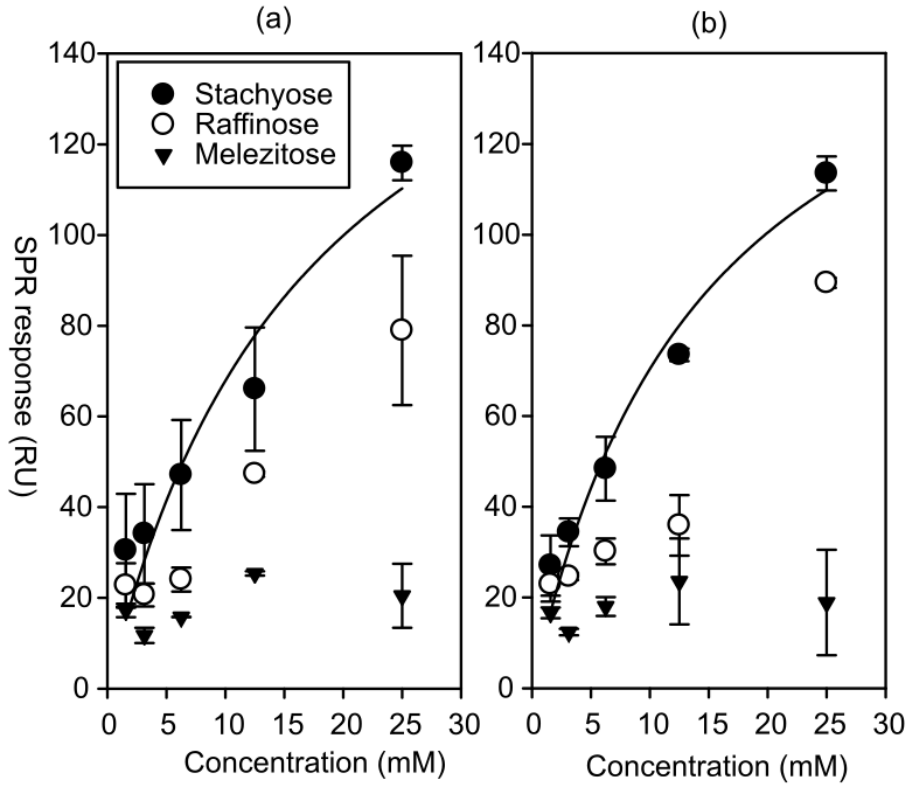


Fig. 82: SPR binding response of (a) AzBA-stachyose complex only and (b) MIS for stachyose following 8-hour reaction of complex to MBDAlk SAM

Table. 20: Binding affinity of AzBA-stachyose complex only SAM and stachyose MIS for stachyose

surface	K_d (mM)	R_{max} (RU)	R^2
Complex only	17.8 ± 10.8	188.8 ± 61.9	0.91
MIS	14.9 ± 5.5	175.4 ± 33.2	0.96

Comparison of the complex only functionalised SAM (*Fig. 82a*) with the stachyose MIS (*Fig. 82b*) shows very similar binding response for all oligosaccharides suggesting addition of AzOEG does not improve selectivity. Instead, these results imply selectivity is imparted solely by expression of stachyose specific PBA motifs. Referring back to thickness values for 8-hour complex reaction time (2.28 ± 0.05 nm), this may be indicative of minimal AzOEG functionalisation seeing the majority of the surface expressing PBA groups. This is confirmed in the higher overall response of the 8-hour complex reacted SAMs and MISs suggesting higher total PBA content than 1- and 4-hour reacted MISs. Despite similarities between complex functionalised SAMs and MISs, a similar trend of minimal melezitose binding is observed while stachyose exhibits binding. In addition, raffinose binding is seen in both SAMs at higher concentrations 12.5 and 25 mM albeit still lower than stachyose. This was expected given the structural homology between these two oligosaccharides where the difference of one galactose unit would decrease affinity for raffinose on the stachyose MIS but still allow raffinose to match a portion of the stachyose-PBA motif.

In spite of similarities between affinities (complex only K_d 17.8 ± 10.8, MIS K_d 14.9 ± 5.5) however, differences between complex only repeats manifest significant error in binding

affinity calculations. Interestingly, inclusion of AzOEG in the MIS seems to greatly reduce this error thereby producing far more reproducible saccharide binding. This perhaps arises through exposure of multiple PBA motifs to individual stachyose units in essence, providing less stable inter-motif binding. Alternativly, a more stable interaction might be produced on inclusion of hydrogen bonding sites along the AzOEG chain (492). By inclusion of a network of weak additional bonds alongside the covalent PBA-saccharide interaction, a more stable binding event would occur between stachyose and PBA motif while retaining selectivity observed with low melezitose binding. Collectively, both surfaces show good affinity for stachyose and present selective binding for the template ligand stachyose over melezitose. While surface concentration of AzOEG appears low, expression of conformational and spatially complimentary BA on the surface provides similar binding affinity to the PBA presenting SAM, MBDAlk-AzBA (K_d 11.3 ± 4.9) and binding capacity (R_{max} 125.8 ± 25.1). While imprinting fails to improve affinity here, selectivity is produced thus confirming the utility of this MIS design for selective saccharide recognition.

5.5 Conclusions

Further to our earlier described objectives we have confirmed higher affinity of PBA terminated SAMs in basic pH

solutions where minimal binding of fructose was observed for pH 7.4 and 8.5. From this, pH 10 was determined to provide sufficient saccharide-PBA binding with which we used in all further saccharide binding experiments. Examination of SAM chemical composition impact on saccharide binding was produced by comparison of McB versus DcB SAMs exhibiting long (C_{10}) and short (C_2) alkane backbone length respectively. While both PBA terminated SAMs supported monosaccharide binding, McB exhibited higher affinity (K_d 2.8 ± 0.6 mM) but lower binding capacity (R_{max} 150.7 ± 6.4 RU) compared to DcB (K_d 8.5 ± 1.5 mM, R_{max} 226.1 ± 12.9 RU) for fructose. Examination of surface organisation through XPS derived Au/S ratios showed lower surface organisation of McB (Au/S 87.58 ± 16.9) over DcB (Au/S 31.19 ± 1.78). Taken together with binding response to fructose, suggested inhibition of saccharide binding through steric hinderance, an effect seen with densely packed SAMs reducing ligand binding. MBDAlk-AzBA equivalent fructose affinity (K_d 7.7 ± 0.7 mM) and binding capacity (R_{max} 206.8 ± 6.4 RU) to DcB implied similar concentration and SAM packing between these surfaces however; MBDAlk-AzBA expressed significantly higher binding capacity for glucose (R_{max} 124.2 ± 8.7) and galactose (R_{max} 184.2 ± 24.2) than seen for DcB glucose (R_{max} 64.4 ± 7.1) and galactose (R_{max} 83.3 ± 7.8). This was explained through spatial arrangement of PBA groups following surface CuAAC reaction reducing steric hindrance hence allowing binding of

conformationally unfavourable saccharides compared to densely packed PBA groups of DcB. Attempts to functionalise DTPAlk with AzBA were made however, DTPAlk-AzBA functionalised SAMs demonstrated excessively low binding. This was attributed to poor reaction yield arising from combination of atmospheric surface contamination and Cu(I) catalyst chelation during the surface reaction. From this we concluded poor functional utility of short (C_2) alkanethiol monomers with the CuAAC reaction hence we did not continue saccharide binding studies with this monomer.

With confirmation of saccharide binding capability, we then developed a MIS specific for stachyose based on the MBDAlk SAM. This was intended as a proof of concept study to demonstrate the utility of this surface in oligosaccharide biosensor design. The AzBA-stachyose complex reaction time was first optimised and studied by ellipsometry where 8 hours reaction time provided highest concentration of immobilised complex. This proved effective with initial saccharide binding seeing an increase in stachyose response and decrease in melezitose response in SPR analysis suggesting selectivity for stachyose. To examine effect of AzOEG capping and reproducibility of the MIS, a complex only functionalised SAM and stachyose MIS was produced in duplicate. In this a similar trend of high stachyose response, low melezitose response was observed suggesting selectivity however, similarity between complex only SAM and the MIS implies

selectivity came from expression of stachyose specific PBA-motifs. This may however be symptomatic of low AzOEG yield on the surface thereby producing chemically homologous complex only SAMs and MISs with minimal AzOEG presentation on the MISs. Despite this, stachyose specific MISs displayed good reproducibility and were able to discriminate stachyose and structurally similar raffinose from melezitose thus confirming MIS production.

Chapter 6.

Conclusions and future work

6.1 Conclusions

The work provided in this thesis describes the fabrication of alkyne terminated SAMs and subsequent functionalisation of SAMs with PBA. Within this we have synchronised saccharide binding studies with SAM compositional studies to optimise the functional sensitivity of our produced SAMs thus; we have unified impact of surface organisation on sensitivity to saccharide binding. Surface characterisation by XPS, ellipsometry and contact angle has demonstrated increased organisation of SAMs on increasing alkane chain length from C_2 to C_{10} while showing low organisation imparted by branched SAM monomers. Attempts at surface CuAAC reaction to functionalise alkyne SAMs with PBA additionally showed dependency on this with short (C_2) SAMs displaying propensity to chelate the Cu(I) catalyst conferring low CuAAC reaction yield. Long (C_{10}) SAMs conversely provided high yield of PBA functionalisation post CuAAC reaction with little residual Cu(I) on the surface. On the contrary, in use of PBA terminated short (C_2) DcB and long (C_{10}) pMcB monomers, DcB showed higher surface organisation than pMcB. From these studies we determined SAM organisation, as facilitated by chemical

composition, arbitrates CuAAC reaction progression with short (C_2) and branched monomers. Inclusion of bulky terminal PBA groups on long chain (C_{10}) SAMs reduced surface organisation compared to alkyne terminated counterpart MBDAlk accounted for by steric interruption of alkane backbone association during initial phases of SAM formation. For short (C_2) chain SAMs however, inclusion of terminal PBA groups on DcB saw negligible reduction in surface organisation. Based on observations of SAM organisation, we determined inclusion of inter-monomer interaction groups are a necessary requirement in forming densely packed SAMs.

Following this we conducted saccharide binding studies of PBA functionalised SAMs using SPR to establish binding *in situ*. Comparison of DcB and McB PBA terminated SAMs response to various monosaccharides showed higher affinity of the McB SAM over DcB despite observed lower surface organisation but contrarily higher binding capacity of DcB over McB. This suggested that while increased concentration of surface PBA provided more binding sites, steric hindrances inhibited saccharide binding thereby lowering sensitivity. Surface functionalization of alkyne terminated short (C_2) and long (C_{10}) proved lack of functional utility with the CuAAC reaction on short (C_2) DTPAlk SAMs with little observed saccharide binding. Long (C_{10}) MBDAlk based SAMs however displayed significant saccharide response in-

line with expected relative affinities of monosaccharides to PBA (161).

Based on these findings we then developed a molecular imprint of the oligosaccharide stachyose using our MBDAlk SAMs and a preformed stachyose-AzBA complex. Optimisation of surface complex immobilisation showed 8 hours to produce highest sensitivity before addition of AzOEG to form the binding pocket. Coinciding, 8 hours additionally showed highest selectivity for stachyose and structurally similar raffinose over melezitose confirming selective recognition of this oligosaccharide configuration. On comparison of molecular imprints alongside imprints lacking AzOEG however, similar selectivity was observed. From this we concluded that at 8 hours, insufficient AzOEG for binding pocket formation was provided but that selectivity was imbued by presentation of stachyose specific PBA motifs on the surface. While this method failed to produce the desired binding pocket we nonetheless have demonstrated a method for immobilisation of PBA motifs on a surface capable of selective oligosaccharide binding.

In providing selective oligosaccharide recognition using an oligosaccharide imprinted SAM, we have demonstrated for the first time the utility of the CuAAC reaction for formation of saccharide imprinted surfaces. Furthermore, we have shown the chemical composition of the SAM monomer influences the reaction

yield and have provided a proof-of-concept foundation for the development of saccharide sensing clickable surfaces. As the CuAAC reaction produces a high yield and highly biocompatible reaction, this method provides a remarkably adaptable framework with the potential for adaption to glycoprotein detection.

6.2 Adaption of the current technique to glycoprotein detection

While a substantial body of research exists on SAMs and molecular imprinting, in biosensing this technology is still in its infancy having yet to produce a clinically approved assay. The biomedical laboratory remains dominated by ELISA assays owing to nature having already deciphered selective binding of biological ligands however; as with all things biological there is an element of fragility to their design. This extends to both labile disposition of antibodies to their environment *i.e.* pH, temperature, solvation *etc.,* but also to some ligand binding affinities as observed for anti-glycan antibodies. With the recognition of the importance of the glycoprofile as a diagnostic tool, overcoming low selectivity, weak affinity and heterogeneity in carbohydrate ligands presents a new biomedical frontier. Glycan profiling is possible through complex analytical techniques however disseminating glycan profiling technology to clinical laboratories remains the challenge. Providing a synthetic route, molecular imprinting might afford

the solution to this problem which, combined with the body of research on glycan sensing through PBA, provides an opportunity in the development of wholly artificial and stable glycan biosensors

With the principle of adaptability and biocompatibility in mind, we report here a method for producing selective oligosaccharide recognition on a SAM through extensive use of the CuAAC reaction. With Selective recognition seemingly arising from expression of unique PBA motifs it is worth addressing the formation of the binding pocket. To produce a multivalent binding site thus improving on sensitivity of this MIP, further optimisation of both imprinting time and perhaps length of the PEG monomer should be pursued. With this, PEG adoption of collapsed (mushroom) conformations under varying molecular weights and surface density might preclude requirement for densely packed PEG monomers. Alternatively, dense packing might provide a deeper binding pocket suitable for large glycoprotein template biomolecules (481,493). In addition, while we only report on the use of PBA expressing binding at pH 10, a number of BA variations exist with lower pKa values. To ensure biocompatibility with glycoprotein imprinting, adopting lower pKa variants such as benzoboroxle or Wulff-type PBA would see saccharide binding at closer to physiological pH than we have currently reported (175,177,178).

Further to development towards a clinical assay, an essential requirement lies in the adaption of this method for use in glycoprotein recognition. If we consider the dilemma of PCa diagnosis, current screening at a cut-off value of >4 ng/mL PSA presents low clinical specificity and sensitivity. Detection of PSA glycoforms however represents a true marker of cellular malignancy thus potentially offers significantly higher clinical specificity and sensitivity (53). Exchanging the oligosaccharide template for PSA, the MIP described in this thesis could readily be applied to glycoprotein detection with further optimisation to the CuAAC reaction time, PEG selection and buffer configuration.

In further adaption towards a clinically useful ultra-sensitive MIP, reduction in steric effects inhibiting surface interactions could be explored through use of mixed SAMs with careful consideration to prevention of phase segregation of monomers (230,450). Higher affinity of the MIP could further be induced by inclusion of additional functional moieties *i.e.* carboxy, sulfonate or amine groups allowing interaction with exposed amino acid residues on the glycoprotein (284). Alternatively, better assay performance might be sought in substituting SPR analysis for electrochemical detection with Rebelo *et al* (2019) reporting lower LOD for an electrochemical based CA-125 MIP sensor over similar SPR based sensor (286).

6.3 Proposed development towards clinical assay design

In line with the goals of this research we propose here a remodelling of this MIP design suited to direct clinical implementation for detection of PSA glycoforms. While we have demonstrated selective oligosaccharide detection in solution, quantification of specific glycoprotein glycan moieties in complex biological media would require pre-isolation of glycan biomarkers to prevent binding of structurally similar saccharides. For instance, using the current method, a MIP developed using a PSA glycoform template would detect both PSA glycoform but also non-PSA bound structurally similar glycans. While ideally, we would avoid use of antibodies given their sensitivity to temperature, pH, solvent *etc.*, we propose a method of immunogenic isolation of PSA as described in *Fig. 83* given the abundance of commercially available PSA antibodies and the urgency required in producing new glycan assays.

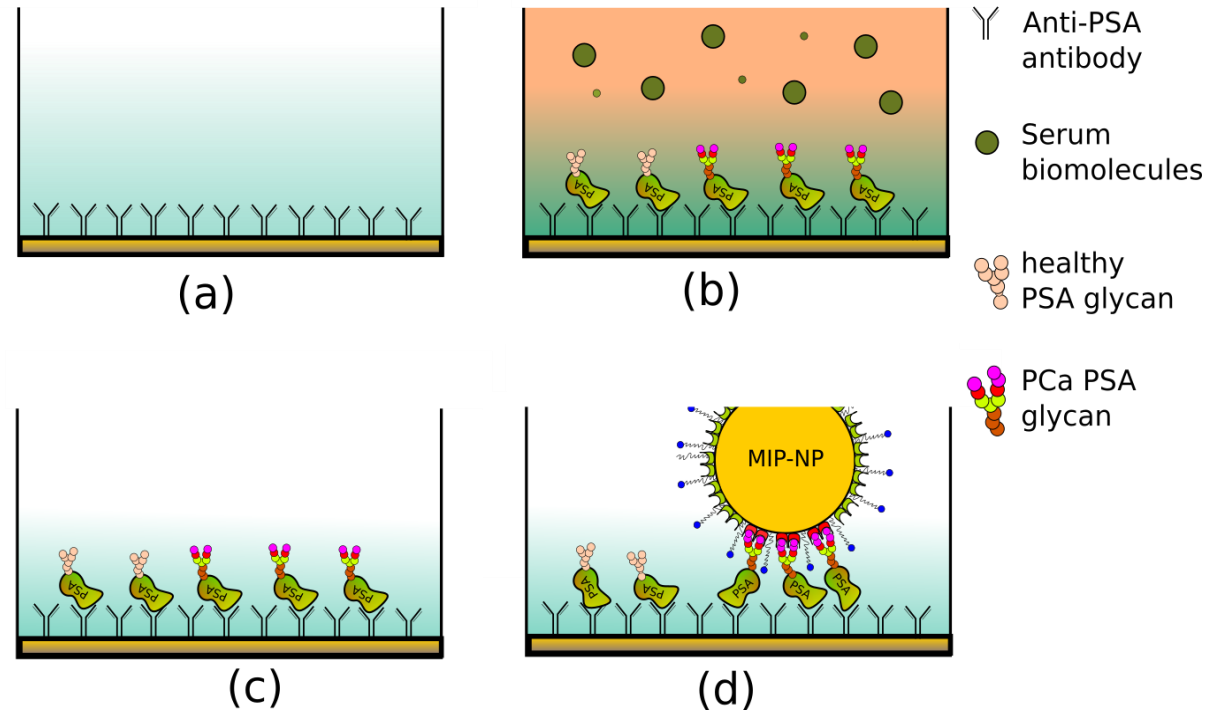


Fig. 83: Schematic for proposed clinical assay design in (a) an SPR adapted 96-well plat with anti-PSA antibody coated well. (b) Injection of patient serum sees binding of PSA, exposing glycan chain at the surface. (c) Washing of the well then removes all unbound material. (d) Injection of MIP nanoparticles (MIP-NP) sees selective binding of only PCa associated glycoforms.

Following selection of a monoclonal anti-PSA antibody capable of binding epitopes present on the opposite face of the PSA to the glycan, these would be immobilised within an SPR adapted 96-well plate (494). Subsequent exposure to patient serum would then see binding of PSA through epitopes favouring

surface exposure of glycan moieties during which time, unbound serum material would be washed away. Here we propose an alteration to our method, in the exchange of solid substrate for nanoparticles. PBA imprinting of PCa associated PSA glycans on gold nanoparticles should impart selective binding. On presentation of exposed PSA glycans with PCa glycan MIPs freely available in solution, we would expect binding thus an increase in SPR RU only where PCa associated glycans are presented. Not only would this allow selective detection of PCa glycans but would also allow two-fold PSA quantification: from initial PSA-antibody association allowing direct PSA quantification and second from nanoparticle-bound PSA MIP binding. Furthermore, significantly increased sensitivity in SPR would be expected on docking of large nanoparticles arising from larger perturbation to surface plasmon than with smaller biomolecule binding. This therefore provides additional signal amplification to only small concentrations of detected PCa glycans further enhancing this assay design (495,496).

Chapter 7.

Methods & settings

7.1.1 NMR spectroscopy

All ^{1}H, ^{13}C and COSY NMR spectra were collected on either a Bruker AV400 or AV300 spectrometer. Solvents used for NMR included: $CDCl_3$, MeOD, or DMSO-d6 with tetramethylsilane reference additive. Chemical shifts are assigned in parts per million (ppm). All data was analysed in either MestReNova Lite v.5.2 or MestReNova Lite SE v.10.1 (Mestrelab) or TopSpin V.3.5 (Bruker). Signal multiplicity is reported as: s=singlet, d=doublet, t=triplet, q=quartet, m=multiplet

7.1.2 Mass spectroscopy

Mass spectrometry was ran on the following equipment for the following samples: **DFC2** (waters micro MX MALDI, resolution 10000, laser power -200-250, reflectron mode +ve), **DFC3** (SYNAPT G2S HDMS waters, resolution 20000, sample loading by Alliance e2695, ESI capillary voltage 2.5 kV, sample cone 40 V). All other spectra were obtained on Waters Xevo-G2-XS, resolution 40000 with sample loading by Alliance e2695. ESI capillary voltage was 3 kV and sample cone set at 40 V.

7.1.3 X-ray photoelectron spectroscopy (XPS)

XPS spectra of SAMS: DFC, DTPA, MBDAlk and boronic acid terminated versions were obtained using Thermo Scientific K-Alpha^{+} XPS spectrophotometer by Harwell XPS laboratory (Cardiff). Elemental composition was obtained using monochromated Al K-alpha X-ray source (1486.69 eV) at 72 W with a spot size of 400 µM and a take-off angle at 90^{o}. High resolution peaks were obtained with a pass energy of 50 eV at a step size of 0.1 eV with an energy resolution of 0.5 eV. Samples were run in duplicate with x2 spots for sample for calculation of error. Peak fitting was completed using casaXPS (version 2.3.18dev1.18) with spectra calibrated using C(1s) peak charge corrected to 284.8 eV. Relative sensitivity factors for each element were as follows: S(2p), 1.68; C(1s), 1.0; N(1s), 1.8; O(1s), 2.93; Au(4f), 17.1.

XPS spectra of SAMS: DCB, pMcB and pinAzBA terminated DTPA were obtained Kratos Supra XPS spectrophotometer by Harwell XPS laboratory (Cardiff). Elemental composition was obtained using monochromated Al K-alpha X-ray source (1486.69 eV) at 225 W with a spot size of 400 µM and a take-off angle at 90^{o}. High resolution peaks were obtained with a pass energy of 40 eV at a step size of 0.1 eV with an energy resolution of 0.5 eV. Two spots were analysed per sample. Peak fitting was completed using casaXPS (version 2.3.18dev1.18) with spectra calibrated using C(1s) peak

charge corrected to 284.8 eV. Relative sensitivity factors for each element were as follows: S(2p), 0.688; C(1s), 0.278; N(1s), 0.477; O(1s), 0.78; Au(4f), 6.25; B(1s), 0.159.

7.1.4 Surface plasmon resonance (SPR)

SPR binding studies were performed with a Reichart SR7000DC dual channel spectrophotometre with SR7100 autosampler (Reichart technologies, Buffalo, NY, USA). Studies were run at 25 °C, flow rate 25 µl/min, injection 100 µl over 2.5 minutes with 5 minutes' equilibration. A baseline was established for each SAM or MIP by running degassed buffer (buffer dependent on experiment) over the sample at 25 µl/min until a stable baseline was achieved. Prior to saccharide injection, running buffer was injected as per sample conditions to provide blank run. Results were collected with SPR autolink software (Reichart, version 1.1.10-F) and analysed with Scrubber (BioLogic, version 2.0.0.4). All SPR experiments with exception of molecular imprinting studies (Chapter 5.4.2) were produced as singular experiments used to inform imprinting methodology. Molecular imprinting of stachyose was performed in duplicate to confirm reproducibility.

7.1.5 Contact angle

Contact angle measurements were taken using an Attension Theta contact angle meter (Biolin scientific) using an automated micosyringe to dispense and retract 4 µL water droplets to the surface. Advancing and receding angles were obtained from recording of water drop-out/ in at 35 frames per second (FPS) with angles automatically calculated at surface-liquid interface using OneAttension software (version 3.2.2.0). Measurements were taken in triplicate from duplicate SAMs and average reported with error calculated from standard deviation.

7.1.6 Ellipsometry

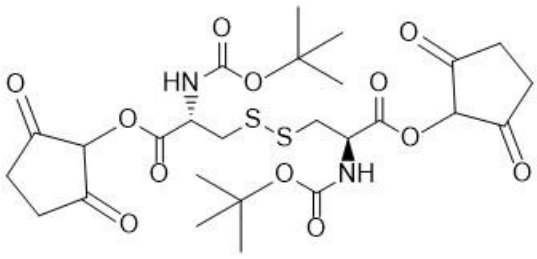
SAM thickness was determined by ellipsometry using an Alpha-SE ellipsometer from J.A. Woolam. Incidence angle was set at 70° with a wavelength range of 300-900 nm. Calculation of film thickness was based on a three-phase ambient atmosphere/SAM/Au model with a refractive index set to 1.5 and extinction coefficient (k) at 0.00. Thickness was calculated using CompleteEase software, version 5.26 based on 4 surface measurements on two surfaces (8 total measurements). Reported error values are calculated from inter-sample standard deviation and do consider systemic sources of error such as angle of incidence error. Error associated with variance of refractive

index was calculated by varying n=1.45 to 1.5 with average thickness difference across refractive index range reported.

7.2 Chemical synthesis

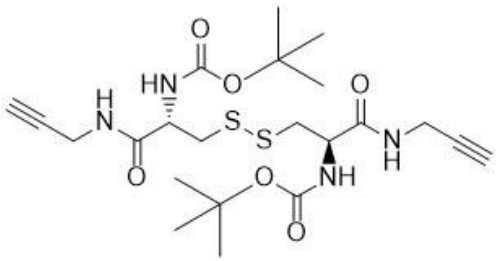
7.2.1 Di-functionalised cystine

7.2.1.1: 2,5-dioxopyrrolidin-1-ylN-(tert-butoxycarbonyl)-S-(((R)-2-((tert-butoxycarbonyl) amino)-3-((2,5-dioxopyrrolidin-1-yl)oxy)-3-oxopropyl)thio)-D-cysteinate (*DFC1)*



Di-Boc-L-cystine (1.00 g, 2.26 mmol) was dissolved in anhydrous THF (50 mL) in a 200 mL round bottomed flask and the solution degassed with argon. To this, DCC (1.17 g, 5.71 mmol) was added. This was left to stir for 1 hour at room temperature after which time NHS (0.65 g, 5.8 mmol) was added and left to stir for 24 hours at room temperature. During this time a white precipitate formed. This was filtered and the filtrate dried *in vacuo* to yield **DFC1,** a loose white solid (1.72 g) and was used immediately without further purification.

7.2.1.2: 2,5-dioxopyrrolidin-1-ylN-(tert-butoxycarbonyl)-S-(((R)-2-((tert-butoxycarbonyl) amino)-3-((2,5-dioxopyrrolidin-1-yl)oxy)-3-oxopropyl)thio)-D-cysteinate (*DFC2*)



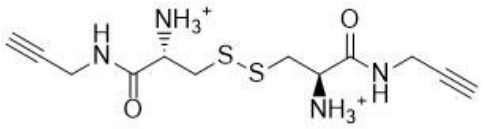
In anhydrous THF (150 mL), **DFC1** (1.72 g, 2.72 mmol) was dissolved and solution cooled in ice bath to 0 °C in a 250 mL round bottomed flask. To this, Et_3N (1.1 mL, 7.88 mmol) was added and solution was stirred for 10 minutes. Proparglyamine (0.52 mL, 8.16 mmol) was then added and solution stirred at room temperature over 24 hours. The formed white precipitate was removed by filtration and the filtrate dried *in vacuo*. The resulting solid was resuspended in DCM and filtered to eliminate any insoluble product. The filtrate was washed with saturated $NaHCO_3$ (3x 25 mL) and the aqueous phases extracted with DCM (3x 25 mL). All organic phases were combined and dried over $MgSO_4$, filtered and dried *in vacuo*. The compound was then purified by silica chromatography employing a mixture of hexane/ EtOAc (7:3) as eluent yielding **DFC2**, as an off-white solid (0.703 g, 50%).

^{1}H NMR (400 MHz, $CDCI_3$) δ (ppm)= 8.09 (t, *J*= 4.8 Hz, 2H, N*H*CH_2CCH), 5.55 (d, *J*= 9.7Hz, 2H, N*H*COO), 4.94 (td, J_1= 10.4 Hz, J_2=3.5 Hz, 2H, SHCH_2C*H*), 4.11 (ddd, J_1= 17.6 Hz, J_2=, 5.6 Hz, J_3=2.6 Hz, 4H, NHC*H*$_2$CCH), 2.96 (dd, J_1= 14.7 Hz, J_2= 3.8 Hz,

2H, SHCH*H*CH), 2.87 (dd, J_1=14.6 Hz, J_2= 11 Hz, 2H, SHC*H*HCH), 2.18 (t, *J*=2.5 Hz, 2H, $NHCH_2CCH$), 1.49 (s, 18H, $NHCOOC(CH_3)_3$.

MS (MALDI, matrix: 2,5-dihydroxybenzoic acid) *m/z* (%)= $[M+Na]^+$, 553.2 $[M+K]^+$.

7.2.1.3: S)-3-(((R)-2-ammonio-3-oxo-3-(prop-2-yn-1-ylamino)propyl)disulfanyl)-1-oxo-1-(prop-2-yn-1-ylamino)propan-2-aminium (*DFC3*)



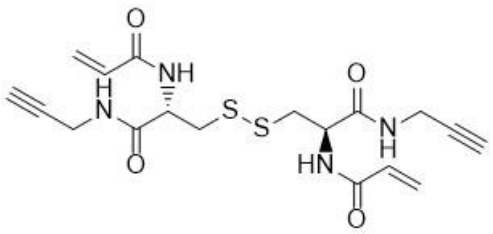
DFC2 (270 mg, 0.525 mmol) was dissolved in DCM (30 mL) in a 100 mL round bottomed flask and degassed with argon. TFA (1.2 mL, 15.75 mmol) was added to this and left stirring under argon for 10 minutes followed by a further addition of 1.2 mL of TFA. Reaction mixture was left stirring for 24 hours at room temperature. The solution was dried *in vacuo* to yield **DF3** as a translucent brown solid (142 mg, 86%).

^{1}H NMR (400 MHz, MeOD) δ (ppm)= 4.21 (dd, J_1= 8.4 Hz, J_2= 5.0 Hz, 2H, $SCH_2CHNH_3^+$), 4.06 (d, *J*= 2.6 Hz, 4H, NH_2CH_2CH), 3.37 (dd, J_1= 14.8 Hz, J_2= 5.0 Hz, 2H, SC*H*HCH), 3.07 (dd, J_1= 14.8 Hz, J_2= 8.4 Hz, 2H, SCH*H*CH), 2.69 (t, *J*= 2.6 Hz, 2H, NH_2CH_2CCH).

^{13}C NMR (100 MHz, MeOD) δ (ppm)= 168.2, 79.7, 73.1, 51.9, 39.2, 34.7, 29.9.

MS (ESI+MS) *m/z* (%)= 315.1 [M], 337.08 [M+Na].

7.2.1.4: N,N'-((2R,2'R)-Disulfanediylbis(1-oxo-1-(prop-2-yn-1-ylamino)propane-3,2-diyl)) diacrylamide (*DFC*)



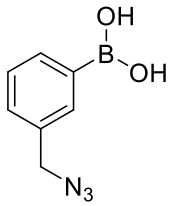
In anhydrous THF (25 mL), **DFC3** (142 mg, 0.45 mmol) was dissolved and degassed with argon in a 100 mL round bottomed flask. To this solution, Et_3N (0.36 mL, 2.7 mmol) was added and left stirring for 30 minutes during which time this solution was cooled to 0 °C in an ice bath. Acryloyl chloride (0.15 mL, 1.66 mmol) was added dropwise allowing good dissolution of acryloyl chloride. During this process triethylammonium chloride precipitated as a white solid. This solution was then left to stir overnight and allowed to warm to room temperature. The solution was then dried *in vacuo* and resuspended in DCM (30 mL) precipitating a significant fraction of the product **DFC** in high purity which was removed by filtration. The filtrate was washed with saturated $NaHCO_3$ (3x 25 mL) and the aqueous phases extracted with DCM (3x 25 mL). All organic phases were combined, dried over $MgSO_4$ and filtered. The filtrate was dried *in vacuo* to yield brown solid. This was purified by silica chromatography using hexane/ EtOAc (1:1) as eluent yielding **DFC** as an off white solid (129.1 mg, 68%).

^{1}H NMR (400 MHz, DMSO) δ (ppm)= 8.61 (t, *J*= 5.5 Hz, 2H, N*H*CH_2CH), 8.49 (d, *J*= 8.4 Hz, 2H, SCH_2CHN*H*), 6.30 (dd, J_1= 17.1 Hz, J_2= 10.2 Hz, 2H, COC*H*CH_2), 6.11 (dd, J_1= 17.1 Hz, J_2= 2.1 Hz, 2H, C=OCHC*H*H), 5.62 (dd, J_1= 10.1 Hz, J_2= 2.1 Hz, 2H, COCHCH*H*), 4.63 (td, J_1= 4.8 Hz, J_2= 5.2 Hz, 1H, SCH_2C*H*), 3.8 - 3.94 (qdd, 4H, NHC*H*$_2$CH), 3.13 (t, *J*= 2.5 Hz, 2H, $NHCH_2$C*H*), 3.09 (dd, *J*= 13.5 Hz, 2H, SC*H*HCH) 2.88 (dd, *J*= 13.5 Hz, 2H, SCH*H*CH).

^{13}C NMR (100 MHz, DMSO) δ (ppm)= 170.0, 165.08, 131.8, 126.4, 81.27, 73.62, 52.2, 28.7.

MS (ESI MS) *m/z* (%)=445.1 $[M+Na]^+$, 461.07 $[M+K]^+$.

7.2.2: 3-((azidomethyl)phenyl) boronic acid (AzBA)



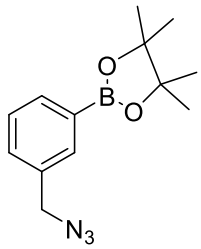
3-((bromomethyl)phenyl) boronic acid (0.25 g, 1.16 mmol) was dissolved in 15 mL acetone/ water (3:1). Sodium azide (0.11 g, 1.74 mmol) was added and the reaction left stirring at room temperature for 2 hours. 25 mL DCM/ water (1:1) was then added and reaction stirred for further 1 hour. The organic phase was separated, washed with water (3x 15 mL) and then dried with $MgSO_4$. This was dried *in vacuo* to yield **AzBA** as an off white solid (192.6 mg, 93%)

^{1}H NMR (400 MHz, DMSO) δ (ppm)= 8.11 (s, 2H, BO*H*), 7.76 (m, 2H, Ph), 7.38 (m, 2H, Ph), 4.43 (s, PhC*H*NNN).

^{13}C NMR (100 MHz, DMSO) δ (ppm)= 134.0, 133.6, 129.9, 127.5, 53.6.

MS (ESI MS) *m/z (%)*= 179.11 $[M]^+$, 164.11 $[M-N]^+$.

7.2.3: 3-((azidomethyl)phenyl) boronic acid pinacol ester



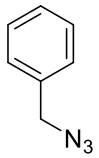
AzBA (168 mg, 0.944 mmol) was dissolved in ether (20 mL) and heated in an oil bath to 50 °C and connected to water fed condenser on a two neck RB flask. Pinacol (1115 mg, 0.944 mmol) was dissolved in 5 mL ether and injected via septum and reaction stirred for 1 hour and monitored by TLC (Hex-EtOAc 6:4). The reaction mixture was then dried *in vacuo* to yield **pinAZBA** as a clear fluid oil (234 mg, 94%).

^{1}H NMR (400 MHz, DMSO) δ (ppm)= 7.67 (m, 2H, Phe), 7.50 (m, 2H, Phe), 4.47 (s, 2H, PhC*H*NNN), 1.29 (s, 12H, CC*H3*C*H3*CC*H3*C*H3*).

^{13}C NMR (100 MHz, DMSO) δ (ppm)= 135.7, 134.9, 134.5, 131.9, 128.8, 84.3, 53.9, 25.2, 25.1.

MS (ESI MS) *m/z (%)*= 232.2 $[M-N_3]^+$, 217.19 $[M-CH_2N_3]^+$.

7.2.4 Benzyl azide (AzBEN)

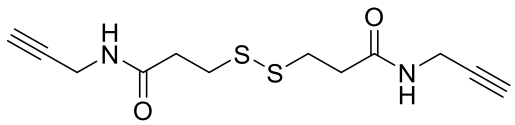


Benzyl bromide (718 mg, 4.2 mmol) and sodium azide (341.25 mg, 5.25 mmol) was dissolved in acetone- MilliQ H_2O (15 mL, 3:1) and stirred for 2 hours at room temperature. DCM (30 mL) and MilliQ H_2O (10 mL) was then added to reaction and stirred for further 1 hour. The organic phase was separated and washed with MilliQ H_2O (3x 10 mL). The organic phase was then dried over $MgSO_4$, filtered and the filtrate dried *in vacuo* to yield **AzBEN** as a clear fluid oil (527 mg, 94%).

^{1}H NMR (300 MHz, DMSO) δ (ppm)= 7.431 (m, 5H, Phe), 4.441 (s, 2H,N3C*H2*Phe).

^{13}C NMR (100 MHz, DMSO) δ (ppm)= 136.0, 129.2, 128.9, 128.6, 54.0.

7.2.5: 3,3′disulfanediylbis(*N*-(prop-2-yn-1-yl)propenamide (DTPAlk)



In a two neck round-bottom flask, 3,3′-dithiopropionic acid (1 g, 4.76 mmol) was dissolved in 150 mL anhydrous THF and the solution purged with argon. To this, N-(3-Dimethylaminopropyl)-N′-ethylcarbodiimide (2.19 g, 11.42 mmol) was added and reaction stirred for 10 minutes. 1-Hydroxybenzotriazole hydrate (1.54 g,

11.42 mmol) was then added and reaction stirred at room temperature for 1 hour after which time a sticky residue precipitated. The reaction was then cooled to 0 °C in an ice bath and propargylamine (0.78 g, 14.28 mmol) dissolved in 30 mL anhydrous THF was added dropwise over 30 minutes under argon. The reaction was then allowed to come to room temperature and stirred overnight. This was then filtered, and the filtrate dried *in vacuo* before being resuspended in MilliQ H_2O forming a precipitate. This precipitate was then dissolved in 30 mL DCM and washed with $NaHCO_3$ (3x 20 mL) and the organic phase dried over $MgSO_4$, filtered and dried *in vacuo* yielding DTPA as a white powder (1.04 g, 76.6%).

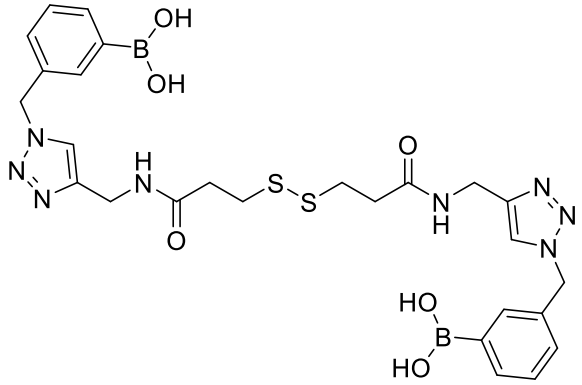
^{1}H NMR (400 MHz, DMSO) δ (ppm)= 8.40 (t, *J*= 5.2 Hz, 2H, CHHCON*H*), 3.87 (dd, *J*= 2.4 Hz, 4H, NHC*HH*CCH), 3.12 (t, *J*= 2.4 Hz, 2H, CHHCC*H*), 2.89 (t, *J*= 7.2 Hz, 4H, SCHHC*HH*), 2.48 (d, *J*= 7.2 Hz, 4H, SC*HH*CHH).

^{13}C NMR (100 MHz, DMSO) δ (ppm)= 170.3, 81.5, 73.5, 35.1, 34.0, 28.3.

MS (ESI MS) *m/z (%)*= 307.06 $[M+Na]^+$, 285.07 $[M]^+$.

7.2.6: ((((((3,3'disulfanediylbis(propanoyl))bis(azanediyl))bis(methylene))bis(4,5-dihydro-1H-1,2,3-triazole-4,1-diyl))bis(methylene))bis(3,1-phenylene))diboronic acid (DCB)

DTPA (193.95 mg, 0.682 mmol) and **AzBA** (364.4 mg, 2.047 mmol)

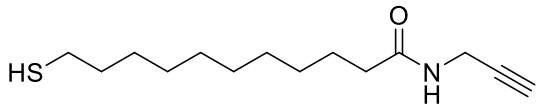


were dissolved in 5 mL DMF and stirred for 1 hour. A pre-mixed catalyst solution was prepared by dissolving Cu(II)SO_4 (40.55 mg, 10 mol%) and sodium ascorbate (65.34 mg, 20 mol%) in 1 mL MilliQ H_2O forming a brown precipitate. To this, tris[(1-benzyl-1H-1,2,3-triazol-4-yl)methyl]amine (108.62 mg, 10 mol%) dissolved in 1 mL DMF was added turning the solution transparent. This catalyst was then added to the reaction mixture and the flask was purged with argon and protected from light. The reaction was stirred overnight at room temperature and then dried *in vacuo.* The crude was resuspended in DCM/ MeOH/ NH_4OH (4:4:2) forming a blue precipitate which was filtered through a cotton filled glass Pasteur pipette and the filtrate dried *in vacuo*. This was further purified by silica chromatography using DCM/ MeOH/ NH_4OH solvent system. The product containing fraction was dried *in vacuo* and resuspended in 250 µL MeOH precipitating **DCB** as an off blue/ white powder (33 mg, 7.5%).

^{1}H NMR (300 MHz, MeOD) δ (ppm)= 7.81 (s, 2H, triazole), 7.74 (s, 2H, Phe), 7.59 (s, 2H Phe), 7.36 (m, 4H, Phe), 5.53 (s, 4H, NC*HH*phe), 4.40 (s, 4H, NHC*HH*CCH), 2.90 (t, J_1= 7.2 Hz, J_2= 6.9 Hz, 4H, SCHHC*HH*CO), 2.57 (t, J_1= 6.9 Hz, J_2= 7.2 Hz, 4H, SC*HH*CHHCO).

MS (ESI MS) *m/z (%)*= 639.29 $[M]^+$, 348.61 $[M+Na]^{2+}$.

7.2.7: 11-mercapto-N-(prop-2-yn-1-yl)undecanamide (MBDAlk)



11-mercpountdecanoic acid (500 mg, 2.29 mmol) was dissolved with N-(3-Dimethylaminopropyl)-N′-ethylcarbodiimide (1.054 g, 5.5 mmol) in 30 mL anhydrous THF in a two neck round-bottom flask, purged with argon and stirred for 30 minutes. 1-hydroxybenzotriazole hydrate (0.743 g, 5.5 mmol) was added to this and stirred for a further 1 hour under argon. The reaction was cooled to 0 °C in an ice bath and proparglyamine (378.3 mg, 6.87 mmol) in 20 mL anhydrous THF was added dropwise over 30 minutes. The reaction was then allowed to warm to room temperature and stirred overnight under argon. This was then dried *in vacuo* and resuspended in 30 mL MilliQ H_2O forming a white precipitate that was filtered and washed with 100 mL MilliQ H_2O. The precipitate was dissolved in 30 mL DCM and washed with

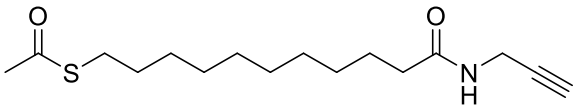
$NaHCO_3$ (3x 20 mL) and the organic phase dried over $MgSO_4$. This was filtered and the filtrate dried *in vacuo* to give **MBDAlk** as a white powdery solid (363 mg, 62.1%).

^{1}H NMR (400 MHz, DMSO) δ (ppm)= 8.22 (t, *J*= 5.2 Hz, 1H, CON*H*CHH), 3.83 (q, *J*= 2.4 Hz, 2H, NHC*HH*CCH), 3.07 (t, J_1= 2.4 Hz, J_2= 2.8 Hz, 1H, CHHCC*H*), 2.46 (t, *J*= 7.2 Hz, 2H, SHC*HH*CHH), 2.23 (t, *J*= 7.6 Hz, 1H, S*H*CHH), 2.07 (t, J_1= 7.6 Hz, J_2= 7.2 Hz, 2H, CHHC*HH*CO), 1.53 (m, 4H, SHCHHC*HH*, CHHC*HH*CHHCO), 1.23 (s, 12H, 6xC*HH*).

^{13}C NMR (100 MHz, DMSO) δ (ppm)= 171.2, 81.4, 72.7, 35.0, 33.4, 28.9, 28.8, 28.7, 28.6, 28.4, 27.7, 27.6, 25.1, 23.7

MS (ESI MS) *m/z (%)*= 278.16 $[M+Na]^+$, 256.18 $[M]^+$.

7.2.8: S-(11-oxo-11-(prop-2-yn-1-ylamino)undecyl) ethanethioate (pMBDAlk)



Pyridine (1 mL) was cooled to 0 °C in an ice bath and **MBDAlk** (25 mg, 0.098 mmol) and acetic anhydride (29.6 mg, 0.29 mmol) was dissolved in this. The flask was flushed with argon and reaction stirred overnight at room temperature. MilliQ H_2O ice cubes (3x 1 mL) were added to the reaction and stirred until melted and the resulting solution washed with EtOAc (3x 18 mL). The organic phase was washed with brine (3x 10 mL), dried over $MgSO_4$ and

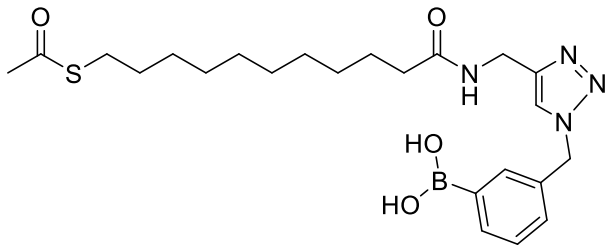
filtered. The filtrate was dried *in vacuo* yielding **pMBDAlk** as an off white solid (20 mg, 68%)

^{1}H NMR (300 MHz, DMSO) δ (ppm)= 8.19 (t, *J*= 5.1 Hz, 1H, CON*H*CHH), 3.84 (q, *J*= 2.4 Hz, 2H, NHC*HH*CCH), 3.07 (t, *J*= 2.4 Hz, 1H, CHHCC*H*), 2.83 (t, *J*= 7.2 Hz, 2H, SHC*HH*CHH), 2.31 (s, 3H, C*HHH*COS), 2.08 (t, J_1= 7.2 Hz, J_2= 7.8 Hz, 2H, CHHC*HH*CO), 1.49 (m, 4H, SHCHHC*HH*, CHHC*HH*CHHCO), 1.23(s, 12H, 6xC*HH*).

^{13}C NMR (100 MHz, DMSO) δ (ppm)= 172.3, 73.2, 35.5, 31.1, 29.6, 29.3. 29.2, 29.1, 28.9, 28.8, 28.6, 28.1, 25.6.

MS (ESI MS) *m/z (%)*= 256.18 $[M-C_2H_3O]^+$, 298.18 $[M]^+$, 509 $[M+M]^+$.

7.2.9: (3-((4-((11-(acetylthio)undecanamido)methyl)-1H-1,2,3-triazol-1-yl)methyl)phenyl)boronic acid (pMcB)



In 2.5 mL DMF, **AzBA** (70 mg, 0.393 mmol) and **pMBDAlk** (48.8 mg, 0.163 mmol) was dissolved and purged with argon. A pre-made catalyst solution was prepared by adding TBTA (20.8 mg, 10 mol%) in 0.5 mL DMF to a mixture of sodium ascorbate (12.5 mg, 20 mol%) and Cu(II)SO_4 (7.78 mg, 10 mol%) in 1 mL MilliQ H_2O. Following dissolution of brown precipitate in catalyst on

addition of TBTA, all 1.5 mL of catalyst was added to the reaction. The reaction was covered from light with aluminium foil and stirred overnight under argon. The reaction was then extracted with DCM (3x 10 mL) and the organic phase washed with MilliQ H_2O (3x 10 mL) before being dried over $MgSO_4$, filtered and the filtrate dried *in vacuo*. This was resuspended in 1.5 mL DCM/ MeOH/ NH_4OH (4:4:2) forming a light blue precipitate and was filtered over silica in a glass Pasteur pipette. The filtrate was further purified by flash chromatography using DCM/ MeOH (99:1) yielding **pMcB** as an off white solid (34 mg, 42%).

^{1}H NMR (300 MHz, DMSO) δ (ppm)= 8.23 (t, J_1= 5.7 Hz, J_2= 5.4 Hz, 1H, CON*H*CHH), 8.09 (s, 1H, pheBO*HH*), 7.90 (s, 1H,triazole), 7.75 (m, 2H, phe), 7.34 (m, 2H, phe), 5.53 (s, 2H, NNNC*HH*phe), 4.26 (d, *J*= 5.4, 2H, NHC*HH*triazole), 2.84 (t, *J*= 7.2 Hz, 2H, CHHC*HH*CO), 2.31 (s, 3H, C*HHH*COS), 2.08 (t, J_1= 7.2 Hz, J_2= 7.8 Hz, 2H, SHC*HH*CHH), 1.50 (m, 4H, SHCHHC*HH,* CHHC*HH*CHHCO), 1.21 (s, 12H, 6xC*HH*).

MS (ESI MS) *m/z (%)*=), 475.26 $[M]^+$.

7.3 Surface preparation & chemical modification

7.3.1 Chemical cleaning of Au substrates

Prior to SAM formation, Au substrates were chemically cleaned as preparation for surface modification. All SAMs were formed on polycrystalline gold substrates comprised of 50 nm gold on a thin layer of chromium on glass purchased from George Albert PVD, Germany. Gold substrates were immersed in piranha solution (7:3 70% H_2SO_4, 30% H_2O_2) for 7 minutes. They were then rinsed liberally with MilliQ H_2O followed by HPLC methanol and dried under argon stream. Clean Au substrates were used immediately in subsequent experiments to minimise fouling of Au surface.

7.3.2 Self-assembled monolayer formation of DFC, DTPAlk or MBDAlk on clean Au substrates

Clean Au substrates were immersed in 1 mL 0.1 mM methanolic solutions of either DFC, DTPAlk or 0.2 mM MBDAlk previously sonicaticated for 2 minutes followed by purging with argon for further 2 minutes. SAMs were allowed to form for minimum of 18 hours at room temperature before being rinsed liberally with

HPLC methanol and dried under argon stream. Dry SAMs were then immediately used in further surface modification or characterisation.

7.3.3 Terminal modification of SAMs by CuAAC reaction with AzOEG, AzBA or AzBEN

Alkyne terminated SAMs (DFC, DTPAlk or MDAlk) were modified post immobilisation by CuAAC reaction with either 1 mM AzOEG, 1 mM AzBA or 1 mM AzBEN dissolved in a pre-prepared catalyst. A 1.85 mM solution of AzOEG, AzBA or AzBEN was prepared using a x10 stock in 2.7 mL DMF. In a separate vial, 50 µL of Cu(II)SO_4 (10 mM) and 50 µL NaAsc (20 mM) were combined forming a brown precipitate. To this 500 µL TBTA (1 mM) was added and the solution mixed thoroughly turning the solution clear. On dissolution, 1.1 mL MilliQ H_2O was added and the whole solution transferred to the azide ligand solution providing Az'' (1 mM), Cu(II)SO_4 (10 mol%), NaAsc (20 mol%), TBTA (10 mol%).

Pre-prepared alkyne terminated SAMs were then submerged in 1 mL of this solution for a minimum of 18 hours at room temperature protected from light on a rotary mixer. SAMs were then sonicated for 10 seconds in solution followed by thorough rinsing and further 10 second sonication in MilliQ H_2O and HPLC MeOH (1:1). SAMs were then rinsed liberally with HPLC grade MeOH

before being dried with argon and used immediately in experiments.

7.3.4 Preparation of DcB monolayer

Boronic acid monolayers were formed using pre-clicked DTPAlk-AzBA (DcB, section: 7.2.6). Chemically cleaned Au substrates were immersed in 1 mL methanolic solution of DcB (0.1 mM) and placed on a rotary mixer for 18 hours at room temperature. DcB SAMs were then sonicated for 10 seconds in solution and rinsed liberally with HPLC MeOH before drying with argon.

7.3.5 *In situ* deprotection of pMcB and formation of McB monolayer

Acetate protecting groups were removed from pMcB thiol moiety with KOH. To 3 mL pMcB (0.26 mM) in EtOH, 1 mL KOH (0.8 mM) was added and solution sonicated for 5 minutes and mixed for 2 hours at room temperature. Post de-protection, clean Au substrates were immersed in 1 mL of this solution for 18 hours at room temperature on a rotary mixer. McB SAMs were then sonicated for 10 seconds in solution and rinsed liberally with MilliQ H_2O and HPLC EtOH before drying under argon.

7.3.6 Stachyose-boronic acid surface template formation through CuAAC reaction

Stachyose-AzBA complex was kindly provided by Dr Stefano Tommasone for this experiment. This was formed by reaction of AzBA (0.175 mmol) with stachyose (0.00546 mmol) in a 6:1 dioxane/ acetonitrile mixture (0.35 mL) heated to 90 °C. This was purged with argon and stirred for 24 hours in with activated molecular sieves 3Å. Solvent was removed *in vacuo* and the crude mixture suspended in toluene (0.6 mL), precipitating the AzBA-stachyose complex. This solution was transferred to a 1 mL Eppendorf and centrifuged and supernatant disposed. The precipitate was then resuspended in toluene (0.6 mL) precipitating the complex. Centrifugation was repeated and supernatant disposed leaving the AzBA-stachyose complex as a precipitate for use in imprinting experiments.

For formation of imprinted surfaces, AzBA-stachyose complex was first immobilised to the MBDAlk SAM. The CuAAC reaction proceeded as previously described (section: 7.3.3), 1.32 mL pre-prepared catalyst of Cu(II)SO_4 (10 mol%), NaAsc (20 mol%) and TBTA (10 mol%) was added to 2 mL DMF and further 1.28 mL MilliQ H_2O added. To this, 2 mL stachyose-AzBA complex (1.5 mM) in DMF was added and mixed thoroughly. To 1 mL of this solution, MBDAlk monolayer on Au substrate was added and SAM mixed on rotary mixer for 18

hours at room temperature protected from light. Stachyose was then removed from the BA template by thorough immersion in MilliQ H_2O for 10 Minutes followed by 20 second sonication. SAMs were then rinsed liberally with MilliQ H_2O and HPLC MeOH before drying with argon.

7.4 Appendix

7.4.1 DFC synthesis and characterisation

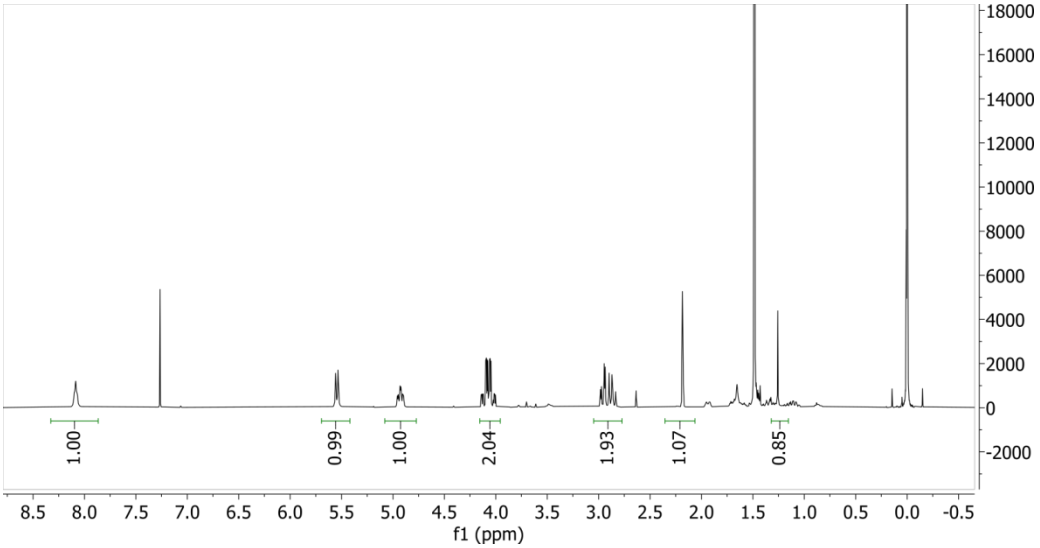


Fig. 84: ^{1}H NMR spectrum of DFC2 ($CDCl_3$, 298K, 400 MHz).

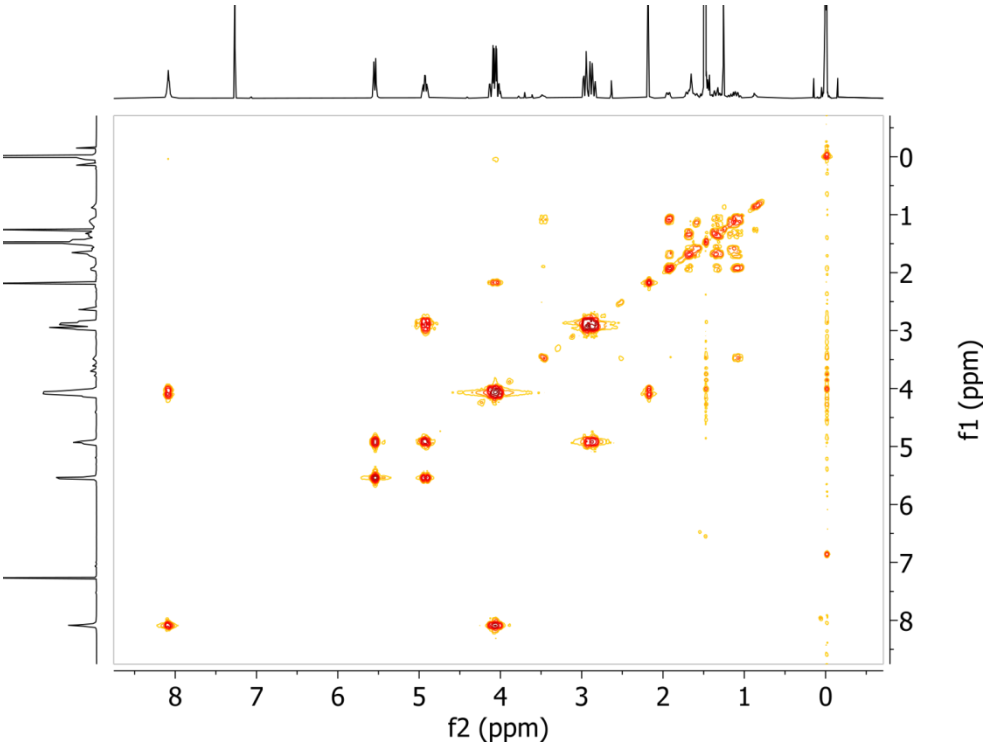


Fig. 85: 2D COSY NMR spectrum of DFC2 ($CDCl_3$, 298K, 400 MHz).

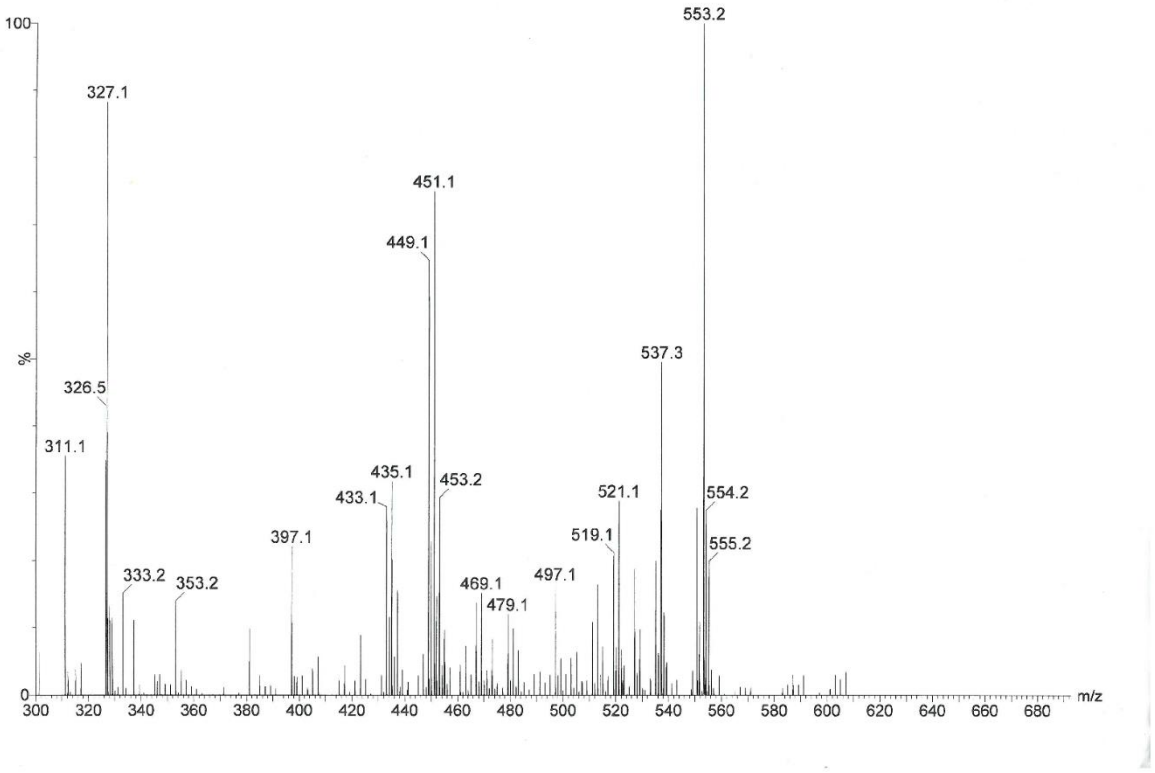


Fig. 86: MALDI-MS spectrum of DFC2.

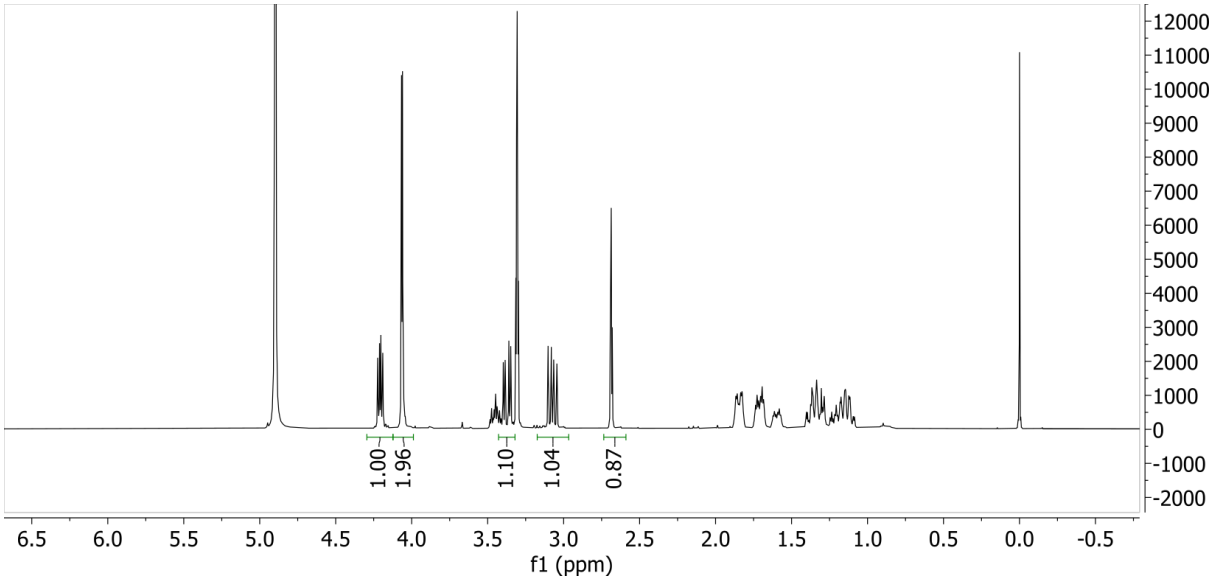


Fig. 87: ^{1}H NMR spectrum of DFC3 (MeOD, 298K, 400 MHz).

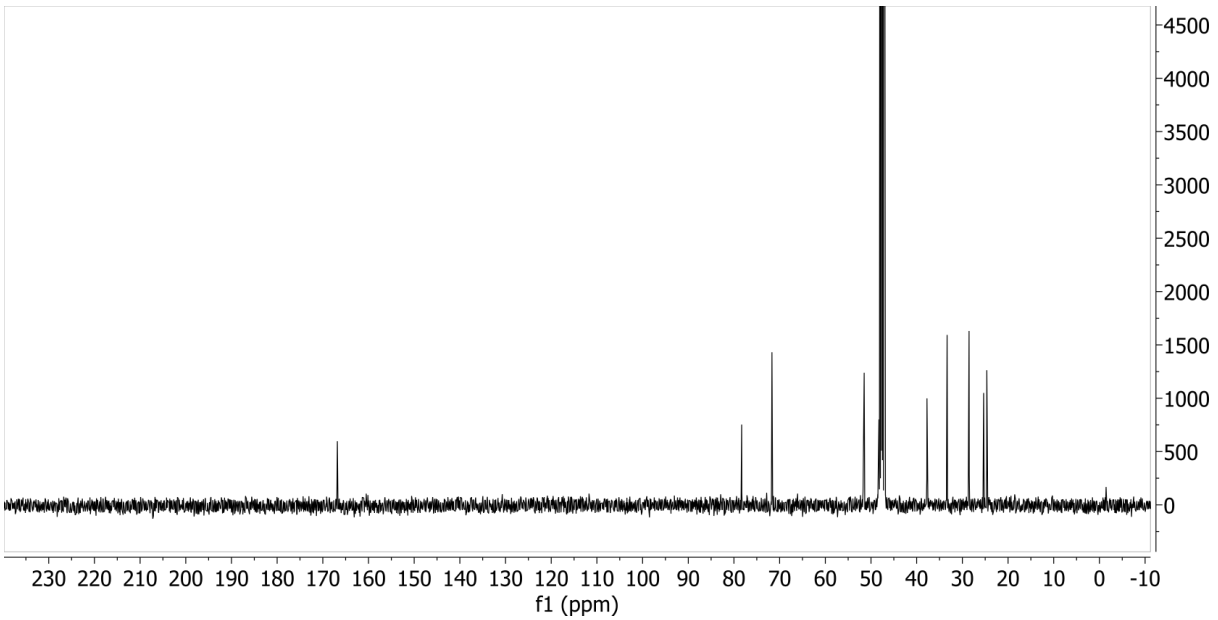


Fig. 88: ^{13}C NMR spectrum of DFC3 (MeOD, 298K, 100 MHz).

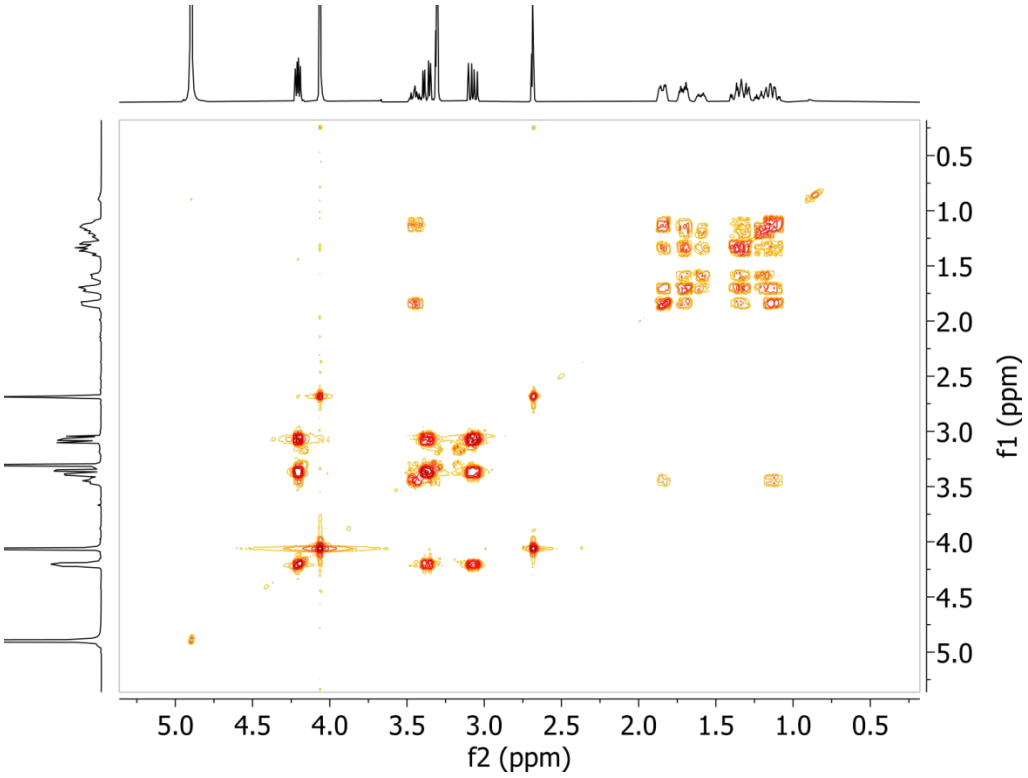


Fig. 89: 2D COSY NMR spectrum of DFC3 (MeOD, 298K, 400 MHz).

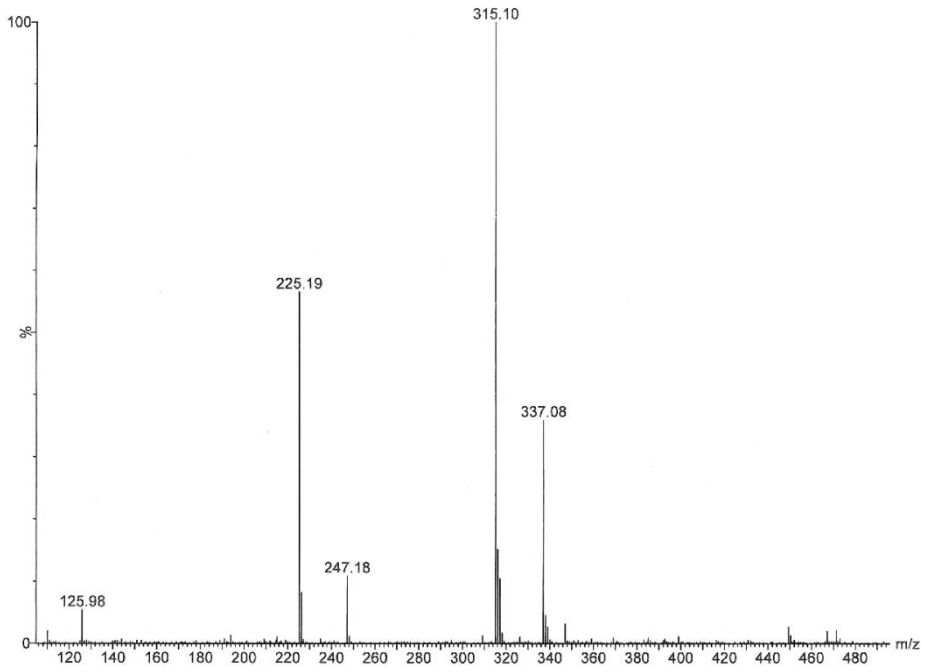


Fig. 90: ESI -(+)MS spectrum of DFC3.

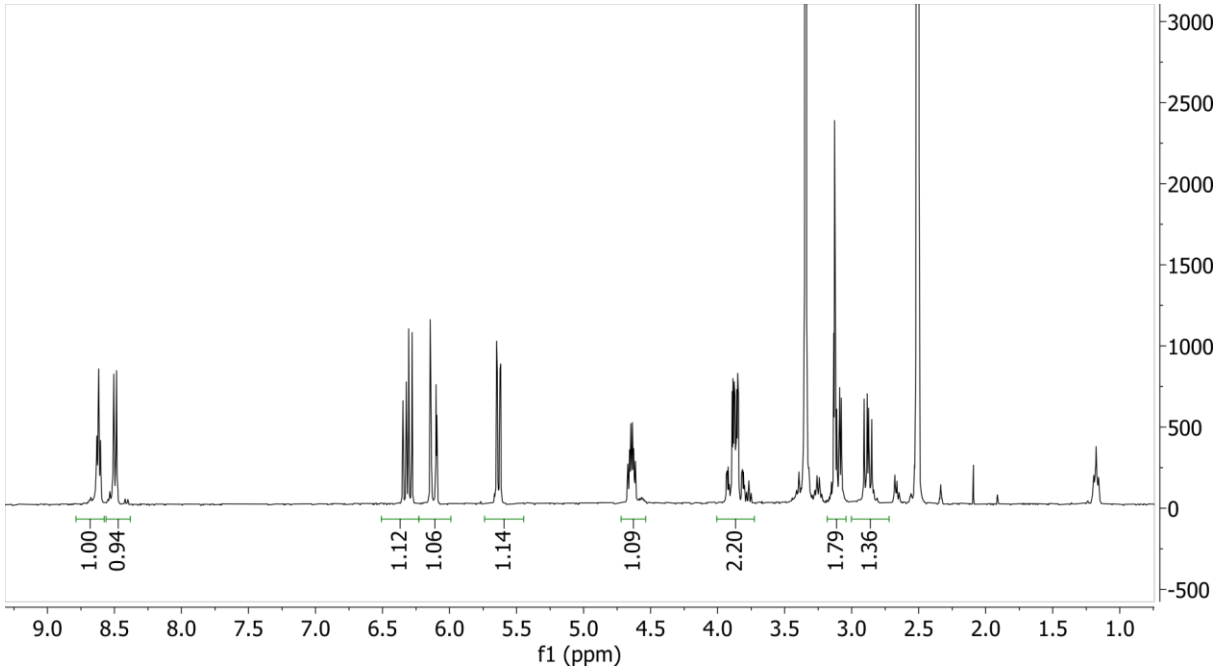


Fig. 91: ^{1}H NMR spectrum of DFC (d6-DMSO, 298K, 400 MHz).

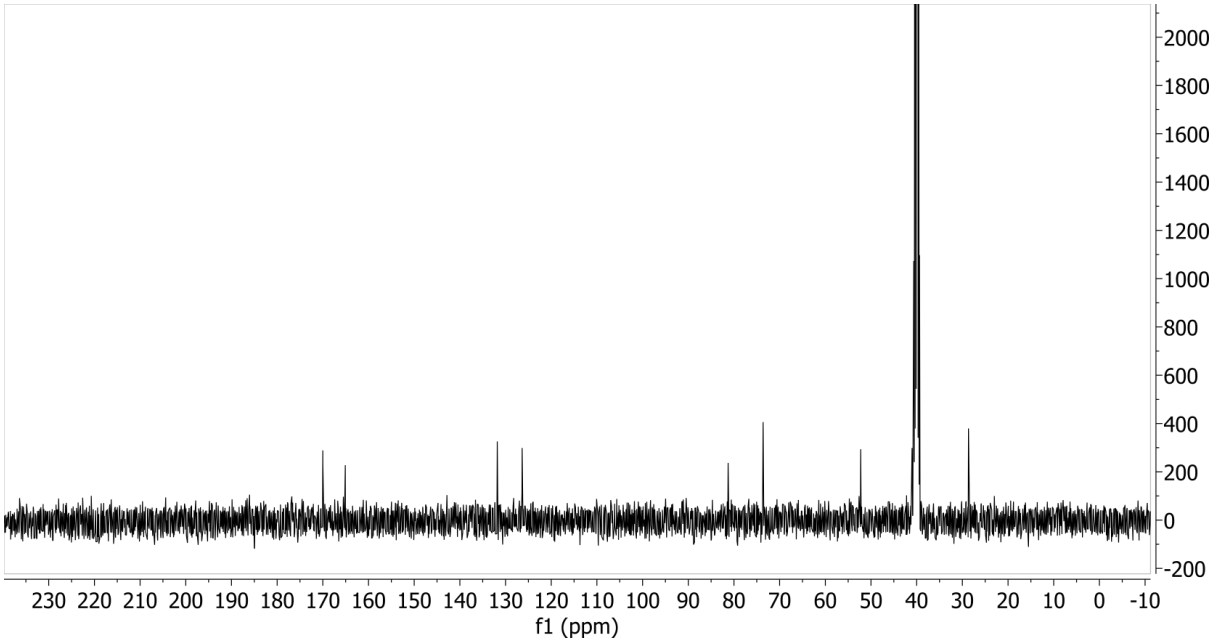


Fig. 92: ^{13}C NMR spectrum of DFC (d6-DMSO, 298K, 100 MHz).

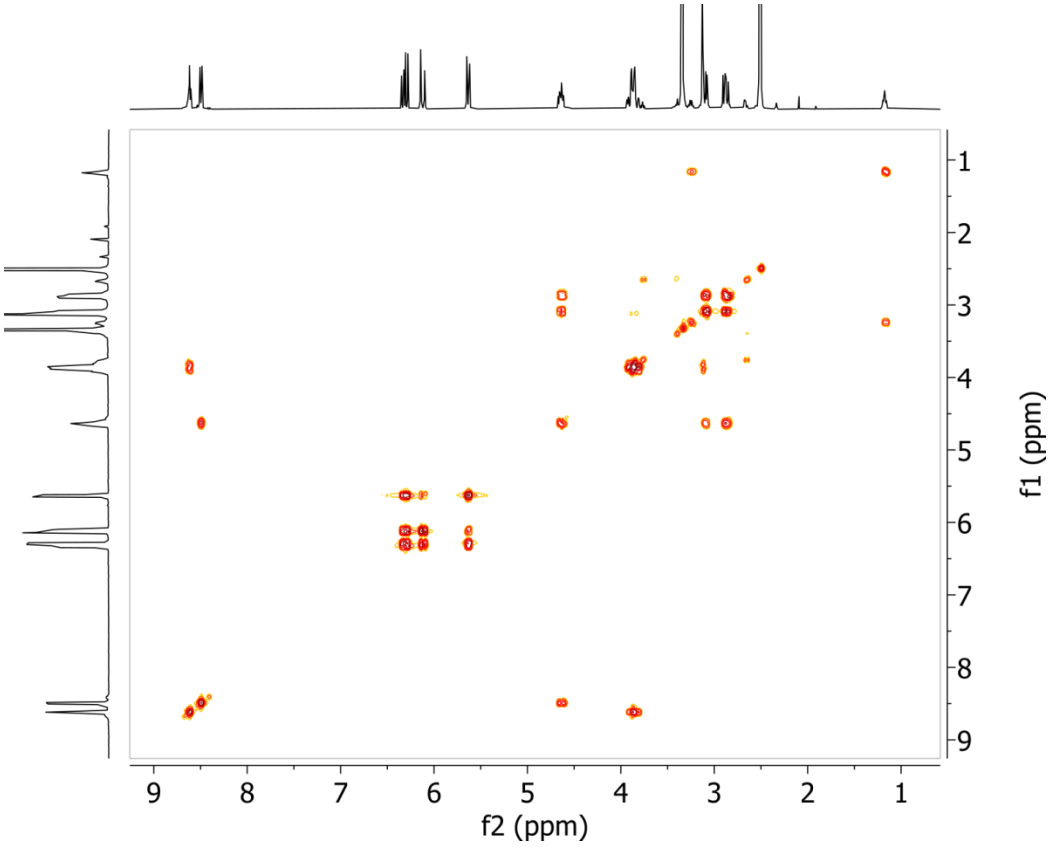


Fig. 93: 2D COSY NMR spectrum of DFC (d6-DMSO, 298K, 400 MHz).

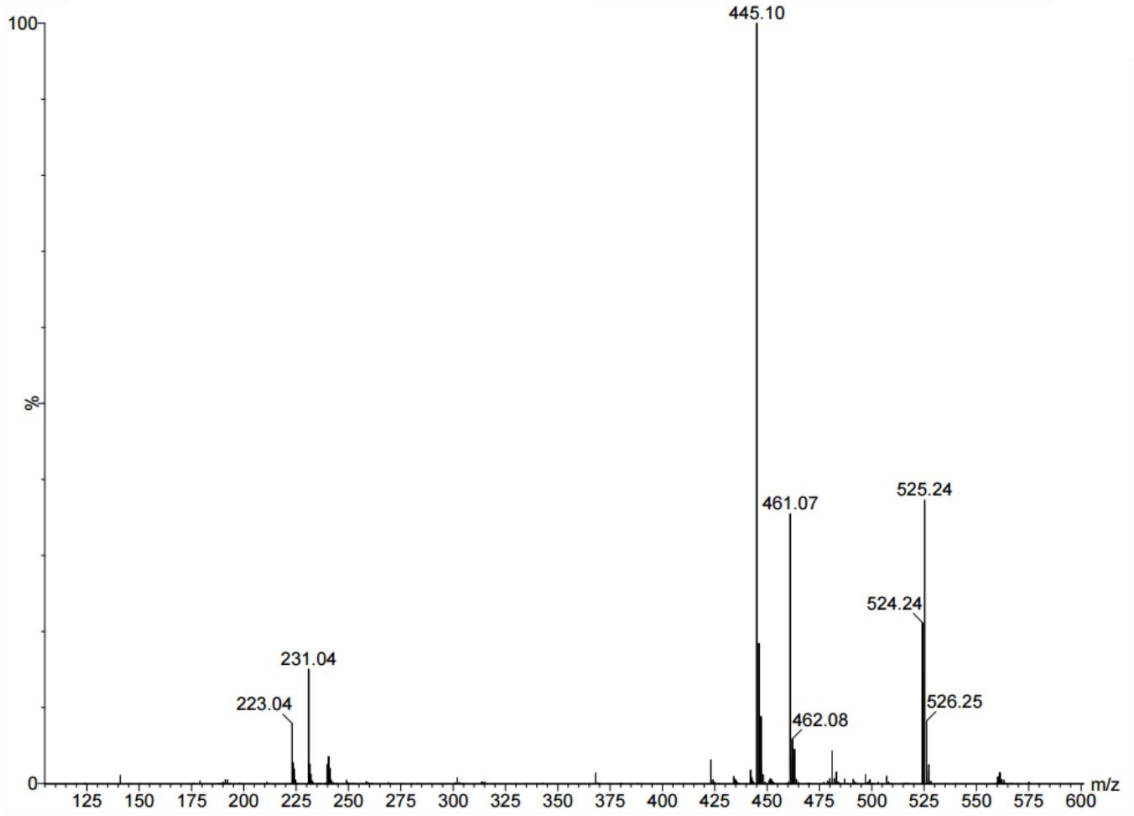


Fig. 94: ESI –(+)MS spectrum of DFC.

7.4.2 Characterisation of DTPAlk

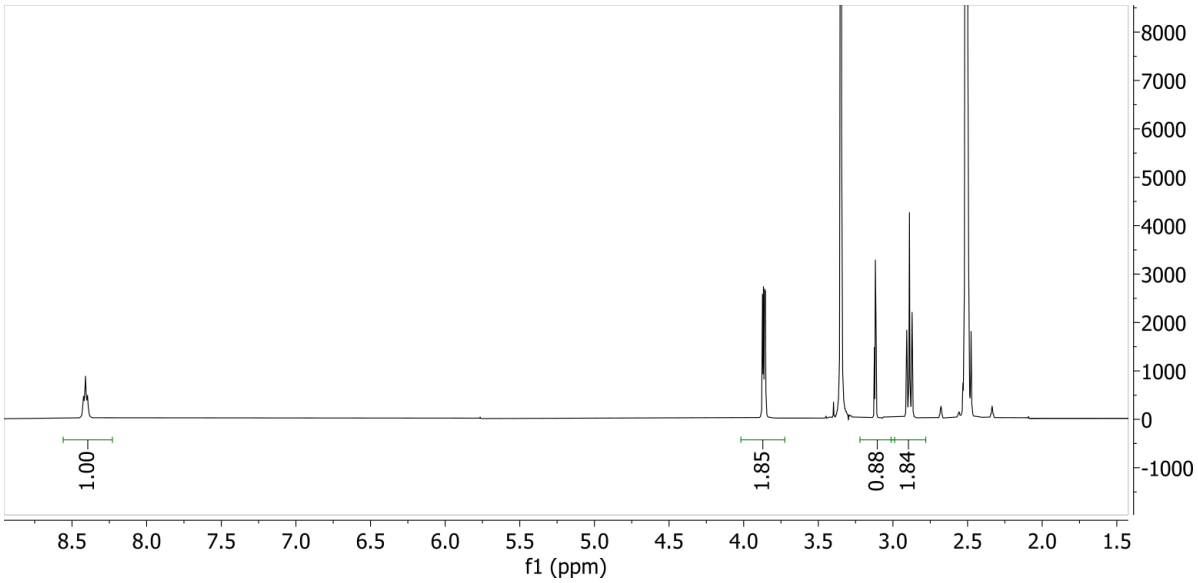


Fig. 95: ^{1}H NMR spectrum of DTPAlk (d6-DMSO, 298K, 400 MHz).

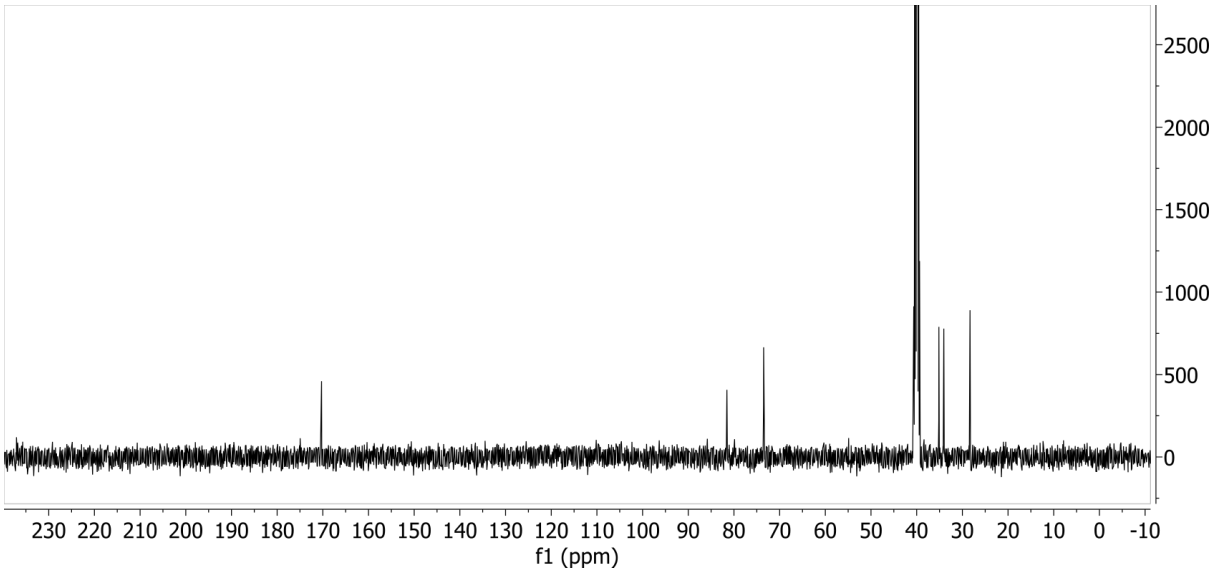


Fig. 96: ^{13}C NMR spectrum of DTPAlk (d6-DMSO, 298K, 100 MHz).

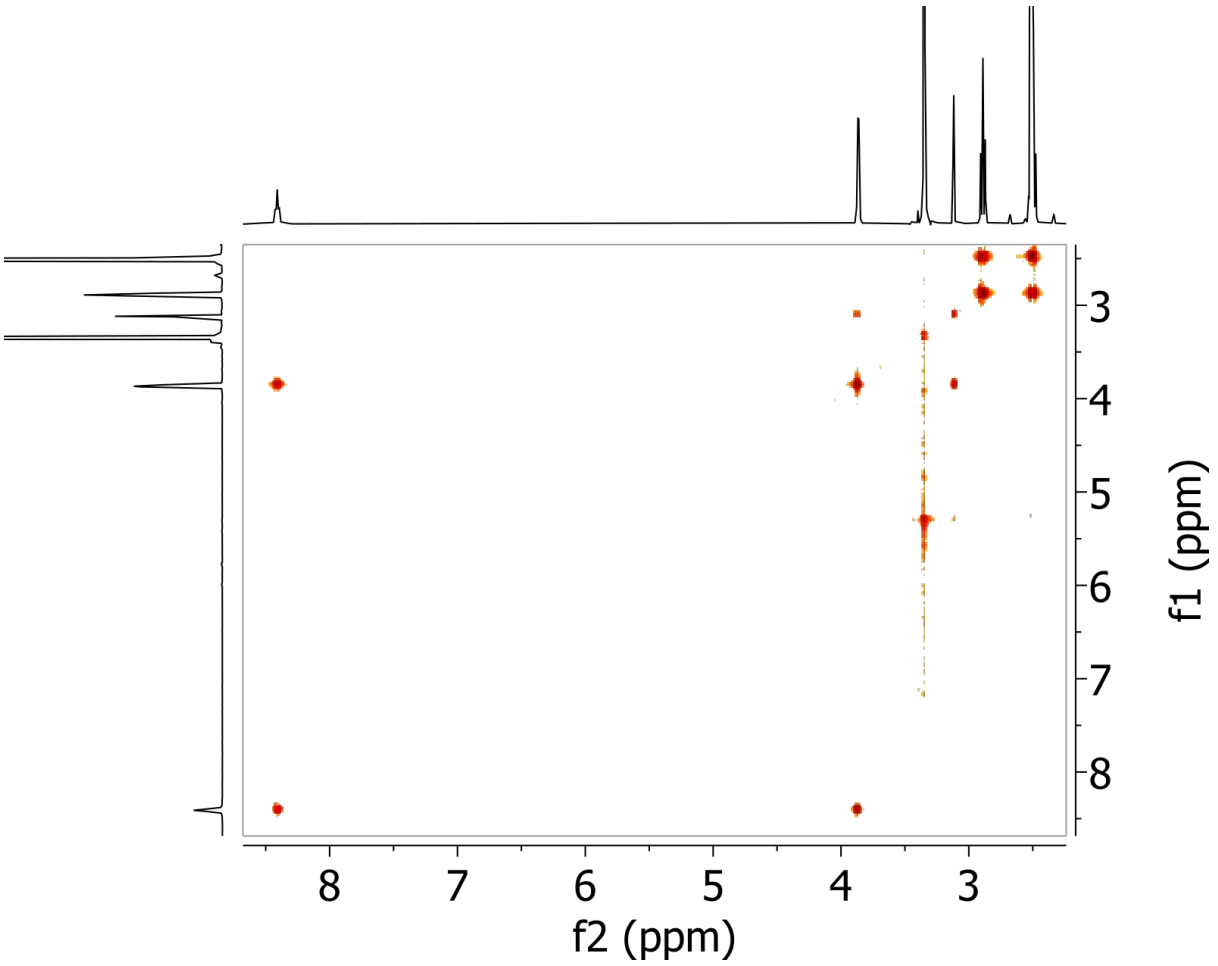


Fig. 97: 2D COSY NMR spectrum of DTPAlk (d6-DMSO, 298K, 400 MHz).

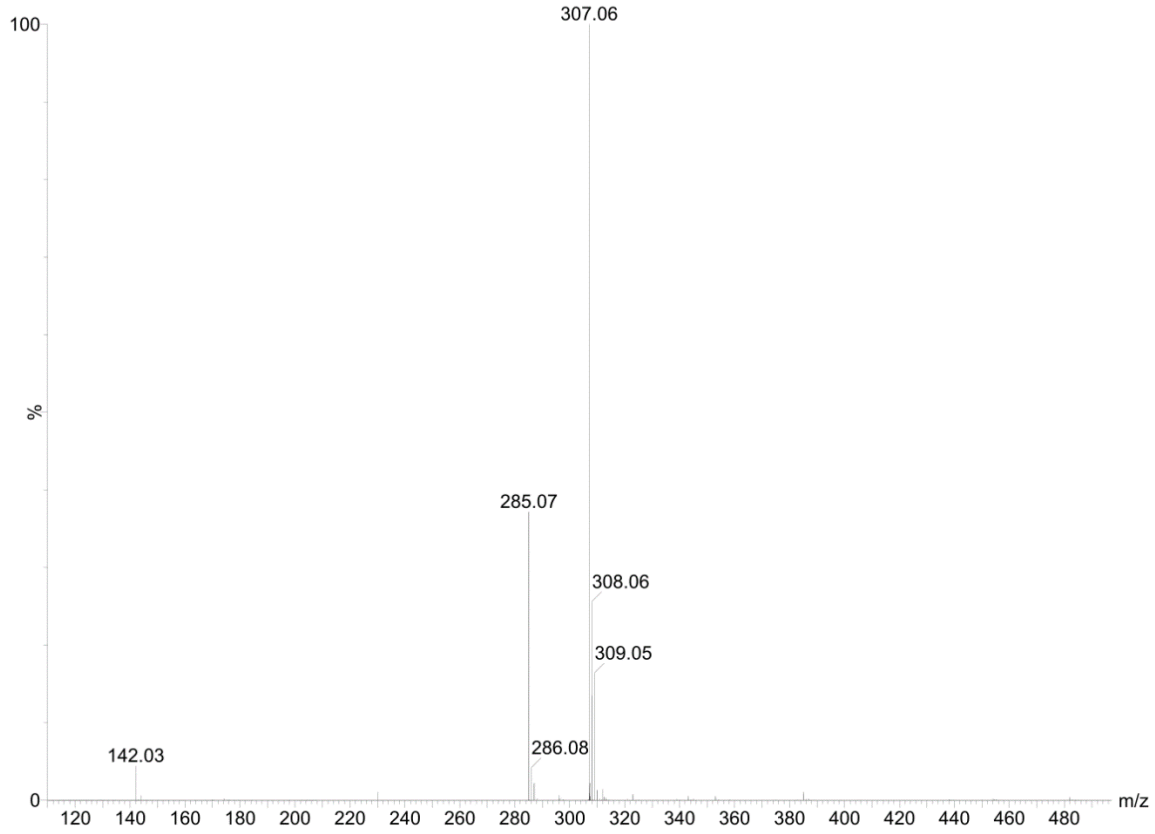


Fig. 98: ESI -(+)MS spectrum of DTPAlk.

7.4.3 Characterisation of MBDAlk

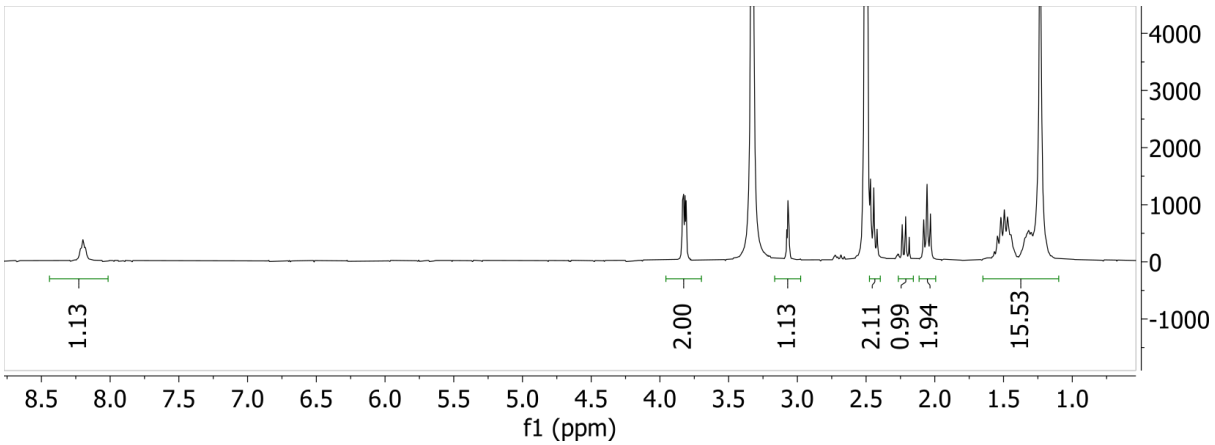


Fig. 99: ^{1}H NMR spectrum of MBDAlk (d6-DMSO, 298K, 300 MHz).

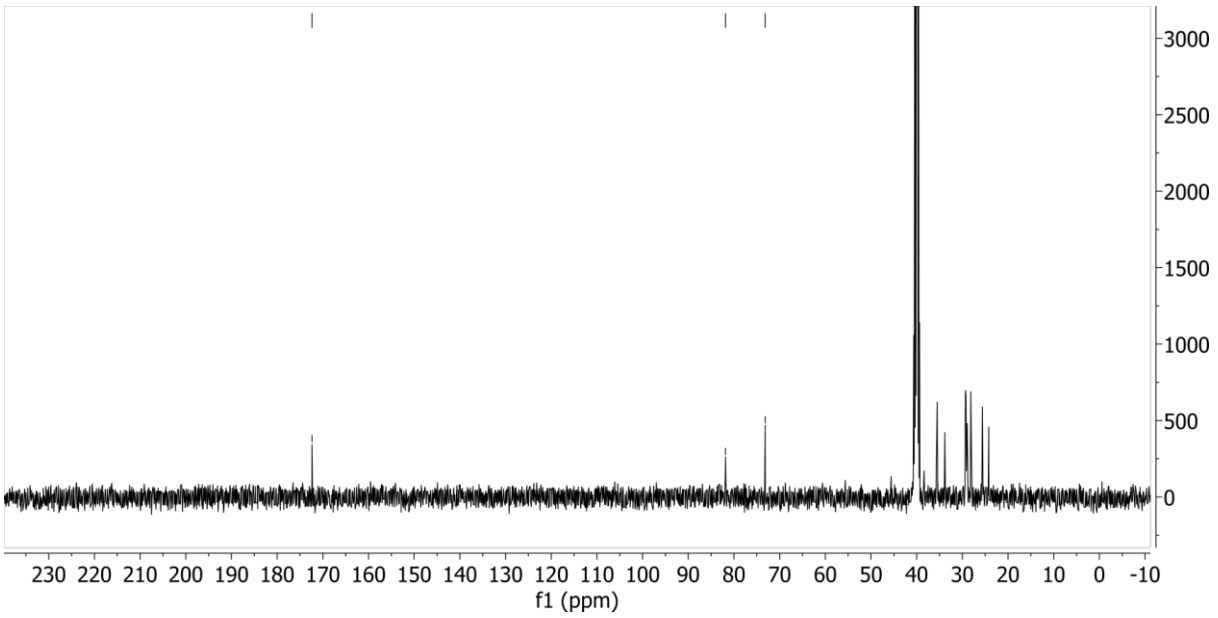


Fig. 100: ^{13}C NMR spectrum of MBDAlk (d6-DMSO, 298K, 100 MHz).

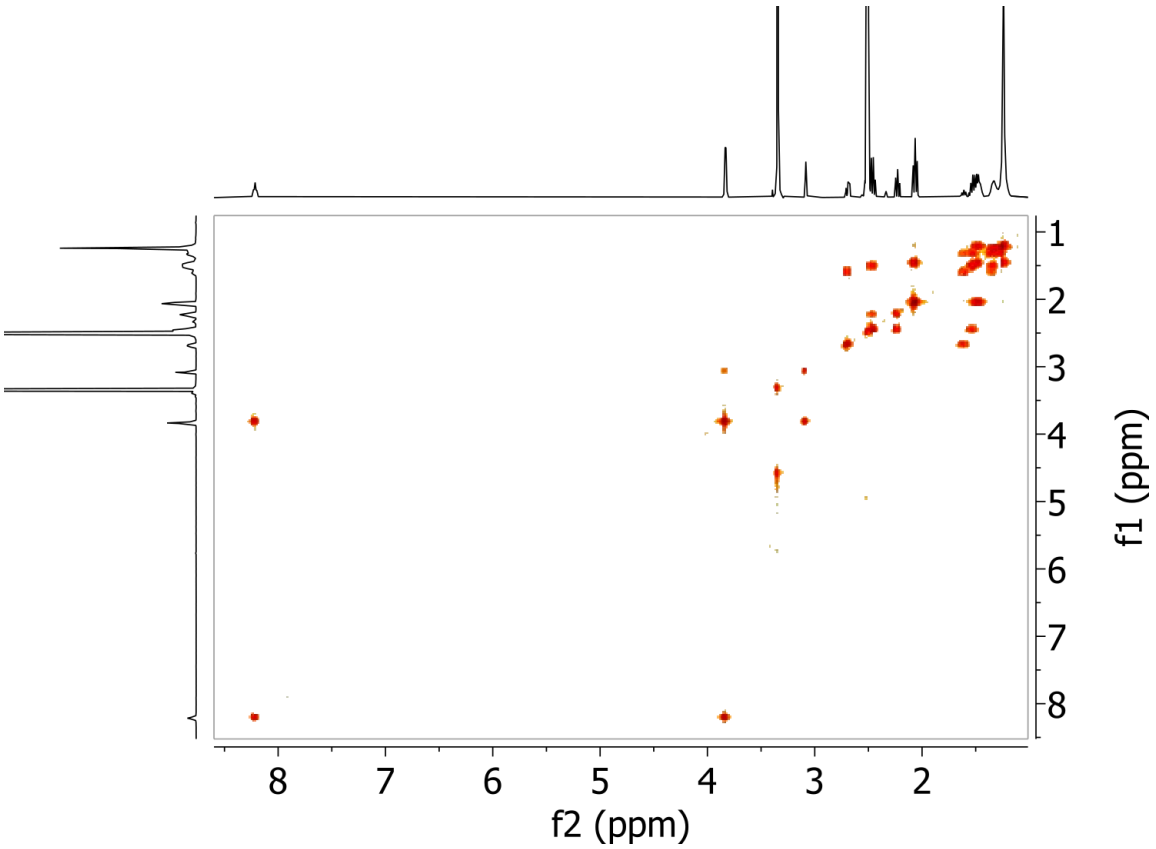


Fig. 101: 2D COSY NMR spectrum of MBDAlk (d6-DMSO, 298K, 400 MHz).

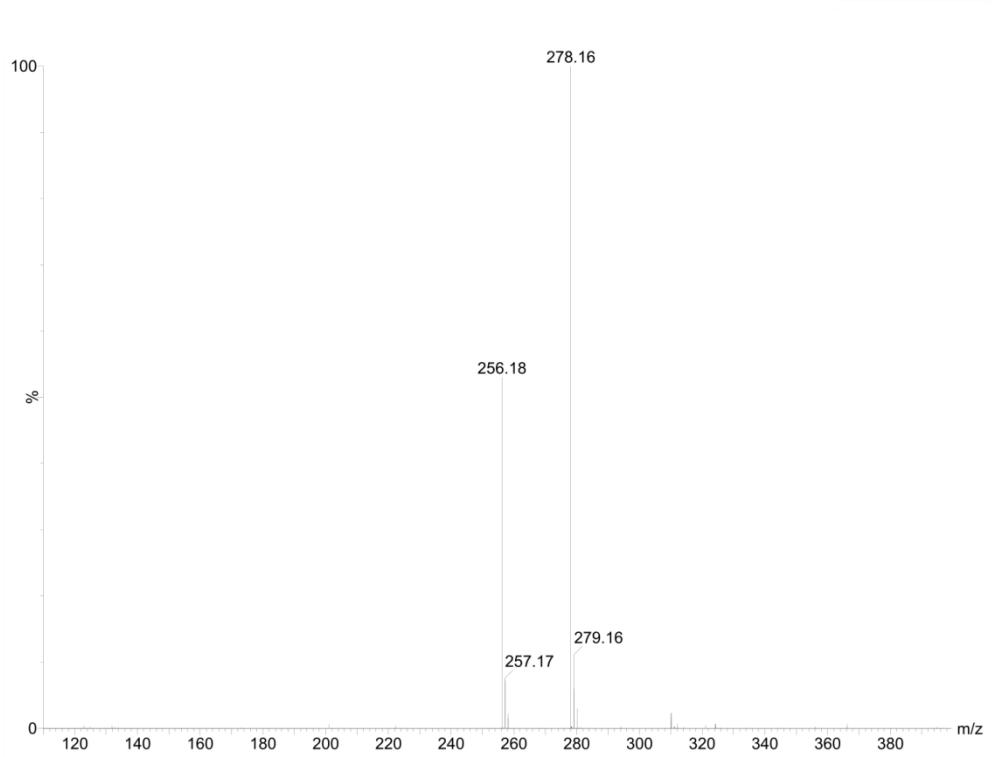


Fig. 102: ESI -(+)MS spectrum of MBDAlk.

7.4.4 Characterisation of pMBDAlk

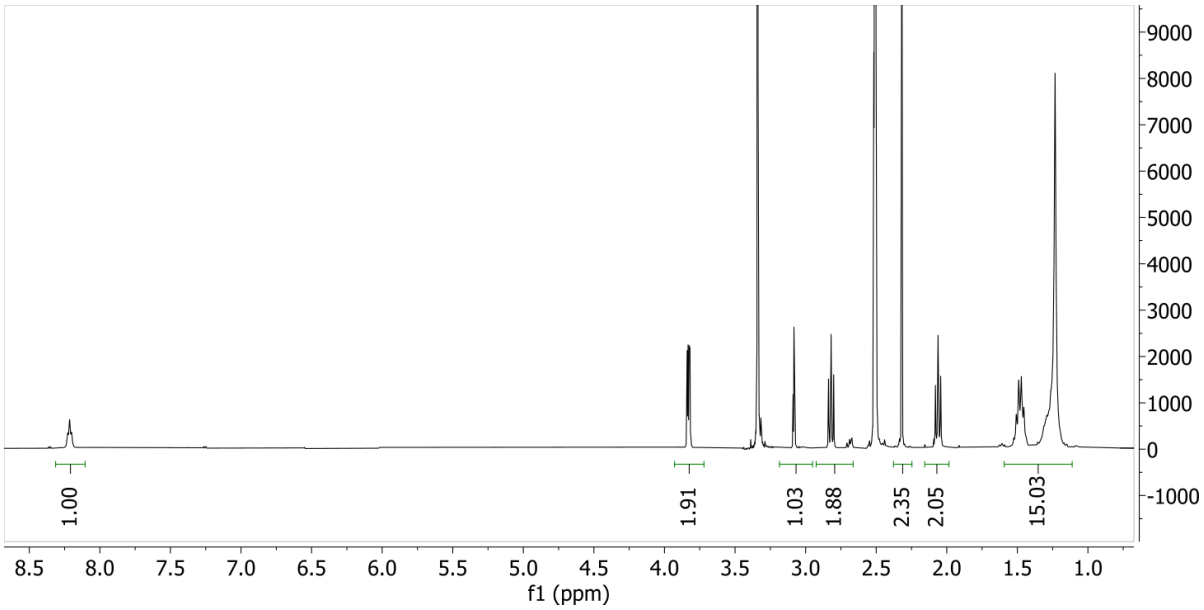


Fig. 103: ^{1}H NMR spectrum of pMBDAlk (d6-DMSO, 298K, 300 MHz).

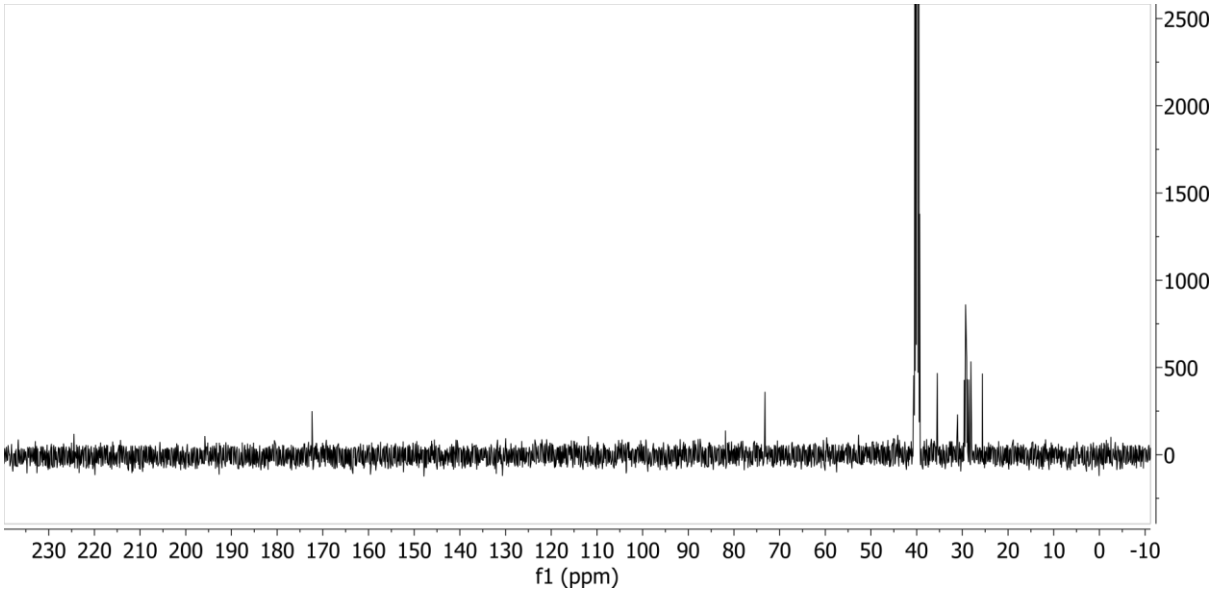


Fig. 104: ^{13}C NMR spectrum of pMBDAlk (d6-DMSO, 298K, 100 MHz).

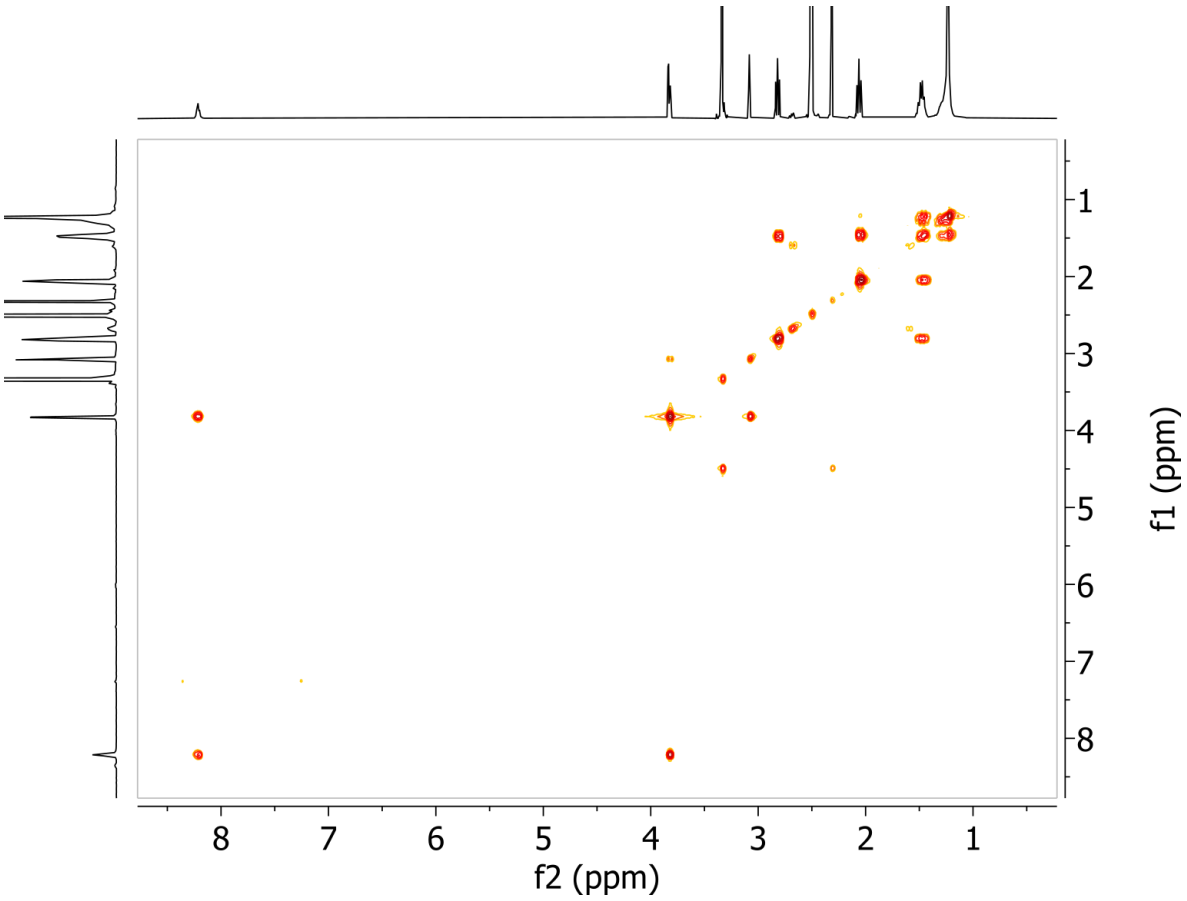


Fig. 105: 2D COSY NMR spectrum of pMBDAlk (d6-DMSO, 298K, 400 MHz).

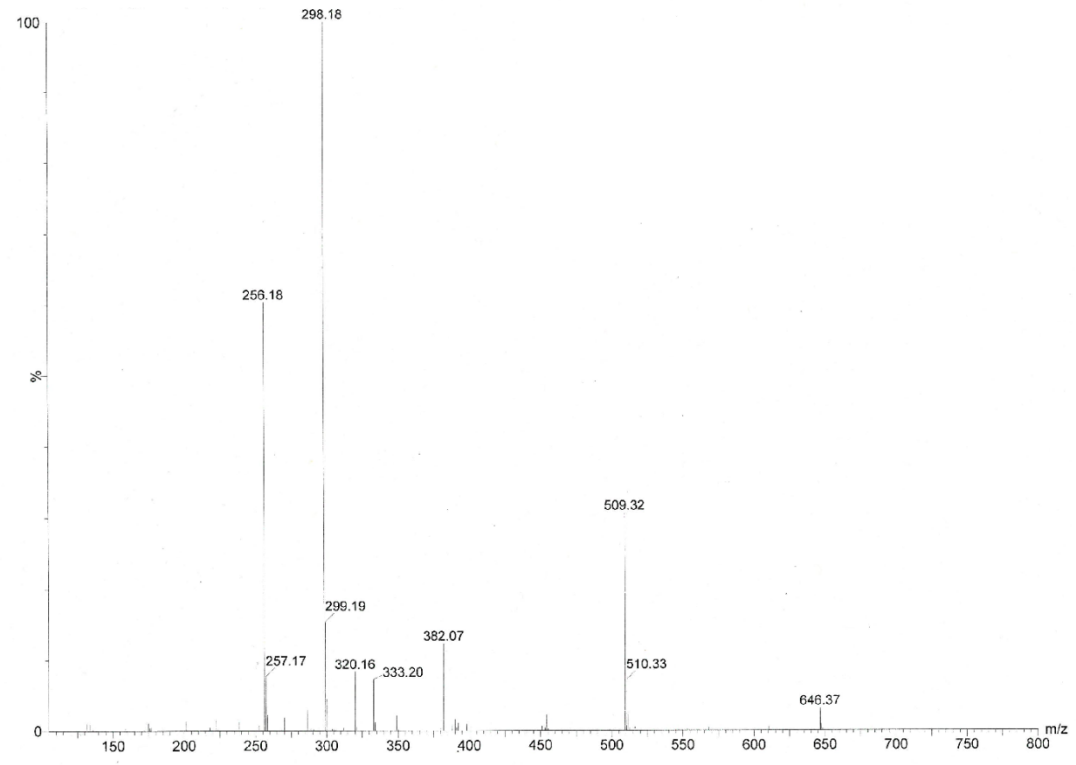


Fig. 106: ESI -(+)MS spectrum of pMBDAlk.

7.4.4 Characterisation of AzBEN

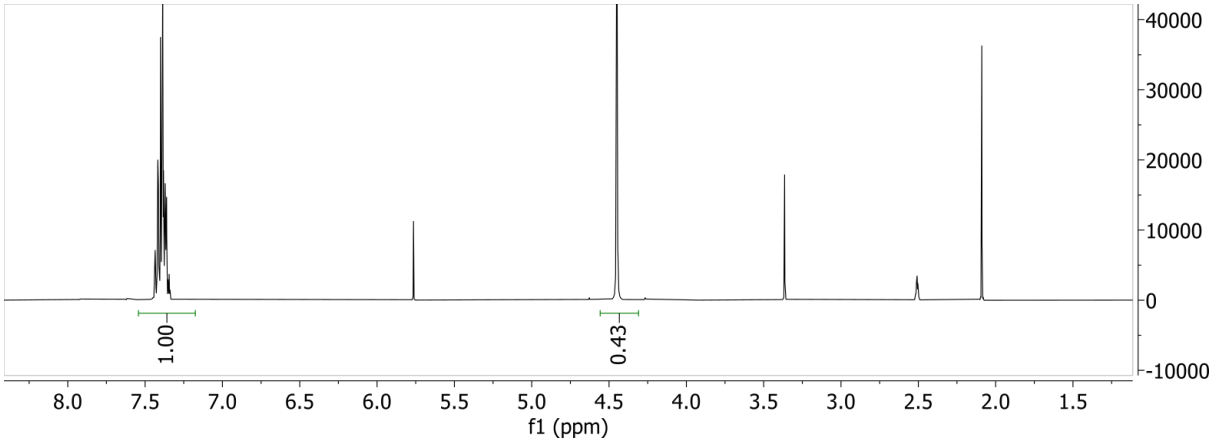


Fig. 107: ^{1}H NMR spectrum of AzBEN (d6-DMSO, 298K, 300 MHz).

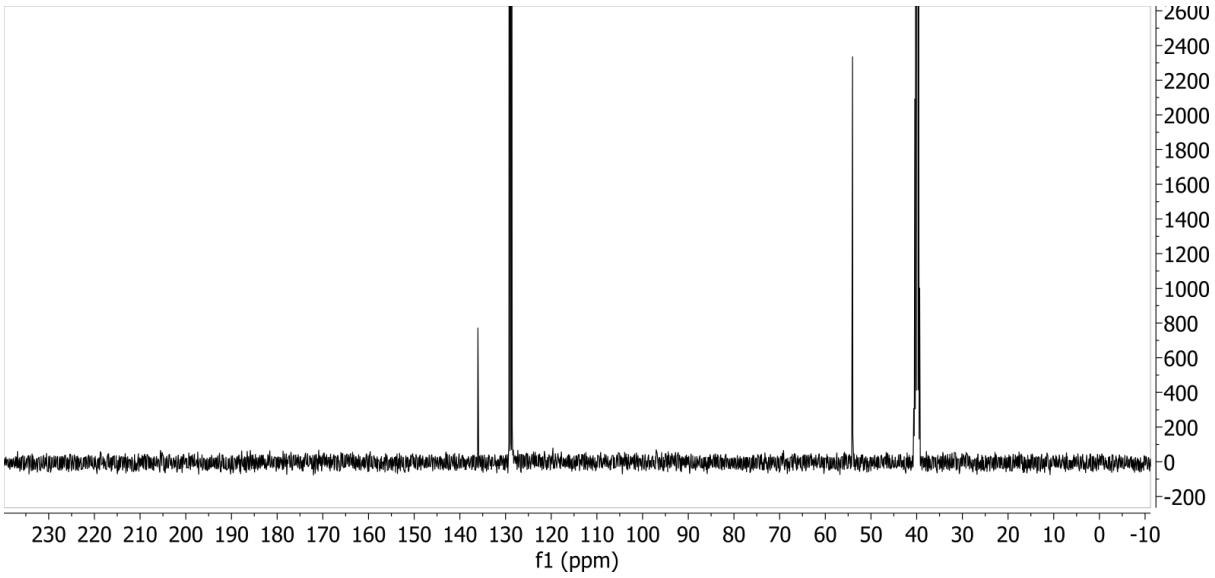


Fig. 108: ^{13}C NMR spectrum of AzBEN (d6-DMSO, 298K, 100 MHz).

7.4.5 Characterisation of AzBA

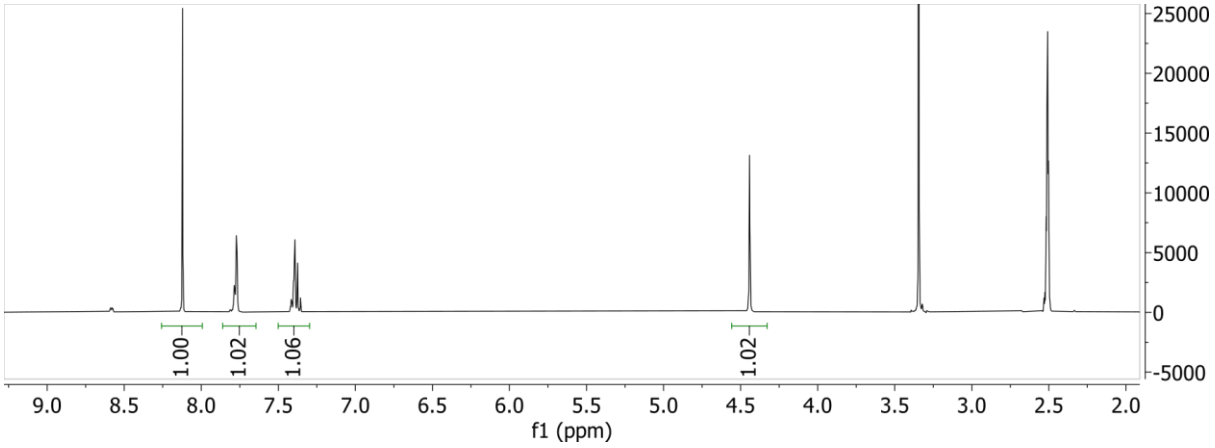


Fig. 109: ^{1}H NMR spectrum of AzBA (d6-DMSO, 298K, 400 MHz).

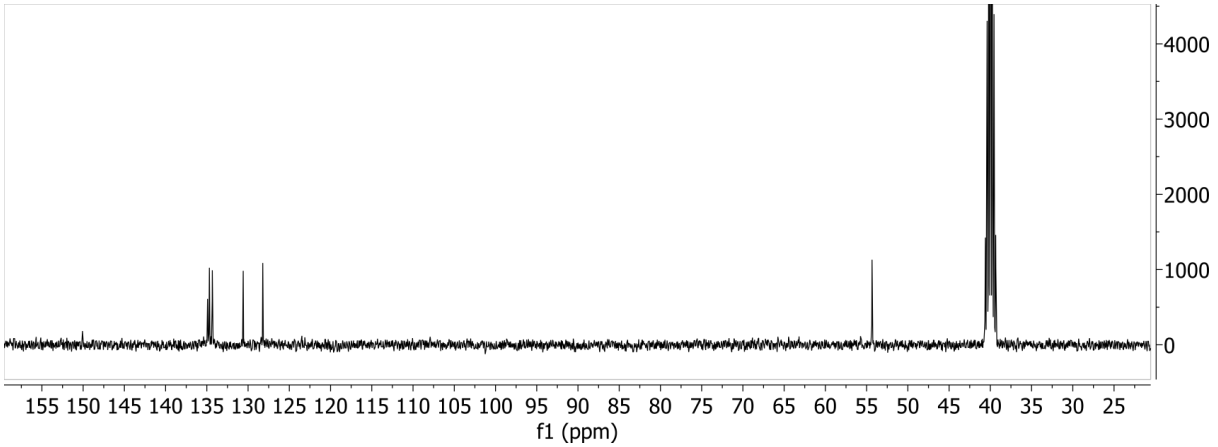


Fig. 110: ^{13}C NMR spectrum of AzBA (d6-DMSO, 298K, 100 MHz).

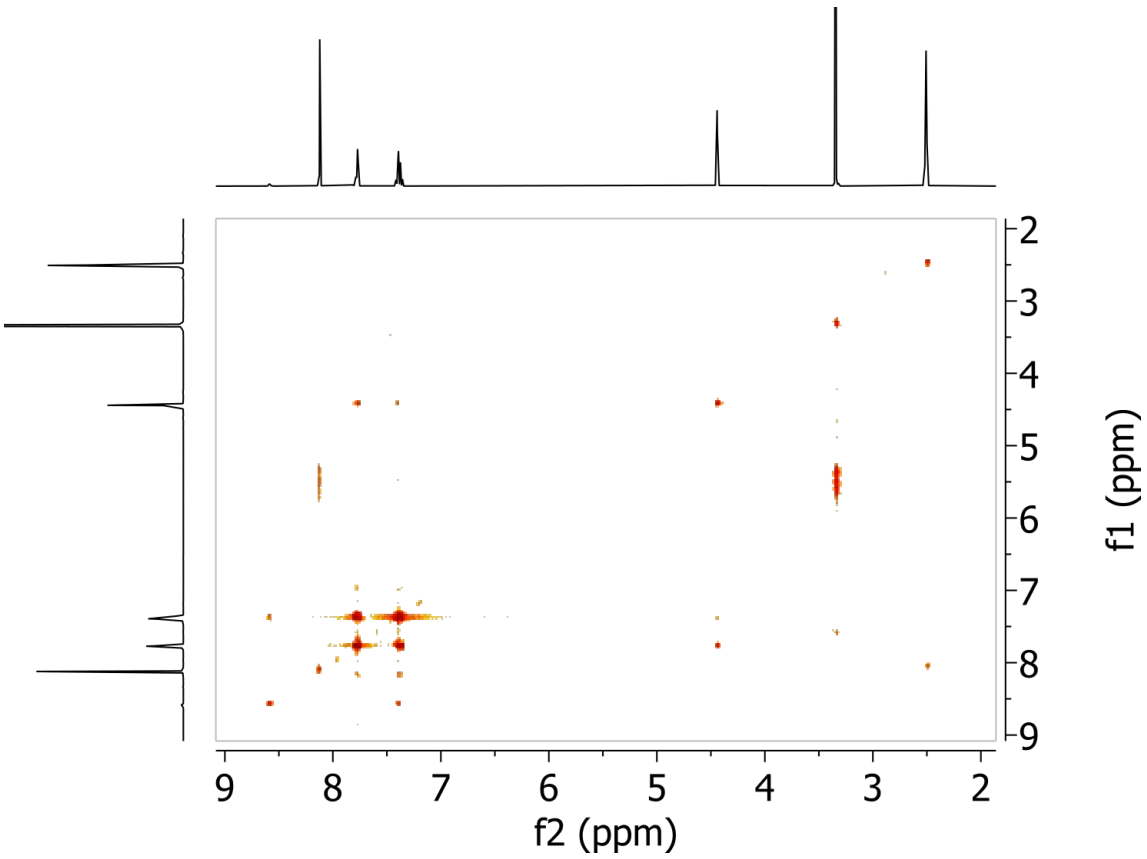


Fig. 111: 2D COSY NMR spectrum of AzBA (d6-DMSO, 298K, 400 MHz).

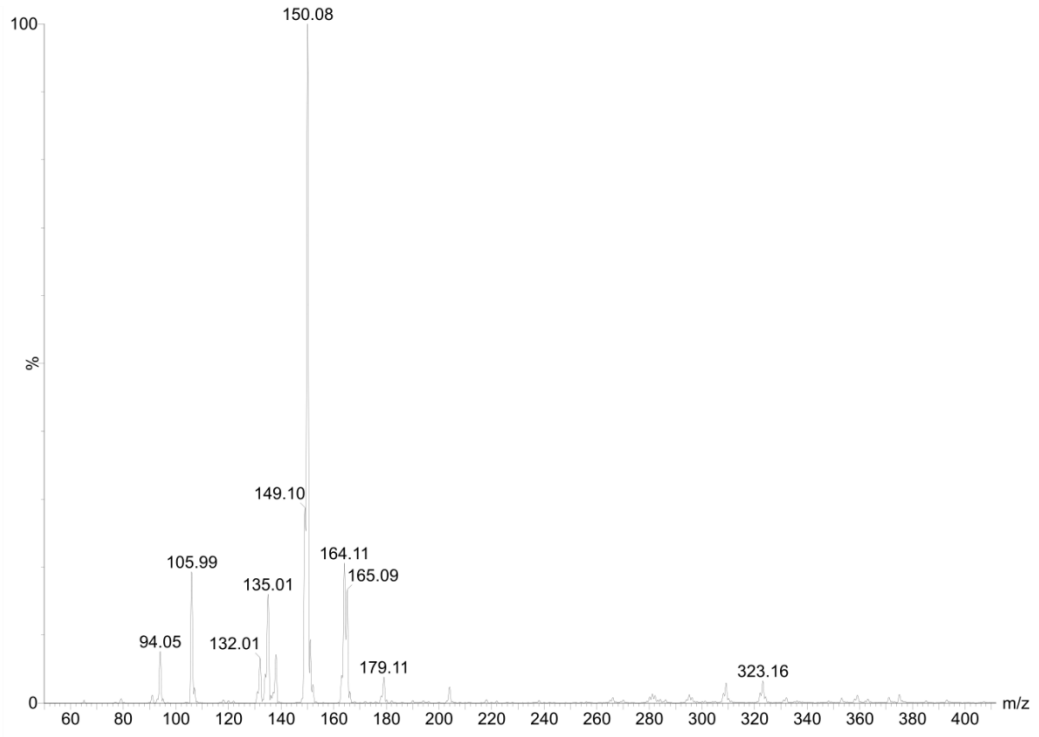


Fig. 112: ESI -(+)MS spectrum for AzBA.

7.4.6 Characterisation of pinAzBA

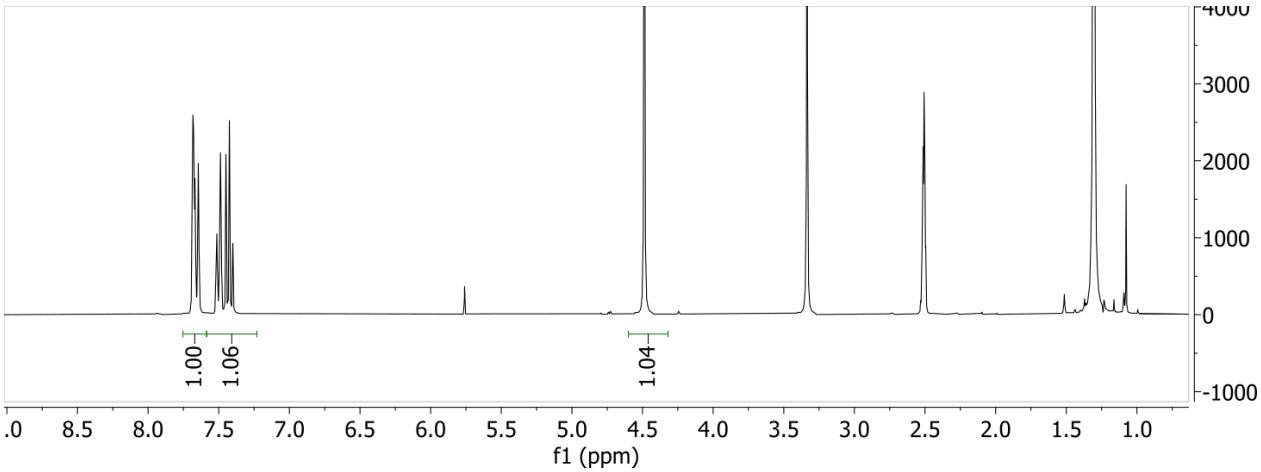


Fig. 113: ^{1}H NMR spectrum of pinAzBA (d6-DMSO, 298K, 300 MHz).

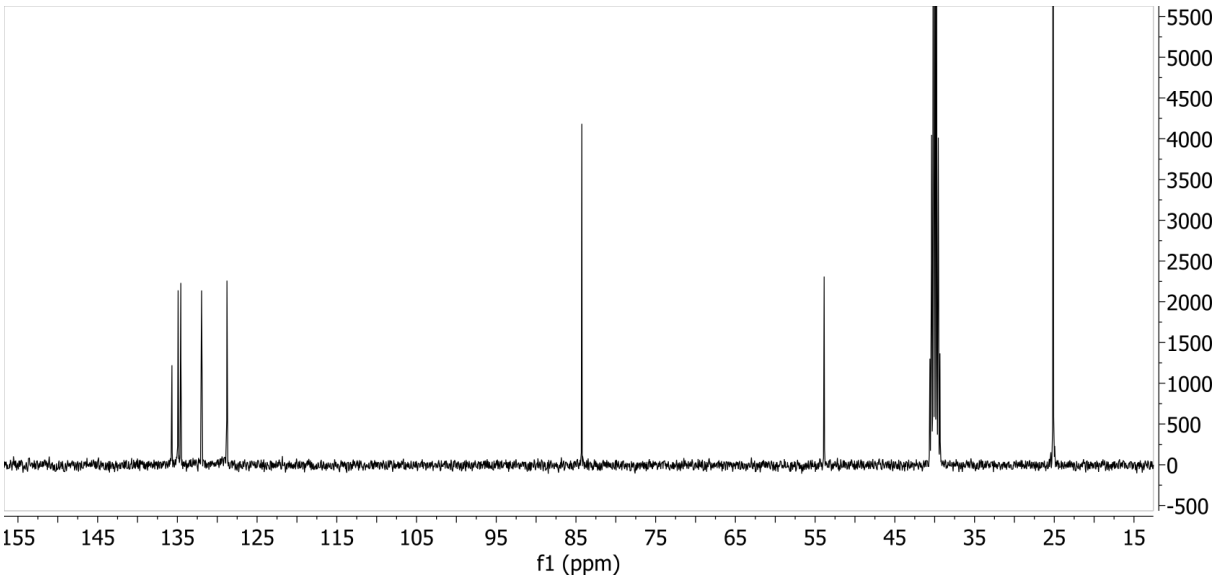


Fig. 114: ^{13}C NMR spectrum of pinAzBA (d6-DMSO, 298K, 100 MHz).

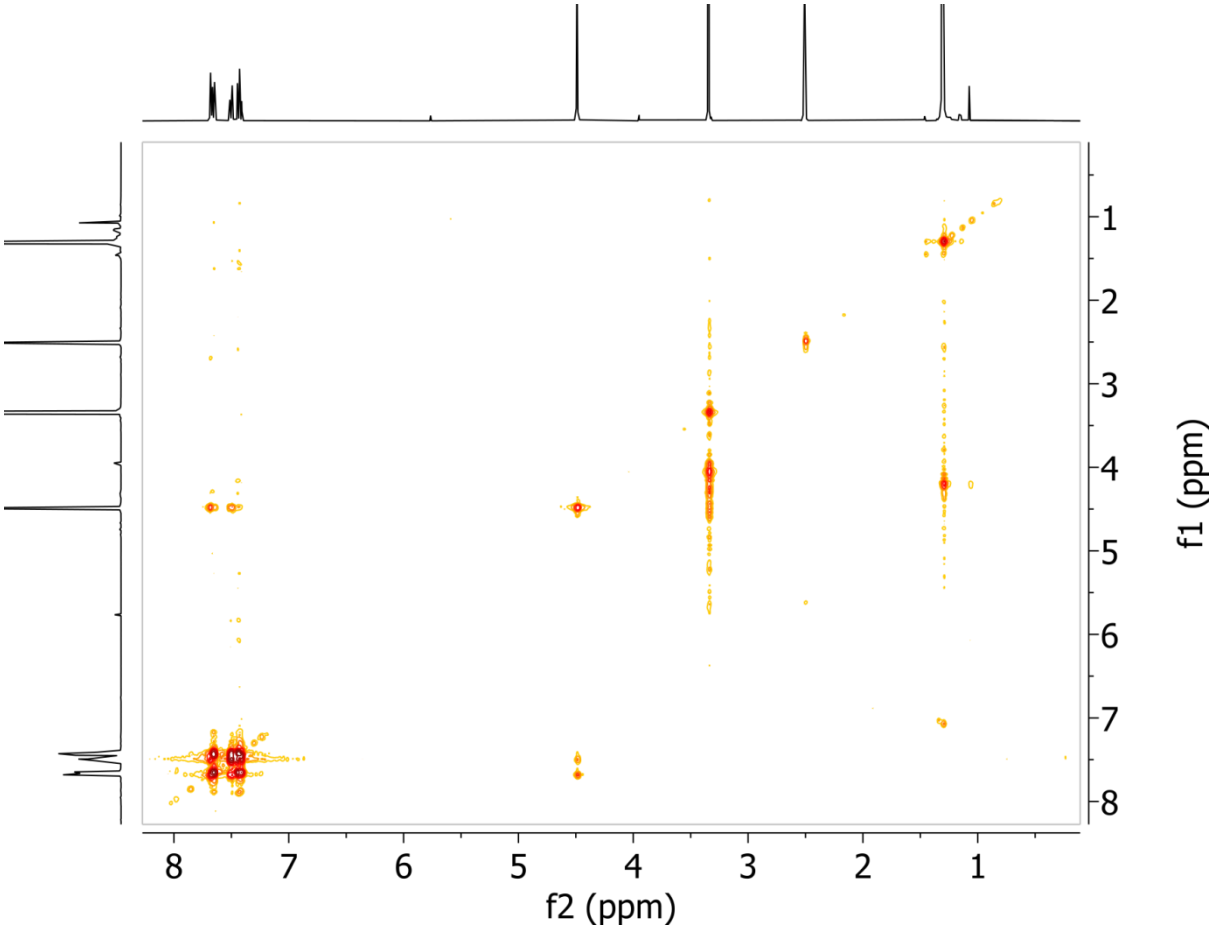


Fig. 115: 2D COSY NMR spectrum of pinAzBA (d6-DMSO, 298K, 400 MHz).

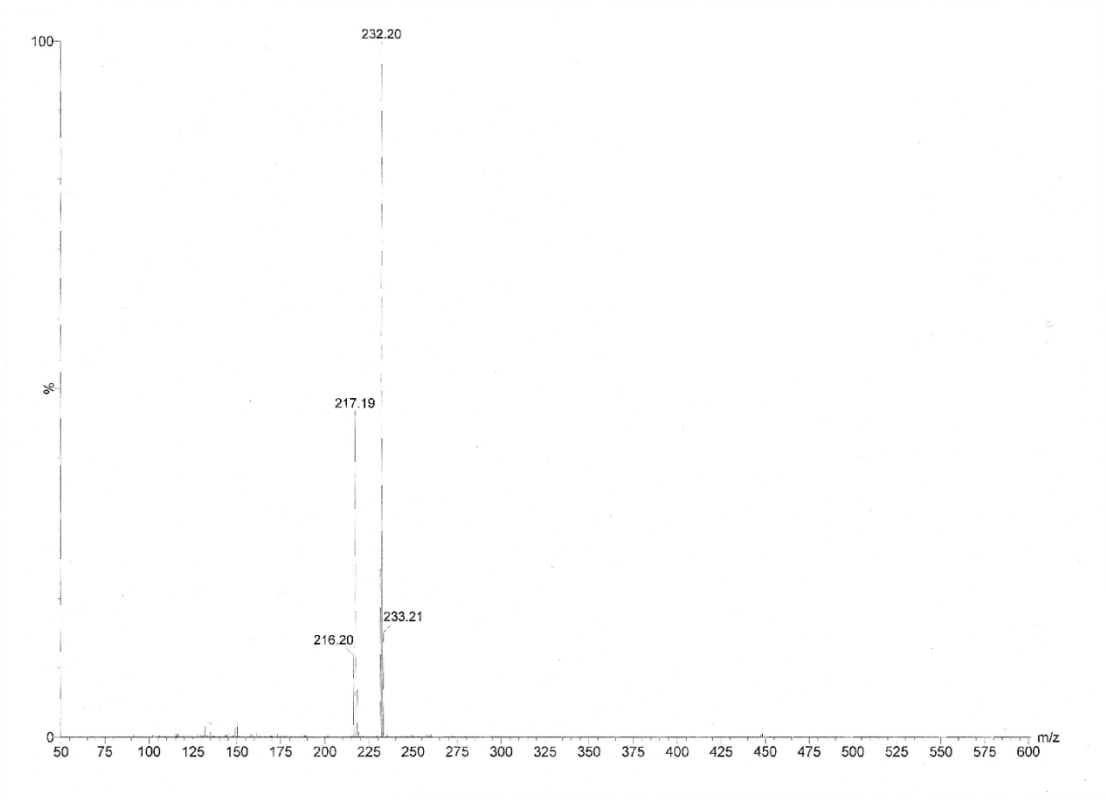


Fig. 116: ESI -(+)MS spectrum of pinAzBA.

7.4.7 Characterisation of DcB

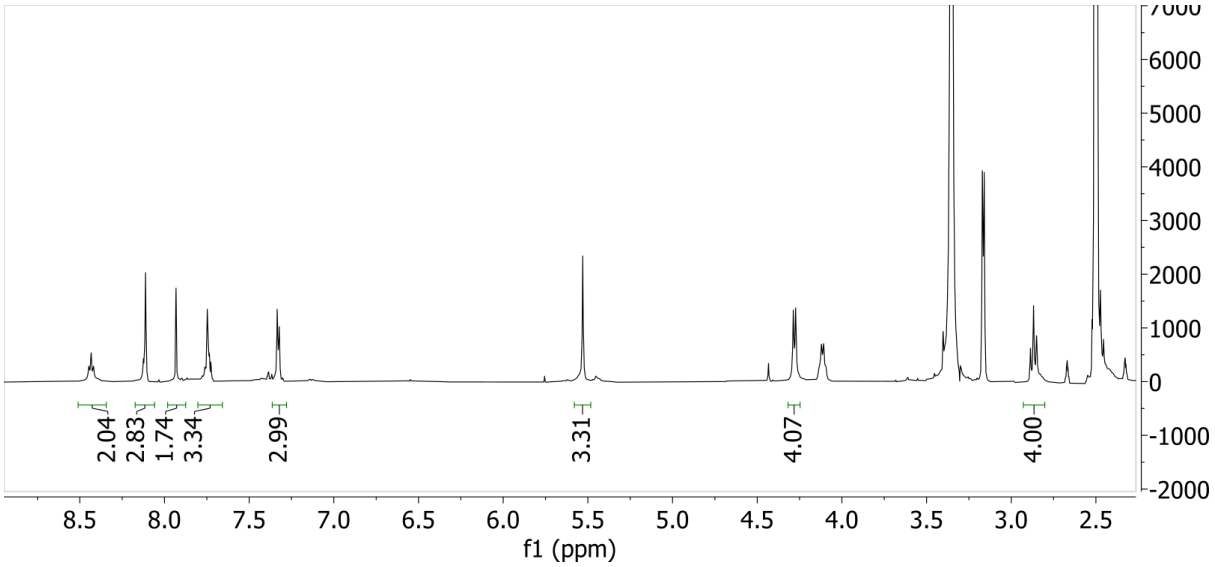


Fig. 117: ^{1}H NMR spectrum of DcB (d6-DMSO, 298K, 400 MHz).

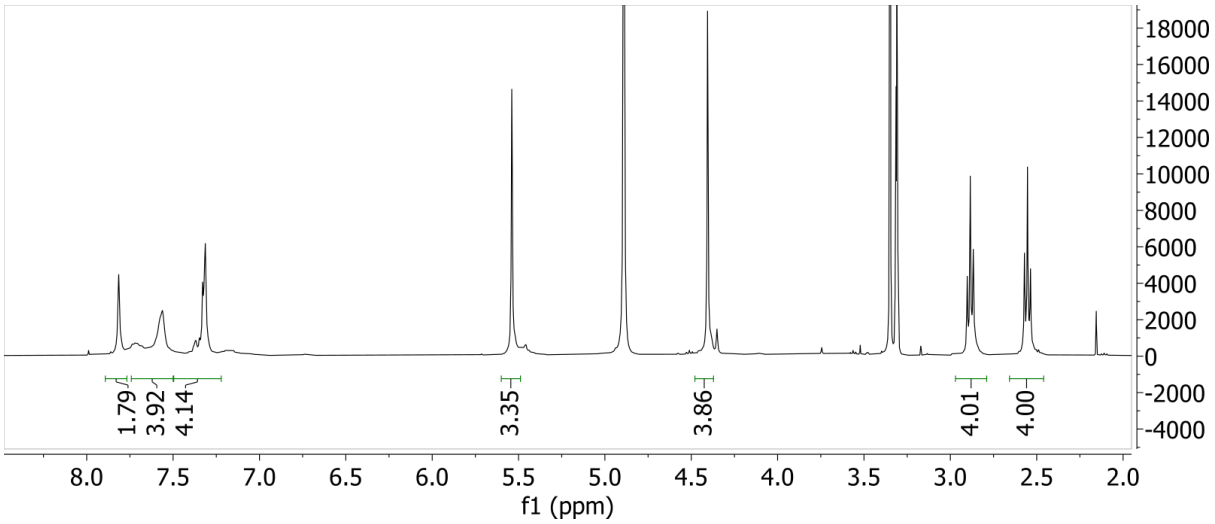


Fig. 118: ^{1}H NMR spectrum of DcB (MeOD, 298K, 400 MHz).

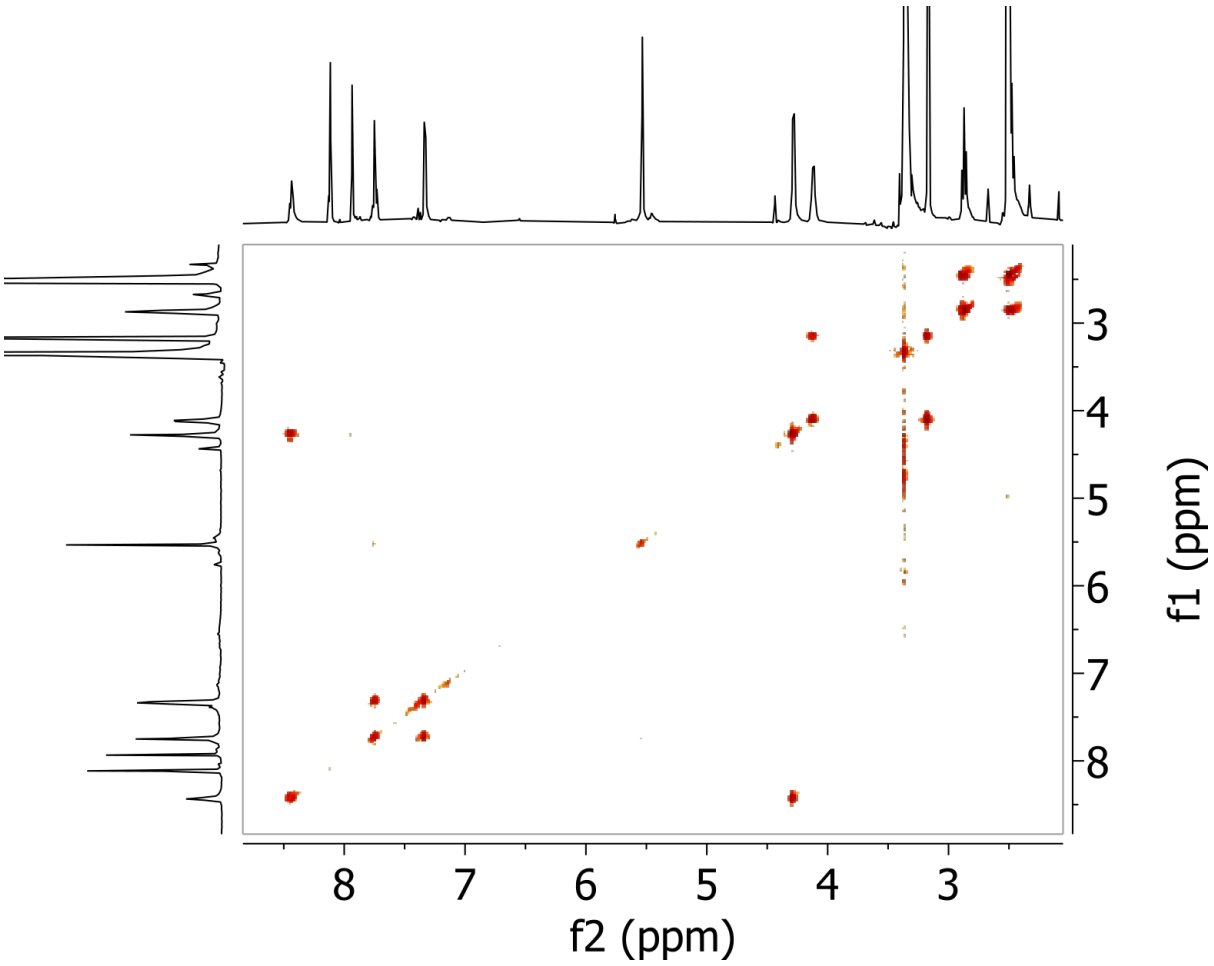


Fig. 119: 2D COSY NMR spectrum of DcB (d6-DMSO, 298K, 400 MHz).

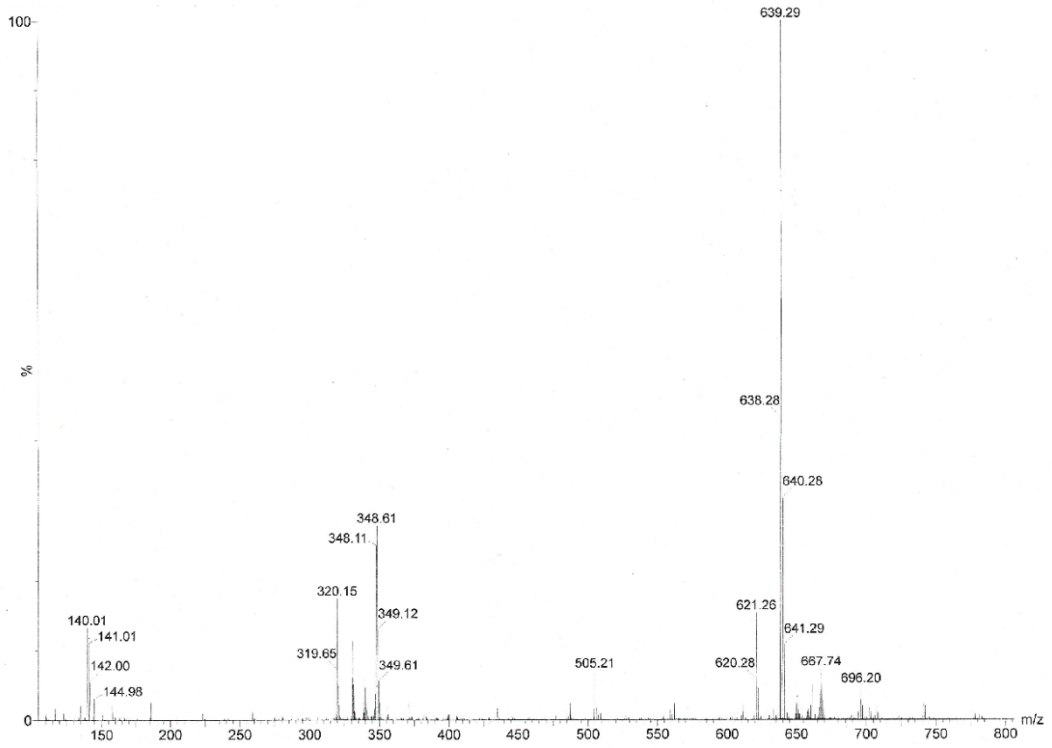


Fig. 120: ESI -(+)MS spectrum of DcB.

7.4.8 Characterisation of pMcB

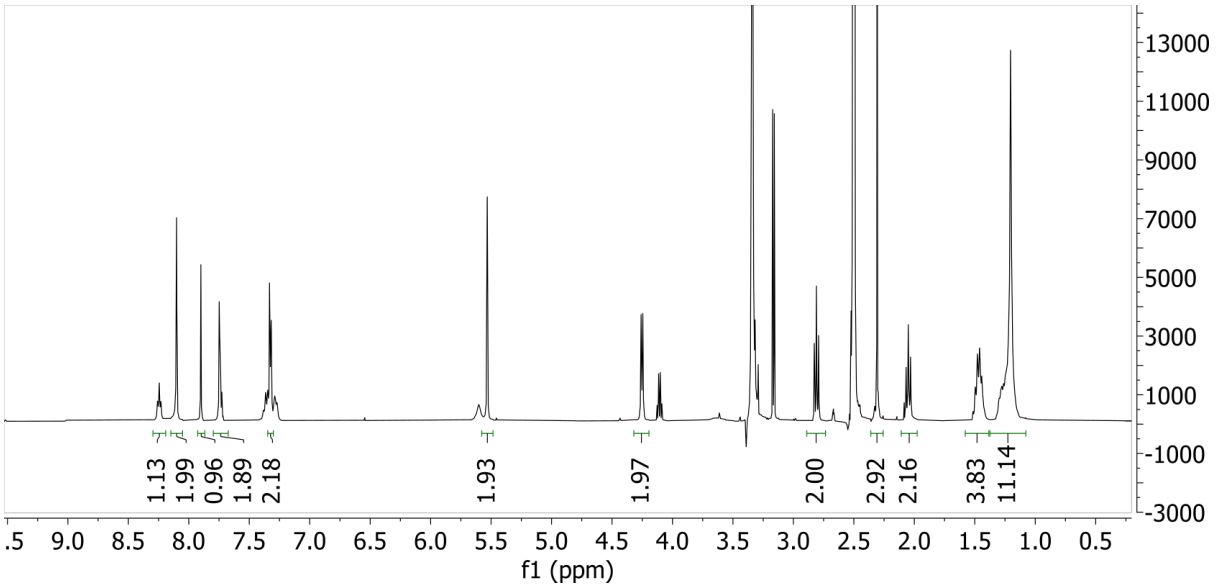


Fig. 121: ^{1}H NMR spectrum of pMcB (d6-DMSO, 298K, 400 MHz).

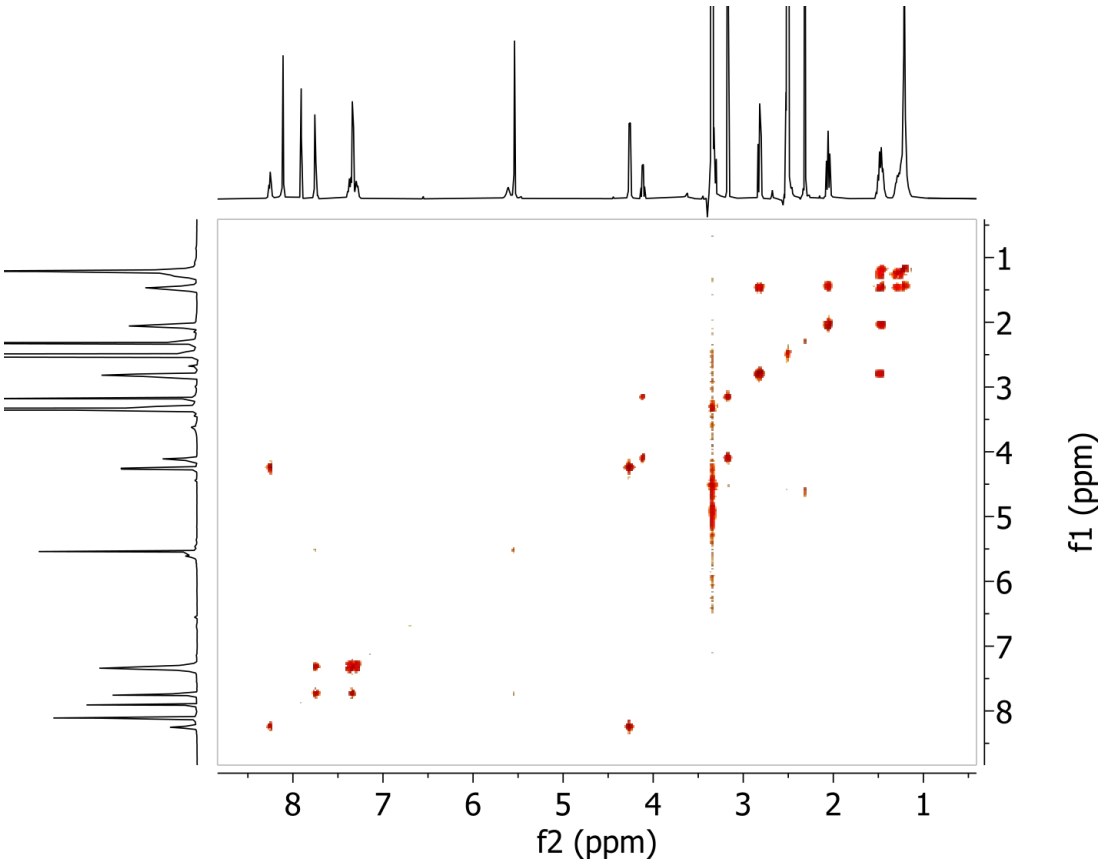


Fig. 122: 2D COSY NMR spectrum of pMcB (d6-DMSO, 298K, 400 MHz).

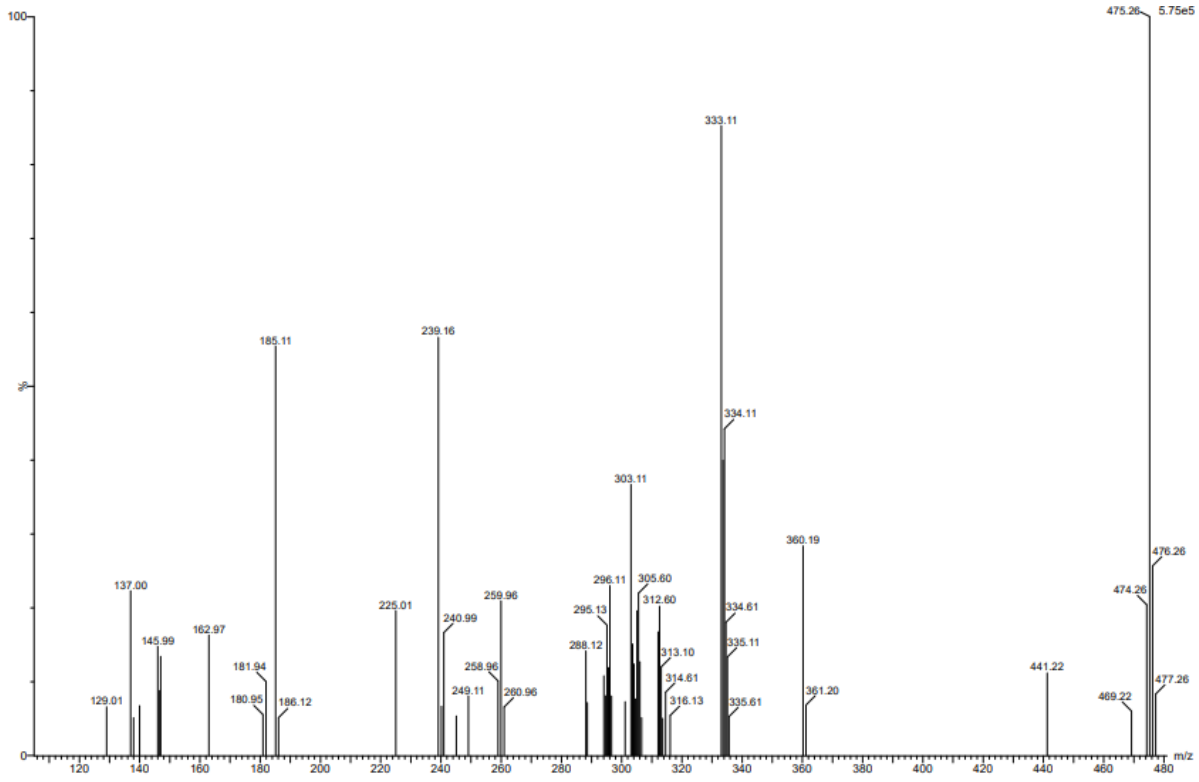


Fig. 123: ESI -(+)MS spectrum of pMcB.

References

1. Varki A, Cummings R, Esko J, Al E. Essentials of glycobiology 3rd edition. 2017.

2. Flitsch SL, Ulijn R V. Sugars tied to the spot. Nature. 2003;421(6920):219–20.

3. Bonora M, Patergnani S, Rimessi A, de Marchi E, Suski JM, Bononi A, et al. ATP synthesis and storage. Purinergic Signal. 2012;8(3):343–57.

4. Iozzo R V., San Antonio JD. Heparan sulfate proteoglycans: Heavy hitters in the angiogenesis arena. J Clin Invest. 2001;108(3):349–55.

5. Turnbull J, Powell A, Guimond S. Heparan sulfate: Decoding a dynamic multifunctional cell regulator. Trends Cell Biol. 2001;11(2):75–82.

6. Uchida T, Ueta H, Xu XD, Hirakawa J, Tahara K, Zhou S, et al. Rapid immunosurveillance by recirculating lymphocytes in the rat intestine: Critical role of unsulfated sialyl-Lewis X on high endothelial venules of the Peyer's patches. Int Immunol. 2018;30(1):23–33.

7. Morgan WTJ, Watkins WM. Unravelling the biochemical basis of blood group ABO and Lewis antigenic specificity. Glycoconj J. 2000;17(7–9):501–30.

8. Freeze HH. Genetic defects in the human glycome. Nat Rev Genet. 2006;7(7):537–51.

9. Maverakis E, Kim K, Shimoda M, Gershwin ME, Patel F, Wilken R, et al. Glycans in the immune system and The Altered Glycan Theory of Autoimmunity: A critical review. J Autoimmun. 2015;57:1–13.

10. Vanhooren V, Desmyter L, Liu X-E, Cardelli M, Franceschi C, Federico A, et al. N-Glycomic Changes in Serum Proteins During Human Aging. Rejuvenation Res. 2007 Dec;10(4):521-531a.

11. Glavey S V., Huynh D, Reagan MR, Manier S, Moschetta M, Kawano Y, et al. The cancer glycome: Carbohydrates as mediators of metastasis. Blood Rev . 2015;29(4):269–79.

12. Rakus JF, Mahal LK. New Technologies for Glycomic Analysis: Toward a Systematic Understanding of the Glycome. Annu Rev Anal Chem. 2011;4(1):367–92.

13. Spiro RG. Protein glycosylation: nature, distribution, enzymatic formation, and disease implications of glycopeptide bonds. Glycobiology .

2002;12(4):43R-56R.

14. Caramelo JJ, Parodi AJ. A sweet code for glycoprotein folding. FEBS Lett . 2015;589(22):3379–87.

15. O'Connor SE, Imperiali B. Modulation of protein structure and function by asparagine-linked glycosylation. Chem Biol. 1996;3(10):803–12.

16. Varki A, Cummings RD, Aebi M, Packer NH, Seeberger PH, Esko JD, et al. Symbol nomenclature for graphical representations of glycans. Glycobiology. 2015;25(12):1323–4.

17. Aebi M. N-linked protein glycosylation in the ER. Biochim Biophys Acta - Mol Cell Res . 2013;1833(11):2430–7.

18. Schwarz F, Aebi M. Mechanisms and principles of N-linked protein glycosylation. Curr Opin Struct Biol . 2011;21(5):576–82.

19. Bause E. Structural requirements of N-glycosylation of proteins. Biochem J . 1983;209(209):331–6.

20. Larkin A, Imperiali B. The expanding horizons of asparagine-linked glycosylation. Biochemistry. 2011;50(21):4411–26.

21. Herscovics A. Importance of glycosidases in mammalian glycoprotein biosynthesis. Biochim Biophys Acta - Gen Subj. 1999;1473(1):96–107.

22. Roth J. Protein N-glycosylation along the Secretory Pathway: Relationship to organelle topography and function, protein quality control, and cell interactions. Chem Rev. 2002;102(2):285–303.

23. Benyair R, Ogen-Shtern N, Lederkremer GZ. Glycan regulation of ER-associated degradation through compartmentalization. Semin Cell Dev Biol . 2015;41:99–109.

24. Jürgensen HJ, Madsen DH, Ingvarsen S, Melander MC, Gårdsvoll H, Patthy L, et al. A novel functional role of collagen glycosylation: Interaction with the endocytic collagen receptor uPARAP/ENDO180. J Biol Chem. 2011;286(37):32736–48.

25. Moloney DJ, Lin AI, Haltiwanger RS. The O -Linked Fucose Glycosylation Pathway . J Biol Chem. 1997;272(30):19046–50.

26. Fulop N, Marchase R, Chatham J. Role of protein O-

linked N-acetyl-glucosamine in mediating cell function and survival in the cardiovascular system. Cardiovasc Res . 2007 Jan 15;73(2):288–97.

27. Drickamer K, Taylor ME. Evolving views of protein glycosylation. Trends Biochem Sci. 1998;23(9):321–4.

28. Yau LF, Liu J, Jiang M, Bai G, Wang JR, Jiang ZH. An integrated approach for comprehensive profiling and quantitation of IgG-Fc glycopeptides with application to rheumatoid arthritis. J Chromatogr B Anal Technol Biomed Life Sci . 2019;1122–1123(March):64–72.

29. Kjaergaard S, Schwartz M, Skovby F. Congenital disorder of glycosylation type Ia (CDG-Ia): Phenotypic spectrum of the R141H/F119L genotype. Arch Dis Child. 2001;85(3):236–9.

30. Kanninen K, Goldsteins G, Auriola S, Alafuzoff I, Koistinaho J. Glycosylation changes in Alzheimer's disease as revealed by a proteomic approach. Neurosci Lett. 2004;367(2):235–40.

31. Montpetit ML, Stocker PJ, Schwetz TA, Harper JM, Norring SA, Schaffer L, et al. Regulated and aberrant glycosylation modulate cardiac electrical signaling. Proc Natl Acad Sci U S A. 2009;106(38):16517–22.

32. Kościelak J. Diseases of aberrant glycosylation. Vol. 42, Acta biochimica Polonica. 1995. p. 1–10.

33. Mestecky J, Tomana M, Moldoveanu Z, Julian BA, Suzuki H, Matousovic K, et al. Role of aberrant glycosylation of IgA1 molecules in the pathogenesis of iga nephropathy. Kidney Blood Press Res. 2008;31(1):29–37.

34. Munkley J, Elliott DJ. Hallmarks of glycosylation in cancer. Oncotarget . 2016;7(23):35478–89.

35. Granovsky M, Fata J, Pawling J, Muller WJ, Khokha R, Dennis JW. Suppression of tumor growth and metastasis in Mgat5-deficient mice. Nat Med. 2000;6(3):306–12.

36. Häuselmann I, Borsig L. Altered tumor-cell glycosylation promotes metastasis. Front Oncol. 2014;4 MAR(February):1–15.

37. Kannagi R, Izawa M, Koike T, Miyazaki K, Kimura N. Carbohydrate-mediated cell adhesion in cancer metastasis and angiogenesis. Cancer Sci. 2004;95(5):377–84.

38. Fuster MM, Esko JD. The sweet and sour of cancer: Glycans as novel therapeutic targets. Nat Rev Cancer. 2005;5(7):526–42.

39. Kim YJ, Varki A. Perspectives on the significance of altered glycosylation of glycoproteins in cancer. Glycoconj J. 1997;14(5):569–76.

40. Arnold JN, Saldova R, Galligan MC, Murphy TB, Mimura-Kimura Y, Telford JE, et al. Novel glycan biomarkers for the detection of lung cancer. J Proteome Res. 2011;10(4):1755–64.

41. Loureiro LR, Carrascal MA, Barbas A, Ramalho JS, Novo C, Delannoy P, et al. Challenges in antibody development against Tn and sialyl-Tn antigens. Biomolecules. 2015;5(3):1783–809.

42. Regnier FE, Cho W. Affinity Targeting Schemes for Biomarker Research . Proteomic and Metabolomic Approaches to Biomarker Discovery.

43. Marcos NT, Bennett EP, Gomes J, Magalhaes A, Gomes C, David L, et al. ST6GalNAc-I controls expression of sialyl-Tn antigen in gastrointestinal tissues. Front Biosci - Elit. 2011;3 E(4):1443–55.

44. Gessner P, Riedl S, Quentmaier A, Kemmner W. Enhanced activity of CMP-neuAc:Gal beta 1-4GlcNAc:alpha 2,6-sialyltransferase in metastasizing human colorectal tumor tissue and serum of tumor patients. Cancer Lett . 1993 Dec 20;75(3):143–9.

45. Guo HB, Randolph M, Pierce M. Inhibition of a specific N-glycosylation activity results in attenuation of breast carcinoma cell invasiveness-related phenotypes: Inhibition of epidermal growth factor-induced dephosphorylation of focal adhesion kinase. J Biol Chem. 2007;282(30):22150–62.

46. Dennis JW, Laferté S, Waghorne C, Breitman ML, Kerbel RS. β1-6 branching of Asn-linked oligosaccharides is directly associated with metastasis. Science (80-). 1987;236(4801):582–5.

47. Seales EC, Jurado GA, Brunson BA, Wakefield JK, Frost AR, Bellis SL. Hypersialylation of β 1 integrins, observed in colon adenocarcinoma, may contribute to cancer progression by up-regulating cell motility. Cancer Res. 2005;65(11):4645–52.

48. Okada M, Chikuma S, Kondo T, Hibino S, Machiyama H, Yokosuka T, et al. Blockage of Core Fucosylation Reduces Cell-Surface Expression of PD-1 and Promotes Anti-tumor Immune Responses of T Cells. Cell Rep . 2017;20(5):1017–28.

49. Cheng K, Zhou Y, Neelamegham S. DrawGlycan-SNFG: A robust tool to render glycans and glycopeptides with fragmentation information. Glycobiology. 2017;27(3):200–5.

50. Thorek DLJ, Evans MJ, Carlsson S V., Ulmert D, Lilja H. Prostate-specific kallikrein-related peptidases and their relation to prostate cancer biology and detection. Thromb Haemost. 2013;110(3):484–92.

51. Balk SP. Biology of Prostate-Specific Antigen. J Clin Oncol . 2003;21(2):383–91.

52. Roche diagnostics. Elecsys total PSA . 2018. p. 1–5.

53. Holmström B, Johansson M, Bergh A, Stenman U-H, Hallmans G, Stattin P. Prostate specific antigen for early detection of prostate cancer: longitudinal study. BMJ. 2009;339:b3537.

54. Song E, Mayampurath A, Yu CY, Tang H, Mechref Y. Glycoproteomics: Identifying the glycosylation of prostate specific antigen at normal and high isoelectric points by LC-MS/MS. J Proteome Res. 2014;13(12):5570–80.

55. Wang X, Chen J, Li QK, Peskoe SB, Zhang B, Choi C, et al. Overexpression of a(1,6) fucosyltransferase associated with aggressive prostate cancer. Glycobiology. 2014;24(10):935–44.

56. Barfeld SJ, East P, Zuber V, Mills IG. Meta-analysis of prostate cancer gene expression data identifies a novel discriminatory signature enriched for glycosylating enzymes. 2014;

57. Chen Z, Gulzar ZG, St. Hill CA, Walcheck B, Brooks JD. Increased expression of GCNT1 is associated with altered O-glycosylation of PSA, PAP, and MUC1 in human prostate cancers. Prostate. 2014;74(10):1059–67.

58. Munkley J, Mills I, Elliot D. Munkley J , Mills IG , Elliott DJ . The role of glycans in prostate cancer development and progression. Nat Rev Urol. 2016;13(October):324–33.

59. Prakash S, Robbins PW. Glycotyping of prostate specific antigen. Glycobiology . 2000;10(2):173–6.

60. Peracaula R, Tabarés G, Royle L, Harvey DJ, Dwek RA, Rudd PM, et al. Altered glycosylation pattern allows the distinction between prostate-specific antigen (PSA) from normal and tumor origins. Glycobiology. 2003;13(6):457–70.

61. Ohyama C, Hosono M, Nitta K, Oh-eda M, Yoshikawa K, Habuchi T, et al. Carbohydrate structure and differential

binding of prostate specific antigen to Maackia amurensis lectin between prostate cancer and benign prostate hypertrophy. Glycobiology. 2004;14(8):671–9.

62. Janković MM, Kosanović MM. Glycosylation of urinary prostate-specific antigen in benign hyperplasia and cancer: Assessment by lectin-binding patterns. Clin Biochem. 2005;38(1):58–65.

63. Tabarés G, Radcliffe CM, Barrabés S, Ramírez M, Aleixandre N, Hoesel W, et al. Different glycan structures in prostate-specific antigen from prostate cancer sera in relation to seminal plasma PSA. Glycobiology. 2006;16(2):132–45.

64. Tajiri M, Ohyama C, Wada Y. Oligosaccharide profiles of the prostate specific antigen in free and complexed forms from the prostate cancer patient serum and in seminal plasma: A glycopeptide approach. Glycobiology. 2008;18(1):2–8.

65. White KY, Rodemich L, Nyalwidhe JO, Comunale MA, Clements MA, Lance RS, et al. Glycomic characterization of prostate-specific antigen and prostatic acid phosphatase in prostate cancer and benign disease seminal plasma fluids. J Proteome Res. 2009;8(2):620–30.

66. Fukushima K, Satoh T, Baba S, Yamashita K. α1,2-Fucosylated and β-N-acetylgalactosaminylated prostate-specific antigen as an efficient marker of prostatic cancer. Glycobiology. 2009;20(4):452–60.

67. Sarrats A, Saldova R, Comet J, O'Donoghue N, de Llorens R, Rudd PM, et al. Glycan characterization of PSA 2-DE subforms from serum and seminal plasma. OMICS . 2010;14(4):465–74.

68. Li Y, Tian Y, Rezai T, Prakash A, Lopez MF, Chan DW, et al. Simultaneous Analysis of Glycosylated and Sialylated PSA Reveals Differential Distribution of Glycosylated PSA Isoforms in Prostate Cancer Tissues. Anal Chem. 2011;83(1):240–5.

69. Llop E, Ferrer-Batall M, Barrabs S, Guerrero PE, Ramrez M, Saldova R, et al. Improvement of Prostate Cancer Diagnosis by Detecting PSA Glycosylation-Specific Changes. Theranostics. 2016;6(8):1190–204.

70. Hsiao C, Tzai T, Chen C, Yang W, Chen C. Analysis of Urinary Prostate-Specific Antigen Glycoforms in Samples of Prostate Cancer and Benign Prostate Hyperplasia. hindawi. 2016;2016.

71. Baynes J. medical biochemistry 5th edition. Elsevier health sciences; 2018.

72. Stick R, Williams SJ. Carbohydrates: The Essential Molecules of Life . Carbohydrates: The Essential Molecules of Life. Elsevier; 2009.

73. Ouelette R, Rawn D. Principles of Organic Chemistry . Elsevier; 2015. 343–370 p.

74. Casu B, Reggiani M, Gallo GG, Vigevani A. NMR Spectra and conformation of glucose and some related carbohydrates in dimethylsulphoxide solution. Tetrahedron Lett. 1965;6(27):2253–9.

75. Bertram F-R, Kuniaki T, Joachim T. glycoscience, chemistry and chemical biology, volume 1, 2nd edition. 2008.

76. Wlodarczyk P. Experimental and theoretical studies on mutarotation in supercooled liquid state Experimental and theoretical studies on mutarotation in supercooled liquid state Patryk Włodarczyk Institute of Physics , Uniwersytecka 4 , 40-008 Katowice , Poland A thesis . 2015;(August).

77. Roach PJ, Depaoli-Roach AA, Hurley TD, Tagliabracci VS. Glycogen and its metabolism: Some new developments and old themes. Biochem J. 2012;441(3):763–87.

78. Sasisekharan R, Venkataraman G. Heparin and heparan sulfate: Biosynthesis, structure and function. Curr Opin Chem Biol. 2000;4(6):626–31.

79. Sacktor B. Trehalase and the transport of glucose in the mammalian kidney and intestine. Proc Natl Acad Sci U S A. 1968;60(3):1007–14.

80. Clark LC, Lyons C. Electrode Systems for Continuous Monitoring in Cardiovascular Surgery. Ann N Y Acad Sci. 1962;102(1):29–45.

81. Lobry M, Lahem D, Loyez M, Debliquy M, Chah K, David M, et al. Non-enzymatic D-glucose plasmonic optical fiber grating biosensor. Biosens Bioelectron. 2019;142(May):111506.

82. Gonzales WV, Mobashsher AT, Abbosh A. The progress of glucose monitoring—A review of invasive to minimally and non-invasive techniques, devices and sensors. Vol. 19, Sensors (Switzerland). 2019.

83. Yoo EH, Lee SY. Glucose biosensors: An overview of use in clinical practice. Sensors. 2010;10(5):4558–76.

84. Sakai T, Yamamoto K, Yokota H, Hakozaki-Usui K, Hino F, Kato I. Rapid, simple enzymatic assay of free L-fucose in serum and urine, and its use as a marker for cancer, cirrhosis, and gastric ulcers. Clin Chem. 1990;36(3):474–6.

85. Bovin N, Obukhova P, Shilova N, Rapoport E, Popova I, Navakouski M, et al. Repertoire of human natural anti-glycan immunoglobulins. Do we have auto-antibodies? Biochim Biophys Acta - Gen Subj. 2012;1820(9):1373–82.

86. Estrada J, Martens G, Li P, Adams A, Newell K, Ford M, et al. evaluation of human and non-human primate antibody binding to pig cells lacking GGTA1/CMAH/b4GalNT2 genes. Xenotransplantation. 2015;22(3):194–202.

87. Makeneni S, Ji Y, Watson DC, Young NM, Woods RJ. Predicting the origins of anti-blood group antibody specificity: A case study of the ABO A- and B-antigens. Front Immunol. 2014;5(AUG):1–9.

88. Muthana SM, Gildersleeve JC. Factors Affecting Anti-Glycan IgG and IgM Repertoires in Human Serum. Sci Rep . 2016;6(January):1–11. Available from: http://dx.doi.org/10.1038/srep19509

89. Paul S, Boschetti G, Rinaudo-Gaujous M, Moreau A, Del Tedesco E, Bonneau J, et al. Association of anti-glycan antibodies and inflammatory bowel disease course. J Crohn’s Colitis. 2015;9(6):445–51.

90. Wandall HH, Blixt O, Tarp MA, Pedersen JW, Bennett EP, Mandel U, et al. Cancer biomarkers defined by autoantibody signatures to aberrant O-glycopeptide epitopes. Cancer Res. 2010;70(4):1306–13.

91. Meany DL, Chan DW. Aberrant glycosylation associated with enzymes as cancer biomarkers. Clin Proteomics . 2011;8(1):7.

92. Guu SY, Lin TH, Chang SC, Wang RJ, Hung LY, Fang PJ, et al. Serum N-glycome characterization and anti-carbohydrate antibody profiling in oral squamous cell carcinoma patients. PLoS One. 2017;12(6):1–18.

93. Tikhonov A, Butvilovskaya V, Chernichenko M, Savvateeva E, Feyzkhanova G, Lysov Y, et al. Diagnostic value of anti-glycan antibodies in patients with colorectal cancer. Ann Oncol . 2017 Oct 1;28(suppl_7).

94. Qin Q, Yin Z, Wu X, Haas KM, Huang X. Valency and density matter: Deciphering impacts of immunogen structures on immune responses against a tumor associated

carbohydrate antigen using synthetic glycopolymers. Biomaterials . 2016 Sep;101(5):189–98.

95. R.D. A, D.R. B. Carbohydrate vaccines: Developing sweet solutions to sticky situations? Nat Rev Drug Discov . 2010;9(4):308–24.

96. MacKenzie CR, Hirama T, Deng SJ, Bundle DR, Narang SA, Young NM. Analysis by surface plasmon resonance of the influence of valence on the ligand binding affinity and kinetics of an anti-carbohydrate antibody. J Biol Chem. 1996;271(3):1527–33.

97. Nemanichvili N, Tomris I, Turner HL, McBride R, Grant OC, van der Woude R, et al. Fluorescent Trimeric Hemagglutinins Reveal Multivalent Receptor Binding Properties. J Mol Biol . 2018.

98. Lehrer RI, Jung G, Ruchala P, Andre S, Gabius HJ, Lu W. Multivalent Binding of Carbohydrates by the Human -Defensin, HD5. J Immunol . 2009;183(1):480–90.

99. Polonskaya Z, Deng S, Sarkar A, Kain L, Comellas-Aragones M, McKay CS, et al. T cells control the generation of nanomolar-affinity anti-glycan antibodies. J Clin Invest. 2017;127(4):1491–504.

100. Yuasa N, Koyama T, Fujita-Yamaguchi Y. Purification and refolding of anti-T-antigen single chain antibodies (scFvs) expressed in Escherichia coli as inclusion bodies. Biosci Trends . 2014 Feb;8(1):24–31.

101. Kubota T, Matsushita T, Niwa R, Kumagai I, Nakamura K. Novel anti-Tn single-chain Fv-Fc fusion proteins derived from immunized phage library and antibody Fc domain. Anticancer Res. 2010;30(9):3397–405.

102. Stewart A, Liu Y, Lai JR. A strategy for phage display selection of functional domain-exchanged immunoglobulin scaffolds with high affinity for glycan targets. J Immunol Methods . 2012;376(1–2):150–5.

103. Lin TY, Lai JR. Interrogation of side chain biases for oligomannose recognition by antibody 2G12 via structure-guided phage display libraries. Bioorganic Med Chem . 2017;25(20):5790–8. Available from: https://doi.org/10.1016/j.bmc.2017.09.013

104. Blixt O, Lavrova OI, Mazurov D V., Cló E, Kračun SK, Bovin N V., et al. Analysis of Tn antigenicity with a panel of new IgM and IgG1 monoclonal antibodies raised against leukemic cells. Glycobiology. 2012;22(4):529–42.

105. Park S, Gildersleeve JC, Blixt O, Shin I. Carbohydrate microarrays. Chem Soc Rev . 2013;42(10):4310–26.

106. Muthana SM, Xia L, Campbell CT, Zhang Y, Gildersleeve JC. Competition between Serum IgG, IgM, and IgA anti-glycan antibodies. PLoS One. 2015;10(3):1–16.

107. de Paz JL, Seeberger PH. Recent Advances and Future Challenges in Glycan Microarray Technology. In 2012. p. 1–12.

108. Sterner E, Flanagan N, Gildersleeve JC. Perspectives on Anti-Glycan Antibodies Gleaned from Development of a Community Resource Database. ACS Chem Biol. 2016;11(7):1773–83.

109. Cao Y, Karsten U, Otto G, Bannasch P. and A2 , 6-Linked Sialic Acid in Hepatocellular Carcinomas and Preneoplastic Hepatocellular Lesions. Virchows Arch. 1999;434:503–9.

110. Mereiter S, Polom K, Williams C, Polonia A, Guergova-Kuras M, Karlsson N, et al. The Thomsen-Friedenreich Antigen: A Highly Sensitive and Specific Predictor of Microsatellite Instability in Gastric Cancer. J Clin Med . 2018;7(9):256.

111. Pereira MS, Alves I, Vicente M, Campar A, Silva MC, Padrão NA, et al. Glycans as Key Checkpoints of T Cell Activity and Function. Front Immunol . 2018;9(November):2754.

112. Julien S, Videira PA, Delannoy P. Sialyl-Tn in cancer: (How) did we miss the target? Biomolecules. 2012;2(4):435–66.

113. Fu C, Zhao H, Wang Y, Cai H, Xiao Y, Zeng Y, et al. Tumor-associated antigens: Tn antigen, sTn antigen, and T antigen. Hla. 2016;88(6):275–86.

114. Lin WM, Karsten U, Goletz S, Cheng RC, Cao Y. Expression of CD176 (Thomsen-Friedenreich antigen) on lung, breast and liver cancer-initiating cells. Int J Exp Pathol. 2011;92(2):97–105.

115. Karacosta LG, Fisk JC, Jessee J, Tati S, Turner B, Ghazal D, et al. Preclinical Analysis of JAA-F11, a Specific Anti–Thomsen-Friedenreich Antibody via Immunohistochemistry and In Vivo Imaging. Transl Oncol . 2018 Apr;11(2):450–66.

116. de Mattos LC. Structural diversity and biological

importance of ABO, H, Lewis and secretor histo-blood group carbohydrates. Rev Bras Hematol Hemoter . 2016;38(4):331–40.

117. Jeyakanthan M, Meloncelli PJ, Zou L, Lowary TL, Larsen I, Maier S, et al. ABH-Glycan Microarray Characterizes ABO Subtype Antibodies: Fine Specificity of Immune Tolerance after ABO-Incompatible Transplantation. Am J Transplant. 2016;16(5):1548–58.

118. Dolscheid-pommerich RC, Keyver-paik M, Hecking T, Kuhn W, Hartmann G, Stoffel-wagner B, et al. Clinical performance of LOCI ™ -based tumor marker assays for tumor markers CA 15-3 , CA 125 , CEA , CA 19-9 and AFP in gynecological cancers. 2017;

119. Srivastava G, Srivastava ÆO, Sucheck ÆSJ, Ichikawa Y, Livingston ÆPO. Synthesis of sialyl Lewis a (sLe a , CA19-9) and construction of an immunogenic sLe a vaccine. 2009;1397–405.

120. Schlom J, Hodge JW, Palena C, Tsang K, Jochems C, Greiner JW, et al. Therapeutic Cancer Vaccines. In 2014. p. 67–124.

121. Dan X, Liu W, Ng TB. Development and Applications of Lectins as Biological Tools in Biomedical Research. Med Res Rev . 2016 Mar;36(2):221–47.

122. Cecioni S, Imberty A, Vidal S. Glycomimetics versus multivalent glycoconjugates for the design of high affinity lectin ligands. Chem Rev. 2015;115(1):525–61.

123. Sumner JB, Howell SF. the Identification of the Hemagglutinin of the jack bean with Concavlin A. J Bacteriol. 1936;32(2):227–37.

124. Beuth J, Ko HL, Uhlenbruck G, Pulverer G. Lectin-Mediated bacterial adhesion to human tissue. Eur J Clin Microbiol. 1987;6(5):591–3.

125. Lu Y, Sun G, Liu G, Shi Y, Han Y, Yu F, et al. Clinical significance of mannose-binding lectin expression in thyroid carcinoma tissues. Pathol Oncol Res. 2013;19(2):259–66.

126. Sundblad V, Quintar AA, Morosi LG, Niveloni SI, Cabanne A, Smecuol E, et al. Galectins in intestinal inflammation: Galectin-1 expression delineates response to treatment in celiac disease patients. Front Immunol. 2018;9(MAR).

127. Tate MD, Brooks AG, Reading PC. Inhibition of

lectin-mediated innate host defences in vivo modulates disease severity during influenza virus infection. Immunol Cell Biol. 2011;89(3):482–91.

128. Zschäbitz A, Krahn V, Schmidt W, Gabius HJ, Weiser H, Biesalski HK, et al. Expression patterns of complex glycoconjugates and endogenous lectins during fetal development of the viscerocranium. Ann Anat. 1999;181(1):117–21.

129. Bojarová P, Křen V. Sugared biomaterial binding lectins: achievements and perspectives. Biomater Sci. 2016;4(8):1142–60.

130. Zhu F, Clemmer DE, Trinidad JC. Characterization of lectin binding affinities: Via direct LC-MS profiling: Implications for glycopeptide enrichment and separation strategies. Analyst. 2017;142(1):65–74.

131. Agostino M, Yuriev E, Ramsland PA. A computational approach for exploring carbohydrate recognition by lectins in innate immunity. Front Immunol. 2011;2(JUN):1–14.

132. Weis WI, Drickamer K. Structural basis of lectin-carbohydrate recognition. Annual reviews. 1996; 65:441-473

133. Gabius HJ, André S, Jiménez-Barbero J, Romero A, Solís D. From lectin structure to functional glycomics: Principles of the sugar code. Trends Biochem Sci. 2011;36(6):298–313.

134. Tommasone S, Allabush F, Tagger YK, Norman J, Köpf M, Tucker JHR, et al. The challenges of glycan recognition with natural and artificial receptors. Chem Soc Rev . 2019;11(2):P003–4.

135. Benevides RG, Ganne G, Simões RDC, Schubert V, Niemietz M, Unverzagt C, et al. A lectin from Platypodium elegans with unusual specificity and affinity for asymmetric complex N-glycans. J Biol Chem. 2012;287(31):26352–64.

136. Faller CE, Guvench O. Terminal sialic acids on CD44 N-glycans can block hyaluronan binding by forming competing intramolecular contacts with arginine sidechains. Proteins Struct Funct Bioinforma . 2014 Nov;82(11):3079–89.

137. Imberty A, Mitchell EP, Wimmerová M. Structural basis of high-affinity glycan recognition by bacterial and fungal lectins. Curr Opin Struct Biol. 2005;15(5):525–34.

138. Dam TK, Brewer CF. Thermodynamic studies of lectin-

carbohydrate interactions by isothermal titration calorimetry. Chem Rev. 2002;102(2):387–429.

139. Millen SH, Lewallen DM, Herr AB, Iyer SS, Weiss AA. Identification and characterization of the carbohydrate ligands recognized by pertussis toxin via a glycan microarray and surface plasmon resonance. Biochemistry. 2010;49(28):5954–67.

140. Sauer AK, Liang CH, Stech J, Peeters B, Quéré P, Schwegmann-Wessels C, et al. Characterization of the sialic acid binding activity of influenza A viruses using soluble variants of the H7 and H9 hemagglutinins. PLoS One. 2014;9(2):1–9.

141. Ng KKS, Drickamer K, Weis WI. Structural analysis of monosaccharide recognition by rat liver mannose-binding protein. J Biol Chem. 1996;271(2):663–74.

142. Quiocho F. Carbohydrate-Binding Proteins: Tertiary Structures and Protein-Sugar Interactions. Annu Rev Biochem. 1986;55(1):287–315.

143. Jin Y, Kim SC, Kim HJ, Ju W, Kim YH, Kim HJ. A lectin-based diagnostic system using circulating antibodies to detect cervical intraepithelial neoplasia and cervical cancer. Glycobiology. 2015;26(1):100–7.

144. Damborský P, Koczula KM, Gallotta A, Katrlík J. Lectin-based lateral flow assay: proof-of-concept. Analyst. 2016;141(23):6444–8.

145. Belický Š, Katrlík J, Tkáč J. Glycan and lectin biosensors. Essays Biochem. 2016;60(1):37–47.

146. Ito H, Hoshi K, Honda T, Hashimoto Y. Lectin-based assay for glycoform-specific detection of α2,6-sialylated transferrin and carcinoembryonic antigen in tissue and body fluid. Molecules. 2018;23(6):1–11.

147. Kufareva I, Stephens B, Gilliland CT, Wu B, Fenalti G, Hamel D, et al. Chapter 7 A Novel Approach to Quantify G-Protein-Coupled Receptor. 2014;1013:227–33.

148. Batisse C, Marquet J, Greffard A, Fleury-Feith J, Jaurand MC, Pilatte Y. Lectin-based three-color flow cytometric approach for studying cell surface glycosylation changes that occur during apoptosis. Cytom Part A. 2004;62(2):81–8.

149. Gutowski KA, Hudson JL, Aminoff D. Flow cytometric analysis of human erythrocytes: I. Probed with lectins and immunoglobulins. Exp Gerontol. 1991;26(4):315–26.

150. Qiu R, Regnier FE. Use of multidimensional lectin affinity chromatography in differential glycoproteomics. Anal Chem. 2005;77(9):2802–9.

151. Pilobello KT, Krishnamoorthy L, Slawek D, Mahal LK. Development of a lectin microarray for the rapid analysis of protein glycopatterns. ChemBioChem. 2005;6(6):985–9.

152. Hirabayashi J, Yamada M, Kuno A, Tateno H. Lectin microarrays: Concept, principle and applications. Chem Soc Rev. 2013;42(10):4443–58.

153. Nakajima K, Inomata M, Iha H, Hiratsuka T, Etoh T, Shiraishi N, et al. Establishment of new predictive markers for distant recurrence of colorectal cancer using lectin microarray analysis. Cancer Med. 2015;4(2):293–302.

154. Zhao J, Patwa TH, Qiu W, Shedden K, Hinderer R, Misek DE, et al. Glycoprotein microarrays with multi-lectin detection: Unique lectin binding patterns as a tool for classifying normal, chronic pancreatitis and pancreatic cancer sera. J Proteome Res. 2007;6(5):1864–74.

155. Li Y, Tao SC, Bova GS, Liu AY, Chan DW, Zhu H, et al. Detection and verification of glycosylation patterns of glycoproteins from clinical specimens using lectin microarrays and lectin-based immunosorbent assays. Anal Chem. 2011;83(22):8509–16.

156. Kuno A, Kato Y, Matsuda A, Kaneko MK, Ito H, Amano K, et al. Focused differential glycan analysis with the platform antibody-assisted lectin profiling for glycan-related biomarker verification. Mol Cell Proteomics. 2009;8(1):99–108.

157. Fry SA, Afrough B, Lomax-Browne HJ, Timms JF, Velentzis LS, Leathem AJC. Lectin microarray profiling of metastatic breast cancers. Glycobiology. 2011;21(8):1060–70.

158. Hu B, Niu X, Cheng L, Yang LN, Li Q, Wang Y, et al. Discovering cancer biomarkers from clinical samples by protein microarrays. Proteomics - Clin Appl. 2015;9(1–2):98–110.

159. Agrawal P, Fontanals-Cirera B, Sokolova E, Jacob S, Vaiana CA, Argibay D, et al. A Systems Biology Approach Identifies FUT8 as a Driver of Melanoma Metastasis. Cancer Cell. 2017;31(6):804-819.e7.

160. Peixoto A, Relvas-Santos M, Azevedo R, Lara Santos L, Ferreira JA. Protein glycosylation and tumor microenvironment alterations driving cancer hallmarks.

Front Oncol. 2019;9(MAY):1–24.

161. Wu X, Li Z, Chen XX, Fossey JS, James TD, Jiang YB. Selective sensing of saccharides using simple boronic acids and their aggregates. Chem Soc Rev. 2013;42(20):8032–48.

162. Arimori S, Bell ML, Oh CS, Frimat KA, James TD. Modular fluorescence sensors for saccharides. J Chem Soc Perkin 1. 2002;(6):803–8.

163. Shiomi Y, Saisho M, Tsukagoshi K, Shinkai S. Specific complexation of glucose with a diphenylmethane-3,3′- diboronic acid derivative: Correlation between the absolute configuration of mono- and di-saccharides and the circular dichroic activity of the complex. J Chem Soc Perkin Trans 1. 1993;(17):2111–7.

164. Tsukagoshi K, Shinkai S. Specific Complexation with Mono- and Disaccharides That Can Be Detected by Circular Dichroism. J Org Chem. 1991;56(13):4089–91.

165. Phillips MD, James TD. Boronic acid based modular fluorescent sensors for glucose. J Fluoresc. 2004;14(5):549–59.

166. Larkin JD, Frimat KA, Fyles TM, Flower SE, James TD. Boronic acid based photoinduced electron transfer (PET) fluorescence sensors for saccharides. New J Chem. 2010;34(12):2922–31.

167. Norrild JC, Eggert H. Boronic acids as fructose sensors. Structure determination of the complexes involved using 1 J CC coupling constants. J Chem Soc Perkin Trans 2 . 1996;53(12):2583.

168. Zhai W, Sun X, James TD, Fossey JS. Boronic Acid-Based Carbohydrate Sensing. Chem - An Asian J. 2015;10(9):1836–48.

169. Bull SD, Davidson MG, Van Den Elsen JMH, Fossey JS, Jenkins ATA, Jiang YB, et al. Exploiting the reversible covalent bonding of boronic acids: Recognition, sensing, and assembly. Acc Chem Res. 2013;46(2):312–26.

170. Hall DG. Boronic Acids: Preparation and Applications in Organic Synthesis, Medicine and Materials (Volume 1 and 2). Boronic Acids Prep Appl Org Synth Med Mater (Volume 1 2). 2011;1–2.

171. Springsteen G, Wang B. A detailed examination of boronic acid-diol complexation. Tetrahedron. 2002;58(26):5291–300.

172. Lampard EV. Benzoxaboroles and Boronic Acids for Sensing Applications Benzoxaboroles and Boronic Acids for Sensing Applications. 2019;

173. Tomsho JW, Pal A, Hall DG, Benkovic SJ. Ring structure and aromatic substituent effects on the p K a of the benzoxaborole pharmacophore. ACS Med Chem Lett. 2012;3(1):48–52.

174. Wang X, Xia N, Liu L. Boronic acid-based approach for separation and immobilization of glycoproteins and its application in sensing. Int J Mol Sci. 2013;14(10):20890–912.

175. Wulff G, Lauer M, Böhnke H. Rapid Proton Transfer as Cause of an Unusually Large Neighboring Group Effect. Angew Chemie Int Ed English. 1984 Sep;23(9):741–2.

176. Liu Z, He H. Synthesis and Applications of Boronate Affinity Materials: From Class Selectivity to Biomimetic Specificity. Acc Chem Res. 2017;50(9):2185–93.

177. Liu Y, Ren L, Liu Z. A unique boronic acid functionalized monolithic capillary for specific capture, separation and immobilization of cis-diol biomolecules. Chem Commun. 2011;47(17):5067–9.

178. Matsumoto A, Yoshida R, Kataoka K. Glucose-responsive polymer gel bearing phenylborate derivative as a glucose-sensing moiety operating at the physiological pH. Biomacromolecules. 2004;5(3):1038–45.

179. Li X, Pennington J, Stobaugh JF, Schöneich C. Synthesis of sulfonamide- and sulfonyl-phenylboronic acid-modified silica phases for boronate affinity chromatography at physiological pH. Anal Biochem. 2008;372(2):227–36.

180. Ma Y, Tian H, Jin Z, Li X, Li Y. Observation of the generation of peroxynitrite in mouse liver after acetaminophen overdose with a boronate-based ratiometric fluorescence probe. RSC Adv. 2019;9(12):6510–4.

181. Sikora A, Zielonka J, Lopez M, Joseph J, Kalyanaraman B. Direct oxidation of boronates by peroxynitrite: Mechanism and implications in fluorescence imaging of peroxynitrite. Free Radic Biol Med . 2009 Nov;47(10):1401–7.

182. Zhao L, Ding J, Xiao C, He P, Tang Z, Pang X, et al. Glucose-sensitive polypeptide micelles for self-regulated insulin release at physiological pH. J Mater Chem. 2012;22(24):12319–28.

183. Stubelius A, Lee S, Almutairi A. The Chemistry of Boronic Acids in Nanomaterials for Drug Delivery. Acc Chem Res. 2019;

184. Zhang X, Wu Y, Ji S, Guo H, Song P, Han K, et al. Effect of the electron donor/acceptor orientation on the fluorescence transduction efficiency of the d-pet effect of carbazole-based fluorescent boronic acid sensors. J Org Chem. 2010;75(8):2578–88.

185. Sun X, James TD, Anslyn E V. Arresting "loose Bolt" Internal Conversion from -B(OH)2 Groups is the Mechanism for Emission Turn-On in ortho-Aminomethylphenylboronic Acid-Based Saccharide Sensors. J Am Chem Soc. 2018;140(6):2348–54.

186. Sandanayake KRAS, Shinkai S. Novel molecular sensors for saccharides based on the interaction of boronic acid and amines: Saccharide sensing in neutral water. J Chem Soc Chem Commun. 1994;(9):1083–4.

187. James TD, Sandanayake KRAS, Shinkai S. A Glucose-Selective Molecular Fluorescence Sensor. Angew Chemie Int Ed English . 1994 Nov 17;33(21):2207–9.

188. James TD, Samankumara Sandanayake KRA, Shinkai S. Chiral discrimination of monosaccharides using a fluorescent molecular sensor. Nature. 1995;374(6520):345–7.

189. Wei J ru, Ni Y li, Zhang W, Zhang Z qi, Zhang J. Detection of glycoprotein through fluorescent boronic acid-based molecularly imprinted polymer. Anal Chim Acta . 2017;960:110–6.

190. Jiang L, Lu R, Ye L. Towards detection of glycoproteins using molecularly imprinted nanoparticles and boronic acid-modified fluorescent probe. Polymers (Basel). 2019;11(1).

191. Mohapatra S, Panda N, Pramanik P. Boronic acid functionalized superparamagnetic iron oxide nanoparticle as a novel tool for adsorption of sugar. Mater Sci Eng C . 2009;29(7):2254–60.

192. Pan M, Sun Y, Zheng J, Yang W. Boronic acid-functionalized core-shell-shell magnetic composite microspheres for the selective enrichment of glycoprotein. ACS Appl Mater Interfaces. 2013;5(17):8351–8.

193. Zhou Y, Huangfu H, Yang J, Dong H, liu L, Xu M. Potentiometric analysis of sialic acid with a flexible carbon cloth based on boronate affinity and molecularly

imprinted polymers. Analyst. 2019;(Cc):6432–7.

194. Awino JK, Gunasekara RW, Zhao Y. Selective Recognition of d -Aldohexoses in Water by Boronic Acid-Functionalized, Molecularly Imprinted Cross-Linked Micelles. J Am Chem Soc. 2016;138(31):9759–62.

195. Ben-Amram Y, Riskin M, Willner I. Selective and enantioselective analysis of mono- and disaccharides using surface plasmon resonance spectroscopy and imprinted boronic acid-functionalized Au nanoparticle composites. Analyst. 2010;135(11):2952–9.

196. Stephenson-Brown A, Wang HC, Iqbal P, Preece JA, Long Y, Fossey JS, et al. Glucose selective Surface Plasmon Resonance-based bis-boronic acid sensor. Analyst. 2013;138(23):7140–5.

197. Zhang J, Geddes CD, Lakowicz JR. Complexation of polysaccharide and monosaccharide with thiolate boronic acid capped on silver nanoparticle. Anal Biochem. 2004;332(2):253–60.

198. Loh XJ, Tsai MH, Barrio J Del, Appel EA, Lee TC, Scherman OA. Triggered insulin release studies of triply responsive supramolecular micelles. Polym Chem. 2012;3(11):3180–8.

199. Matsumoto A, Ishii T, Nishida J, Matsumoto H, Kataoka K, Miyahara Y. A synthetic approach toward a self-regulated insulin delivery system. Angew Chemie - Int Ed. 2012;51(9):2124–8.

200. Ji M, Li P, Sheng N, Liu L, Pan H, Wang C, et al. Sialic Acid-Targeted Nanovectors with Phenylboronic Acid-Grafted Polyethylenimine Robustly Enhance siRNA-Based Cancer Therapy. ACS Appl Mater Interfaces. 2016;8(15):9565–76.

201. Naito M, Yoshinaga N, Ishii T, Matsumoto A, Miyahara Y, Miyata K, et al. Enhanced Intracellular Delivery of siRNA by Controlling ATP-Responsivity of Phenylboronic Acid-Functionalized Polyion Complex Micelles. Macromol Biosci. 2018;18(1):1–10.

202. Whitesides GM, Boncheva M. Beyond molecules: Self-assembly of mesoscopic and macroscopic components. Proc Natl Acad Sci U S A. 2002;99(8):4769–74.

203. Whitesides GM, Grzybowski B. Self-assembly at all scales. Science (80-). 2002;295(5564):2418–21.

204. Subramani K, Ahmed W. Chapter 12 - Self-assembly of

proteins and peptides and their applications in bionanotechnology and dentistry. In: Subramani K, Ahmed WBT-EN in D (Second E, editors. Micro and Nano Technologies . William Andrew Publishing; 2018. p. 231–49.

205. Hartgerink JD, Beniash E, Stupp SI. Self-assembly and mineralization of peptide-amphiphile nanofibers. Science (80-). 2001;294(5547):1684–9.

206. Clark TD, Tien J, Duffy DC, Paul KE, Whitesides GM. Self-assembly of 10-μm-sized objects into ordered three-dimensional arrays. J Am Chem Soc. 2001;123(31):7677–82.

207. Guha Thakurta S, Subramanian A. Fabrication of dense, uniform aminosilane monolayers: A platform for protein or ligand immobilization. Colloids Surfaces A Physicochem Eng Asp. 2012;414:384–92.

208. Morgenthaler S, Zink C, Spencer ND. Surface-chemical and -morphological gradients. Soft Matter. 2008;4(3):419–34.

209. Phan HTM, Bartelt-Hunt S, Rodenhausen KB, Schubert M, Bartz JC. Investigation of bovine serum albumin (BSA) attachment onto self-assembled monolayers (SAMs) using combinatorial quartz crystal microbalance with dissipation (QCM-D) and spectroscopic ellipsometry (SE). PLoS One. 2015;10(10).

210. Chaudhury MK. Self-assembled monolayers on polymer surfaces. Biosens Bioelectron. 1995;10(9–10):785–8.

211. Casalini S, Bortolotti CA, Leonardi F, Biscarini F. Self-assembled monolayers in organic electronics. Chem Soc Rev. 2017;46(1):40–71.

212. Badia A, Lennox RB, Reven L. A dynamic view of self-assembled monolayers. Acc Chem Res. 2000;33(7):475–81.

213. Wink T, Van Zuilen SJ, Bult A, Van Bennekom WP. Self-assembled monolayers for biosensors. Analyst. 1997;122(4):43–50.

214. Schwartz DK. Mechanisms and kinetics of self-assembled monolayer formation. Annu Rev Phys Chem . 2001 Oct;52(1):107–37.

215. Vericat C, Vela ME, Benitez G, Carro P, Salvarezza RC. Self-assembled monolayers of thiols and dithiols on gold: New challenges for a well-known system. Chem Soc Rev. 2010;39(5):1805–34.

216. Rouhana LL, Moussallem MD, Schlenoff JB. Adsorption of short-chain thiols and disulfides onto gold under

defined mass transport conditions: Coverage, kinetics, and mechanism. J Am Chem Soc. 2011;133(40):16080–91.

217. Biener MM, Biener J, Friend CM. Revisiting the S-Au(111) interaction: Static or dynamic? Langmuir. 2005;21(5):1668–71.

218. Lusteinberg PG, Vericat C, Benitez GA, Vela ME, Tognalli N, Fainstein A, et al. Spontaneously formed sulfur adlayers on gold in electrolyte solutions: Adsorbed sulfur or gold sulfide? J Phys Chem C. 2008;112(30):11394–402.

219. Millone MAD, Hamoudi H, Rodríguez L, Rubert A, Benítez GA, Vela ME, et al. Self-assembly of alkanedithiols on Au(111) from solution: Effect of chain length and self-assembly conditions. Langmuir. 2009;25(22):12945–53.

220. Bain CD, Biebuyck HA, Whitesides GM. Comparison of Self-Assembled Monolayers on Gold: Coadsorption of Thiols and Disulfides1. Langmuir. 1989;5(3):723–7.

221. Pensa E, Cortés E, Corthey G, Carro P, Vericat C, Fonticelli MH, et al. The chemistry of the sulfur-gold interface: In search of a unified model. Acc Chem Res. 2012;45(8):1183–92.

222. Vericat C, Vela ME, Salvarezza RC. Self-assembled monolayers of alkanethiols on Au(111): Surface structures, defects and dynamics. Phys Chem Chem Phys. 2005;7(18):3258–68.

223. Bucher JP, Santesson L, Kern K. Selective imaging of self-assembled monolayers by tunneling microscopy. Appl Phys A Solids Surfaces. 1994;59(2):135–8.

224. Chen J, Chang B, Oyola-Reynoso S, Wang Z, Thuo M. Quantifying Gauche Defects and Phase Evolution in Self-Assembled Monolayers through Sessile Drops. ACS Omega. 2017;2(5):2072–84.

225. Guo Q, Li F. Self-assembled alkanethiol monolayers on gold surfaces: Resolving the complex structure at the interface by STM. Phys Chem Chem Phys. 2014;16(36):19074–90.

226. Ramin L, Jabbarzadeh A. Odd-even effects on the structure, stability, and phase transition of alkanethiol self-assembled monolayers. Langmuir. 2011;27(16):9748–59.

227. Chinwangso P, Lee HJ, Jamison AC, Marquez MD, Park CS, Lee TR. Structure, Wettability, and Thermal Stability

of Organic Thin-Films on Gold Generated from the Molecular Self-Assembly of Unsymmetrical Oligo(ethylene glycol) Spiroalkanedithiols. Langmuir. 2017;33(8):1751–62.

228. Lacour V, Moumanis K, Hassen WM, Elie-Caille C, Leblois T, Dubowski JJ. Formation Kinetics of Mixed Self-Assembled Monolayers of Alkanethiols on GaAs(100). Langmuir. 2019;35(13):4415–27.

229. Sato Y, Yoshioka K, Murakami T, Yoshimoto S, Niwa O. Design of biomolecular interface for detecting carbohydrate and lectin weak interactions. Langmuir. 2012;28(3):1846–51.

230. Laibinis PE, Nuzzo RG, Whitesides GM. Structure of monolayers formed by coadsorption of two n-alkanethiols of different chain lengths on gold and its relation to wetting. J Phys Chem. 1992;96(12):5097–105.

231. Oyerokun FT, Vaia RA, Maguire JF, Farmer BL. Role of solvent selectivity in the equilibrium surface composition of monolayers formed from a solution containing mixtures of organic thiols. Langmuir. 2010;26(14):11991–7.

232. Asakawa H, Inada N, Hirata K, Matsui S, Igarashi T, Oku N, et al. Self-assembled monolayers of sulfonate-terminated alkanethiols investigated by frequency modulation atomic force microscopy in liquid. Nanotechnology. 2017;28(45).

233. Nicosia C, Huskens J. Reactive self-assembled monolayers: From surface functionalization to gradient formation. Mater Horizons. 2014;1(1):32–45.

234. Ko S, Han G, Lee JK. Surface organic chemistry for application to organic electronics. Tetrahedron Lett . 2015;56(24):3721–31.

235. Movilli J, Rozzi A, Ricciardi R, Corradini R, Huskens J. Control of Probe Density at DNA Biosensor Surfaces Using Poly(l -lysine) with Appended Reactive Groups. Bioconjug Chem. 2018;29(12):4110–8.

236. Lee C-Y, Nguyen P-CT, Grainger DW, Gamble LJ, Castner DG. Structure and DNA hybridization properties of mixed nucleic acid/maleimide-ethylene glycol monolayers. Anal Chem . 2007 Jun 15;79(12):4390–400.

237. Yeo WS, Mrksich M. Electroactive self-assembled monolayers that permit orthogonal control over the adhesion of cells to patterned substrates. Langmuir. 2006;22(25):10816–20.

238. Houseman BT, Gawalt ES, Mrksich M. Maleimide-functionalized self-assembled monolayers for the preparation of peptide and carbohydrate biochips. Langmuir. 2003;19(5):1522–31.

239. Escorihuela J, Bañuls MJ, Puchades R, Maquieira Á. DNA microarrays on silicon surfaces through thiol-ene chemistry. Chem Commun. 2012;48(15):2116–8.

240. Sheppard G, Oseki T, Baba A, Patton D, Kaneko F, Mao L, et al. Thiolene-based microfluidic flow cells for surface plasmon resonance imaging. Biomicrofluidics. 2011;5(2):1–6.

241. Du N, Chou J, Kulla E, Floriano PN, Christodoulides N, McDevitt JT. A disposable bio-nano-chip using agarose beads for high performance immunoassays. Biosens Bioelectron . 2011 Oct 15;28(1):251–6.

242. Norberg O, Lee IH, Aastrup T, Yan M, Ramström O. Photogenerated lectin sensors produced by thiol-ene/yne photo-click chemistry in aqueous solution. Biosens Bioelectron . 2012 Apr 15;34(1):51–6.

243. Belbekhouche S, Guerrouache M, Carbonnier B. Thiol-Maleimide Michael Addition Click Reaction: A New Route to Surface Modification of Porous Polymeric Monolith. Macromol Chem Phys. 2016;217(8):997–1006.

244. Yousaf MN, Mrksich M. Diels-Alder reaction for the selective immobilization of protein to electroactive self-assembled monolayers. J Am Chem Soc. 1999;121(17):4286–7.

245. De Araújo AD, Palomo JM, Cramer J, Köhn M, Schröder H, Wacker R, et al. Diels-Alder ligation and surface immobilization of proteins. Angew Chemie - Int Ed. 2005;45(2):296–301.

246. Hammer N, Brandl FP, Kirchhof S, Messmann V, Goepferich AM. Protein compatibility of selected cross-linking reactions for hydrogels. Macromol Biosci. 2015;15(3):405–13.

247. Sun XL, Stabler CL, Cazalis CS, Chaikof EL. Carbohydrate and protein immobilization onto solid surfaces by sequential Diels-Alder and azide-alkyne cycloadditions. Bioconjug Chem. 2006;17(1):52–7.

248. Huisgen R. 1,3-Dipolar Cycloadditions. Past and Future. Angew Chemie Int Ed English . 1963 Oct;2(10):565–98.

249. Rostovtsev V V., Green LG, Fokin V V., Sharpless KB.

A stepwise huisgen cycloaddition process: Copper(I)-catalyzed regioselective "ligation" of azides and terminal alkynes. Angew Chemie - Int Ed. 2002;41(14):2596–9.

250. Totobenazara J, Burke AJ. New click-chemistry methods for 1,2,3-triazoles synthesis: Recent advances and applications. Tetrahedron Lett . 2015;56(22):2853–9.

251. Wei F, Wang W, Ma Y, Tung C, Xu Z. Regioselective synthesis of multisubstituted 1,2,3-triazoles: moving beyond the copper-catalyzed azide–alkyne cycloaddition. 2016;14188–99.

252. Worrell BT, Malik JA, Fokin V V. Direct Evidence of a Dinuclear Copper Intermediate in Cu(I)-Catalyzed Azide-Alkyne Cycloadditions. Science (80-) . 2013 Apr 26;340(6131):457–60.

253. Ben El Ayouchia H, Bahsis L, Anane H, Domingo LR, Stiriba SE. Understanding the mechanism and regioselectivity of the copper(i) catalyzed [3 + 2] cycloaddition reaction between azide and alkyne: A systematic DFT study. RSC Adv. 2018;8(14):7670–8.

254. Wei F, Wang W, Ma Y, Tung CH, Xu Z. Regioselective synthesis of multisubstituted 1,2,3-triazoles: Moving beyond the copper-catalyzed azide-alkyne cycloaddition. Chem Commun. 2016;52(99):14188–99.

255. Rohde RD, Agnew HD, Yeo WS, Bailey RC, Heath JR. A non-oxidative approach toward chemically and electrochemically functionalizing Si(111). J Am Chem Soc. 2006;128(29):9518–25.

256. Ciampi S, Böcking T, Kilian KA, James M, Harper JB, Gooding JJ. Functionalization of acetylene-terminated monolayers on Si(100) surfaces: A click chemistry approach. Langmuir. 2007;23(18):9320–9.

257. Chelmowski R, Kafer D, Köster SD, Klasen T, Winkler T, Terfort A, et al. Postformation modification of SAMs: Using click chemistry to functionalize organic surfaces. Langmuir. 2009;25(19):11480–5.

258. Abbenante G, Le GT, Fairlie DP. Unexpected photolytic decomposition of alkyl azides under mild conditions. Chem Commun. 2007;1(43):4501–3.

259. Pickens CJ, Johnson SN, Pressnall MM, Leon MA, Berkland CJ. Practical Considerations, Challenges, and Limitations of Bioconjugation via Azide-Alkyne Cycloaddition. Bioconjug Chem. 2018;29(3):686–701.

260. Hudalla GA, Murphy WL. Immobilization of peptides with distinct biological activities onto stem cell culture substrates using orthogonal chemistries. Langmuir. 2010;26(9):6449–56.

261. Yaakov N, Chaikin Y, Wexselblatt E, Tor Y, Vaskevich A, Rubinstein I. Application of Surface Click Reactions to Localized Surface Plasmon Resonance (LSPR) Biosensing. Chem - A Eur J. 2017;23(42):10148–55.

262. Stephenson-Brown A, Acton AL, Preece JA, Fossey JS, Mendes PM. Selective glycoprotein detection through covalent templating and allosteric click-imprinting. Chem Sci. 2015;

263. Wang RE, Zhang Y, Cai J, Cai W, Gao T. Aptamer-based fluorescent biosensors. Curr Med Chem . 2011;18(27):4175–84.

264. Ellington AD, Szostak JW. In vitro selection of RNA molecules that bind specific ligands. Nature. 1990;346(6287):818–22.

265. Cai S, Yan J, Xiong H, Liu Y, Peng D, Liu Z. Investigations on the interface of nucleic acid aptamers and binding targets. Analyst. 2018;143(22):5317–38.

266. Sundaram P, Kurniawan H, Byrne ME, Wower J. Therapeutic RNA aptamers in clinical trials. Eur J Pharm Sci . 2013;48(1–2):259–71.

267. Pleiko K, Saulite L, Parfejevs V, Miculis K, Vjaters E, Riekstina U. Differential binding cell-SELEX method to identify cell-specific aptamers using high-throughput sequencing. Sci Rep . 2019;9(1):1–12.

268. Li J, Tan S, Chen X, Zhang C-Y, Zhang Y. Peptide Aptamers with Biological and Therapeutic Applications. Curr Med Chem. 2011;18(27):4215–22.

269. Bardou C, Borie C, Bickle M, Rudkin BB, Colas P. Peptide Aptamers for Small Molecule Drug Discovery. In: Encyclopedic Reference of Genomics and Proteomics in Molecular Medicine . 2009. p. 373–88.

270. Colombo M, Mizzotti C, Masiero S, Kater MM, Pesaresi P. Peptide aptamers: The versatile role of specific protein function inhibitors in plant biotechnology. J Integr Plant Biol. 2015;57(11):892–901.

271. Kaur H, Bruno JG, Kumar A, Sharma TK. Aptamers in the therapeutics and diagnostics pipelines. Theranostics. 2018;8(15):4016–32.

272. Savory N, Abe K, Sode K, Ikebukuro K. Selection of DNA aptamer against prostate specific antigen using a genetic algorithm and application to sensing. Biosens Bioelectron . 2010;26(4):1386–91.

273. Walsh R, DeRosa MC. Retention of function in the DNA homolog of the RNA dopamine aptamer. Biochem Biophys Res Commun . 2009;388(4):732–5.

274. Bala J, Chinnapaiyan S, Dutta RK, Unwalla H. Aptamers in HIV research diagnosis and therapy. RNA Biol . 2018;15(3):327–37.

275. Cho S, Lee BR, Cho BK, Kim JH, Kim BG. In vitro selection of sialic acid specific RNA aptamer and its application to the rapid sensing of sialic acid modified sugars. Biotechnol Bioeng. 2013;110(3):905–13.

276. Gong S, Ren H, Lin C, Hu P, Tian R, Liu Z, et al. Immunochromatographic strip biosensor for the rapid detection of N-glycolylneuraminic acid based on aptamer-conjugated nanoparticle. Anal Biochem . 2018;561–562(June):52–8.

277. Li M, Lin N, Huang Z, Du L, Altier C, Fang H, et al. Selecting aptamers for a glycoprotein through the incorporation of the boronic acid moiety. J Am Chem Soc. 2008;130(38):12636–8.

278. Díaz-Fernández A, Miranda-Castro R, de-los-Santos-Álvarez N, Rodríguez EF, Lobo-Castañón MJ. Focusing aptamer selection on the glycan structure of prostate-specific antigen: Toward more specific detection of prostate cancer. Biosens Bioelectron. 2019;128(November 2018):83–90.

279. Pauling L, Campbell DH. The manufacture of antibodies in vitro. J Exp Med. 1942;76(2):211–20.

280. Arshady R, Mosbach K. Synthesis of substrate-selective polymers by host-guest polymerization. Die Makromol Chemie. 1981;182(2).

281. Wulff G, Grobe-Einsler R, Vesper W, Sarhan A. Enzyme-analogue built polymers. On the specificity distribution of chiral cavities prepared in synthetic polymers. Die Makromol Chemie. 1977;178(10).

282. Takeuchi T, Sunayama H. Beyond natural antibodies-a new generation of synthetic antibodies created by post-imprinting modification of molecularly imprinted polymers. Chem Commun. 2018;54(49):6243–51.

283. Takeuchi T, Murase N, Maki H, Mukawa T, Shinmori H. Dopamine selective molecularly imprinted polymers via post-imprinting modification. Org Biomol Chem. 2006;4(3):565–8.

284. Sunayama H, Kitayama Y, Takeuchi T. Regulation of protein-binding activities of molecularly imprinted polymers via post-imprinting modifications to exchange functional groups within the imprinted cavity. J Mol Recognit. 2018;31(3):1–6.

285. Matsumoto H, Sunayama H, Kitayama Y, Takano E, Takeuchi T. Site-specific post-imprinting modification of molecularly imprinted polymer nanocavities with a modifiable functional monomer for prostate cancer biomarker recognition. Sci Technol Adv Mater . 2019;20(1):305–12.

286. Rebelo TSCR, Costa R, Brandão ATSC, Silva AF, Sales MGF, Pereira CM. Molecularly imprinted polymer SPE sensor for analysis of CA-125 on serum. Anal Chim Acta. 2019;1082:126–35.

287. Carneiro MCCG, Sousa-Castillo A, Correa-Duarte MA, Sales MGF. Dual biorecognition by combining molecularly-imprinted polymer and antibody in SERS detection. Application to carcinoembryonic antigen. Biosens Bioelectron . 2019;146(October):111761.

288. Zhang R, Zhang T, Lv Y, Qin P, Li H, Li J ping, et al. Selective binding of heparin oligosaccharides in a magnetic thermoresponsive molecularly imprinted polymer. Talanta . 2019;201(November 2018):441–9.

289. Medina Rangel PX, Laclef S, Xu J, Panagiotopoulou M, Kovensky J, Tse Sum Bui B, et al. Solid-phase synthesis of molecularly imprinted polymer nanolabels: Affinity tools for cellular bioimaging of glycans. Sci Rep. 2019;9(1):1–9.

290. Zhang L, Zhu C, Chen C, Zhu S, Zhou J, Wang M, et al. Determination of kanamycin using a molecularly imprinted SPR sensor. Food Chem . 2018;266(March):170–4.

291. Saeki T, Sunayama H, Kitayama Y, Takeuchi T. Orientationally Fabricated Zwitterionic Molecularly Imprinted Nanocavities for Highly Sensitive Glycoprotein Recognition. Langmuir. 2019;35(5):1320–6.

292. Mitchell P, Tommasone S, Angioletti-Uberti S, Bowen J, Mendes PM. Precise Generation of Selective Surface-Confined Glycoprotein Recognition Sites. ACS Appl Bio Mater. 2019;2(6):2617–23.

293. Cui F, Zhou Z, Zhou HS. Molecularly imprinted polymers and surface imprinted polymers based electrochemical biosensor for infectious diseases. Sensors (Switzerland). 2020;20(4).

294. Verheyen E, Schillemans JP, Van Wijk M, Demeniex MA, Hennink WE, Van Nostrum CF. Challenges for the effective molecular imprinting of proteins. Biomaterials . 2011;32(11):3008–20.

295. Tommasone S, Allabush F, Tagger YK, Norman J, Köpf M, Tucker JHR, et al. The challenges of glycan recognition with natural and artificial receptors. Chem Soc Rev. 2019;48(22):5488–505.

296. Young T. An Essay on the cohesion of fluids. R Soc. 1805;95:65–87.

297. Bormashenko E. Wetting of Real Surfaces. 2017;(October).

298. Krishnan A, Liu YH, Cha P, Woodward R, Allara D, Vogler EA. An evaluation of methods for contact angle measurement. Colloids Surfaces B Biointerfaces. 2005;43(2):95–8.

299. Kwok DY, Neumann AW. Contact angle measurement and contact angle interpretation. Vol. 81, Advances in Colloid and Interface Science. 1999. 167–249 p.

300. Sharma A. Equilibrium Contact Angles and Film Thicknesses in the Apolar and Polar Systems: Role of Intermolecular Interactions in Coexistence of Drops with Thin Films. Langmuir. 1993;9(12):3580–6.

301. Kabza K, Gestwicki JE, McGrath JL. Contact Angle Goniometry as a Tool for Surface Tension Measurements of Solids, Using Zisman Plot Method: A Physical Chemistry Experiment. J Chem Educ. 2000;77(1):63–5.

302. Michalski M, Desobry S, Pons M, Hardy J. Michalski-1998_Adhesion of Edible Oils to Food Contact Surfaces. 1998;75(4):2–9.

303. Forch R, Schonherr H, Jenkins ATA. Surface Design: Applications in Bioscience and Nanotechnology . Förch R, Schönherr H, Jenkins ATA, editors. Wiley; 2009.

304. Annamalai M, Gopinadhan K, Han SA, Saha S, Park HJ, Cho EB, et al. Surface energy and wettability of van der Waals structures. Nanoscale. 2016;8(10):5764–70.

305. Bruel C, Queffeulou S, Darlow T, Virgilio N, Tavares JR, Patience GS. Experimental methods in chemical

engineering: Contact angles. Can J Chem Eng. 2019;97(4):832–42.

306. Miyama M, Yang Y, Yasuda T, Okuno T, Yasuda HK. Static and Dynamic Contact Angles of Water on Polymeric Surfaces. 1997;7463(6):5494–503.

307. Njobuenwu DO, Oboho EO, Gumus RH. Leonardo Electronic Journal of Practices and Technologies Determination of Contact Angle from Contact Area of Liquid Droplet Spreading on Solid Substrate. 2007;(10):29–38.

308. Bormashenko E. Wetting of real solid surfaces: New glance on well-known problems. Colloid Polym Sci. 2013;291(2):339–42.

309. Chibowski E, Curie-sklodowska M. Surface free energy of a solid from contact angle hysteresis. 2003;103:149–72.

310. Good RJ. Contact Angle, Wetting, and Adhesion: A Critical Review. Vol. 6, Journal of Adhesion Science and Technology. 1992. 1269–1302 p.

311. Strobel M, Lyons CS. An essay on contact angle measurements. Plasma Process Polym. 2011;8(1):8–13.

312. Drude P. The theory of optics. dover, new york. 1902;

313. Rothen A. The ellipsometer, an apparatus to measure thickness of thin surface films. Rev Sci Instrum. 1945;16(2):26–30.

314. Aspnes DE. Spectroscopic ellipsometry — Past , present , and future. Thin Solid Films . 2014;571:334–44.

315. Goncalves D, Irene EA. Fundamentals and applications of spectroscopic ellipsometry. Quim Nov. 2002;(November).

316. Theeten, J B, Aspnes DE. Ellipsometry in thin film analysis. Ann Rev Mater Sci. 1981;11:97–122.

317. Harland. G T. A users guide to ellipsometry. academic press limited; 1993.

318. Gonçalves D, Irene EA. Fundamentals and applications of spectroscopic ellipsometry. Quim Nova. 2002;25(5):794–800.

319. Canepa M, Maidecchi G, Toccafondi C, Cavalleri O, Prato M, Chaudhari V, et al. Spectroscopic ellipsometry of self assembled monolayers: Interface effects. the case of phenyl selenide SAMs on gold. Phys Chem Chem Phys. 2013;15(27):11559–65.

320. Brundle CR, Tompkins HG, Hilfiker JN. Spectroscopic Ellipsometry: Practical Application to Thin Film Characterisation. 2016.

321. Cody D, Babeva T, Madjarova V, Kharchenko A, Sabad-e-Gul, Mintova S, et al. In-Situ Ellipsometric Study of the Optical Properties of LTL-Doped Thin Film Sensors for Copper(II) Ion Detection. Coatings. 2020;10(4):423.

322. Nestler P, Helm CA. Determination of refractive index and layer thickness of nm-thin films via ellipsometry. Opt Express. 2017;25(22):27077.

323. Prato M, Moroni R, Bisio F, Rolandi R, Mattera L, Cavalleri O, et al. Optical Characterization of Thiolate Self-Assembled Monolayers on Au(111). J Phys Chem C. 2008;112(10):3899–906.

324. Hilfiker JN, Stadermann M, Sun J, Tiwald T, Hale JS, Miller PE, et al. Determining thickness and refractive index from free-standing ultra-thin polymer films with spectroscopic ellipsometry. Appl Surf Sci . 2017;421:508–12.

325. Canepa M, Maidecchi G, Toccafondi C, Cavalleri O, Prato M, Chaudhari V, et al. Spectroscopic ellipsometry of self assembled monolayers: interface effects. The case of phenyl selenide SAMs on gold †. 2013;11559–65.

326. Shi J, Hong B, Parikh AN, Collins RW, Allara DL. Optical characterization of electronic transitions arising from the Au/S interface of self-assembled n-alkanethiolate monolayers. Chem Phys Lett. 1995;246(1–2):90–4.

327. Durgapal P, Ehrstein JR, Nguyen N V. Thin film ellipsometry metrology. 2009;121(March 2008):121–31.

328. Hilfiker JN, Synowicki R a, Tompkins HG. Spectroscopic Ellipsometry Methods for Thin Absorbing Coatings. Soc Vac Coaters. 2008;(1):511–6.

329. Cushman C, Smith N, Kaykhaii M, Podraza N, Linford M. An Introduction to Modeling in Spectroscopic Ellipsometry, Focusing on Models for Transparent Materials: the Cauchy and Sellmeier Models. Vac Technol Coat. 2016 Jul 1;

330. Othman MT, Lubguban JA, Lubguban AA, Gangopadhyay S, Miller RD, Volksen W, et al. Characterization of porous low- k films using variable angle spectroscopic ellipsometry. J Appl Phys. 2006;99(8):1–7.

331. Losurdo M, Bergmair M, Bruno G, Cattelan D, Cobet C,

De Martino A, et al. Spectroscopic ellipsometry and polarimetry for materials and systems analysis at the nanometer scale: State-of-the-art, potential, and perspectives. J Nanoparticle Res. 2009;11(7):1521–54.

332. Woollam Co JA. CompleteEase Software Manual, Version 4.63. 2011;

333. Hilfiker JN, Woollam JA. A Tutorial on Spectroscopic Ellipsometry (SE), 2. The Cauchy Model. 2019;(April). Available from: www.vtcmag.com

334. Petsko GA. An Introduction to Modeling Structure. Curr Protoc Bioinforma. 2006;(June):5.1.1-5.1.3.

335. Mattox DM. Substrate ("Real") Surfaces and Surface Modification. Handbook of Physical Vapor Deposition (PVD) Processing. 1998. 56–126 p.

336. Bluhm H. X-ray photoelectron spectroscopy (XPS) for in situ characterisation of thin film growth. Electron Opt Mater. 2011;75–98.

337. Seah MP. A review of the analysis of surfaces and thin films by AES and XPS. Vacuum. 1984;34(3–4):463–78.

338. Aguilar ZP. Types of Nanomaterials and Corresponding Methods of Synthesis. In: Nanomaterials for Medical Applications . Elsevier; 2013. p. 33–82.

339. Watts, John F, Wolstenholme J. An introduction to surface analysis by XPS and AES. Wiley; 2003.

340. Zakaznova-Herzog VP, Nesbitt HW, Bancroft GM, Tse JS, Gao X, Skinner W. High-resolution valence-band XPS spectra of the nonconductors quartz and olivine. Phys Rev B - Condens Matter Mater Phys. 2005;72(20):1–13.

341. Lanje AS, Sharma SJ. Functional Nanomaterial Synthesis and Charaterization Electrical , Magnetic and Optical. 2014;(August 2017).

342. Easton CD, Kinnear C, McArthur SL, Gengenbach TR. Practical guides for x-ray photoelectron spectroscopy: Analysis of polymers. J Vac Sci Technol A . 2020;38(2):023207.

343. Greczynski G, Hultman L. X-ray photoelectron spectroscopy: Towards reliable binding energy referencing. Prog Mater Sci . 2020;107(July 2019):100591.

344. Watcharinyanon S. Structure of Self-Assembled Monolayers on Gold Studied by NEXAFS and Photoelectron Spectroscopy. 2008. 81 p.

345. Wagner CD, Naumkin A, Kraut-Vass J., Allison J., Powell C., Rumble JRJ. NIST standard reference databse 20. version 3.4. 2003.

346. Baer DR, Artyushkova K, Richard Brundle C, Castle JE, Engelhard MH, Gaskell KJ, et al. Practical guides for x-ray photoelectron spectroscopy: First steps in planning, conducting, and reporting XPS measurements. J Vac Sci Technol A. 2019;37(3):031401.

347. Deimel P, Allegretti F. Elemental and Chemical Analysis with X-ray X-ray Photoelectron Spectroscopy. Electron Spectrosc Surfaces. 2011;(35):1–22.

348. Banwell C. Fundamentals of Molecular Spectroscopy. Third Edit. McGraw-Hill Book Company; 1983. 20–23 p.

349. Hofstetter YJ, Vaynzof Y. Quantifying the Damage Induced by X-ray Photoelectron Spectroscopy Depth Profiling of Organic Conjugated Polymers. ACS Appl Polym Mater. 2019;1(6):1372–81.

350. Ward RJ, Wood BJ. A comparison of experimental and theoretically derived sensitivity factors for XPS. Surf Interface Anal. 1992;18(9):679–84.

351. Berkeley L. X-ray photoelectron spectroscopy (XPS) for in situ characterisation of thin film growth. 2011;

352. Schulze M, Bolwin K, Gülzow E, Schnurnberger W. XPS analysis of PTFE decomposition due to ionizing radiation. Fresenius J Anal Chem. 1995;353(5–8):778–84.

353. H T, K M. surface damage of organic materials during XPS analysis. J Surf Anal. 1999;5(2).

354. Wood RW. On a remarkable case of uneven distribution of light in a diffraction grating spectrum. Proc Phys Soc London. 1902;18(1):269–75.

355. Kretschmann E, Raether H. Radiative Decay of Non Radiative Surface Plasmons Excited by Light. Zeitschrift fur Naturforsch - Sect A J Phys Sci. 1968;23(12):2135–6.

356. Otto A. Excitation of nonradiative surface plasma waves in silver by the method of frustrated total reflection. Zeitschrift für Phys. 1968;216(4):398–410.

357. Gupta BD, Verma RK. Surface plasmon resonance-based fiber optic sensors: Principle, probe designs, and some applications. J Sensors. 2009;2009.

358. Daghestani HN, Day BW. Theory and applications of surface plasmon resonance, resonant mirror, resonant

waveguide grating, and dual polarization interferometry biosensors. Sensors. 2010;10(11):9630–46.

359. Howe CL, Webb KF, Abayzeed SA, Anderson DJ, Denning C, Russell NA. Surface plasmon resonance imaging of excitable cells. J Phys D Appl Phys. 2019;52(10).

360. Menon PS, Gan SM, Mohamad NR, Jamil NA, Tarumaraja KA, Razak NR, et al. Kretschmann based surface plasmon resonance for sensing in visible region. 2019 IEEE 9th Int Nanoelectron Conf INEC 2019. 2019;4–9.

361. Papathanassoglou DA, Vohnsen B. Direct visualization of evanescent optical waves. Am J Phys. 2003;71(7):670–7.

362. Homola J, Yee SS, Gauglitz G. Surface plasmon resonance sensors: review. Sensors Actuators, B Chem. 1999;54(1):3–15.

363. Tang Y, Zeng X, Liang J. Surface Plasmon Resonance: An Introduction to a Surface Spectroscopy Technique. J Chem Educ . 2010 Jul;87(7):742–6.

364. Wang D, Loo JFC, Chen J, Yam Y, Chen SC, He H, et al. Recent advances in surface plasmon resonance imaging sensors. Sensors (Switzerland). 2019;19(6).

365. Chlebus R, Chylek J, Ciprian D, Hlubina P. Surface Plasmon Resonance Based Measurement of the Dielectric Function of a Thin Metal Film. Sensors (Basel). 2018;18(11):8–19.

366. Schasfoort R. Introduction to surface plasmon resonance. Handb Surf Plasmon Reson . 2008;1–14.

367. Ahmed FE, Wiley JE, Weidner DA, Bonnerup C, Mota H. Surface plasmon resonance (SPR) spectrometry as a tool to analyze nucleic acid-protein interactions in crude cellular extracts. Cancer Genomics and Proteomics. 2010;7(6):303–10.

368. Englebienne P, Van Hoonacker A, Verhas M. Surface plasmon resonance: Principles, methods and applications in biomedical sciences. Spectroscopy. 2003;17(2–3):255–73.

369. Wang HB, Dembo M, Hanks SK, Wang Y. Focal adhesion kinase is involved in mechanosensing during fibroblast migration. Proc Natl Acad Sci U S A. 2001;98(20):11295–300.

370. Nelson DE. Current considerations in the use of the APTT in monitoring unfractionated heparin. Clin Lab Sci. 1999;12(6):359–64.

371. Varki A. Biological roles of glycans. Glycobiology. 2017;27(1):3–49.

372. Mody R, Joshi SH antara., Chaney W. Use of lectins as diagnostic and therapeutic tools for cancer. J Pharmacol Toxicol Methods. 1995;33(1):1–10.

373. Manning MC, Chou DK, Murphy BM, Payne RW, Katayama DS. Stability of protein pharmaceuticals: An update. Pharm Res. 2010;27(4):544–75.

374. Wang W, Singh S, Zeng DL, King K, Nema S. Antibody Structure, Instability, and Formulation. J Pharm Sci . 2007 Jan;96(1):1–26.

375. Hayes B, Murphy C, Crawley A, O'Kennedy R. Developments in Point-of-Care Diagnostic Technology for Cancer Detection. Diagnostics. 2018;8(2):39.

376. Vermassen T, Speeckaert MM, Lumen N, Rottey S, Delanghe JR. Glycosylation of prostate specific antigen and its potential diagnostic applications. Clin Chim Acta . 2012;413(19–20):1500–5.

377. Wang X, Wang L, He X, Zhang Y, Chen L. A molecularly imprinted polymer-coated nanocomposite of magnetic nanoparticles for estrone recognition. Talanta. 2009;78(2):327–32.

378. Xia N, Deng D, Zhang L, Yuan B, Jing M, Du J, et al. Sandwich-type electrochemical biosensor for glycoproteins detection based on dual-amplification of boronic acid-gold nanoparticles and dopamine-gold nanoparticles. Biosens Bioelectron . 2013;43(1):155–9.

379. Hein CD, Liu X-M, Wang D. Click Chemistry, A Powerful Tool for Pharmaceutical Sciences. Pharm Res . 2008 Oct 29;25(10):2216–30.

380. Chen J, Chang B, Oyola-Reynoso S, Wang Z, Thuo M. Quantifying Gauche Defects and Phase Evolution in Self-Assembled Monolayers through Sessile Drops. ACS Omega . 2017 May 31;2(5):2072–84.

381. Turner NW, Jeans CW, Brain KR, Allender CJ, Hlady V, Britt DW. From 3D to 2D: A Review of the Molecular Imprinting of Proteins.

382. Presolski SI, Hong VP, Finn MG. Copper-Catalyzed Azide–Alkyne Click Chemistry for Bioconjugation. Curr Protoc Chem Biol . 2011 Dec;3(4):153–62.

383. Hong V, Presolski S, Ma C, Finn MG. Analysis and optimization of CuAAC for bioconjugation. October.

2008;141(4):520–9.

384. Chi Q, Zhang J, Ulstrup J. Surface microscopic structure and electrochemical rectification of a branched alkanethiol self-assembled monolayer. J Phys Chem B. 2006;110(3):1102–6.

385. Chechik V, Schönherr H, Vancso GJ, Stirling CJM. Self-assembled monolayers of branched thiols and bisulfides on gold: Surface coverage, order and chain orientation. Langmuir. 1998;14(11):3003–10.

386. Hager G, Brolo AG. Adsorption/desorption behaviour of cysteine and cystine in neutral and basic media: Electrochemical evidence for differing thiol and disulfide adsorption to a Au(1 1 1) single crystal electrode. J Electroanal Chem. 2003;550–551:291–301.

387. Chan LC, Cox BG. Kinetics of amide formation through carbodiimide/N-hydroxybenzotriazole (HOBt) couplings. J Org Chem. 2007;72(23):8863–9.

388. Kleinert M, Winkler T, Terfort A, Lindhorst TK. A modular approach for the construction and modification of glyco-SAMs utilizing 1,3-dipolar cycloaddition. Org Biomol Chem. 2008;6(12):2118–32.

389. Lee M, Kim T Il, Kim KH, Kim JH, Choi MS, Choi HJ, et al. Formation of a self-assembled phenylboronic acid monolayer and its application toward developing a surface plasmon resonance-based monosaccharide sensor. Anal Biochem. 2002;310(2):163–70.

390. Kanayama N, Kitano H. Interfacial recognition of sugars by boronic acid-carrying self-assembled monolayer. Langmuir. 2000;16(2):577–83.

391. Brewer SH, Allen AM, Lappig SE, Chasse TL, Briggman KA, German CB, et al. Infrared detection of a phenylboronic acid terminated alkane thiol monolayer on gold surfaces. Langmuir. 2004;20(13):5512–20.

392. McKay CS, Finn MG. Click Chemistry in Complex Mixtures: Bioorthogonal Bioconjugation. Chem Biol . 2014 Sep;21(9):1075–101.

393. Clayden J, Greeves N, Warren S. Organic chemistry. Ed. 2nd, editor. Oxford University Press; 2001.

394. Howzen SE, Scott P. Formation of benzyl azide from benzyl bromide; Benzyl azide. ChemSpider. 2010;SyntheticP:SyntheticPage 408.

395. Ross SA, Lowe G. Downfield displacement of the NMR

signal of water in deuterated dimethylsulfoxide by the addition of deuterated trifluoroacetic acid. Tetrahedron Lett. 2000;41(17):3225–7.

396. Kuwata K, Matumoto T, Cheng H, Nagayama K, James TL, Roder H. NMR-detected hydrogen exchange and molecular dynamics simulations provide structural insight into fibril formation of prion protein fragment 106-126. Proc Natl Acad Sci U S A. 2003;100(25):14790–5.

397. Li Y, Hoskins JN, Sreerama SG, Grayson SM. MALDI–TOF Mass Spectral Characterization of Polymers Containing an Azide Group: Evidence of Metastable Ions. Macromolecules . 2010 Jul 27;43(14):6225–8.

398. Abramovitch RA, Kyba EP, Scriven EFV. Mass Spectrometry of Aryl Azides. J Org Chem. 1971;36(24):3796–803.

399. Lennox AJJ, Lloyd-Jones GC. Selection of boron reagents for Suzuki-Miyaura coupling. Chem Soc Rev. 2014;43(1):412–43.

400. Berg R, Straub BF. Advancements in the mechanistic understanding of the copper-catalyzed azide-alkyne cycloaddition. Beilstein J Org Chem. 2013;9:2715–50.

401. Hein JE, Krasnova LB, Iwasaki M, Fokin V V. Cu-Catalyzed Azide-Alkyne Cycloaddition: Preparation of Tris((1-Benzyl-1 H -1,2,3-Triazolyl)Methyl)Amine . Org Synth. 2011;(September):238–46.

402. Tikekar R V., Anantheswaran RC, Elias RJ, Laborde LF. Ultraviolet-induced oxidation of ascorbic acid in a model juice system: Identification of degradation products. J Agric Food Chem. 2011;59(15):8244–8.

403. Hitosugi S, Tanimoto D, Nakanishi W, Isobe H. A facile chromatographic method for purification of pinacol boronic esters. Chem Lett. 2012;41(9):972–3.

404. Silva AMS, Santos CMM, Pinto DCGA. Advanced NMR techniques for structural characterization of heterocyclic structures. Vol. 661, Recent Research Developments in Heterocyclic Chemistry. 2007. 397–475 p.

405. Xu HJ, Zhao YQ, Feng T, Feng YS. Chan-lam-type s-arylation of thiols with boronic acids at room temperature. J Org Chem. 2012;77(6):2878–84.

406. Taniguchi N. Convenient synthesis of unsymmetrical organochalcogenides using organoboronic acids with dichalcogenides via cleavage of the S-S, Se-Se, or Te-Te

bond by a copper catalyst. J Org Chem. 2007;72(4):1241–5.

407. Attri P, Gupta S, Kumar R. Green methodology for the preparation of disulfide. Green Chem Lett Rev. 2012;5(1):33–42.

408. Wang M, Tang T. Surface treatment strategies to combat implant-related infection from the beginning. J Orthop Transl . 2019;17:42–54.

409. Ostuni E, Chapman RG, Liang MN, Meluleni G, Pier G, Ingber DE, et al. Self-assembled monolayers that resist the adsorption of proteins and the adhesion of bacterial and mammalian cells. Langmuir. 2001;17(20):6336–43.

410. Hosseinpour S, Johnson CM, Leygraf C. Alkanethiols as inhibitors for the atmospheric corrosion of copper induced by formic acid: Effect of chain length. J Electrochem Soc. 2013;160(6):270–6.

411. Rajkumar G, Sethuraman MG. Corrosion protection ability of self-assembled monolayer of 3-amino-5-mercapto-1,2,4-triazole on copper electrode. Thin Solid Films . 2014;562:32–6.

412. Chaki NK, Vijayamohanan K. Self-assembled monolayers as a tunable platform for biosensor applications. Biosens Bioelectron. 2002;17(1–2):1–12.

413. Narayan T, Kumar S, Kumar S, Augustine S, Yadav BK, Malhotra BD. Protein functionalised self assembled monolayer based biosensor for colon cancer detection. Talanta . 2019;201(February):465–73.

414. Kim J, Park W, Hong HG. The effect of steric hindrance on rate constant of a Diels-Alder reaction on the hydroquinone-terminated self-assembled monolayer. Bull Korean Chem Soc. 2004;25(7):1081–4.

415. Bienaime A, Leblois T, Gremaud N, Chaudon MJ, Osta M El, Pecqueur D, et al. Influence of a thiolate chemical layer on GaAs (100) biofunctionalization: An original approach coupling atomic force microscopy and mass spectrometry methods. Materials (Basel). 2013;6(11):4946–66.

416. Hutchins DO, Weidner T, Baio J, Polishak B, Acton O, Cernetic N, et al. Effects of self-assembled monolayer structural order, surface homogeneity and surface energy on pentacene morphology and thin film transistor device performance. J Mater Chem C . 2013;1(1):101–13.

417. Devaraj NK, Collman JP. Copper catalyzed azide-

alkyne cycloadditions on solid surfaces: Applications and future directions. QSAR Comb Sci. 2007;26(11–12):1253–60.

418. Yáñez-Sedeño P, González-Cortés A, Campuzano S, Pingarrón JM. Copper(I)-catalyzed click chemistry as a tool for the functionalization of nanomaterials and the preparation of electrochemical (Bio)sensors. Sensors (Switzerland). 2019;19(10).

419. Schlenoff JB, Li M, Ly H. Stability and Self-Exchange in Alkanethiol Monolayers. J Am Chem Soc. 1995;117(50):12528–36.

420. Stephenson-brown AJ. synthetic sensors for saccharides and glycoproteins. Univ Birmingham Thesis. 2015;

421. James M, Ciampi S, Darwish TA, Hanley TL, Sylvester SO, Gooding JJ. Nanoscale water condensation on click-functionalized self-assembled monolayers. Langmuir. 2011;27(17):10753–62.

422. Kwok DY, Neumann AWU. Contact angle measurement and contact angle interpretation. 1999.

423. Chen S, Smith LM. Photopatterned Thiol Surfaces for Biomolecule Immobilization. Langmuir. 2009 Oct;25(20):12275–82.

424. Castner DG, Hinds K, Grainger DW. X-ray photoelectron spectroscopy sulfur 2p study of organic thiol and bisulfide binding interactions with gold surfaces. Langmuir. 1996;12(21):5083–6.

425. Barriet D, Yam CM, Shmakova OE, Jamison AC, Lee TR. 4-mercaptophenylboronic acid SAMs on gold: Comparison with SAMs derived from thiophenol, 4-mercaptophenol, and 4-mercaptobenzoic acid. Langmuir. 2007;23(17):8866–75.

426. Wieliczka DM, Ding X, Dubowski JJ. X-ray photoelectron spectroscopy study of self-assembled monolayers of alkanethiols on (001) GaAs. J Vac Sci Technol A Vacuum, Surfaces, Film. 2006;24(5):1756–9.

427. Snow AW, Jernigan GG, Ancona MG. Packing density of HS(CH2)nCOOH self-assembled monolayers. Analyst. 2011;136(23):4935–49.

428. Zhang J, Welinder AC, Chi Q, Ulstrup J. Electrochemically controlled self-assembled monolayers characterized with molecular and sub-molecular resolution. Phys Chem Chem Phys. 2011;13(13):5526–45.

429. Lilge I, Schönherr H. Covalently cross-linked

poly(acrylamide) brushes on gold with tunable mechanical properties via surface-initiated atom transfer radical polymerization. Eur Polym J. 2013;49(8):1943–51.

430. G B, D B. High Resolution XPS of Organic Polymers: The Scienta ESCA300 Database. J Chem Educ . 1993 Jan;70(1):A25.

431. Liu J, Schüpbach B, Bashir A, Shekhah O, Nefedov A, Kind M, et al. Structural characterization of self-assembled monolayers of pyridine-terminated thiolates on gold. Phys Chem Chem Phys . 2010;12(17):4459.

432. Rolandi R, Cavalleri O, Toneatto C, Ricci D. Scanning electron microscopy and atomic force microscopy of alkanethiol monolayers on gold. Thin Solid Films. 1994;243(1–2):431–6.

433. Terada Y, Takeuchi N, Yoshida S, Taninaka A, Takeuchi O, Shigekawa H. Effect of defects buried in pentacene/alkanethiol self-assembled monolayer/Au film on its electronic properties visualized by scanning tunneling microscopy/spectroscopy. Jpn J Appl Phys. 2010;49(8 PART 4):1–4.

434. Patel DA, Weller AM, Chevalier RB, Karos CA, Landis EC. Ordering and defects in self-assembled monolayers on nanoporous gold. Appl Surf Sci . 2016;387:503–12.

435. Mar W, Klein ML. Molecular Dynamics Study of the Self-Assembled Monolayer Composed of S(CH2)14CH3 Molecules Using an All-Atoms Model. Langmuir. 1994;10(1):188–96.

436. Tiwari A, Terada D, Yoshikawa C, Kobayashi H. An enzyme-free highly glucose-specific assay using self-assembled aminobenzene boronic acid upon polyelectrolytes electrospun nanofibers-mat. Talanta . 2010;82(5):1725–32.

437. Dou RF, Ma XC, Xi L, Yip HL, Wong KY, Lau WM, et al. Self-assembled monolayers of aromatic thiols stabilized by parallel-displaced π-π stacking interactions. Langmuir. 2006;22(7):3049–56.

438. Fenter P, Eberhardt A, Liang KS, Eisenberger P. Epitaxy and chainlength dependent strain in self-assembled monolayers. J Chem Phys . 1997 Jan 22;106(4):1600–8.

439. Zareie MH, Ma H, Reed BW, Jen AKY, Sarikaya M. Controlled assembly of conducting monomers for molecular electronics. Nano Lett. 2003;3(2):139–42.

440. Fabre B, Hauquier F. Boronic Acid-Functionalized Oxide-Free Silicon Surfaces for the Electrochemical

Sensing of Dopamine. 2017;

441. Fortgang P, Tite T, Barnier V, Zehani N, Maddi C, Lagarde F, et al. Robust Electrografting on Self-Organized 3D Graphene Electrodes. ACS Appl Mater Interfaces. 2016;8(2):1424–33.

442. Collins RW. Measurement Technique of Ellipsometry. In 2018. p. 19–58.

443. Frederick E, Shaw TW, Frith MG, Bernasek SL. Synthesis of a surface mounted metal-organic framework on gold using a Au-carbene self-assembled monolayer linkage. Mater Chem Front. 2019;3(4):636–9.

444. Ciampi S, Bo T, Kilian KA, James M, Harper JB, Gooding JJ. Functionalization of Acetylene-Terminated Monolayers on Si (100) Surfaces : A Click Chemistry Approach. 2007;(100):9320–9.

445. Zaba T, Noworolska A, Bowers CM, Breiten B, Whitesides GM, Cyganik P. Formation of highly ordered self-assembled monolayers of alkynes on Au(111) substrate. J Am Chem Soc. 2014;136(34):11918–21.

446. Silin V, Weetall H, Vanderah DJ. SPR studies of the nonspecific adsorption kinetics of human IgG and BSA on gold surfaces modified by self-assembled monolayers (SAMs). J Colloid Interface Sci. 1997;185(1):94–103.

447. Zhang D, Yan Y, Cheng W, Zhang W, Li Y, Ju H, et al. Streptavidin-enhanced surface plasmon resonance biosensor for highly sensitive and specific detection of microRNA. Microchim Acta. 2013;180(5–6):397–403.

448. Chen H, Lee M, Lee J, Kim JH, Gal YS, Hwang YH, et al. Formation and characterization of self-assembled phenylboronic acid derivative monolayers toward developing monosaccharide sensing-interface. Sensors. 2007;7(8):1480–95.

449. Shon YS, Lee S, Perry SS, Lee TR. The adsorption of unsymmetrical spiroalkanedithiols onto gold affords multi-component interfaces that are homogeneously mixed at the molecular level. J Am Chem Soc. 2000;122(7):1278–81.

450. Shevade A V., Zhou J, Zin MT, Jiang S. Phase behavior of mixed self-assembled monolayers of alkanethiols on Au(111): A configurational-bias Monte Carlo simulation study. Langmuir. 2001;17(24):7566–72.

451. Jeuken LJC, Daskalakis NN, Han X, Sheikh K, Erbe A, Bushby RJ, et al. Phase separation in mixed self-assembled

monolayers and its effect on biomimetic membranes. Sensors Actuators, B Chem. 2007;124(2):501–9.

452. Contreras-Naranjo JE, Aguilar O. Suppressing non-specific binding of proteins onto electrode surfaces in the development of electrochemical immunosensors. Biosensors. 2019;9(1).

453. Spiwok V. CH/π interactions in carbohydrate recognition. Molecules. 2017;22(7):1–11.

454. Hudson KL, Bartlett GJ, Diehl RC, Agirre J, Gallagher T, Kiessling LL, et al. Carbohydrate-Aromatic Interactions in Proteins. J Am Chem Soc. 2015;137(48):15152–60.

455. Lee J, Park JM, Jang WD. Fructose-sensitive thermal transition behaviour of boronic ester-bearing telechelic poly(2-isopropyl-2-oxazoline). Chem Commun. 2019;55(23):3343–6.

456. Rich RL, Myszka DG. Survey of the year 2007 commercial optical biosensor literature. J Mol Recognit. 2008;21(6):355–400.

457. Brooks WLA, Deng CC, Sumerlin BS. Structure-Reactivity Relationships in Boronic Acid-Diol Complexation. ACS Omega. 2018;3(12):17863–70.

458. Wang HC, Zhou H, Chen B, Mendes PM, Fossey JS, James TD, et al. A bis-boronic acid modified electrode for the sensitive and selective determination of glucose concentrations. Analyst. 2013;138(23):7146–51.

459. Zhang Q, Schepmoes AA, Brock JWC, Wu S, Moore RJ, Purvine SO, et al. Improved methods for the enrichment and analysis of glycated peptides. Anal Chem. 2008;80(24):9822–9.

460. Yan J, Springsteen G, Deeter S, Wang B. The relationship among pK a, pH, and binding constants in the interactions between boronic acids and diols - It is not as simple as it appears. Tetrahedron. 2004;60(49):11205–9.

461. Lorand JP, Edwards JO. Polyol Complexes and Structure of the Benzeneboronate Ion. J Org Chem. 1958;24(6):769–74.

462. Sun X, Zhai W, Fossey JS, James TD. Boronic acids for fluorescence imaging of carbohydrates. Chem Commun. 2016;52(17):3456–69.

463. Flink S, Van Veggel FCJM, Reinhoudt DN. Functionalization of self-assembled monolayers on glass

and oxidized silicon wafers by surface reactions. J Phys Org Chem. 2001;14(7):407–15.

464. Abad JM, Vélez M, Santamaría C, Guisán JM, Matheus PR, Vázquez L, et al. Immobilization of peroxidase glycoprotein on gold electrodes modified with mixed epoxy-boronic acid monolayers. J Am Chem Soc. 2002;124(43):12845–53.

465. Lee JW, Sim SJ, Cho SM, Lee J. Characterization of a self-assembled monolayer of thiol on a gold surface and the fabrication of a biosensor chip based on surface plasmon resonance for detecting anti-GAD antibody. Biosens Bioelectron. 2005;20(7):1422–7.

466. Bonanno LM, DeLouise LA. Steric crowding effects on target detection in an affinity biosensor. Langmuir. 2007;23(10):5817–23.

467. Matsumoto A, Matsumoto H, Maeda Y, Miyahara Y. Simple and robust strategy for potentiometric detection of glucose using fluorinated phenylboronic acid self-assembled monolayer. Biochim Biophys Acta - Gen Subj . 2013;1830(9):4359–64.

468. Fabre B, Hauquier F. Boronic Acid-Functionalized Oxide-Free Silicon Surfaces for the Electrochemical Sensing of Dopamine. Langmuir. 2017;33(35):8693–9.

469. Takahashi S, Anzai JI. Phenylboronic acid monolayer-modified electrodes sensitive to sugars. Langmuir. 2005;21(11):5102–7.

470. Choi S, Chae J. Methods of reducing non-specific adsorption in microfluidic biosensors. J Micromechanics Microengineering. 2010;20(7).

471. Love JC, Estroff LA, Kriebel JK, Nuzzo RG, Whitesides GM. Self-Assembled Monolayers of Thiolates on Metals as a Form of Nanotechnology. Chem Rev . 2005 Apr;105(4):1103–70.

472. Erb RA. The wettability of gold. J Phys Chem. 1968;72(7):2412–7.

473. Bromba C, Carrie P, Chui JKW, Fyles TM. Phenyl boronic acid complexes of diols and hydroxyacids. Supramol Chem. 2009;21(1–2):81–8.

474. Reichvilser MM, Heinzl C, Klüfers P. Boronic acid mono- and diesters of the aldopentoses. Carbohydr Res. 2010;345(4):498–502.

475. Norrild JC, Eggert H. Boronic acids as fructose

sensors. Structure determination of the complexes involved using 1 J CC coupling constants. J Chem Soc Perkin Trans 2. 1996;53(12):2583.

476. Frederix F, Bonroy K, Laureyn W, Reekmans G, Campitelli A, Dehaen W, et al. Enhanced performance of an affinity biosensor interface based on mixed self-assembled monolayers of thiols on gold. Langmuir. 2003;19(10):4351–7.

477. Zaccari I, Catchpole BG, Laurenson SX, Davies AG, Wälti C. Improving the dielectric properties of ethylene-glycol alkanethiol self-assembled monolayers. Langmuir. 2014;30(5):1321–6.

478. Pazur JH, Miskiel FJ, Liu B. The identification of furanose and pyranose ring forms of the reducing units of oligosaccharides. Anal Biochem. 1988;174(1):46–53.

479. Nicholls MP, Paul PKC. Structures of carbohydrate-boronic acid complexes determined by NMR and molecular modelling in aqueous alkaline media. Org Biomol Chem. 2004;2(10):1434–41.

480. Bérubé M, Dowlut M, Hall DG. Benzoboroxoles as efficient glycopyranoside-binding agents in physiological conditions: Structure and selectivity of complex formation. J Org Chem. 2008;73(17):6471–9.

481. Heuberger M, Drobek T, Spencer ND. Interaction forces and morphology of a protein-resistant poly(ethylene glycol) layer. Biophys J. 2005;88(1):495–504.

482. Silberring J, Ekman R. Mass Spectrometry and Hyphenated Techniques in Neuropeptide Research. 1st editio. John Wiley & Sons; 2002. 218–221 p.

483. Okutucu B, Önal S. Molecularly imprinted polymers for separation of various sugars from human urine. Talanta . 2011;87(1):74–9.

484. Tan J, Wang HF, Yan XP. Discrimination of saccharides with a fluorescent molecular imprinting sensor array based on phenylboronic acid functionalized mesoporous silica. Anal Chem. 2009;81(13):5273–80.

485. Nikitina VN, Zaryanov N V., Kochetkov IR, Karyakina EE, Yatsimirsky AK, Karyakin AA. Molecular imprinting of boronate functionalized polyaniline for enzyme-free selective detection of saccharides and hydroxy acids. Sensors Actuators, B Chem . 2017;246:428–33.

486. Kugimiya A, Takeuchi T. Surface plasmon resonance

sensor using molecularly imprinted polymer for detection of sialic acid. Biosens Bioelectron. 2001;16(9–12):1059–62.

487. Piletsky SS, Rabinowicz S, Yang Z, Zagar C, Piletska E V., Guerreiro A, et al. Development of molecularly imprinted polymers specific for blood antigens for application in antibody-free blood typing. Chem Commun. 2017;53(11):1793–6.

488. Gunasekara RW, Zhao Y. A general method for selective recognition of monosaccharides and oligosaccharides in water. J Am Chem Soc. 2017;139(2):829–35.

489. Stephenson-Brown A, Acton AL, Preece JA, Fossey JS, Mendes PM. Selective glycoprotein detection through covalent templating and allosteric click-imprinting. Chem Sci. 2015;6(9):5114–9.

490. Jin J, Han Y, Zhang C, Liu J, Jiang W, Yin J, et al. Effect of grafted PEG chain conformation on albumin and lysozyme adsorption: A combined study using QCM-D and DPI. Colloids Surfaces B Biointerfaces. 2015;136:838–44.

491. Silberring J, Ekman R, Dass C. Erratum to: Mass spectrometry and hyphenated techniques in neuropeptide research. J Am Soc Mass Spectrom . 2003 Mar;14(3):287–287.

492. Turhan KN, Sahbaz F, Güner A. A spectrophotometric study of hydrogen bonding in methylcellulose-based edible films plasticized by polyethylene glycol. J Food Sci. 2001;66(1):59–62.

493. Labouta HI, Gomez-Garcia MJ, Sarsons CD, Nguyen T, Kennard J, Ngo W, et al. Surface-grafted polyethylene glycol conformation impacts the transport of PEG-functionalized liposomes through a tumour extracellular matrix model. RSC Adv . 2018;8(14):7697–708.

494. Couture M, Ray KK, Poirier-Richard HP, Crofton A, Masson JF. 96-Well Plasmonic Sensing with Nanohole Arrays. ACS Sensors. 2016;1(3):287–94.

495. Matsishin M, Rachkov A, Lopatynskyi A, Chegel V, Soldatkin A, El’skaya A. Selective Amplification of SPR Biosensor Signal for Recognition of rpoB Gene Fragments by Use of Gold Nanoparticles Modified by Thiolated DNA. Nanoscale Res Lett. 2017;12(1):0–5.

496. Szunerits S, Spadavecchia J, Boukherroub R. Surface plasmon resonance: Signal amplification using colloidal gold nanoparticles for enhanced sensitivity. Rev Anal

Chem. 2014;33(3):153-64.